Universität für Bodenkultur Wien.

Department für Biotechnologie.

Instituts für Angewandte Mikrobiologie (IAM)

Vorstand. Ao.Univ.Prof. Dipl.-Ing. Dr.nat.tech. Florian Rücker

Betreuer. Assoc.Prof. Dipl.-Ing. Dr. Johannes Grillari

Characterization of SNEV function in DNA repair and adipogenic differentiation.

Dissertation zur Erlangung des Doktorgrades an der Universität für Bodenkultur Wien.

Abdulhameed khan (M.Phil.)

Date -05- 2015.

Dedicated to my parents and Uncle.

Appendix C: Delineation of the key aspects in the regulation of epithelial monolayer formation.

ACKNOWLEDGMENT.

First and foremost, I would like to express gratitude from the bottom of my heart to **Dr. Johannes Grillari** to supervise my PhD. I really appreciate all his guidance, support, and encouragement in both scientific and nonscientific matters, which not only helped me to complete this study but also prepared me to meet the future challenges.

I am also very thankful to **Dr. Regina Grillari** for introducing me to the world of cell culture. I am very grateful to **Hanna Dellago** for her great collaborative support in performing life span experiments**.** I am very thankful to **Markus Schosserer** for his collaboration on performing adipogenesis experiments in C.elegans and his innovative ideas, fruitful discussions and valuable suggestions that helped to complete this study.

I would like to extends my gratitude to all members of Grillari's lab; **Matthias Wieser, Ingo Lämmermann, Sylvia Weilner, Rita Reynoso, Rossella Monteforte, Lisa Schraml, Matthias Hackle, , Lukas Fliedl, Barbara Preschitz-Kammerhofer, Eva Harreither, Vinod Shanmukam** for their valuable support, suggestions and the great time we had together in the lab.

I am also very grateful to **Marcel Scheideler and Michael Karbiener** for their valuable collaborative support in performing micro array experiments.

I gratefully acknowledge the contribution of **Higher Education Commission (HEC) of Pakistan** who provided funds for this study.

Finally, I would like to express my heartfelt thanks to all friends and relatives who have supported me throughout my study. Special thanks to my parents, and my Uncle **Zaridad Khan**, for their support in difficult and frustrating times, and without them my study will only be a dream.

Thank you

Abdulhameed Khan

Abstract.

The long average life span that we are currently enjoying is a big success story of the advancement in medicine, nutrition and improved hygiene. On the other hand, at the same time poses challenges to our health care system in terms of frailty and age related diseases. However, the molecular mechanism controlling the development of age related pathologies is not well understood. It is therefore of prime importance to identify and characterize factors that promote healthy aging.

Recently, it has been shown that upon ectopic over expression of DNA repair factor SNEV, the life span of endothelial cells is prolonged more than double, accompanied by lower level of basal DNA damage and apoptosis as well as increased resistance to oxidative stress. In keeping with this, decreased SNEV level accelerate the entry into cellular senescence, therefore SNEV is considered as a promising modulator of healthy aging.

Here, this study shows that SNEV is a potential phosphorylation target of ATM Kinase, an enzyme that trigger a cellular stress response. SNEV is phosphorylated by ATM kinase upon oxidative stress and DNA damage. ATM dependent phosphorylation of SNEV modulates not only SNEV functions in DNA repair and suppression of apoptosis but also its life span extending effect as well.

In addition to this, SNEV expression is increased gradually during adipogenic differentiation of human adipose derived mesenchymal stem cells (hASCs). Knock down of SNEV inhibits adipogenesis both in hASCs and in C. elegans, whereas over expression of SNEV accelerates adipogenesis in hASCs. In addition to SNEV, Werner (WRN) is also required for adipogenesis in hASCs and C. elegans.

In sum, this report revealed novel functions of SNEV that will enhance our understanding of SNEV in DNA repair and adipogenesis.

Zusammenfassung.

Die lange durchschnittliche Lebensdauer, die wir derzeit genießen, ist eine große Erfolgsgeschichte des Fortschrittes in der Medizin, der Ernährung und der verbesserten Hygienebedingungen. Gleichzeitig stellt diese hohe Lebenserwartung eine große Herausforderung an unser Gesundheitssystem dar, vor allem in Bezug auf die damit verbundene Gebrechlichkeit und die altersbedingten Krankheiten. Der molekulare Mechanismus, der die Entwicklung dieser altersbedingten Krankheiten kontrolliert, ist noch weitgehend unbekannt. Es ist daher von größter Bedeutung, jene Faktoren zu identifizieren und zu charakterisieren, die ein gesundes Altern fördern.

Diese Studie zeigt, dass SNEV ein potentielles target der ATM Kinase ist, ein Enzym, das eine zelluläre Stressreaktion auslöst. SNEV wird von der ATM-Kinase bei oxidativen Stress und DNA-Schäden phosphoryliert. ATM abhängige Phosphorylierung von SNEV moduliert nicht nur SNEV Funktionen in der DNA-Reparatur und der Unterdrückung der Apoptose, sondern hat auch lebensverlängernde Wirkung.

In jüngster Zeit hat sich gezeigt, dass bei ektopischen Überexpression des DNA-Reparatur-Faktors SNEV sich die Lebensdauer von Endothelzellen mehr als verdoppelt, begleitet von geringeren basalen DNA-Schäden und Apoptose sowie eine erhöhter Beständigkeit gegenüber oxidativem Stress. Übereinstimmend damit beschleunigt ein verminderter SNEV -Level den Einstieg in zelluläre Seneszenz. Wir betrachten daher SNEV als vielversprechenden Regulator des gesunden Alterns.

Zusätzlich wird SNEV Expression während der adipogenen Differenzierung von humanen, mesenchymalen Stammzellen gesteigert. Ein Knock Down von SNEV hemmt Adipogenese sowohl in hASCs als auch in C. elegans, während Überexpression von SNEV die Adipogenese in hASC beschleunigt. Neben SNEV ist auch Werner (WRN) für die Adipogenese in hASCs und C. elegans erforderlich.

In Summe zeigt diese Studie neue Funktionen SNEV, die unser Verständnis von SNEV im Bezug auf DNA-Reparatur und Adipogenese verbessern werden.

Aim of the Thesis

Aim of the Thesis.

This thesis is a compilation of two independent research projects and is prepared in accordance to the guidelines of the University of Natural resources and Life Sciences, Vienna.

The objective of this thesis was to further characterize the role of human protein SNEV in DNA damage repair and adipogenic differentiation of human adipose derived mesenchymal stem cells (hASCs) and in *C. elegans*.

In one project, SNEV phosphorylation and its physiological relevance in the context of oxidative stress induced DNA damage, cellular life span regulation and apoptosis was investigated. The respective paper has been published and my contribution was to perform all cell culture and protein analysis work but the life span experiment and the mass spectrometry for identification of the SNEV phosphorylation site. In addition, I have helped in interpreting the results, drafting the images and commenting on the manuscript.

In the second project, the role of SNEV in adipogenic differentiation of human adipose derived stem cells and in C. elegans was investigated. This paper is currently under revision. My contribution was in planning the experiments, performing them, and drafitng the manuscript. The work on C. elegans was kindly planned and performed by Markus Schosserer.

The contents of this thesis include a combined introduction and material & methods section. The results are described separately, followed by a combined discussion and references.

1- Introduction

1. Introduction

State of the art.

1.1. *Aging*

Aging is nearly a universal biological process observed in a diverse array of species ranging from unicellular yeast to multicellular human beings. In simple words aging is a biological process of getting old in a deleterious sense. In advance age, the physiological functions of cells, tissues, organs decrease and vulnerability to diseases and death increase. This may explain why the incidence of various diseases such as cancer, atherosclerosis, osteoporosis, cataract, diabetes, hypertension, loss of fat, neurodegeneration, renal failure are more common in old age then in young once. Therefore, it will be more likely to say that aging is an important mortality factor and according to an estimate, every day 100,000 peoples die all over the world due to aging and age related diseases(Lopez et al., 2006). Besides increasing mortality, aging also negatively influence economic development by reducing the availability of work force, rise in wages and increase in medical expenses associated with health care.

'Why do we age?' is the question which is not yet fully answered despite the efforts of centuries, and in this struggle, thousands of books were written and hundreds of theories were proposed, however none of these efforts were sufficient in explaining all aspects of aging. These theories blamed various factors, such as accumulation of cross linked proteins, increased metabolic rate, generation of free radicals, wear and tear out of vital constituents of cell, immune deficiency, DNA damage are responsible for aging (Rose, 1988). No doubt, these theories are fantastic efforts and somehow explain some, but not all aspects of aging. However, one of these is the best accepted theory so far, the disposable soma theory by Tom Kirkwood(Kirkwood, 1977), which also comprises the idea that genomic instability is the precipitating factor of aging, which gained significant popularity among gerontologist because it withstood many tests and keeps on being reaffirmed (Davidovic et al., 2010).

1.2. *DNA damage and aging*

It has long been suspected that aging is closely linked with damage to the cellular machinery which is constantly exposed to both intrinsic and extrinsic threats. UV, ionizing radiation and other environmental toxic agents are important extrinsic sources of damage, whereas, intrinsic sources of damage are reactive oxygen species (ROS) and spontaneous hydrolysis reactions, generated during normal metabolic activities. These agents harm both micro and macro-molecular structures of the cell, including DNA. In principle, all other macromolecules are renewable except DNA. DNA is the most precious and prime information molecule of cellular machinery and any error it acquire is deleterious and poses detrimental consequences on cellular and organismal homeostasis. Due to the importance of DNA in cellular machinery, nature has heavily invested in maintaining its integrity, by developing a mechanism that senses, signals, and repairs any discontinuity or distortion in DNA structure. This prompt cellular response is called DNA damage response (DDR)(Garinis et al., 2008). By contrast, if the damage is too severe or cells are defective in DNA repair, they acquire one of three possible fates:

a) Cells may undergo death (by any form including apoptosis, necrosis and other), a cellular form of suicide that removes damaged cells from a cell population.

b) Cells may stop dividing and enter into an irreversible state of growth arrest, called senescence.

c) Cells may acquire harmful mutations and bypass the cell cycle arrest barrier and become cancerous.

Therefore, it is speculated that deficiency in DNA repair capacity contribute to aging via increasing cell senescence/apoptosis (Best, 2009). Further support to this notion is provided by patients suffering from premature aging syndromes (PS). PS such as Werner syndrome (WS), Cockayne syndrome (CS), Trichothiodystrophy (TTD), Xeroderma pigmentosa (XP), are rare genetic disorders that arise due to defective

DNA repair and results in earlier appearance of aging symptoms(Ariyoshi et al., 2007; Bertola et al., 2006). Werner syndrome, is a type of premature aging syndrome, arise due to mutation in the Werner gene (WRN). WRN is a RecQ helicase involved in DNA repair. Patients suffering from Werner syndrome display signs and symptoms of normal aging such as gray hair, loss of subcutaneous fat, alopecia, high blood pressure, atherosclerosis etc., at an early stage of life, that normally appear in late life (Goto, 2000). Cells deficient in Werner gene are more prone to senescence (Kipling et al., 2004) and apoptosis (Pichierri et al., 2001). Furthermore mice deficient in nucleotide excision repair (NER) and non-homologous end joining (NHEJ) pathways also acquire aging early (Rossi et al., 2007; Ruzankina et al., 2007).

Although these models are extremely valuable in improving our knowledge of defective aging, the question is if life span can be extended by improving DNA repair machinery in multicellular organisms? Various studies were conducted to find the answer, but the results are somehow ambiguous.

Over expression of poly (ADP-ribose) polymerase 1, sensor of DNA breaks and important component of BER (Base Excision Repair) pathway, reduce life span in mice (Mangerich et al., 2010) and fungal model of aging, Podospora anserine(Muller-Ohldach et al., 2011). Over expression of DNA repair factor GADD45 in the nervous system of D. melanogaster reduced single strand (SS) breaks and significantly extend life span (Plyusnina et al., 2011), while over expression in the whole animal was lethal (Perets et al., Genetics 2007).

In contrast to this, some reports show that life span can be prolonged by enhancing the activity of the DNA repair machinery. Over expression of SIRT1 homologue in Drosophila and C. elegans and prolonged life span (Rogina and Helfand, 2004; Tissenbaum and Guarente, 2001). Over expression of BubR1, an essential component of mitotic check point, in mice extends their life span (Baker et al., 2013). Pharmacological interventions specifically decreasing the load of DNA damage also supported the fact that better repair can extend life span. For example, Aspirin reduced oxidative DNA damage (Hsu and Li, 2002) and extend life span in mice (Strong et al., 2008).

1.3. *Senescence, the link between DNA damage and aging.*

The second possible fate acquired by cells with poor DNA repair capacity is an irreversible state of growth arrest called senescence. Senescence in its simplest term is a condition in which cells, despite being alive, are unable to proliferate. Senescent cells are large, flat granular and metabolically active but lack replicative potential and are positive for senescence-associated β-galactosidase staining. In addition to morphological changes, senescent cells also differ in their chromatin organization and gene expression profile, as compared to normal cells. These changes include secretion of numerous pro inflammatory cytokines, chemokines, growth factors, and proteases, a feature named senescence-associated secretory phenotype (SASP) (Campisi, 2013).

Initially, senescence was discovered by Leonard Hayflick in the early 60ies in human fibroblasts which lost their replicative potential after extensive serial passaging in culture(HAYFLICK and MOORHEAD, 1961). This process was later on given the name of replicative senescence and was causally linked to telomere loss (Harley et al., 1990). Later on, subsequent studies showed that in addition to telomeric loss, senescence can also be induced prematurely in early passage cells by inducing DNA damage (Di Leonardo et al., 1994), disruption of heterochromatin (Ogryzko et al., 1996) and by activation of oncogenes (Serrano et al., 1997). These studies demonstrate that even though senescence can be triggered by different stimuli, but what is common in these stimuli is that they all involve a DNA damage response (DDR).

The role of senescence in aging postulated by Hayflick (HAYFLICK and MOORHEAD, 1961) was further strengthened by subsequent studies. Senescent cells accumulate in tissues of human (Minamino et al., 2004), primate (Herbig et al., 2006), and rodents (Melk et al., 2003) with increasing age. This increase in senescent cells may contribute to aging and age related degenerated pathologies either by interfering with tissue renewal, or by altering the microenvironment of tissue via secretion of various inflammatory cytokines (Campisi, 2005). This notion is further supported by study conducted in BubR1 progeroid mice in which targeted removal senescent cells delayed onset of at least three prominent age-associated diseases, cataract, sarcopenia, and loss of adipose tissue (Baker et al., 2011). Similarly, telomerase gene therapy in mice remarkably improved insulin sensitivity, osteoporosis, neuromuscular

coordination and several others molecular biomarkers of aging(Bernardes de Jesus et al., 2012).

In addition to its detrimental role in organismal aging (Baker et al., 2011), senescence also has some positive aspects. Historically, senescence has been viewed as a cell protective response against tumorigenesis, because senescent cells do not divide, and therefore will limit the spread of tumor(Serrano et al., 1997). In addition to this, recent discoveries showed that senescence is also beneficial in complex biological processes such as embryonic development (Muñoz-Espín et al., 2013), tissue repair (Krizhanovsky et al., 2008), wound healing (Jun and Lau, 2010).

1.4. *DNA damage, Aging and adipose tissue:*

Cells defective in DNA repair capacity are highly prone to senescence and apoptosis. Increased senescence/apoptosis in stem /progenitor cell pools reduce the number of stem cells and impair their differentiation potential. This reduction in number and functional impairment of stem cells interfere with tissue homeostasis, and leads to tissue degeneration, a hall mark of aging. Adipose tissue is one of those tissues which undergo degeneration in both premature and normal aging.

Adipose tissue in mammals, including humans it is divided into two categories, white adipose tissue (WAT) and brown adipose tissue (BAT), which are histologically and functionally different (Saely et al., 2011).

Adipose tissue or body fat is a form of loose connective tissue, present at several anatomical site, mainly below the skin (subcutaneous fat), around internal organs (visceral fat), bone marrow (yellow fat) and breast tissues, etc. It is mainly composed of adipose stem cells (precursor of adipocytes) adipocytes (fat storing cells), adipose tissue macrophages , fibroblast, vascular endothelial cells and nerve (Musi and Guardado-Mendoza, 2014). Adipocytes are the functional fat storing cells arise from differentiation of pre adipocytes in response to positive caloric imbalance (Rosen et al., 2000). This process is called adipogenesis.

1.5. *Impact of adipose tissue on health.*

Adipocytes, the functional unit of adipose tissue, extract free fatty acids from the blood stream and store them as neutral triglycerides. This stored energy is released during starvation time in the form of fatty acids and glycerol by means of lipolysis (Ahmadian et al., 2010). In addition to fat storage, adipose tissue also regulates various physiological processes such as food intake, insulin sensitivity, and inflammation, via secretion of various hormones such as leptin, adiponectin, resistin, complement components, plasminogen activator inhibitor-1, TNF-α, IL-6, visfatin, (Fonseca-Alaniz et al., 2007; Musi and Guardado-Mendoza, 2014). Furthermore, adipose tissue also protect internal organs from mechanical shock and prevent heat loss by insulation. Changes in adipose mass, either increase or decrease, always impose various health complications. On the one hand, increase in adipose mass leads to obesity, which further give birth to type 2 diabetes, cardiovascular disease, sleep apnea, hypertension, high blood pressure, high blood cholesterol, high triglyceride level, osteoarthritis (Haslam and James, 2005). On the other hand loss of adipose tissue or lipodystrophy increase insulin resistance, dyslipidemia, deregulated thermogenesis in elder, hepatic steatosis, acanthosis nigricans, polycystic ovarian disease and hypertension (Garg and Agarwal, 2009).

1.6. *Impact of aging on adipose tissue.*

Adipose tissue, now doubt is one of the largest tissue of human body, but its connection to aging has come into focus only recently and is considered to be at the junction of mechanisms involved in genesis of age related diseases, inflammation, metabolic dysfunction, and longevity (Tchkonia et al., 2010). Aging induce profound alterations in mass, distribution and functions of adipose tissue. Adipose mass expand and reach its peak by early or mid-old age followed by a decline in very old age (Cartwright et al., 2007). In advance age, fat becomes dysfunctional and redistributed from the subcutaneous adipose reservoir into visceral adipose depot. In addition to this, deposition of fat at non adipose sites such ectopic sites including liver, bone marrow and muscles also increase (Sepe et al., 2010,Caso et al.,2013). This in turn increase the risk of diabetes, hypertension, cancers, cognitive dysfunction, and atherosclerosis (Tchkonia et al., 2010). Loss of subcutaneous fat in physiological and

premature aging, provides a possible link of involvement of DNA metabolism in adipogenesis because DNA damage is an important regulator of both form of aging. Loss of subcutaneous fat is observed at an early age in patients suffering from premature aging syndromes such as Werner syndrome (Caso et al., 2013; Mori et al., 2001), and Cockayne syndrome A (Kamenisch et al., 2010). Mouse models deficient in NER repair pathway (Karakasilioti et al., 2013) and BubR1 (Baker et al., 2004) showed increased ablation of fat tissue. The reasons of the resulted fat loss may lies in the reduced adipocyte size (Bertrand et al., 1980), or reduced adipogenesis (Karagiannides et al., 2001) or functional impairment of adipocyte due to reduce DNA repair capacity (Karakasilioti et al., 2013).

DNA repair, aging and fat metabolism are apparently different mechanism, how are these different mechanisms inter-linked? Which key players and pathways are involved?.

One of the possibility is that deficiency in DNA repair capacity increases the rate of cellular senescence or apoptosis(Best, 2009). Apoptosis deplete the stem/progenitor cell pool and thus impair tissue homeostasis. Similarly, increased number of senescent cells impairs stem/progenitor cells self-renewal and differentiation potential, and thus limit the tissue regeneration potential. In addition to this, senescent cells also secrete numerous cytokines and inflammatory factors that exert negative effect on tissue microenvironment and thus impair tissue homeostasis that leads to aging (Figure 1). Therefore, interventions that delay or limit fat tissue turnover, redistribution, or dysfunction might increase longevity and delay the onset of clinical consequences similar to those common in aging.

Thousands of proteins have been identified that are involved in different cellular processes. Many of those proteins are multifunctional. For example ataxia-telangiectasia mutated (ATM) and Rad3-related (ATR) proteins are stress-response kinases that respond to a variety of insults including ionizing radiation, replication arrest, ultraviolet radiation and hypoxia (Hammond and Giaccia, 2004). Similarly, Werner protein deficient in Werner syndrome, is involved in DNA repair and adipogenic differentiation (Lee et al., 2005; Turaga et al., 2009). One of those multitasker protein is SNEV (senescence evasion).

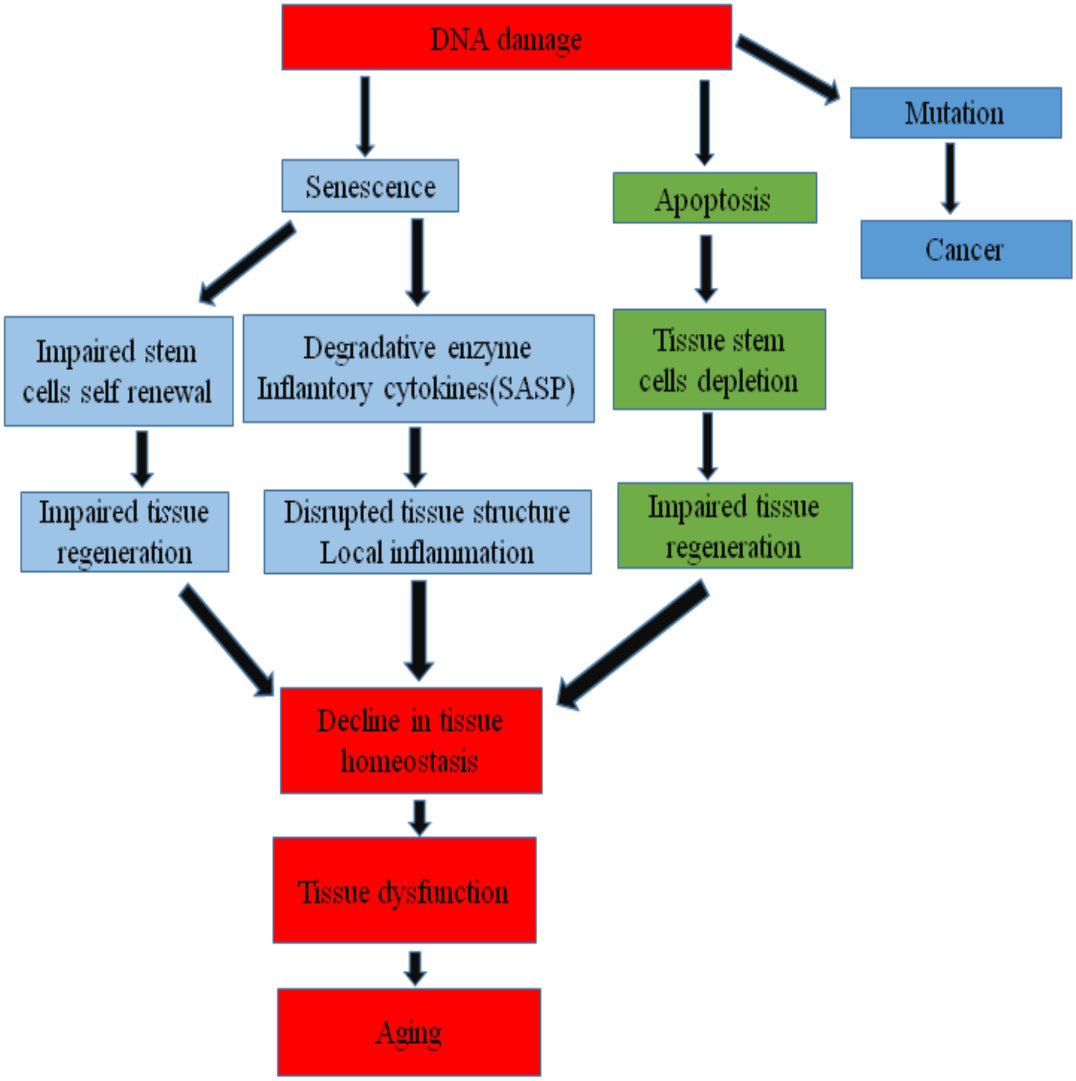

Figure 1-1: The possible pathways through which DNA damage may contribute to the aging process. DNA damage induce cellular senescence and apoptosis. Cell senescence impair the self-renewal capacity of stem cells and secrete cytokines such as degradative enzymes, inflammatory cytokines and epithelial growth factors, and thus interfere with regeneration of tissues or disrupt tissue structure, and cause local inflammation. Apoptosis interferes with tissue renewal and homeostasis by depleting the stem cell pool. Both pathways can cause compromised tissue homeostasis and function, which ultimately lead to aging.

2-Meet the Multifunctional protein SNEV

2. Meet the Multifunctional protein SNEV (Senescent evasion factor).

SNEV, a 56Kda multifunctional protein, is known by many synonyms due to its functionality, such as Prp19 (precursor RNA processing protein19), Pso4 (Psoralen resistant 4), xs9 (X rays sensitive mutant 9) or due to its localization in the cell such as hNMP200 (human nuclear matrix protein 200)(Brendel et al., 2003; Gotzmann et al., 2000; Grillari et al., 2005). To merge the different names of SNEV that derive from the yeast homologue that were synonymously termed Pso4 as well as Prp19, we suggest here to use SNEV.

SNEV is highly conserved among a diverse range of species including yeast, Drosophila melanogaster, metazoans (C. elegans), rodents, human, Arabidopsis thaliana (Gotzmann et al., 2000). SNEV is involved in pre-mRNA splicing, DNA repair, life span and apoptosis regulation and cellular differentiation. SNEV has been identified as an integral member of human CDC5l complex, tightly associated with CDC5L, PLRG1, and SPF27 (Grote et al., 2010). In addition to this, SNEV has also been identified as a member of Xab2 complex (Kuraoka et al., 2008).

1.7. *Structure of SNEV*

SNEV structural analysis showed that it contain a U-box domain at its N- terminal, followed by Self-interacting domain (SID), a low complexity region, a central coiled-coil domain, a globular domain, a charged region, and 7 consecutive WD 40 repeats at the C-terminal. These domains are essential for various functions of SNEV.

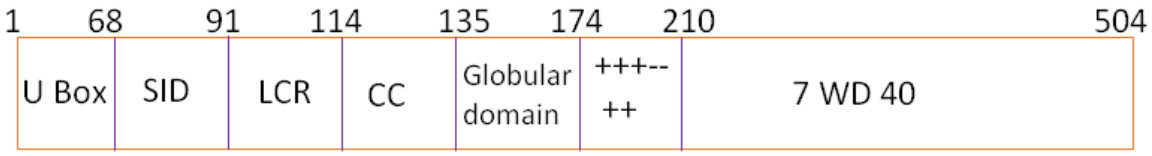

Figure 2.1: Domain architecture of human SNEV consists of a UFD2 like box (U-box), self-interacting domain (SID), a low complexity region (LCR), a coiled coil region (CC), a charged region and 7WD 40 repeats.

For example, U-box domain of SNEV is essential for its ubiquitin E3 ligase activity (Marechal et al., 2014); the coiled coil domain is required for its oligomerization and interaction with proteins (Ohi et al., 2003), whereas the 7 bladed WD 40 domain also mediate its interaction with other proteins(Vander Kooi et al., 2010).

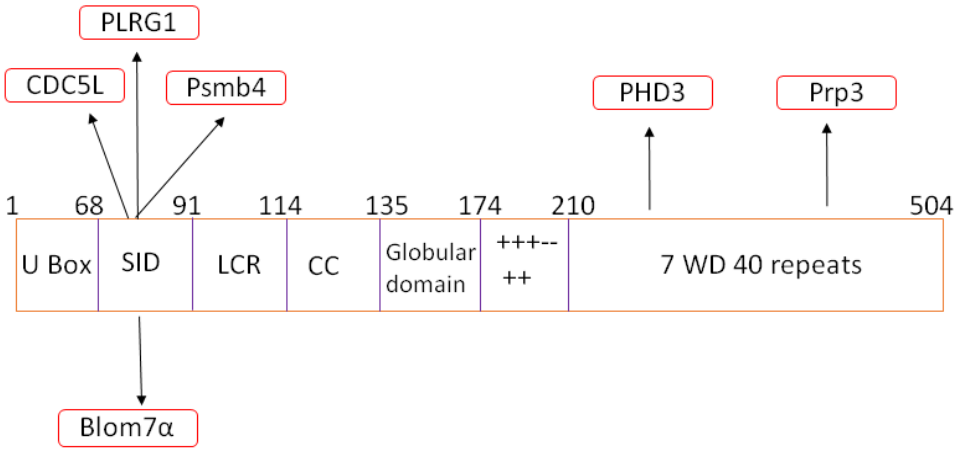

Figure 2.2: Characterized domains within SNEV structure and binding region of partner proteins

1.8. *SNEV role in Pre mRNA Splicing*

Removal of non-coding sequence (intron) and rejoining of the coding sequences (exon) of primary messenger RNA (pre mRNA) transcript to form a mature RNA (mRNA) is an essential post transcriptional modification, necessary for protein synthesis. This process is called splicing and is performed by a large megadalton and dynamic protein complex, called spliceosome, which comprised of five small nuclear ribonucleoproteins (snRNPs U1, U2, U4, U5, and U6) and more than 100 different polypeptides(Wahl et al., 2009). During splicing, spliceosome form a highly dynamic complex which due to joining and removal of various small ribonucleoprotein (snRNPs) and other protein factors undergo transitions into various complexes.

Spliceosomal assembly and transition into various complexes are shown in figure 2.3 (Matera and Wang, 2014).

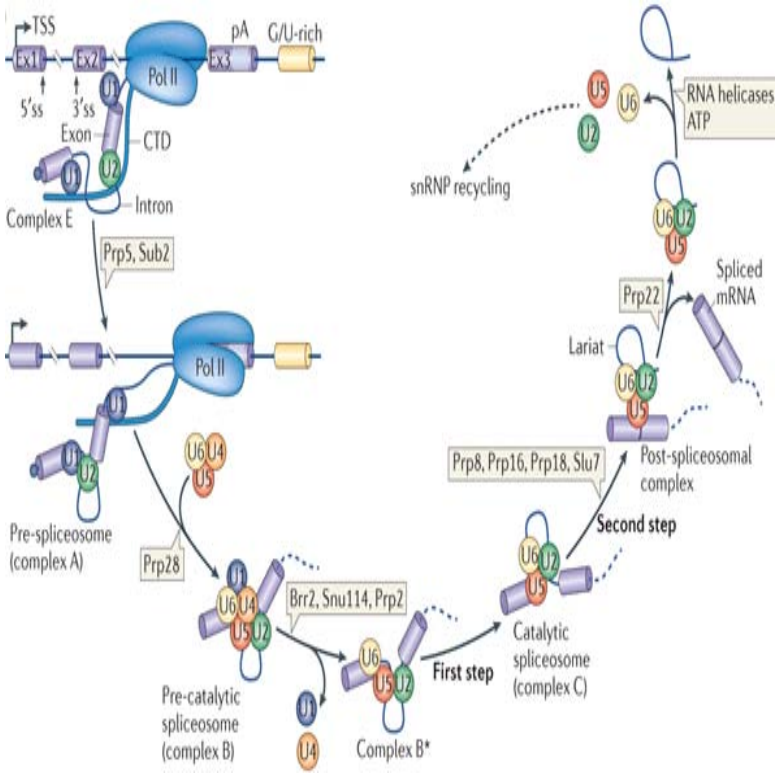

Figure 2.3: NTC in various spliceosomal (Hogg et al., 2010). Initially U1 and U2 assemble onto pre-mRNA in a co-transcriptional manner through recognition of the 5′ splice site (5′ss) and 3′ss and form complex E. U1 and U2 snRNPs then interact with each other to form the pre-spliceosome (complex A). In a subsequent reaction catalyzed by Prp28, the preassembled tri-snRNP U4–U6-U5complex is recruited to form complex B. Complex B undergoes a series of rearrangements to form a catalytically active complex B (complex B^*). Complex B^* then carries out the first catalytic step of splicing, generating complex C. Complex C undergoes additional rearrangements and then carries out the second catalytic step, resulting in the formation of post-spliceosomal complex. Finally, U2, U5 and U6 snRNPs are released from the mRNP particle and recycled for additional rounds of splicing.

SNEV sequence analysis and domain architecture shows high similarity with yeast Prp19 (Grillari et al., 2005). As yeast Prp19 is an integral component of nineteen complex (NTC) and is involved in pre-mRNA splicing. NTC interacts with the spliceosome prior to catalysis and remains associated with proteins identified in various spliceosomal complex as shown in figure 2.4(Hogg et al., 2010).

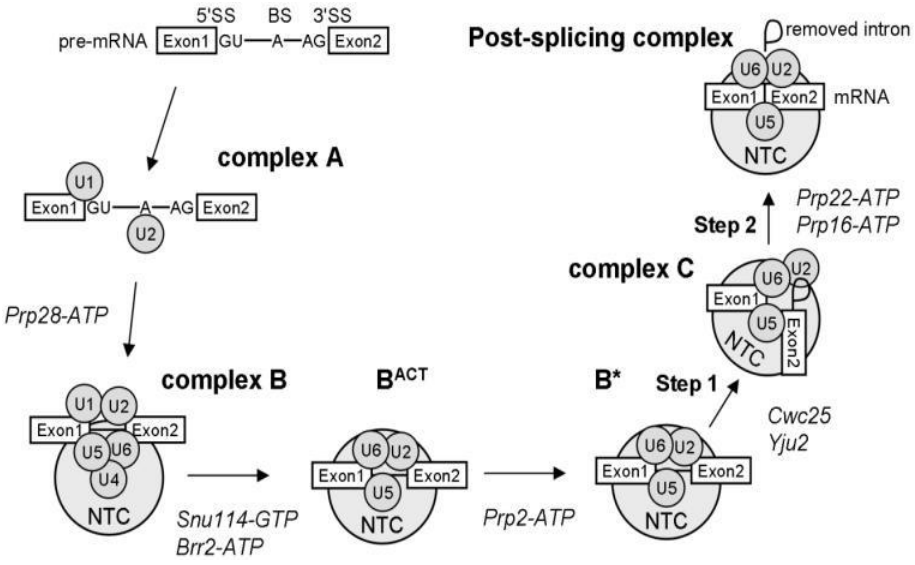

Figure 2.4: NTC in various spliceosomal (Hogg et al., 2010).

Based on SNEV sequence similarity with yeast Prp19, it was speculated that SNEV might also be involved in pre-mRNA splicing. This hypothesis was later on confirmed by various studies, conducted in different labs.

SNEV localized within the nucleus in discrete nuclear regions called nuclear speckles (Gotzmann et al., 2000) which are rich in splicing factors. SNEV colocalized within nuclear speckles with sm proteins. We also showed that SNEV interact with pre-mRNA splicing proteins bloom7α (Grillari et al., 2009) and exo70 (Dellago et al., 2011). Depletion of SNEV in Hela cells nuclear extract, impair splicing by interfering with spliceosomal assembly which is restored upon addition of SNEV (Grillari et al., 2005).

1.9. *SNEV and the ubiquitin proteasome system*

Ubiquitination is a multistep posttranslational modification of proteins, by which Ubiquitin, a small regulatory polypeptide, comprised of 76 amino acids, is transferred through a series of enzymes to its substrate and alter their function and/or localization. Ubiquitination starts by activation of ubiquitin by ubiquitin activating enzyme (E1), which then transfer it to ubiquitin conjugating enzyme (E2), and finally to the amino group of substrate lysine (K) via ubiquitin ligase (E3). Figure 2.5 describe how ubiquitin is transferred to the substrate.

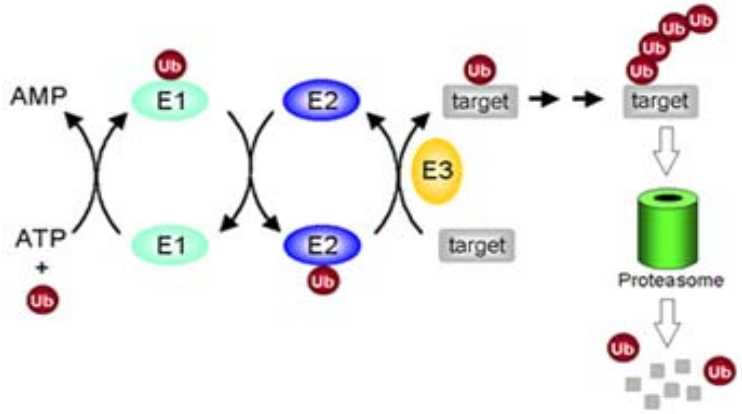

Figure 2.5: Ubiquitin is first activated by an E1, or ubiquitin-activating protein which couples ATP hydrolysis to the formation of a thioester bond between the active-site cysteine of the E1 and the carboxyl terminus of ubiquitin. The E1 then transfers the activated ubiquitin to the active-site cysteine of an E2, or ubiquitin-conjugating enzyme. Finally, the E3, or ubiquitin-protein ligase, facilitates the transfer of the ubiquitin from the E2 to a lysine on the target protein (Matyskiela et al., 2009).

The fate of substrate depend on which lysine of the ubiquitin is used. For example binding of the ubiquitin with Lys^{48}, is the major signal that target proteins for proteosomal degradation (Weissman, 2001). On the other hand ubiquitination at Lys^{63} linked chains usually does not result in proteolysis, but regulate protein localization, assembly of DNA repair complexes, or activation of the NF-κB transcription factor (Chen and sun, 2009).

SNEV bears a U box domain and Ubox containing proteins has been identified as a new class of E3 ligases (Hatakeyama et al., 2001), therefore it was speculated that SNEV might also be involved in ubiquitination of the substrate. Later on subsequent studies confirmed that SNEV possess an E3 ligase function and mediate ubiquitination of heterologous substrates at heterologous lysine residues (Hatakeyama et al., 2001; Marchal et al., 2014; Song et al., 2010). SNEV displays E3 ligase activity both in vitro (Hatakeyama et al., 2001) and in vivo(Löscher et al., 2005). In vitro SNEV interact with ubiquitin conjugating enzyme Ubc3 via its U box domain and mediate lys^{48}linked poly ubiquitination of substrate (Hatakeyama et al., 2001). Since lys^{48} linked poly ubiquitin chains are a signal for proteosomal degradation (Weissman, 2001), therefore it is suggested that SNEV direct its substrate for proteosomal degradation. This hypothesis has been further supported by the fact that SNEV interact with proteosome (Löscher et al., 2005), and this interaction is also conserved in other species (Davy et al., 2001; Sihn et al., 2007). As SNEV does not accumulate

in the cells upon proteosomal inhibition, but its localization with proteosome increase, therefore it is suggested that SNEV might bring its substrate to the proteosome for degradation. Hatakeyama et al also showed that SNEV not only ubiquitinate other substrates but also decorate itself with ubiquitin (Hatakeyama et al., 2001). Ubiquitinated SNEV loses its affinity for members of CDC5L complex, suggesting that ubiquitination induce conformational changes in SNEV (Lu and Legerski, 2007).

1.10. *SNEV has yet undefined role in DNA Repair.*

Yeast homologue of SNEV has been implicated in the repair of damaged DNA (Grey et al., 1996; Henriques et al., 1989) and these observations has also been tested and confirmed in human cells by several independent studies.

SNEV expression is strongly induced in response to DNA damage (Mahajan and Mitchell, 2003). SNEV interact with DNA in a sequence independent manner. We previously demonstrated that SNEV over expressing HUVECs were more resistant to DNA damage induced apoptosis (Voglauer et al., 2006). SNEV knock down is associated with increased accumulation of unrepaired DNA and apoptosis (Mahajan and Mitchell, 2003). SNEV over-expression also protect UV induced apoptosis while its knock down has the opposite effect (Lu et al., 2014).

SNEV act upstream of ATR (Ataxia telangiectasia and Rad3 related) kinase, famous in sensing DNA damage. Depletion of SNEV destabilized ATR and impair its role in S phase cell cycle arrest (Zhang et al., 2009). SNEV localized at DNA damage site via direct binding with RPA in response to DNA damage and facilitate the recruitment of ATR regulatory partner ATRIP at the damage site. Depletion of SNEV impair ATR activation, resumption of stalled replication fork and its progression on damaged DNA (Marchal et al., 2014). SNEV is required for resumption of DNA replication fork stability and/ or replication restart after hydroxyl urea (HU) induced replication stress and also reduced both spontaneous and HU induced DNA double strand lesions (Abbas et al., 2014).SNEV also participates in the initial end-resection step of homologous recombination (HR) pathway of DSBs repair, possibly by regulating the protein level of BRCA1 (Abbas et al., 2014).

1.11. *SNEV Role in Cellular differentiation*

Besides playing an important role in pre mRNA splicing, ubiquitin proteosome system and DNA repair, murine Prp19beta, a splice variant of mPrp19alpha is involved in cellular differentiation. The notion that SNEV is involved in cellular differentiation stem first from the observation that SNEV mRNA is down-regulated in the hippocampus of Alzheimer's disease patients (Blalock et al., 2004). Forced expression of the alpha variant enhanced neuronal differentiation (Urano-Tashiro et al., 2010) whereas over expression of Prp19beta suppressed neuronal differentiation and stimulated astroglial cell differentiation (Urano et al., 2006). Cho et al reported that murine SNEV is involved in regulation of adipogenic differentiation of 3T3 cells (Cho et al., 2007). As 3T3 cells are valuable model of adipogenesis, however due to species-specific differences, studies conducted using 3T3 cells are less convincing in interpreting human adipogenesis, and give rise the question if SNEV is also involved in adipogenesis of human adipose derived mesenchymal stem cells(hASCs)?.

3.Open questions and strategies

3. Open questions and Strategies

Proteins translated from mRNA undergo chemical decoration, such as phosphorylation, acetylation, ubiquitination, summoylation etc. These modifications collectively are called post translational modifications (PTM). PTM is an essential cellular mechanism to regulate protein functions and signaling networks. For example, phosphorylation of ATM at S1981 in response to DNA damage activate its kinase function (So et al., 2009). Upon activation, ATM phosphorylate a large number of downstream targets to elicit a proper DNA damage repair. In consequence to inhibition of ATM phosphorylation, cells were found defective in DNA damage repair and cell cycle progression. Ubiquitination of p53 by MDM2, signal for its proteosomal degradation, a mechanism used by cancerous cells to proliferate (Qi et al., 2014). Lagerski lab reported that SNEV undergoes ubiquitination in response to DNA damage. SNEV ubiquitination brings conformational change in the structure of SNEV/ CDC5L complex and increased SNEV binding affinity towards chromatin and reduced towards CDC5L and PLRG1, members of the SNEV/ CDC5L core complex (Lu and Legerski, 2007).

Proteomic screens performed to analyze proteins phosphorylated in response to DNA damage on ATM and ATR consensus site, which identified more than 900 phosphorylation sites in more than 700 proteins. The target list contain proteins previously known to be involved in DDR, but also identified some novel proteins which were previously not known to involved in DDR. The target proteins have been postulated to contain a consensus sequence that is phosphorylated by ATM in response to DNA damage (Figure 3.1) (Matsuoka et al, 2007).

Surprisingly, we found, that SNEV amino acid sequence contain the published ATM target consensus site (Figure 3.2) which is highly conserved among vertebrates but not in invertebrates. In this context an open question was:

3.1 Is SNEV a novel ATM Kinase substrate, and does its phosphorylation modulate its function in DNA repair and life-span regulation?

Previous studies in yeast showed that Prp19/SNEV is a direct phosphorylation target of Tel1 and/or Mec1, the yeast homologues of ATM and ATR, respectively (Smolka et al., 2007) The identification of this consensus site, the high degree of conservation of this motif strongly suggest that SNEV is a promising potential ATM kinase target.

Figure 3.1: Distribution of amino acids surrounding the SQ-ATM target site (from: (Matsuoka et al, 2007).

```
M. musculus     113 ACRVIARLTKEVTAAREALATLKPQAGLI-VPQAVPSS*QPSVVGAG-EPMDLGELVGMTP 170
R. norvegicus   113 ACRVIARLTKEVTAAREALATLKPQAGLI-VPQAVPSS*QPSVVGAG-EPMDLGELVGMTP 170
H. sapiens      113 ACRVIARLTKEVTAAREALATLKPQAGLI-VPQAVPSS*QPSVVGAG-EPMDLGELVGMTP 170
D. rero         113 ACRVIARLTKEVTAAREALATLKPQAGLV-APQAAPAS*QPAAVGAGGEAMEVSEQVGMTP 171
D. melanogaster113 ACRVIARLNKEVAAAREALATLKPQAGIANAPTAIPQPALASEAGG-AAAHPMEQAGMSA 171
C. elegans      114 ACRVISRLSKELTAAREALSTLKPHTSAK-VDDDVSID------------ESEDQQGLSE 160
S. cerevisiae   119 AKLVAAQLLMEKNEDSKDLPKSS*QQAVAITREEFLQGLLQSSR-------DFVARGKLKA 171
```

Fig. 3.2: The consensus sequence surrounding the putative phosphorylation site is conserved in the SNEV amino acid sequence across different vertebrate species.

Therefore, we designed experiments to confirm if SNEV is phosphorylated by ATM and its cytoprotective role in DNA damage/oxidative stress and life-span extension in various model cells.

In sum, based on preliminary data and previous work from our lab, we generated the hypothesis depicted in figure 3.3.

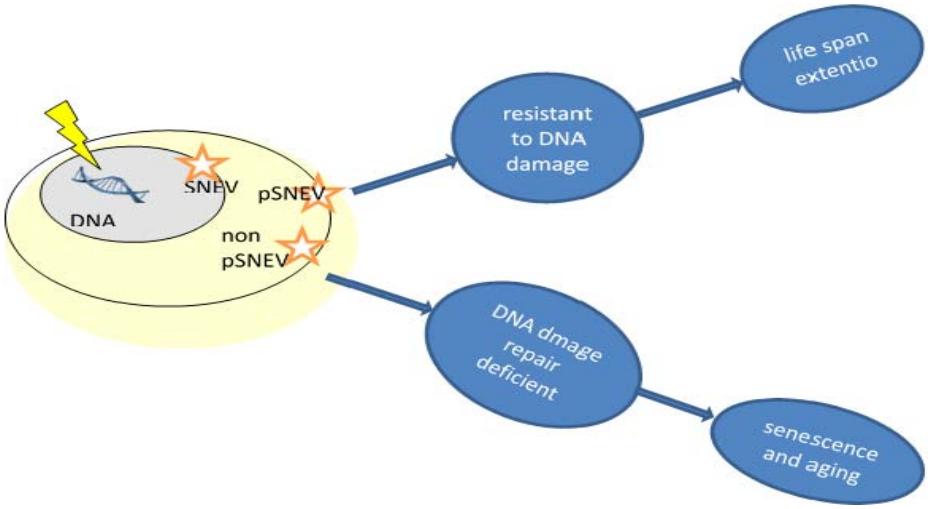

Figure 3.3: Overview of our working hypothesis: SNEV stable over expression extends cellular life span upon by increasing cellular resistance to DNA damage, while disrupting the conserved ATM dependent phosphorylation site might accelerate senescence and aging, probably due to DNA repair defect.

In order to verify our working hypothesis, we used a combination of approaches, which I will describe in the following in brief and which we also published recently (Dellago, Khan et al., 2012).

Phospho-specific SNEV antibody was generated in rabbit by injecting a synthetic 10 amino acid phosphopeptide, spanning the ATM target site. The specificity of the antibody was characterized by immunoflourescence (IF) and western blotting and was given the name anti-pSNEV (S149). Use of anti-pSNEV (S149) antibody, both in IF and western blotting, helped to track the dynamics of SNEV phosphorylation in response to DNA damage.

Use of ATM specific inhibitory molecule named Kudos 55933 (Hickson et al., 2004), helped in confirming, that SNEV Phosphorylation at Serine 149 (S149) is ATM dependent. The physiological relevance of SNEV phosphorylation was determined by generating stable HUVECs, overexpressing either wtSNEV (wtSNEV HUVECs) or point mutant SNEV (S149A HUVECs). The point mutant SNEV was generated by replacing Serine 149 (S149) amino acid with Alanine amino acid. Another point mutant that mimic constitutive phosphorylation was generated by substituting Serine149 by Aspartic acid (S149D) and expressed (SNEV S149D HUVEC). The structural and electrostatic properties of Aspartic acid resemble those of phospho-Serine and therefore mimic constitutive phosphorylation (Paleologou et

al., 2008). These cells were characterized with respect to their resistance to DNA damage and oxidative stress, their replicative life span, subcellular localization of SNEV. Single cell gel electrophoresis under alkaline condition was used to study basal level DNA double strand breaks (Wojewódzka et al., 2002). The principal of this assay, called comet assay is that DNA due to the presence of –VE charge, move towards cathode in an electric field and form a tail (comet). The length of the DNA tail (comet) is proportional to the DNA damage. As undamaged DNA retains its compact and highly organized structure and is too large to migrate in the field, whereas the DNA double strand break disrupt this organization and the fragments migrate and form a tail when an electric field is applied. DNA specific fluorescence probe was used to visualize the DNA. The fluorescence in the tail content was calculated and used to determine the extent of DNA damage. The importance of S149 phosphorylation in the context of oxidative stress and DNA damage was assessed by treating wt, S149A and S149D HUVEC cell lines with BSO and Bleomycin. BSO deplete cellular glutathione stores by inhibiting γ-glytamyl synthase (Griffith, 1982). Bleomycin treatment following BSO treatment catalyzes the formation of single and double strand breaks by direct binding with DNA in the presence of iron(Fe^{2+}) and O_2, and induce apoptosis (Chen & Stubbe, 2005). Annexin-V-FITC and Propidium Iodide staining assessed the rate of apoptosis after combined treatment of BSO and bleomycin. Annexin-V binds to phosphatidylserine, which is displayed on the cytosolic face of the plasma membrane in live cells and externalize by apoptotic cells (Koopman et al, 1994). Propidium Iodide (PI) is a DNA intercalating flouresecent molecule. Viable cells are impermeable to PI and therefore it is used to identify dead cells (Moore et al., 2007). This approach of combined use of Annexin-V & PI helped us to discriminate between early and late apoptotic cells. Early apoptotic cells stain positive for Annexin V but negative for PI, whereas both Annexin-V & PI stained the late apoptotic /necrotic cells. The percentage of apoptotic/necrotic cells were analyzed by flow cytometry, a technique used for counting and examining cells and other microscopic particles suspended in a fluid, when they passed through a laser beam in the flow chamber. Cells passing through the laser beam scatter the light, and fluorescent molecule found in or attached to the cell are excited and emit light at a longer wavelength than the light source. This combination of scattered and fluorescent

light is picked up by the detectors, and gave various types of information about the physical and chemical structure of each individual cell (Raveche et al., 2010).

3.2 Is SNEV involved in regulation of adipogenic differentiation of human adipose derived stem cell differentiation?

A previous study showed that the murine homologue of SNEV, mPrp19 is involved in adipogenic differentiation of 3T3-L1 cells (Cho et al., 2007). As 3T3 cell line is a valuable model of adipogenesis, however due to species-specific differences, studies conducted using 3T3 cells are less convincing in interpreting onset of human diseases. 3T3-L1 adipogenesis require essentially two round of cell division, called mitotic clonal expansion (MCE) before entering into adipogenic differentiation cycle (Tang et al., 2003), whereas human mesenchymal cells do not require MCE for adipogenesis (Qian et al., 2010). Previous study of Lindroos et al also revealed the differences in mouse and human adipogenesis. LMO3 has been shown to be non-essential for mouse adipogenesis but is critical for human adipogenesis (Lindroos et al., 2013). Due to the above mentioned differences in mouse and human adipogenesis, it is needed to confirm mouse results in human cells as well. Therefore, we went on to confirm, if SNEV is essential for adipogenesis, in human adipose derived mesenchymal stem cells (hASCs), which are the progenitor of adipocytes and is a more relevant model of human adipogenic differentiation. hASCs are multipotent mesenchymal cells that can successfully differentiate into adipogenic, osteogenic, chondrogenic lineage when exposed to appropriate lineage inducing reagents (Rodriguez et al., 2005).

Expression of SNEV both at mRNA and protein level and its intra cell localization was analyzed during adipogenesis. SNEV expression was inhibited via siRNA and its effect on adipogenesis was analyzed at molecular level by measuring the expression of PPARγ and FASN, which are the markers of adipogenesis. As an end point measurement of adipogenesis Oil red O staining was performed, which stain intracellular lipid droplets. In addition to this also triglyceride accumulation was quantified via triglyceride quantification kit. In order to test if SNEV is required of organismal adiopogenesis, the effect of SNEV knock-down in C. elegans was also analyzed. Micro array analysis of SNEV knock down hASCs and control culture after 3 days of adipogenic stimuli was performed to identify the molecular mechanism of

how SNEV effect adipogenesis, which revealed that down regulation of SNEV inhibit the expression of genes involved in PPARγ and insulin signalling pathways, whereas expression of genes involved in anti adipogenic TGF-β signalling pathway are up regulated in SNEV knock down hASCs. We next went on to investigate if SNEV overexpression accelerate adipogenesis. hASCs transiently transduced with SNEV and empty vector were subjected to adipogenesis. Adipogenesis was assessed by measuring the expression of PPARγ and FASN. Lipid droplets were stained by Oil red O and intracellular triglyceride accumulation was quantified by triglyceride quantification kit.

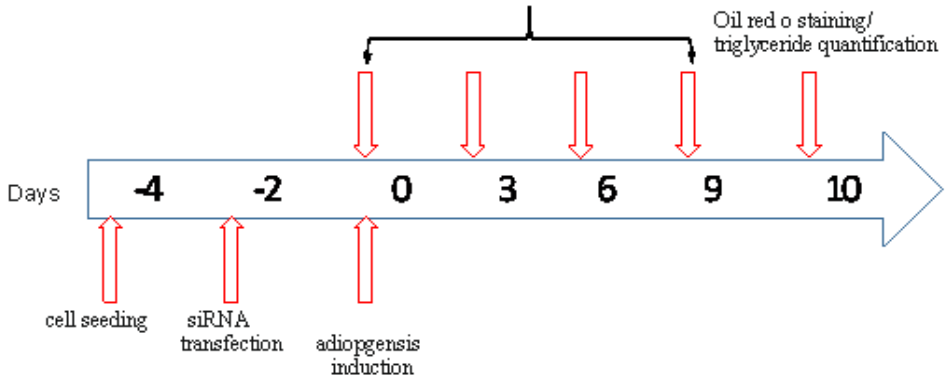

Figure 3-2: Schematic representation of our experimental plan.

4- Material and Methods

4. Material and Methods

4.1. *Cells and culture conditions*

HeLa cells were grown in RPMI1640 (Biochrom AG, Berlin, Germany) supplemented with 10% fetal calf serum (FCS).

Human diploid fibroblasts (HDF) were grown in DMEM/HAM's F12 1:2 (Biochrom AG, Berlin, Germany) supplemented with 10%FCS.

Human umbilical vein endothelial cells (HUVEC) were cultivated in EBM Basal medium plus EGM Single Quot Supplements & Growth Factors (Lonza, Basel, Switzerland) supplemented with FCS to a final 10%. For HUVEC, flasks were pre coated with 0.1% gelatin in PBS.

GFP-SNEV-Hela were established by transfecting Hela cells with a SNEV-BAC construct containing all regulatory elements obtained from Ina Poser, Max Planck Institute for molecular Cell Biology and Genetics, Dresden, Germany. GFP-SNEV-Hela were cultivated in RPMI1640 (Biochrom AG, Berlin, Germany) supplemented with 10% fetal calf serum (FCS) and 800 µg/ml G418 (Life technologies, Grand Island, NY, USA).

Confluent adherent cultures were detached using 0.1% trypsin and 0.02% EDTA and were passaged with an appropriate split ratio of 1:2 or 1:4 once or twice a week depending on confluence and population doubling level (PD). Subsequently, cumulative PDs were calculated as a function of passage number and split ratio.

4.2. *hASCs isolation and maintenance*

hASCs were isolated according to the protocol (Wolbank et al., 2009) and maintained in DMEM (4.5g/l glucose) supplemented with 4mM L-Glutamine (VWR #1.00286.1000), 10% FCS, 1 ng/ml βFGF(Sigma # F0291-25UG), 1x Primocin (Eubio # ant-pm-1) at 37°C and 5% CO_2. The donors gave informed consent before providing adipose samples. Thus, the study was performed in accordance with the declaration of Helsinki.

4.3. *C. elegans maintenance*

C. elegans strains were cultured under standard laboratory conditions on NGM agar as described previously (Brenner, 1974). Strains used in this work include N2 (provided by V. Jantsch) and CF1814 [rrf-3(pk1426) II and daf-2(e1370) III]. All strains are available through the Caenorhabditis Genetics Center (CGC). Worms were synchronized by timed-egg lay on fresh RNAi plates and transferred to FuDR containing plates upon adulthood (usually on day 4 after hatching).

4.4. *SNEV over-expression*

SNEV cDNA was amplified by PCR and cloned into the retroviral plasmid pLenti6. The negative control vector contained only the Blasticidin resistance gene. Retroviral particles were generated according to the manufacturer's protocol (Life Technologies). For SNEV over-expression 14000/1.9cm^2 hASCs were seeded in growth medium 48 hours prior to transduction and infected with retroviral particles according to the manufacturer's protocol (Life Technologies) at a multiplicity of infection (MOI) of 2 in DMEM (4.5 g/l glucose), supplemented with 4 mM L-Glutamine, 10% FCS, 1 ng/ml βFGF, 8 µg/ml Polybrene. The medium was replaced with adipogenesis inducing medium 48 hours post transduction

4.5. *RNA interference assays in C. elegans*

For the inactivation of DNA repair factors, feeding of double-stranded RNA expressed in bacteria was used as previously described (Timmons et al., 2001). RNAi constructs against *prp-19*, *wrn-1*, *xpe-1* and *M18.5*, derived from J. Ahringer's RNAi library, were distributed by Source BioScience. The HT115 strain of *E. coli* carrying the RNAi-construct, or the empty vector (L4440) as control, was cultured overnight in liquid LB medium with ampicillin and tetracyclin at 37°C. The bacteria were harvested by centrifugation, re-suspended in LB to a concentration of 60 mg/ml and 200 µl of this suspension was seeded on NGM plates containing 1 mM IPTG and 25 µg/ml Carbenicillin. The plates were incubated at 37°C overnight and used within one week.

4.6. *Stress treatment*

For hydrogen peroxide treatment, $2x10^5$ fibroblasts(HDF5)/ well were seeded in 6 well plates for 24 hours, followed by treatment with H_2O_2 (100,200, 400 µM/ml) for 1 hour and 100 µM/ml H_2O_2 for different time points (5, 15, 30, 60, 120 minutes).

For Bleomycin treatment, $2x10^5$ fibroblasts(HDF5)/ well were seeded in 6 well plates for 24 hours, followed by treatment with 2.5, 5, 10, 25, 50, 100µg/ml of Bleomycin for 1 hour and 25 µg/ml for different time points(5, 15, 30, 60, 120 minutes).

For Mitomycin C (MMC) treatment, $2x10^5$ fibroblasts (HDF5)/ well were seeded in 6 well plates for 24 hours. The next day cells were treated with different concentrations of MMC (2.5, 5, 10, 25, 50 µg/ml) for 24 hours.

4.7. *Oxidative Stress treatment*

To induce apoptosis, cells were seeded into 12-well cell culture plates at a density of 10000 cells /cm^2. To enhance the sensitivity of the cells to bleomycin-induced apoptosis cells were cultivated in the presence of 1mM BSO (buthionine-sulfoximine, Sigma Aldrich, USA) for 48 hours before treatment with 100 µg/ml of bleomycin (Sigma Aldrich) for further 24 hours.

Alternatively, cells were treated with 100 µg/ml of cisplatin (Sigma Aldrich, USA) for 24h to assay apoptosis induction by DNA cross-links.

Cell were scraped directly on ice in two fold (2X) SDS loading dye, sonicated and boiled. Proteins were separated by SDS gel electrophoresis in 4-12% BT gel (Life technologies, USA).

4.8. *Adipogenic differentiation*

14000 hASCs were seeded in 1.9 cm^2 plates in growth medium (DMEM) for two days prior to adipogenic induction. Adipogenesis was induced by replacing the growth medium with fresh DMEM supplemented with 549µM 3-Isobutyl-1-methylxanthine (#I5879-100MG Sigma), 1µM Dexamethasone (Sigma Adrich), 549µM Hydrocortisone (Sigma Aldrich, #H-0396) and 66µM Indomethacin (Sigma Aldrich,

I7378-5G), 100 µg/ml Primocin (Life Technologies, # ant-pm-1). Medium was exchanged twice a week until day 10, followed by Oil Red O staining. hASCs grown in DMEM low glucose/Ham`s F12,1:1(PAA # E15-012) supplemented with 10% FCS, 4 mM L-Glutamine, 100 µg/ml Primocin(Invivogen) were used as control. Total RNA and protein were isolated at specified time points during differentiation. Triglyceride contents were quantified by infinity T^m triglyceride quantification kit (ThermoScientific, #TR 22421) according to the manufacturer's recommended protocol and normalized to total protein concentration, measured by using the BCA kit (ThermoScientific).

4.9. *Oil red O staining of ASCs*

Oil red O staining of hASCs was performed on day 10 of differentiation. Differentiation medium was removed and cells were washed briefly with PBS twice and fixed by incubating in 3.6% formaldehyde in PBS for 1 hour at room temperature. Cells were then washed twice for 5 minutes each with PBS and incubated with 70% ethanol for 2 minutes, followed by 10 minutes incubation in Oil red O working solution (1.8mg/ml, Sigma). Cells were washed with PBS until all visible traces of remaining dye were removed. Pictures were taken by Leica DM IL LED Inverted Microscope with a 10x dry objective (Leica Microsystems CMS, Mannheim, Germany).

4.10. *Oil-Red-O staining in C. elegans*

Oil-Red-O staining in *C. elegans* was performed on day 6 after hatching as previously described (Soukas et al., 2009). Stained worms were embedded in Mowiol and pictures were taken on the next day on a Leica DM IL LED Inverted Microscope with a 10x dry objective

4.11. *Osteogenic differentiation*

2000 hASCs were seeded in 1.9 cm^2 plate 72 hours prior to induction of osteogenesis. Osteogenesis was induced by replacing the growth medium with fresh DMEM (low glucose GE Healthcare) supplemented with 10% FCS, 4 mM L-Glutamine (Sigma), 10mM L-Glycerophosphate (sigma), 150 µM Ascorbate-2-phosphate, 10nM vitamin-

D3 (Sigma), 10nM Dexamethasone (Sigma), 100 µg/ml Primocin. hASCs grown in DMEM low glucose/Ham`s F12, 1:1(PAA # E15-012) supplemented with 10% FCS, 4 mM L-Glutamine, 1x Primocin were used as control. The medium was replaced every third day with fresh medium until day 12. Osteogenic differentiation was assessed by Alizarin Red staining. To perform Alizarin Red staining, osteogenesis inducing medium was removed and cells were washed three times briefly with PBS, incubated with 70% ethanol for 1 hour at -20°C, and washed 3 times with PBS. Cells were then incubated for 10 minutes with gentle shaking with alizarin Red solution (200mg/ml)(Applichem # A2306,0025) followed by thorough washing with PBS until all visible traces of the remaining dye were removed. Pictures were taken on a Leica DM IL LED Inverted Microscope with a 10x dry objective.

4.12. *siRNA transfection in ASCs*

SNEV siRNA and control siRNA (Dharmacon, D-001810-10-20) was purchased from Dharmacon (Thermo Scientific, J-004668-05). For knock down of Werner, CSA, XPE, a pool of 4 pre-designed IBONI® siRNA (riboxx Life sciences) and control were used. 14000 hASCs were seeded in 1.9 cm^2 well plates 48 hours prior to siRNA transfections using 50 nM of the respective siRNAs. The siRNAs were introduced into cells using DharmaFECT1 transfection reagent (Dharmacon) according to the manufacturer instructions. Knock-down efficiency of siRNAs was determined 48 hours after transfection by qPCR.

4.13. *siRNA Treatment of C. elegans*

For the inactivation of DNA repair factors, feeding of double-stranded RNA expressed in bacteria was used as previously described (Timmons et al., 2001, Gene). RNAi constructs against *prp-19*, *wrn-1*, *xpe-1* and *M18.5*, derived from J. Ahringer's RNAi library, were distributed by Source BioScience. The HT115 strain of *E. coli* carrying the RNAi-construct, or the empty vector (L4440) as control, was cultured overnight in liquid LB medium with ampicillin and tetracyclin at 37°C. The bacteria were harvested by centrifugation, re-suspended in LB to a concentration of 60 mg/ml and 200 µl of this suspension was streaked out on NGM plates containing 1 mM IPTG and 25 µg/ml Carbenicillin. The plates were incubated at 37°C overnight and used within one week.

4.14. *qPCR analysis*

Total RNA from cells isolated at various time points was extracted using Trizol reagent (Life Technologies) according to the manufacturer's protocol. cDNA was synthesized from 500 ng of total RNA with the Dynamo cDNA synthesis kit (Thermo scientific) according to manufacturer instructions. qPCR analysis was performed using 5x Hot Firepol Eva green qPCR mix (MEDIBENA). Primers designed for qPCR are listed in the following Table. mRNA expression was normalized to GAPDH.

Gene name	Forward primer	Reverse primer
SNEV	TCATTGCCCGTCTCACCAAG	GGCACAGTCTTCCCTCTCTTC
PPARγ	AGCCTGCGAAAGCCTTTTGGTGA	GCAGTAGCTGCACGTGTTCCGT
FASN	AACTTGCAGGAGTTCTGGGAC	TGAATCTGGGTTGATGCCTCCG
GAPDH	TGTGAGGAGGGGAGATTCAG	CGACCACTTTGTCAAGCTCA
Werner	GTGGCGCTCCACAGTCAT	TCTTCCGAACACATGCCTTTC
CSA	GAGGACACGATATGCTGGGG	CCAGTCCCAAAACTCTCCGT
XPE	AAGAAACGCCCAGAAACCCA	ACATCTTCTGCTAGGACCGGA

4.15. *Microarray analysis*

Global gene expression analysis was performed by two-color microarrays for hASCs upon SNEV knock-down, as well as for hMADS cells at various stages of adipocyte differentiation. Metadata (experimental parameters and detailed procedures), raw data files and final (filtered and normalized) data are accessible via Gene Expression Omnibus (GEO, series records GSE64937 and GSE64845).

4.16. *ATM deletion in mouse embryonic fibroblasts*

Primary mouse embryonic fibroblasts (MEF) were prepared from E13.5 fetuses (*ATMflox/flox*). Cells were cultured in DMEM high glucose medium (Sigma-Aldrich) supplemented with 15% fetal bovine serum (Lonza), 1% L-glutamine (Gibco, now life technologies, Grand Island, NY, USA), 1% penicillin and strepromycin, 1% NEAA (non-essential amino acids, Gibco), 1% sodium pyruvate (Gibco) and β-mercaptoethanol (1:140000). Large T-Antigen was used to immortalize MEFs (*ATMflox/flox*). For the generation of retrovirus, Large T- Antigen -MSCVneo plasmid was co-transfected with the packaging plasmid pCL-Eco and the enveloping plasmid VSV-G in 293T cells. Supernatant was collected after 24 and 48 hours.

MEFs were transduced using 5 ml of filtered supernatant added to 5 ml cell culture medium in the presence of 8 mg/ml polybrene (Sigma-Aldrich). After 24 hours virus was removed. 14 days selection was started 72 hours after infection using 400µg/ml neomycin (Sigma-Aldrich).

In a second infection step, Large T-Antigen- immortalized MEFs were transduced with the Cre- pBabe-puro retrovirus for the Cre-mediated deletion of *ATM*. Selection was started 72 hours after transduction with 2µg/ml puromycin for 7 days. Medium was exchanged every 3rd day. Deletion of ATM was verified by PCR of genomic DNA using primer 1 (5' ATC AAA TGTAAA GGC GGC TTC 3') primer 2 (5'CAT CCT TTAATG TGC CTC CCT TCG CC 3') and primer 3(5'GCC CAT CCC GTC CAC AAT ATC TCT GC 3') giving rise to three fragments representing absence or presence of loxP sites or deletion of ATM.

4.17. *Plasmid construction, generation of recombinant retroviruses and cell line establishment*

SNEV cDNA was amplified by PCR and ligated into the retroviral plasmid pLenti6. The SNEV S149A point mutant was generated using the Quick-change Multi Site-Directed Mutagenesis Kit (Agilent, Santa Clara, CA, USA). The negative control vector contained only the blasticidin resistance gene. Retroviral particles were generated according to the manufacturer's protocol (Invitrogen). For cell line establishment, HUVECs (PD14) were infected with retroviral particles according to the manufacturer's protocol (Invitrogen, now life technologies, Grand Island, NY, USA) at a multiplicity of infection (MOI) of 4 in EBM with 10% FCS supplemented with 8 µg/ml Polybrene. Thereafter, transfectants were selected using 5 µg/ml blasticidin. Arising cell clones (similar number in all experiments) were grown as a mass culture. PDs post transfection (pT) were calculated starting with the first passage after selection was completed.

4.18. *Antibodies*

Prp19/Pso4 rabbit polyclonal antibody was from Bethy Laboratories (Montgomery, TX, USA) #A300-102A. ATM antibody [2C1] mouse monoclonal antibody was from Gene Tex (Irvina, CA, USA) #GTX70103. Moravian Biotechnology Ltd

(Bratislava, Slovakia) generated anti-pSNEV (S149) rabbit polyclonal antibody. Gamma H2A.X (phospho S139) mouse monoclonal antibody [9F3] was from Abcam (Cambridge, UK) #26350. ß-Actin mouse monoclonal antibody was from Sigma-Aldrich (St.Louis, MO, USA) #A-5441. GAPDH rabbit antibody FL-335 was from Santa Cruz (Santa Cruz, CA, USA) #sc-25778.

4.19. *SDS PAGE and Western Blotting*

For SDS PAGE, protein samples were mixed with 4x SDS loading dye (240 mTris-Cl pH 6.8, 8% SDS, 40 % glycerol, 0.05% bromophenol blue, 5% ß-Mercaptoethanol) and heated to 75°C for 10min. Samples were separated on a NuPAGE 4–12% Bis/Tris polyacrylamide gel (Invitrogen, Carlsbad, CA; USA) in MOPS buffer at 200V. Electrophoresis and blotting to PVDF membrane (Roth, Karlsruhe, Germany) were performed using the XCell SureLock® Mini-Cell (Invitrogen, now life technologies, Grand Island, NY, USA) in accordance to the manufacturer's protocol. After incubating with blocking buffer (3% skim milk powder in PBS with 0.1% Tween-20) on an orbital for 1hour at room temperature or overnight at 4°C, the membranes were incubated for 1hour or overnight with the primary antibody diluted in blocking buffer, followed by 1hour incubation with secondary anti-Rabbit-IR-Dye 800 and/or antiMouse-Alexa 680 (Licor), both diluted 1:10000 in blocking buffer. Both antibody incubations were followed by 3 washes with PBS with 0.1% Tween-20. Membranes were scanned using the Odyssey infrared imaging system (LI-COR, Lincoln, NE, USA). Mouse anti-ßActin (Sigma-Aldrich, St.Louis, MO, USA) or rabbit anti-GAPDH (Santa Cruz, Santa Cruz, CA, USA) were used as loading controls.

4.20. *Phosphatase treatment*

For dephosphorylation experiments, H_2O_2 treated or untreated HeLa cells were harvested by trypsinization, collected by centrifugation at 170g for 10 min, washed twice with PBS and resuspended in NEB3 Buffer (New England Biolabs, Ipswich, MA, USA), in which Calf intestinal phosphatase (CIP; New England Biolabs, Ipswich, MA, USA) has optimal activity. Cells were lysed by sonication and subsequent centrifugation at maximum speed for 30 min at 4°C. Cleared lysates

were splitted and one-half was incubated with 10U CIP for 30 min at 37°C, whereas the other half was mock treated. Subsequently, samples were subjected to Western Blot analysis.

4.21. *Anti-GFP Trap IP*

GFP-SNEV-Hela were grown to 90% confluence in T175 roux flask and incubated with 100 µM H_2O_2 to induce SNEV phosphorylation or left untreated as negative control. Cells were scraped on ice in 3ml Lysis buffer (50 mM Hepes-KOH pH 7.5, 5 mM EDTA pH8, 150 mM KCl, 10% glycerol, 1% Triton X- 100, 20 mM ß-glycerophosphate, 10mM Napyrophosphate, 10 mM NaF, 1 mM DTT, 1 mM Na3VO4, 0.1mM PMSF, 20 µg/ml Leupeptin, 20 µg/ml Chymostatin, 20 µg/ml Pepstatin, 1µM Okadaic acid) per T175 and sonicated using 3 bursts of 10s. Lysates were cleared by centrifugation for 30 min at full speed. All centrifugation steps were carried out at 4°C. 30 µl GFP-Trap Beads (ChromoTek, Munich, Germany) were equilibrated by washing thrice in 500 µl ice cold wash buffer (50mM Hepes-KOH pH 7.5, 5mM EDTA pH8, 150mM KCl, 10% glycerol, 0.05% NP-40, 20 mM ß-glycerophosphate, 10 mM Na-pyrophosphate, 10mM NaF, 20 µg/ml Leupeptin, 20 µg/ml Chymostatin, 20 µg/ml Pepstatin) and collected by centrifugation at 2700 x g for 2 min. 1 ml Lysate corresponding to 1 mg total protein was added to the beads mixed on an overhead shaker for 1h at 4°C. Beads were collected by centrifugation for 2 minutes at 2,000 x g. Discard supernatant and wash beads 5x times with 500µL ice cold wash buffer (ocadaic acid added only for the first two washing steps) and finally resuspended in washing buffer.

4.22. *Mass spectrometric analysis*

Beads were washed five times with ammonium bicarbonate buffer (50mM ABC). Disulfide bonds were reduced by incubation with dithiothreitol (DTT, 5% w/w of the estimated amount of protein) for 30 min at 56°C and Cys-residues were subsequently alkylated with iododacetamide (IAA, 25% w/w of the estimated amount of protein) for 20 min at RT in the dark. DTT (2.5% w/w of the estimated amount of protein) was added to consume excess IAA and proteins were digested with subtilisin for 1 hour at 37°C. Digests were stopped by addition of trifluoro

acetic acid (TFA) to approx. pH 3. 10% of the peptide mixture was analysed directly, the remaining 90% were enriched for phosphopeptides by the use of TiO2 as described in(Mazanek et al., 2007). Peptides were separated on a U3000- HPLC-system (Dionex, Sunnyvale, CA, USA). Peptides were loaded on a trapping column (PepMAP C18, 0.3 × 5 mm, Dionex) with 0.1 % TFA as loading solvent and then eluted onto an analytical column (PepMAP C18, 75 µm × 150 mm, Dionex) with a flow rate of 300 nl/min and a gradient from 0 % solvent B to 100 % solvent B in 90 min, followed by a washing step of 10 min with 10 % solvent B and 90 % solvent C (solvent B: 40 % acetonitril (ANC), 0.08 % formic acid, solvent C: 80% ACN, 10% trifluorethanol, 0.08 % formic acid). The HPLC system is online coupled to a Velos Orbitrap mass spectrometer (Thermo Scientific, Waltham, MA, USA) equipped with an ESI-source (Proxeon, now Thermo Scientific). A full scan (scan range 400-1800 Th, resolution 60.000) was followed by MS2 analysis by collision-induced dissociation (CID) of the 20 most intense precursors in the linear iontrap. Normalized collision energy was set to 35%, activation Q at 25 and activation time at 30 ms. Peptide identification was performed using the SEQUEST algorithm in the ProteomeDiscoverer 1.3.0.339 software package (Thermo Scientific). Carbamidomethylation of Cys was set as static modifications, phosphorylation of Ser/Thr/Tyr and oxidation of Met were set as variable modifications. Spectra were searched against a small database plus contaminants for a fast PTM analysis. Search parameters include no protease specificity, a peptide tolerance of 2 ppm, a fragment ions tolerance of 0.8 Da. The results were filtered at the XCorr values to an FDR of 1% on the peptide level. The probability of phosphosite localization was calculated using the phosphoRS 2.0 software (Taus et al., 2011) implemented into the Proteome Discoverer.

4.23. *Indirect immunofluorescence staining Hela cells*

Cells were seeded on coverslips one day prior to immunofluorescence staining. The next day, cells were washed with PBS and fixed with 3.7% (w/v) for 20 min at room temperature. Permeabilization was performed with 0.1% Triton X-100 in PBS for 10 min at room temperature. Cells were incubated with primary antibodies diluted in PBS with 10% FCS for 1 h, washed 3 times for 10 min with PBS, incubated for 1 h with the appropriate secondary antibodies diluted in PBS with 10% FCS, and

washed 3 times for 10 min with PBS. Anti-pSNEV (S149) was diluted 1:250. As secondary antibodies, anti-mouse dyelight488 1:1000 and dyelight649 1:1000 anti-rabbit or anti-mouse antibodies were used. Microscope as described previously. To visualize the nuclei, cells were counterstained with 4', 6-diamidino-2-phenylindole (DAPI). Cells were washed and fixed as above and subsequently incubated with 100ng/ml DAPI in PBS for 10 min at room temperature. After staining, slides were mounted on cover slips using slow fade gold Mounting Medium for Fluorescence (Life technologies, Grand Island, NY, USA) and sealed with nail polish. Microscopy and image analysis were carried out using a Leica SP5 II laser scanning confocal microscope (Leica Microsystems CMS, Mannheim, Germany).

4.24. *Indirect immune-fluorescence of hASCs*

60000 hASCs were grown in DMEM medium (4.5 g/l glucose) on coverslips in a six well plate. 48 hours after seeding growth medium was replaced by adipogenic differentiation media containing Indomethacin, Dexamethasone, Hydrocortisone and IBMX. Medium was changed after each 3 days until day 10. At day10, cells were washed twice with PBS and fixed in 4% formaldehyde for 20 minutes at room temperature. After subsequent three times washing with PBS, cells were permeabilized in 0.25% Triton in PBS for 20 minutes and blocked in 20% FCS (in PBS) for 1 hour. Cells were washed with PBS three times for 5 minutes each and stained with anti-Prp19 antibody (Bethyllab #A300-102A) diluted 1: 500 in PBS containing 20% FCS for 1 hour. Cells were again washed with PBS for 3 x 5 minutes each prior to application of Dyelight 649 anti-rabbit antibody (Jackson Immunoresearch, # 111-495-144) diluted 1:500 in PBS containing 20% FCS for 1 hour. Cells were washed again with PBS for 3 x 5 minutes each. For nuclear DNA staining DAPI at 200 ng/ml concentration was applied for 10 minutes and then washed with PBS for 5 minutes. Slides were mounted with Vectashield mounting medium (Vector Laboratories, Burlingame, U.S.A) and sealed with nail polish. Microscopy and image analysis were done by using Leica SP5 II laser scanning confocal microscope (Leica Microsystems CMS, Mannheim, Germany).

4.25. *Comet assay*

Single and double stranded DNA damage in SNEVwt and SNEV S149A overexpressing HUVECs under basal condition was measured by single-cell gel electrophoresis (comet assay) under alkaline conditions as described previously (Wojewódzka et al., 2002). At least 100 randomly selected cells per slide were examined for the presence or absence of comets using fluorescence microscopy. The cells were assigned to five different categories according to their DNA content in tail using the TriTek CometScore software. Percentage of cells in each category was calculated.

4.26. *Apoptosis staining*

Cells were detached using 0.1% Trypsin/0,02%EDTA and stained with Annexin V–Bacific Blue (Invitrogen, now life technologies) and PI (Roche, Basel, Switzerland) according to the manufacturer's instructions. Analysis of the percentages of apoptotic and necrotic/late-apoptotic cells was performed by using a BD FACS Canto II flow cytometer (Becton Dickinson, Franklin Lakes, NJ, USA) and the FCS Express V3 software (De Novo Software,USA).

5- Results:

A) ATM-dependent phosphorylation of SNEV is involved in extending cellular life span and suppression of apoptosis.

Results 5A).

ATM-dependent phosphorylation of SNEV is involved in extending cellular life span and suppression of apoptosis.

4.27. *Oxidative stress induces an additional SNEV protein band in Western blotting.*

Previous findings revealed that SNEV expression is induced upon oxidative stress and DNA DSB damage (Mahajan and Mitchell, 2003; Voglauer et al., 2006). To further study the effect of oxidative stress on SNEV expression, we treated HeLa cells with 1mM hydrogen peroxide for different time points and whole cell protein lysates were isolated and subjected to western blotting to see whether oxidative stress influence SNEV protein expression. Figure 1A showed that an additional band above the 56 kda band is induced and its intensity increased in a time dependent manner. The appearance of this additional SNEV band made us curious to know if this additional band is a phosphorylated form of SNEV? In order to get the answer we performed phosphatase assay. The protein lysates of stress treated and untreated Hela cells were splitted into two half. One-half was incubated with Calf intestinal phosphatase (CIP) and the other half was mock treated. Western blot analysis showed that the additional SNEV band goes away upon phosphatase treatment, indicating that SNEV undergo phosphorylation in response to DNA damage and oxidative stress (Figure 5.1A). This high molecular band was also induced in human dermal fibroblasts (HDF5) in response to bleomycin treatment. The intensity of this high molecular band increased in a dose and as well as time dependent manner (Figure 5.1 B). β-actin was used to ensure equal loading of protein.

In order to get a more clear picture that this additional band of SNEV represent phosphorylated form of SNEV by mass spectrometry, we over express GFP tagged SNEV under the control of endogenous promoter according to method(Poser et al., 2008). The advantage of using GFP-SNEV-Hela lies in allowing the use of a commercially available GFP-antibody for IP which is covalently coupled to agarose beads, thus avoiding predominant detection of immunoglobulins in the mass spectrometric analysis. In order to make sure that GFP-SNEV behaves similarly to endogenous SNEV in cells we confirmed its nuclear localization (figure 5.1C), as well as its integration into SNEV/CDC5L complex by co-precipitation of SNEV and CDC5L with GFP SNEV by GFP antibodies (Fig. 5.1D). GFP tagged SNEV overexpressing Hela cells were treated with hydrogen peroxide and isolate GFP SNEV by GFP Immunoprecipitation. Purified proteins were subjected to mass spectrometric analysis. Mass spectrometric data showed that SNEV is phosphorylated at S149, with a probability of 76.5% (Figure 5.1E). Figure 1F and 1G shows that the signal detected by MS is specific for H_2O_2-treated cells and not due to differences in the efficiency of the IP, because Western Blot (Figure 1D) clearly shows that comparable amounts of GFP-SNEV was precipitated under both conditions.

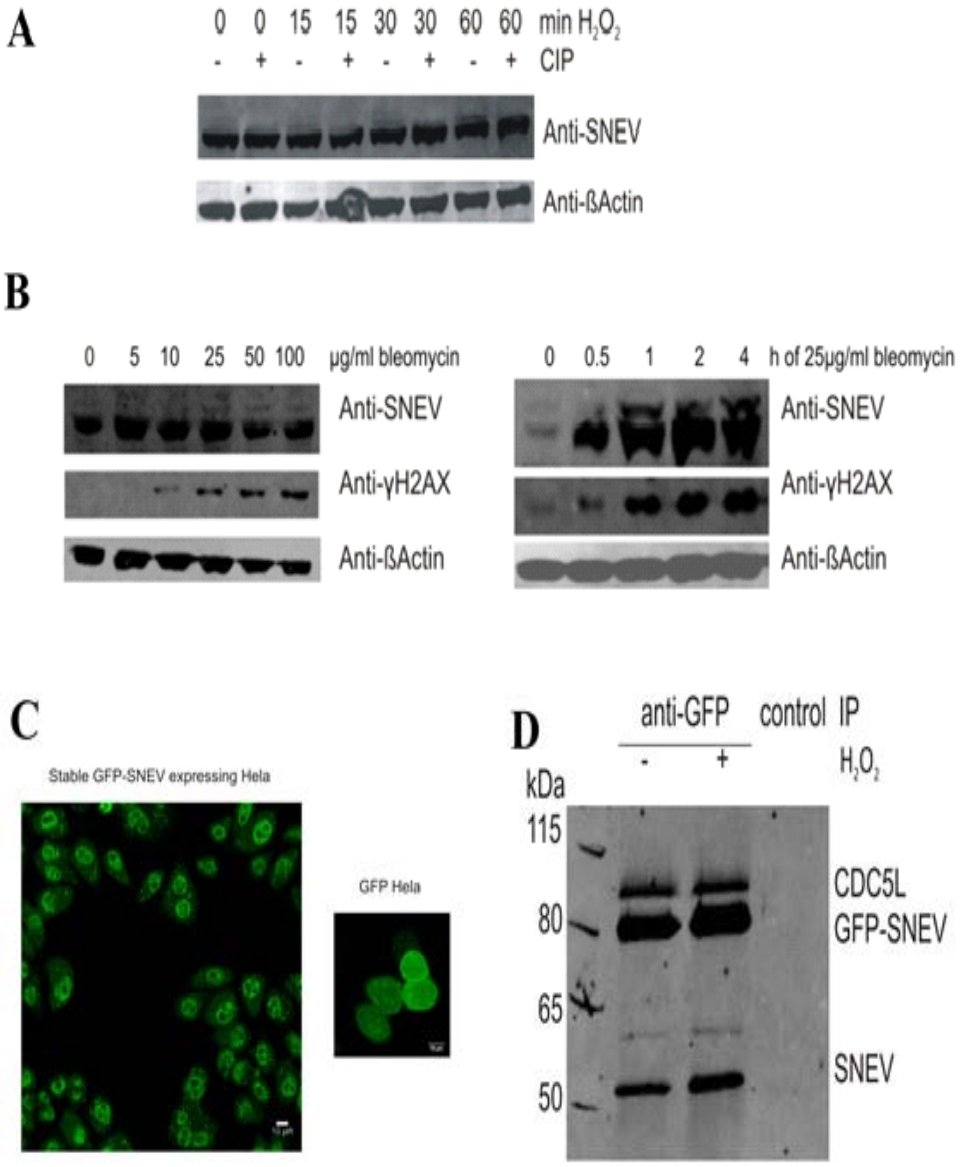
A
0 0 15 15 30 30 60 60 min H_2O_2
- + - + - + - + CIP
Anti-SNEV
Anti-ßActin
B
0 5 10 25 50 100 µg/ml bleomycin
Anti-SNEV
Anti-γH2AX
Anti-ßActin
0 0.5 1 2 4 h of 25µg/ml bleomycin
Anti-SNEV
Anti-γH2AX
Anti-ßActin
C
Stable GFP-SNEV expressing Hela
GFP Hela
D
anti-GFP control IP
- +
H_2O_2
kDa
115
80
65
50
CDC5L
GFP-SNEV
SNEV

E)

AVPSS(ph)QPSVVGAGEPM(ox)DLGELVGM(ox)TPEIIQKL

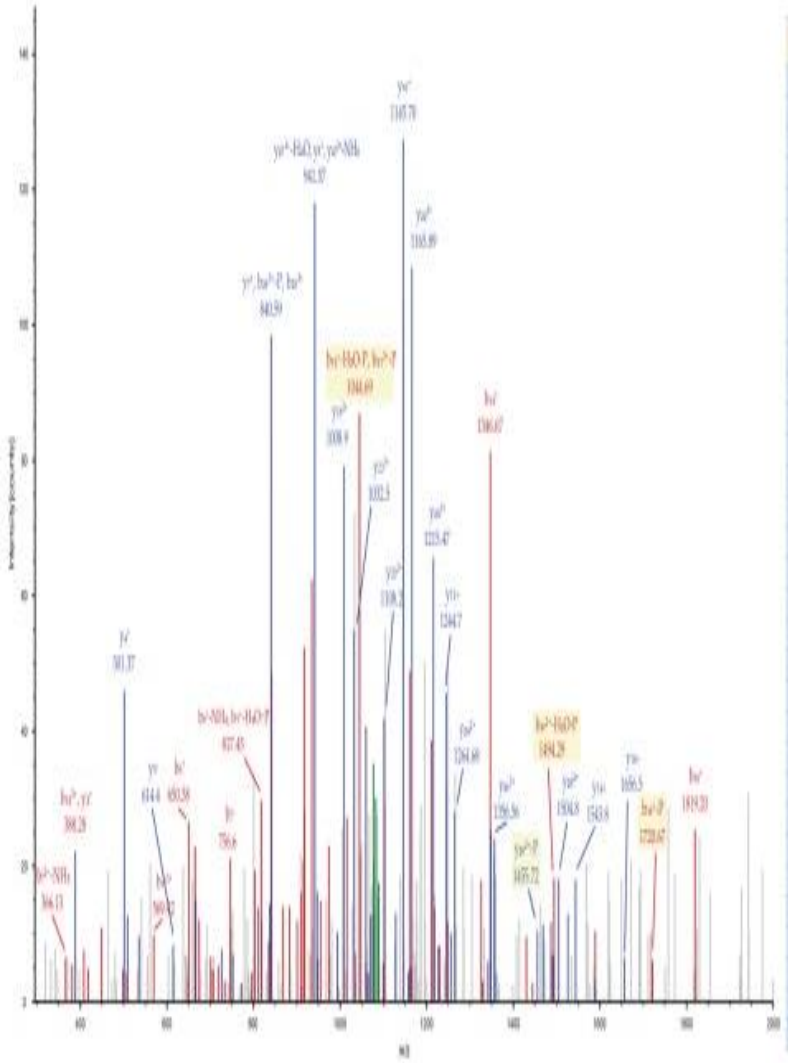

#1	b+	b2+	b3+	Seq.	y+	y2+	y3+	#2
1	72.0	36.5	24.7	A				32
2	171.1	86.1	57.7	V	3290.6	1645.8	1097.5	31
3	268.2	134.6	90.1	P	3191.5	1596.3	1064.5	30
4	355.2	178.1	119.1	S	3094.5	1547.7	1032.2	29
5	522.2	261.6	174.7	S-Phospho	3007.4	1504.2	1003.2	28
6	650.3	325.6	217.4	Q	2840.4	1420.7	947.5	27
7	747.3	374.2	249.8	P	2712.4	1356.7	904.8	26
8	834.3	417.7	278.8	S	2615.3	1308.2	872.4	25
9	933.4	467.2	311.8	V	2528.3	1264.7	843.4	24
10	1032.5	516.7	344.8	V	2429.2	1215.1	810.4	23
11	1089.5	545.3	363.8	G	2330.2	1165.6	777.4	22
12	1160.5	580.8	387.5	A	2273.1	1137.1	758.4	21
13	1217.6	609.3	406.5	G	2202.1	1101.6	734.7	20
14	1346.6	673.8	449.5	E	2145.1	1073.0	715.7	19
15	1443.7	722.3	481.9	P	2016.0	1008.5	672.7	18
16	1590.7	795.8	530.9	M-Oxidation	1919.0	960.0	640.3	17
17	1705.7	853.4	569.2	D	1772.0	886.5	591.3	16
18	1818.8	909.9	606.9	L	1656.9	829.0	553.0	15
19	1875.8	938.4	625.9	G	1543.8	772.4	515.3	14
20	2004.9	1002.9	669.0	E	1486.8	743.9	496.3	13
21	2117.9	1059.5	706.7	L	1357.8	679.4	453.3	12
22	2217.0	1109.0	739.7	V	1244.7	622.8	415.6	11
23	2274.0	1137.5	758.7	G	1145.6	573.3	382.5	10
24	2421.1	1211.0	807.7	M-Oxidation	1088.6	544.8	363.5	9
25	2522.1	1261.6	841.4	T	941.6	471.3	314.5	8
26	2619.2	1310.1	873.7	P	840.5	420.8	280.8	7
27	2748.2	1374.6	916.7	E	743.5	372.2	248.5	6
28	2861.3	1431.2	954.4	I	614.4	307.7	205.5	5
29	2974.4	1487.7	992.1	I	501.3	251.2	167.8	4
30	3102.4	1551.7	1034.8	Q	388.3	194.6	130.1	3
31	3230.5	1615.8	1077.5	K	260.2	130.6	87.4	2
32				L	132.1	66.6	44.7	1

Site probability according to Phospho RS 2.0
S(4): 18.7; S(5) 76.5; S(8):4.8; T(25): 0.0

F)

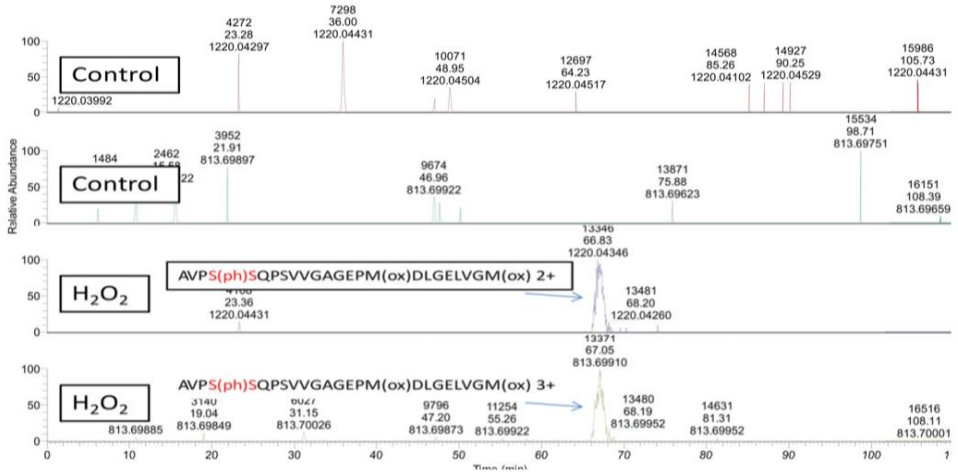
Control
Control
H2O2
H2O2
AVPS(ph)SQPSVVGAGEPM(ox)DLGELVGM(ox) 2+
AVPS(ph)SQPSVVGAGEPM(ox)DLGELVGM(ox) 3+
Relative Abundance
Time (min)

G)

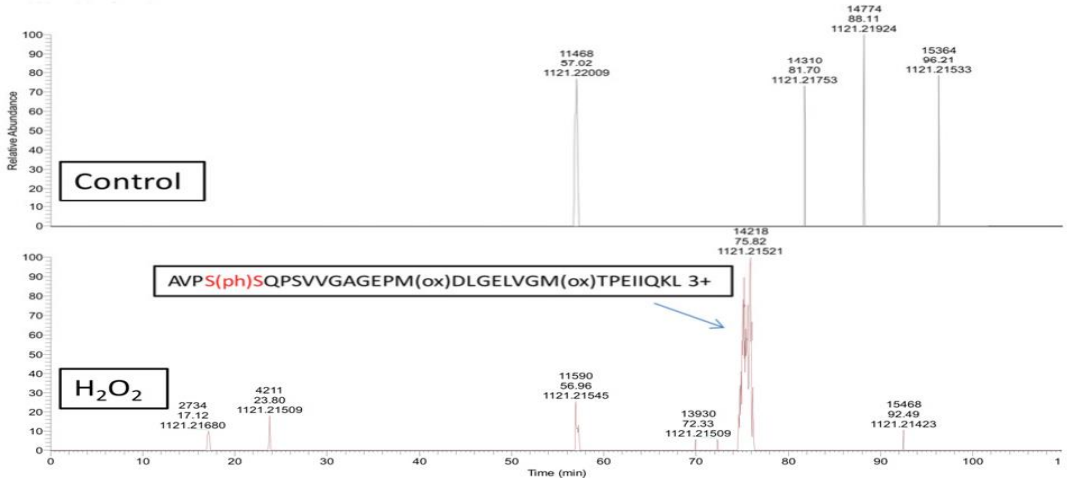
Control
H2O2
AVPS(ph)SQPSVVGAGEPM(ox)DLGELVGM(ox)TPEIIQKL 3+
Relative Abundance
Time (min)

Figure 4-1: Upon oxidative stress, SNEV is detected as double band, probably representing a phosphorylated species.

Hela cells treatment with H_2O_2 induce an additional bands of SNEV which goes away upon phosphatase treatment. (B) Similar high molecular band was also induced upon bleomycin treatment in fibroblasts detected with anti-SNEV antibody. The intensity of this additional band increased in a dose- and time-dependent manner. Fibroblasts were incubated with 0, 5, 10, 25, 50 or 100µg/ml bleomycin for 1hour (left panels) or with 25µg/ml bleomycin for 0, 0.5, 1, 2, 4 hours (right panels), scraped on ice in 2x SDS loading dye and subjected to Western blotting. Membranes were probed with anti-SNEV antibody. Anti-β-actin antibody was used to ensure equal loading of protein. Anti-γH2AX antibody was used as a marker of DNA damage (C) GFP SNEV is predominantly localized to the nucleus (left panel), while GFP alone was detected throughout the cell (right panel).D) Endogenous SNEV and its known interaction partner CDC5L is coprecipitated with GFP IP indicating that GFP SNEV behave similarly to endogenous SNEV. E) Collision-induced dissociation spectrum of the SNEV peptide AVPSS(ph)QPSVVGAGEPM(ox)DLG. Indeed, a phosphorylation was detected and assigned to S149 with a probability of 76.5% . While the consistence of three different spectra with different m/z ratios underscores the correct assignment of phosphorylation to this site, the remaining uncertainty comes from the presence of 3 serine residues within a quite long peptide. Together with the problem of lack of trypsin or chymotrypsin proteolytic sites near these serine, a better proof of S149 as the really phosphorylated serine by mass spectrometry is hampered. F) Extracted ion chromatogram with a mass window of 3ppm of the m/z of the phosphopeptide AVPS(ph)SQPSVVGAGEPM(ox)DLGELVGM(ox)(doubly and triply charged) show a signal in H_2O_2 treated cells only and not in the control sample. G) Extracted ion chromatograms of the m/z of the AVPS(ph)SQPSVVGAGEPM(ox)DLGELVGM(ox)TPEIIQKL (doubly and triply charged) show a signal in H_2O_2 treated cells only. Figure 1E, F, G were kindly provided by our collaborator Dorothea Anrather, University of Vienna).

4.28. *SNEV sequence contain conserved ATM kinase consensus target site.*

Previous proteomic screens were performed to analyze proteins phosphorylated in response to DNA damage on ATM and ATR consensus site. More than 900 regulated phosphorylated sites in more than 700 proteins. The target list contain proteins previously known to involved in DDR, but also identify some novel protein involved in DDR (Matsuoka et al., 2007). The target proteins contain a specific sequence of amino acids phosphorylated by ATM and ATR in response to DDR (Figure 5.2 A). Interestingly the SNEV amino acid sequence analysis revealed that SNEV contains an ATM target sequence which is conserved among vertebrates only (Figure 5.2 B).

Taken together, the mass spectrometry spectra, the presence of an ATM kinase consensus site, and ATM's known function as a kinase signalling oxidative stress drive us to generate an anti-pSNEV (S149) specific antibody.

A)

B)

```
M. musculus     113 ACRVIARLTKEVTAAREALATLKPQAGLI-VPQAVPSS*QPSVVGAG-EPMDLGELVGMTP 170
R. norvegicus   113 ACRVIARLTKEVTAAREALATLKPQAGLI-VPQAVPSS*QPSVVGAG-EPMDLGELVGMTP 170
H. sapiens      113 ACRVIARLTKEVTAAREALATLKPQAGLI-VPQAVPSS*QPSVVGAG-EPMDLGELVGMTP 170
D. rero         113 ACRVIARLTKEVTAAREALATLKPQAGLV-APQAAPAS*QPAAVGAGGEAMEVSEQVGMTP 171
D. melanogaster113 ACRVIARLNKEVAAAREALATLKPQAGIANAPTAIPQPALASEAGG-AAAHPMEQAGMSA 171
C. elegans      114 ACRVISRLSKELTAAREALSTLKPHTSAK-VDDDVSID------------ESEDQQGLSE 160
S. cerevisiae   119 AKLVAAQLLMEKNEDSKDLPKSS*QQAVAITREEFLQGLLQSSR-------DFVARGKLKA 171
```

Figure 4.2: SNEV sequence contain ATM kinase consensus site is highly conserved. A) Bioinformatically identified sequence of amino acid phosphorylated by ATM (Matsuoka et al, 2007). B) Sequence comparison of SNEV homologues in the putative ATM target site. The consensus sequence surrounding the phospho-SQ site on ATM substrates that are regulated by DNA damage is conserved in the SNEV amino acid sequences across different vertebrates, but not in non-vertebrates.

4.29. *Characterization of pSNEV (S149) antibody*

The antibody against S149 pSNEV was generated and characterized by Western blotting and indirect immunofluorescence. The antibody detects a band at the expected size of SNEV upon oxidative stress treatment of Hela cells and goes away upon phosphatase treatment. Besides the bands at the expected size, other bands were also detected by anti-pSNEV(S149) antibody on western blot of Hela lysates (Fig. 5.3 A, B, C), but at higher molecular weights. These bands might represent post-translationally modified SNEV similar to the ones described (Melk et al., 2003). For indirect immunofluorescence analysis, the antibodies were pre-blocked with synthetic phosphorylated and non-phosphorylated peptide of the same sequence against which the antibody was generated and applied to cells treated with 1mM H_2O_2. Figure 5.3D shows that staining was abolished by anti-pSNEV (S149) pre-blocked with synthetic phosphorylated SNEV peptide, and not after pre-incubation with the non-phospho-peptide.

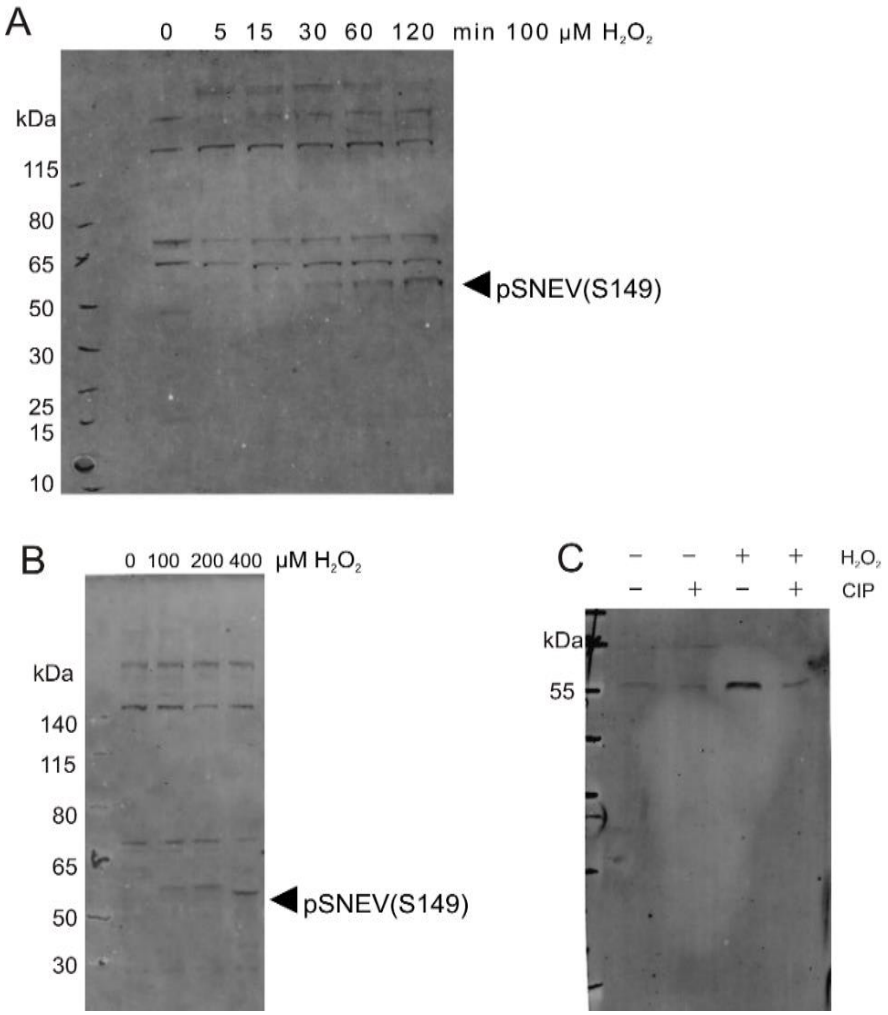

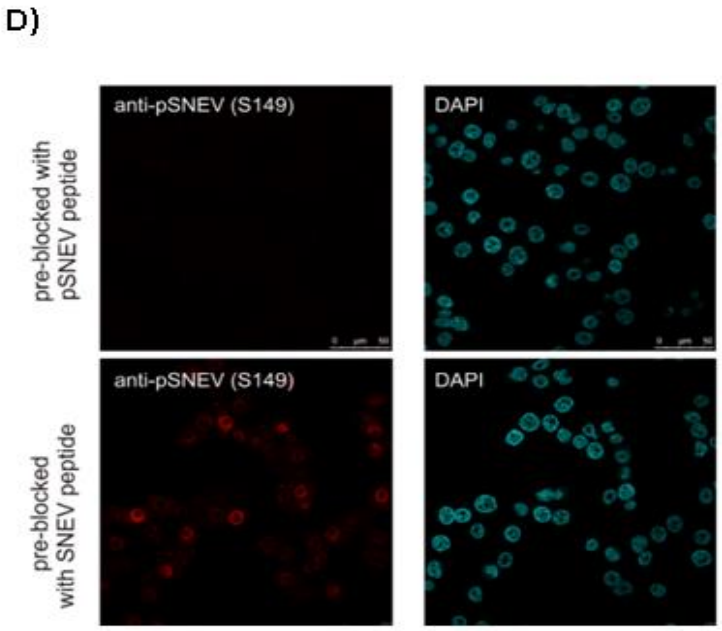

Figure 4-3: Characterization of pSNEV (S149) antibody by western blot and IF.

Hela cells treated with H_2O_2 were harvested and probed with anti pSNEV (s149) antibody. A, B, C). Western blot shows that the antibody detect some bands of SNEV at higher molecular weight in addition to 56Kda band. This SNEV band goes away upon CIP treatment. D) Pre incubation of pSNEV(S149) antibody with synthetic phospho SNEV and synthetic SNEV peptide abolish signal confirmed the specificity of pSNEV(S149) antibody.

4.30. *Phosphorylation of SNEV at S149 is induced by oxidative stress in different cell types.*

Total protein lysates from Hela cells treated with 1Mm H_2O_2 were isolated and treated with CIP, and subjected to western blotting. The membranes were probed with anti-pSNEV (S149) antibody. Western blot in figure 5.3A showed that the antibody detects a band at the expected size of SNEV in stress treated sample, and its signals abolished upon phosphatase treatment (Fig.5 3A). Based on these results, we were curious to confirm our hypothesis that SNEV phosphorylation was induced by DNA damage in normal cells as well; we analyzed SNEV expression in response to DNA damage in human dermal fibroblast cells (HDF5). HDF5 cells were exposed to

different concentration of H_2O_2 for 1 hour and 100μM H_2O_2 for different time points. Total cell lysates were subjected to western blotting and probed with anti-pSNEV (S149). Figure 5.4B and 5.4C showed that SNEV is phosphorylated in response to oxidative stress in a time as well as dose dependent manner and phosphorylation was observed as quickly as after 5 minutes exposure and reached to its peak after 1 hour.

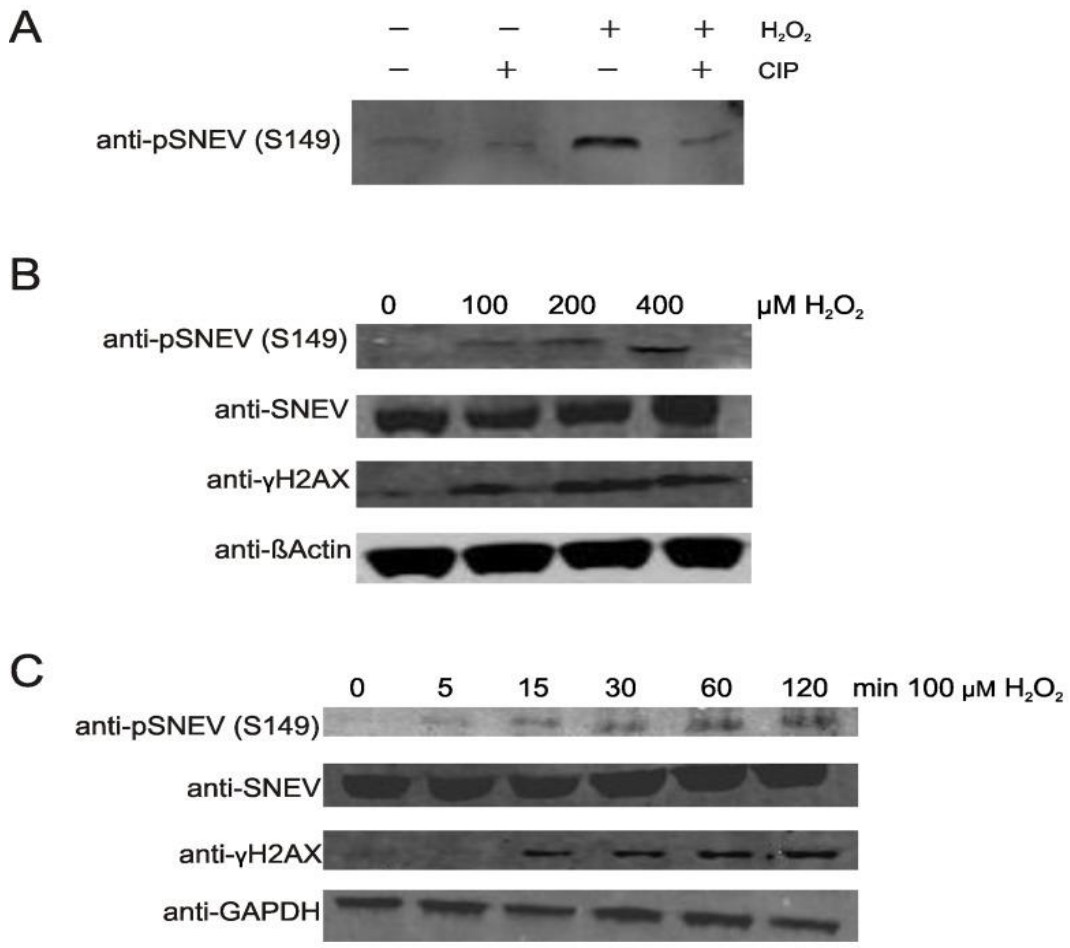

Figure 4-4: Phosphorylation of SNEV at serine 149 is induced by oxidative stress in a time and dose dependent manner

(A) Oxidative stress treatment increased the intensity of higher molecular band of SNEV detected by a phospho-SNEV specific antibody (anti-pSNEV(S149) and diminishes upon phosphatase treatment. HeLa cells were treated for 1 hour with 1mM H_2O_2. Lysates were incubated with CIP and subjected to Western Blotting with a specific anti-phosphoSNEV(S149) antibody, generated by immunizing rabbits with an artificial SNEV-phosphopeptide. (B) Human dermal fibroblasts (HDF) treated for 1 hour with 0, 100, 200 or 400 μM H_2O_2, scraped on ice in 2x SDS loading dye and

subjected to western blot. Membranes were probed with anti-pSNEV(S149) and anti-SNEV to compare pSNEV to total SNEV levels. Anti-γH2AX antibody was used as positive control. Anti-β-actin was used as loading control. (C) HDF5 cells were treated with 100 μM H_2O_2 for 0, 5, 15, 30, 60 or 120 min, followed by Lysis and Western Blotting as described in B.

4.31. *Different types of DNA damage induce nuclear localization of pSNEV.*

In order to trace the intracellular localization of phosphorylated SNEV we performed indirect immunofluorescence. Hela cells treated with 1mM H_2O_2 for 1 hour and stained with anti-pSNEV (S149 antibody. In addition to strong and predominant nuclear signal in response to oxidative stress, the phosphorylated form of SNEV is also detected in cytoplasm but it is not cleared if this phosphorylation is a signal for shuttling of SNEV between nucleus and cytoplasm. However, in any case, under normal conditions only very few cells display positive staining for phospho SNEV, which seems to localize to the cytoplasm (figure 5.5A).To test if phosphorylation of SNEV is a general DNA damage response or is only restricted to oxidative stress, we stressed cells with Mitomycin C (MMC), a potent DNA cross linker. HeLa cells incubated with 25μg/ml MMC for 24 hours and stained with anti-pSNEV (S149). As observed for H_2O_2, MMC also induces phosphorylation of SNEV, and the phosphorylated SNEV is mainly confined in the nucleus (Fig. 5.5 B).

These results showed that phosphorylation of SNEV is an integral part of the nuclear DNA damage response.

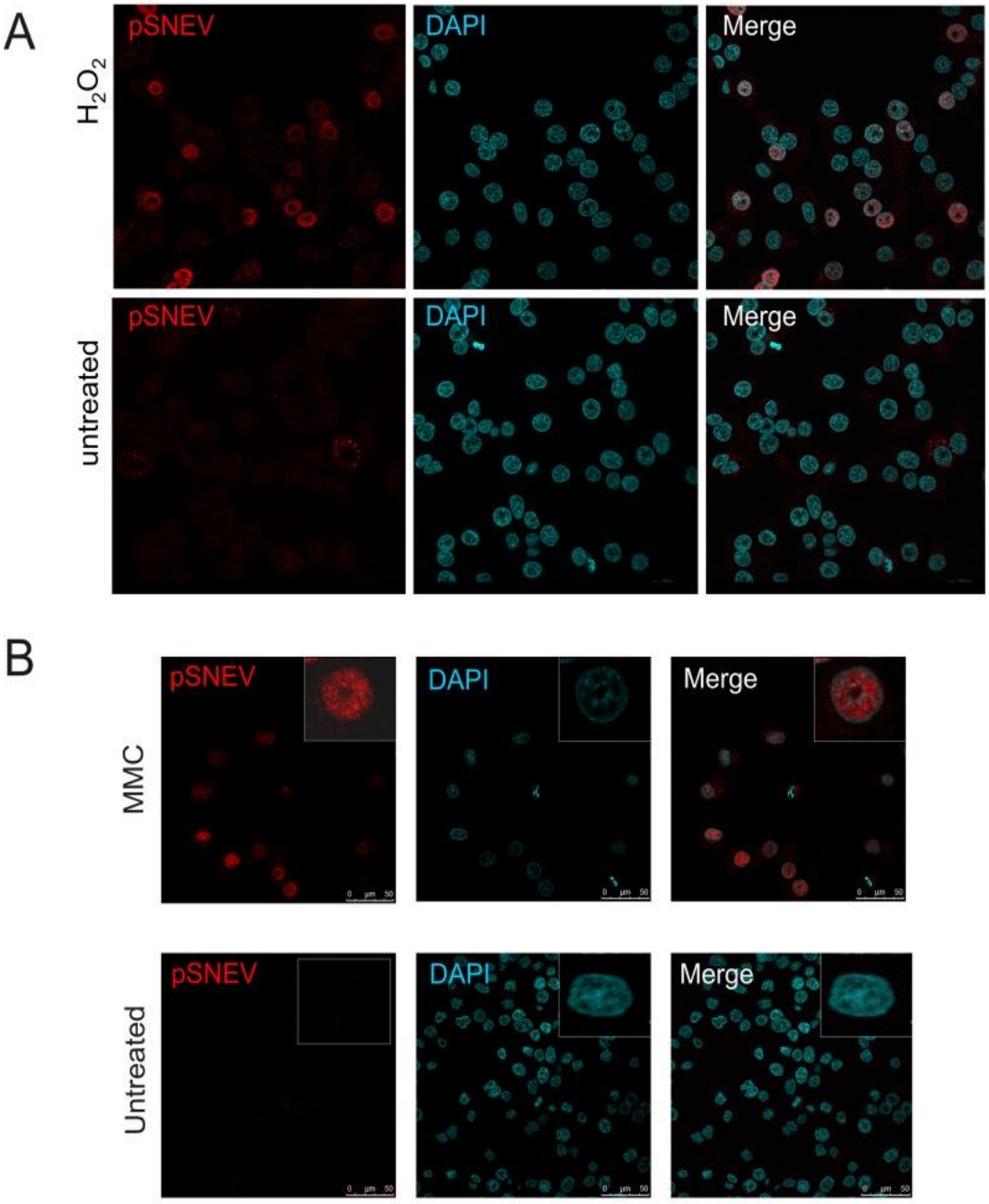

Figure 4-5: Upon oxidative stress, SNEV is phosphorylated and localizes mainly to the nucleus. (A) Hela cells were seeded on coverslips and treated for 1 hour with 100µM H_2O_2 followed by staining with anti-pSNEV(S149) and DAPI as described in the Materials and Methods section and analyzed by fluorescence microscopy. (B) HeLa cells were treated with 25 µg/ml MMC for 24 hours and stained with anti-pSNEV(S149) antibody.

4.32. *Phosphorylation of SNEV at serine 149 is ATM dependent.*

In order to confirmed our hypothesis that SNEV phosphorylation is ATM dependent, we chemically blocked ATM kinase activity by 2-(4-Morpholinyl)-6-(1-thianthrenyl)-4H-pyran-4-one (KU-55933), a specific inhibitor of ATM kinase activity (Hickson et al., 2004). Hela cells pretreated with Ku-55933 followed by H_2O_2. Total cellular protein lysates were subjected to western blotting and probed with anti-pSNEV (S149) antibody. Indeed, we observed a marked reduction in the level of phosphorylated SNEV upon Ku-55933 treatment (Figure 5.6A). However, phospho SNEV bands did not disappear completely. This could be due to another kinase that back up ATM function. It is also known that both ATM and ATR share substrates such as H2AX (Stiff et al., 2004), which also explains that H2AX phosphorylation is only slightly reduced upon ATM inhibition.

To confirm that ATM modulates SNEV S149 phosphorylation with an independent method, we used mouse embryonic fibroblasts in which ATM was flanked by loxP sites and cut out using Cre recombinase (ATM -/- MEF). As shown in fig. 5.6B, the induction of pSNEV (S149) upon H_2O_2 treatment was reduced to less than half of that observed in wild type MEF. ß-Actin actin was used to ensure equal amount of protein loading. The lower panel in fig. 5.6B shows an agarose gel of the genotyping PCR. Using a combination of three primers, three different fragments were amplified according which cells can be genotyped. The 320 bp fragment indicating the absence of loxP sites is amplified only in wild type cells, whereas presence of loxP sites gives rise to a 420 bp fragment. Only after introduction of Cre recombinase, ATM is cutted out and a fragment of 920 bp is amplified. Since the 420 bp fragment is still present inspite of Cre transfection, there is still residual ATM activity in our ATM -/- MEF, which might explain why we still detect some pSNEV in these cells, although to a lesser extent then in wt MEF.

Taken together, these results suggest that SNEV is phosphorylated in response to DNA damage in an ATM dependent manner and the presence of the ATM target motif suggest that it might be a novel direct substrate for ATM.

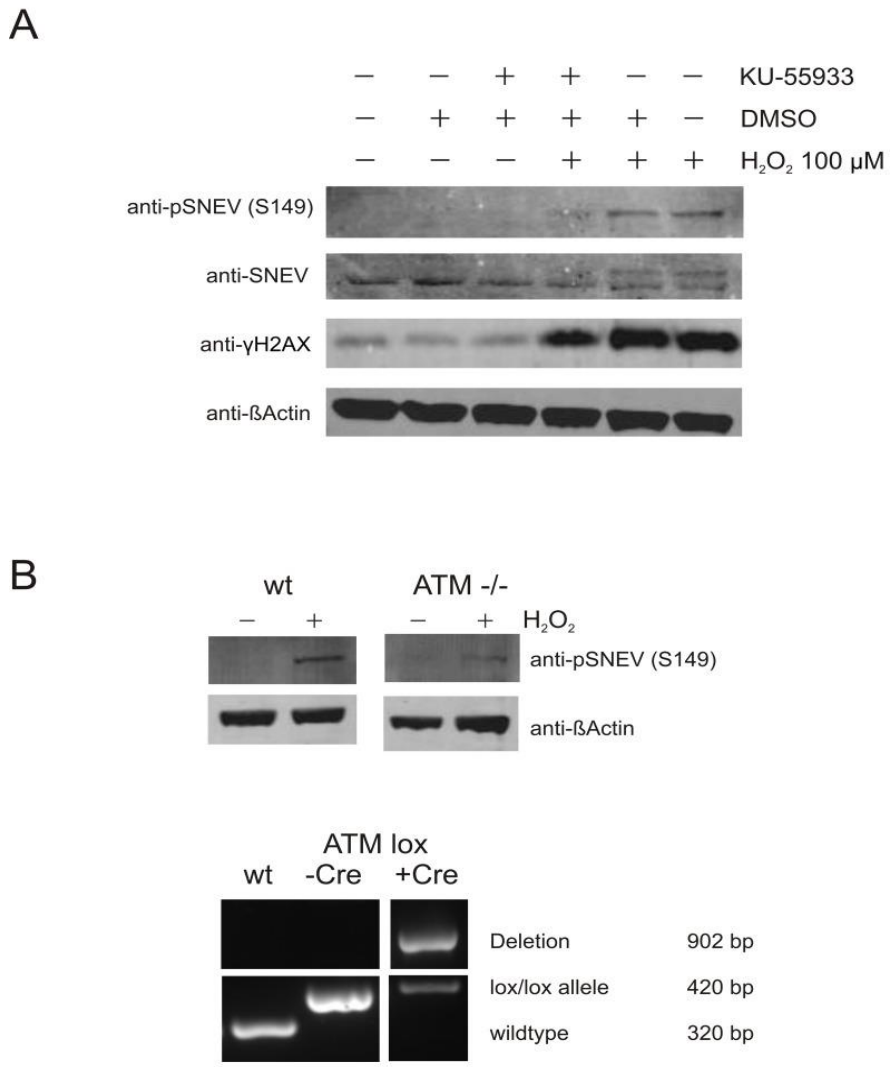

Figure 4-6: Phosphorylation of SNEV at S149A is ATM-dependent.

(A) ATM inhibition reduces phosphorylation of SNEV in response to oxidative stress treatment. HDFs were treated with 100µM H_2O_2 and the specific ATM inhibitor KU-55933. DMSO, the solvent for Ku-99533, was used as negative control. Phosphorylation of SNEV and known ATM target γH2AX was reduced by inhibition of ATM. (B) Phosphorylation of SNEV at S149 is reduced in ATM conditional knockout MEF. Upper panel: wt and ATM -/- MEF were treated with 200 µM H_2O_2 for 1hour, harvested in 2x SDS loading dye and subjected to SDS PAGE. Western Blot was detected with anti-pSNEV (S149) antibody and anti-ß-Actin was used to ensure equal loading.(Lower panel): Genomic DNA was isolated from wt and ATM lox/lox MEF before and after transfection with Cre and used in genotyping PCR. The band for deleted ATM is present only after transfection with Cre, nonetheless the deletion is not quantitative and a small portion of ATM is retained.

5.7. Effect of phosphorylation on life span and stress resistance in HUVEC.

To investigate the physiological effect of the SNEV phosphorylation at S149, we generated stable HUVEC cell lines overexpressing either wild type SNEV (wtSNEV HUVEC) or a point mutant SNEV in which ATM target site was abolished by exchanging serine 149 for alanine (SNEV S149A HUVEC). Both recombinant cell lines showed comparable overexpression of SNEV versus untransfected HUVEC (Figure 5.7A). By using these cell strains, we investigated how the lack of SNEV phosphorylation at S149 affect DNA damage level, stress resistance and life span. As described previously(Voglauer et al., 2006) that SNEV overexpression extends replicative life span. Indeed, SNEV wt HUVEC underwent 30-population doublings post transduction, while empty vector control HUVEC reached senescence already upon PD 8 post transduction, thus wtSNEV overexpression more than tripled the replicative life span. Surprisingly, SNEV S149A overexpression also extend the replicative life span but to a significantly lower extent of around 18 PD post transduction (Figure 5.7B). Replicative senescence at the respective replication end point, was confirmed by SA ß-galactosidase staining, a widely accepted marker of senescence.

Since we observed that SNEV undergoes phosphorylation in response to treatment with DNA damage inducing agents, we hypothesized that phosphorylation might be necessary to elicit a proper DNA damage response. Therefore, we tested the integrity of DNA under basal conditions by comet assay (Figure 5.7C). wtSNEV overexpressing cells show very low or no damage at all and were place in categories II or I. On the other hand, SNEV S149 HUVEC acquires lower levels of DNA damage than empty vector control, but increased damage as compared to wtSNEV HUVEC. Based on these results, we conclude that increased in SNEV level lead to better DNA maintenance under basal conditions while the full effect of more efficient repair unfolds only if SNEV can be phosphorylated at S149. In addition to basal levels of DNA damage, we also assessed cellular response to treatment with genotoxic and/or oxidative stress inducing reagents. Therefore, we used combinations of BSO/bleomycin treatment as described previously (Voglauer et al., 2006). We found that WtSNEV HUVEC did not enter apoptosis upon treatment in accordance to

our previous findings (Voglauer et al., 2006). This is also in line with the previous report showing a twofold reduction in apoptosis in Hela cells upon MMS treatment(Lu and Legerski, 2007). In contrast, in SNEV S149A HUVEC the BSO/bleomycin treatment clearly induced apoptosis/necrosis (Figure 5.7 D). Since it has been shown previously that SNEV is also required for DNA interstrand cross-links(ICL) repair (Zhang et al., 2005). Therefore, we also tested if SNEV overexpression protect cells from the deleterious effect of DNA cross-linker, cisplatin. Cisplatin strongly induce apoptosis in control HUVEC as well as in SNEV S149A HUVEC, while wtSNEV HUVEC were clearly more resistant to this treatment. Therefore, we conclude that phosphorylation of SNEV at S149 is necessary for efficient crosslink-repair activity of SNEV (Figure 7E).

In summary, the overexpression of S149 phosphorylation incompetent SNEV does have a small but discernible effect on the DNA damage status under normal culture conditions when compared to wtSNEV overexpression, but does not exert the strong anti-apoptotic effect of wtSNEV after induction of DNA damage by either oxidative stress or inter strands crosslinks. In any case, the life-span extending and DNA repair functions of SNEV do partially depend on phosphorylation at S149, most probably in dependence of ATM.

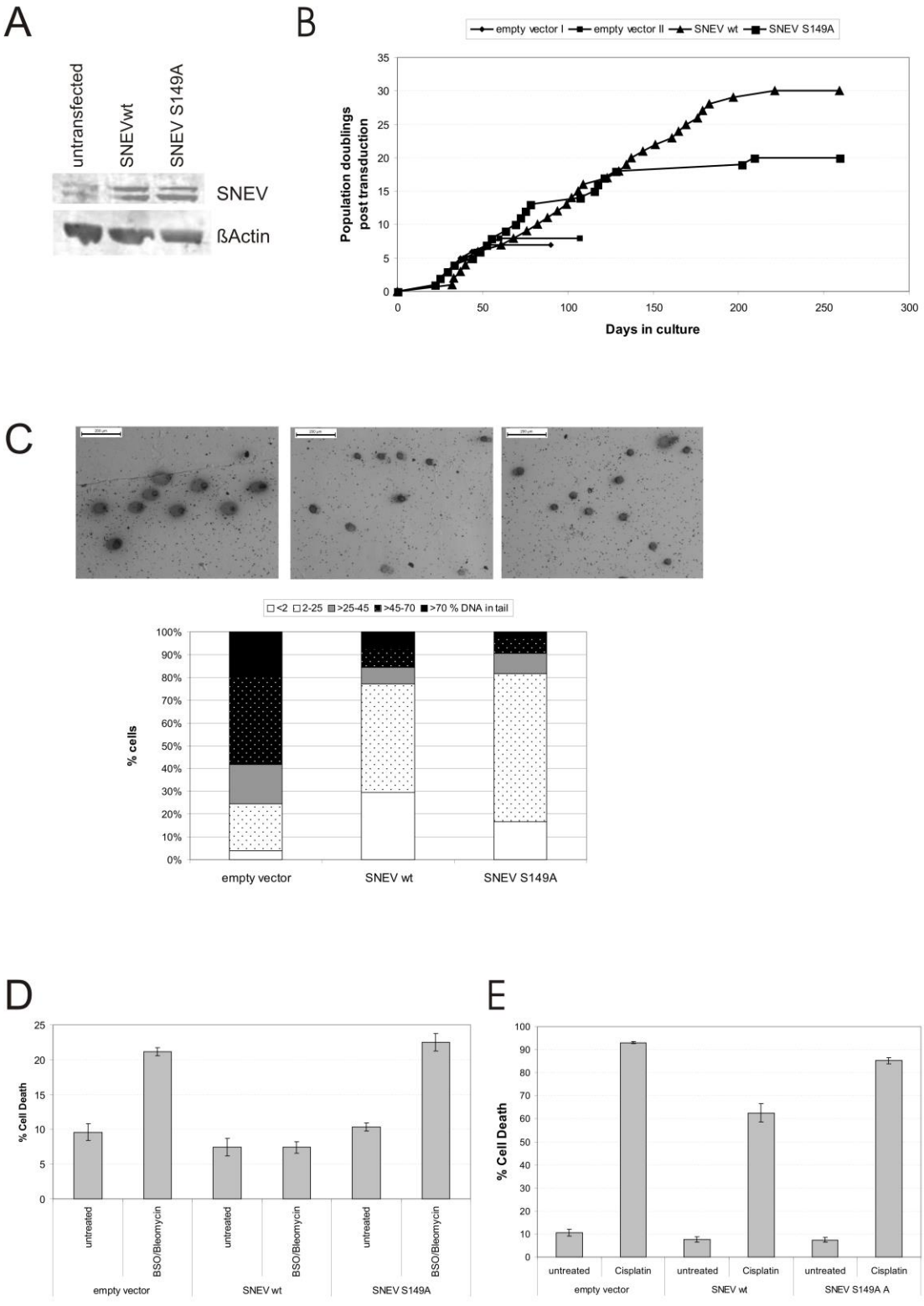
A
untransfected
SNEVwt
SNEV S149A
SNEV
ßActin
B
empty vector I
empty vector II
SNEV wt
SNEV S149A
Population doublings post transduction
Days in culture
C
□<2 □2-25 ▨>25-45 ■>45-70 ■>70 % DNA in tail
% cells
empty vector
SNEV wt
SNEV S149A
D
% Cell Death
untreated
BSO/Bleomycin
empty vector
SNEV wt
SNEV S149A
E
% Cell Death
untreated
Cisplatin
empty vector
SNEV wt
SNEV S149A A

Figure 5.7: Phosphorylation at S149 is necessary for apoptosis resistance and partially for life span extension conferred by SNEV.

A). Normal HUVEC as well as stable HUVEC overexpressing SNEV wt, SNEV S149A or empty vector control cells were lysed and subjected to Western blotting. Western Blots were probed with anti-SNEV and anti-β-Actin antibodies. SNEV protein expression levels are increased five-fold in SNEV wt and ten-fold in SNEV S149A HUVEC as compared to untransfected HUVEC. B) Growth curves of HUVECs overexpressing SNEV wt, SNEV S149A and empty. C) SNEV wt as well as SNEV S149A overexpression reduces the basal level of DNA damage. Upper panel: Representative pictures of Comet assay performed with empty vector, SNEV wt and S149A point mutant overexpressing HUVEC. Lower panel: Comets were classified into 5 categories depending on the percentage of the DNA content in the tail. DNA damage levels of SNEV S149A. D) Cells were incubated for 48 hours with 1 mM BSO for 48h, followed by treatment with 100 µg/ml Bleomycin for 24h. Apoptosis was measured by Annexin-FITC and PI staining and subsequent flow cytometric analysis. E) Cells were incubated with 100µg/ml Cisplatin for 24h. Apoptosis was measured as described in D. (Figure 5.7 is kindly provided by Hanna Dellago, a former PhD student of BOKU).

5.Results.

B) SNEV regulates adipogenesis of human adipose derived mesenchymal stem cells.

Results 5B). SNEV regulates adipogenesis of human adipose derived mesenchymal stem cells

5.1. SNEV expression is induced at both mRNA and Protein level during adipogenesis.

In order to investigate the role of SNEV in adipogenesis we first analyzed its expression during adipogenesis in a time course dependent manner. Human ASCs were induced to differentiate into adipocytes by medium supplemented with a cocktail of known adipogenesis inducing agents and total RNA and protein were isolated at indicated time points during differentiation. Non-differentiated hASCs were used as control. Indeed, SNEV mRNA (Fig. 5.1A) as well as protein levels (Fig. 5.1B) increased in a time course dependent manner over 9 days. As SNEV is mainly a nuclear protein (Gotzmann et al., 2000), we used indirect immunofluorescence to monitor SNEV localization during adipogenesis. SNEV was detected both in the nucleus and in the cytoplasm of differentiated cells, while only nuclear staining was observed in the undifferentiated controls (Fig.5.1C). Adipogenic differentiation was confirmed by quantitation of PPARγ and FASN mRNA (Fig. 5.1D& 5.1E), both well accepted markers of adipogenesis (Heikkinen et al., 2007; Mayas et al., 2010). Oil red O staining after 10 days also confirmed extensive lipid droplet formation in the differentiated culture, whereas no lipid droplets were observed in the control These results show that SNEV expression is induced during adipogenesis and that its localization is not restricted to the nucleus, similar to the observation in mouse 3T3 cell line (Cho et al., 2007).

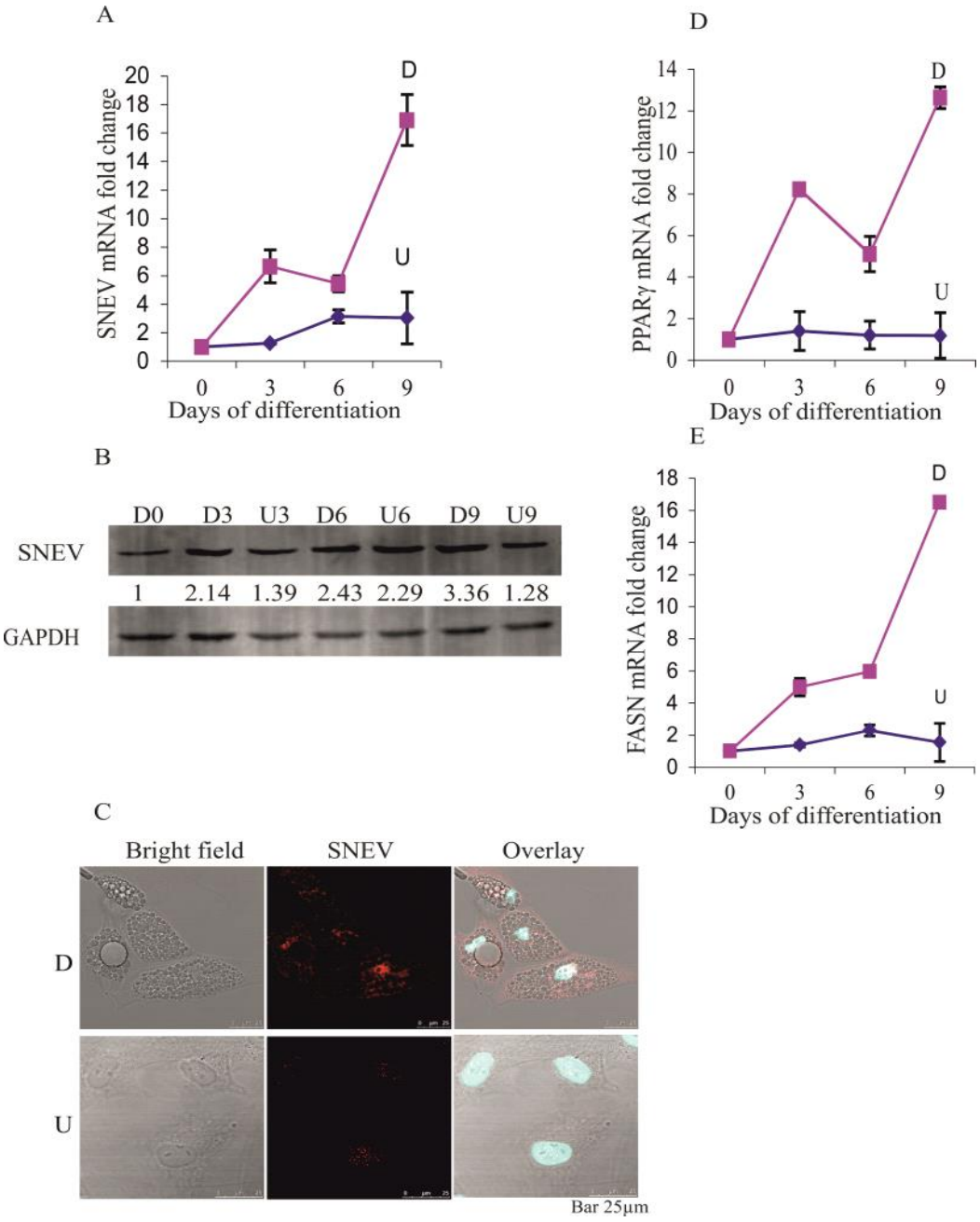

Figure 5.1: Expression of SNEV is induced during adipogenesis.

(A) Total RNA isolated from differentiated and undifferentiated hASCs were subjected to qPCR for quantitation of SNEV. The data were normalized to GAPDH. D represents differentiated and U undifferentiated cells and numbers represent the day of harvesting RNA. (B) hASCs differentiated (D) and undifferentiated (U) at various time points were harvested and whole cell lysate were prepared for Western blotting. GAPDH was used to ensure equal amount of protein loading. Numbers represent intensities of bands, normalized to GAPDH. (C) Differentiated and (D) undifferentiated (U) hASCs were fixed on day 10 and stained with anti SNEV hPrp19/hPso4 antibody (red) and DAPI (blue). Images were taken by Leica SP5 II laser scanning confocal microscope. Scale bar = 25µM. (D, E) Quantification of adipogenic differentiation was performed using PPARγ (D) and FASN (E) as marker

mRNAs. Data shown here is a representative of three independent experiments from 3different donors (n=3).

5.2. SNEV is required for adipogenic differentiation in human ASCs.

In order to determine whether SNEV is not only regulated during but also necessary for adipogenesis of hASCs, we performed siRNA mediated knock-down of SNEV followed by adipogenic induction. hASCs were transfected with siSNEV and control siRNA and were induced to differentiate 48 hours after transfection. Adipogenic differentiation was assessed by Oil red O staining and measurement of intracellular triglyceride content 10 days after start of differentiation according to the experimental design shown in figure 2A (Fig. 5.2A). siSNEV transfection resulted in around 90% knock-down efficiency on mRNA level over the 9 day period of differentiation tested (Fig. 2B). Non-targeting control siRNA transfected cells underwent normal lipid droplet formation, whereas SNEV knock-down resulted in formation of fewer lipid droplets as shown by Oil red O staining (Fig. 5.2C). Accordingly, intracellular triglyceride content was also 5-fold reduced after SNEV knock-down as compared to control (Fig.5.2D).

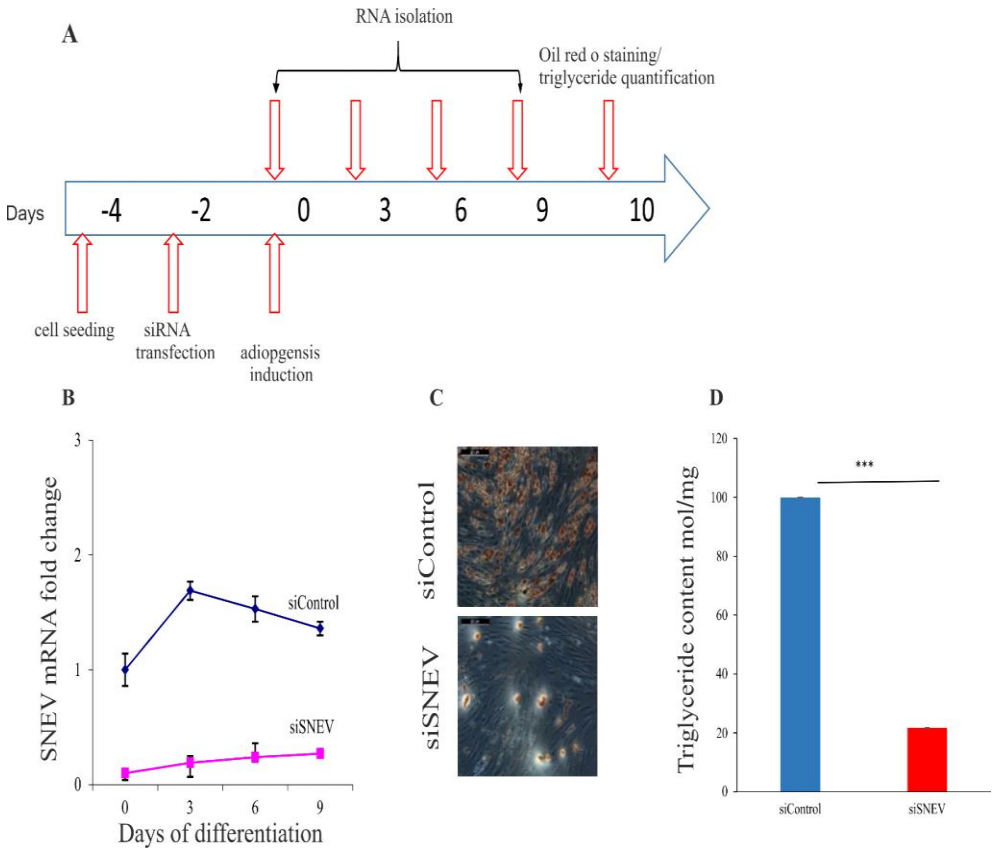

Figure 5.2: Knock-down of SNEV inhibits adipogenic differentiation in hASCs. A) Schematic representation of experimental design, where hASCs were transfected with siRNA against SNEV (siSNEV) or with control siRNA (siControl) to down-regulate SNEV and then induced to differentiate. Total RNA isolated at specified time points was subjected to qPCR analysis. (B) mRNA expression of SNEV during adipogenic differentiation. Data shown are representative of three independent experiments and were normalized to GAPDH mRNA (*P<0.01; **P<0.001). (C) Oil red O staining for triglyceride content in transfected hASCs after 10 days of differentiation. (D) Intracellular triglyceride levels in transfected hASCs after 10 days of differentiation. Triglyceride content was normalized to total protein content. Data shown is a representative of two independent experiments performed in quadruplicates (*P<0.01; ***P<0.0001).

4.3. *Reduced adipogenesis by SNEV knock-down is accompanied by down regulated PPARγ and insulin signaling axis.*

We next sought to investigate how SNEV might inhibit the early steps of adipogenesis. Thus, we performed microarray analysis to visualize profile changes in gene expression in response to SNEV down regulation during adipogenesis. hASCs transfected with siSNEV and siControl were induced to differentiate. Total RNA was

collected at day 3 of differentiation (see material & methods) and subjected to microarray analysis. SNEV mRNA expression is efficiently down regulated in response to siSNEV transfection (Fig.5.3A). The microarray data identified 163 genes that showed at least two fold differential expression in siSNEV vs siControl culture. In order to identify the pathways that might be addressed by SNEV knock-down, we performed gene set enrichment analysis (GSEA). In accordance to the observed inhibition in adipogenesis, genes involved in the pro-adipogenic PPARγ (Fig.5.3B) and insulin signaling (Fig 5.3C) pathways were down-regulated by siSNEV, whereas genes involved in the anti-adipogenic TGFβ signaling (Fig 5.3D) pathway were up regulated. We further confirmed our microarray data by qPCR of PPARγ (Fig 5.3E) and FASN (Fig 5.3F) during the entire course of adipogenesis. Collectively, these data suggest that SNEV is necessary in an early step as it inhibits the global changes of the transcriptome towards adipogenesis induced by starting the differentiation process.

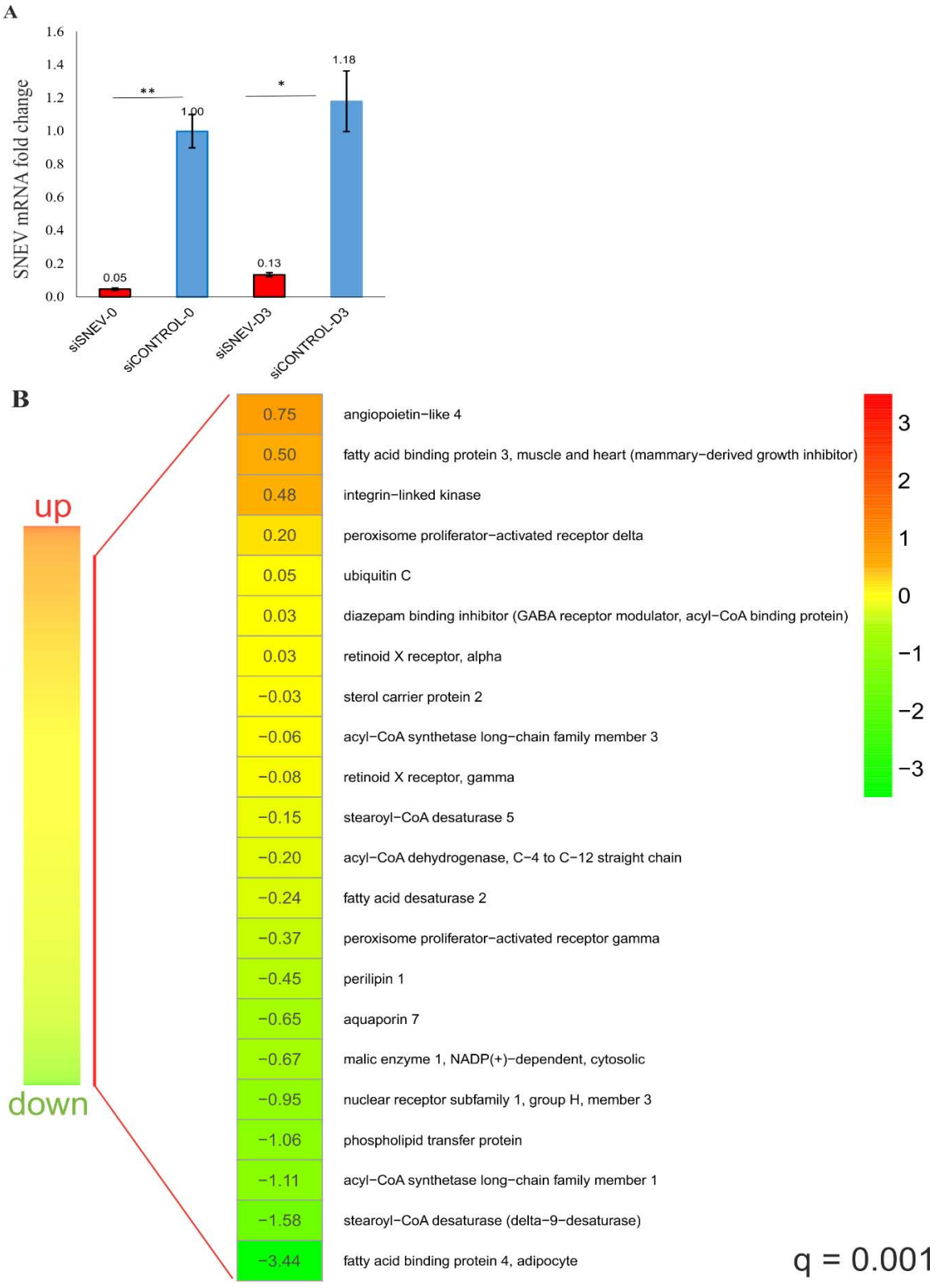
A
SNEV mRNA fold change
1.6
1.4
1.2
1.0
0.8
0.6
0.4
0.2
0.0
**
*
1.00
1.18
0.05
0.13
siSNEV-0
siCONTROL-0
siSNEV-D3
siCONTROL-D3
B
up
down
0.75 angiopoietin−like 4
0.50 fatty acid binding protein 3, muscle and heart (mammary−derived growth inhibitor)
0.48 integrin−linked kinase
0.20 peroxisome proliferator−activated receptor delta
0.05 ubiquitin C
0.03 diazepam binding inhibitor (GABA receptor modulator, acyl−CoA binding protein)
0.03 retinoid X receptor, alpha
−0.03 sterol carrier protein 2
−0.06 acyl−CoA synthetase long−chain family member 3
−0.08 retinoid X receptor, gamma
−0.15 stearoyl−CoA desaturase 5
−0.20 acyl−CoA dehydrogenase, C−4 to C−12 straight chain
−0.24 fatty acid desaturase 2
−0.37 peroxisome proliferator−activated receptor gamma
−0.45 perilipin 1
−0.65 aquaporin 7
−0.67 malic enzyme 1, NADP(+)−dependent, cytosolic
−0.95 nuclear receptor subfamily 1, group H, member 3
−1.06 phospholipid transfer protein
−1.11 acyl−CoA synthetase long−chain family member 1
−1.58 stearoyl−CoA desaturase (delta−9−desaturase)
−3.44 fatty acid binding protein 4, adipocyte
3
2
1
0
−1
−2
−3
q = 0.001

C

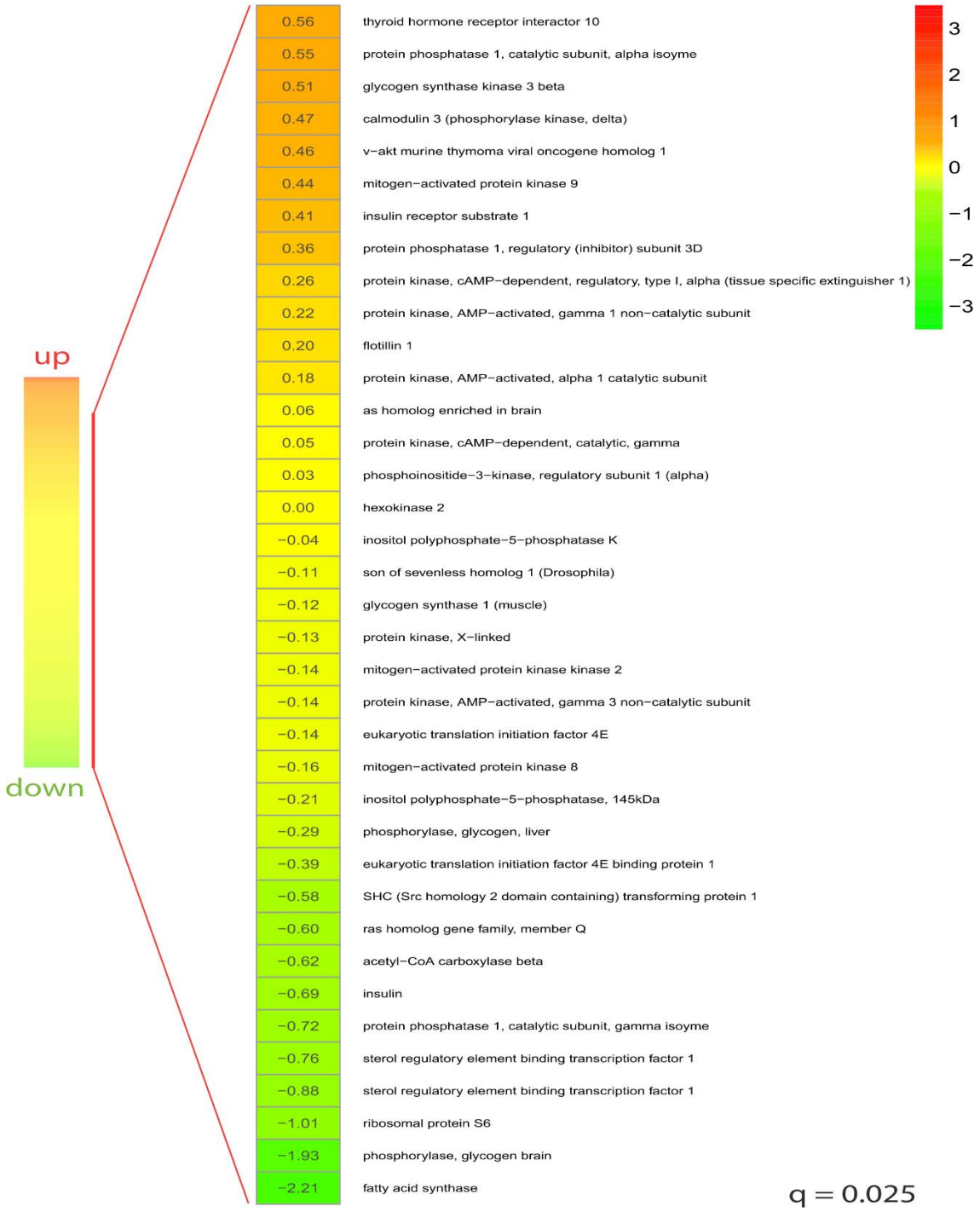
up
down
0.56 thyroid hormone receptor interactor 10
0.55 protein phosphatase 1, catalytic subunit, alpha isoyme
0.51 glycogen synthase kinase 3 beta
0.47 calmodulin 3 (phosphorylase kinase, delta)
0.46 v−akt murine thymoma viral oncogene homolog 1
0.44 mitogen−activated protein kinase 9
0.41 insulin receptor substrate 1
0.36 protein phosphatase 1, regulatory (inhibitor) subunit 3D
0.26 protein kinase, cAMP−dependent, regulatory, type I, alpha (tissue specific extinguisher 1)
0.22 protein kinase, AMP−activated, gamma 1 non−catalytic subunit
0.20 flotillin 1
0.18 protein kinase, AMP−activated, alpha 1 catalytic subunit
0.06 as homolog enriched in brain
0.05 protein kinase, cAMP−dependent, catalytic, gamma
0.03 phosphoinositide−3−kinase, regulatory subunit 1 (alpha)
0.00 hexokinase 2
−0.04 inositol polyphosphate−5−phosphatase K
−0.11 son of sevenless homolog 1 (Drosophila)
−0.12 glycogen synthase 1 (muscle)
−0.13 protein kinase, X−linked
−0.14 mitogen−activated protein kinase kinase 2
−0.14 protein kinase, AMP−activated, gamma 3 non−catalytic subunit
−0.14 eukaryotic translation initiation factor 4E
−0.16 mitogen−activated protein kinase 8
−0.21 inositol polyphosphate−5−phosphatase, 145kDa
−0.29 phosphorylase, glycogen, liver
−0.39 eukaryotic translation initiation factor 4E binding protein 1
−0.58 SHC (Src homology 2 domain containing) transforming protein 1
−0.60 ras homolog gene family, member Q
−0.62 acetyl−CoA carboxylase beta
−0.69 insulin
−0.72 protein phosphatase 1, catalytic subunit, gamma isoyme
−0.76 sterol regulatory element binding transcription factor 1
−0.88 sterol regulatory element binding transcription factor 1
−1.01 ribosomal protein S6
−1.93 phosphorylase, glycogen brain
−2.21 fatty acid synthase
3
2
1
0
−1
−2
−3
q = 0.025

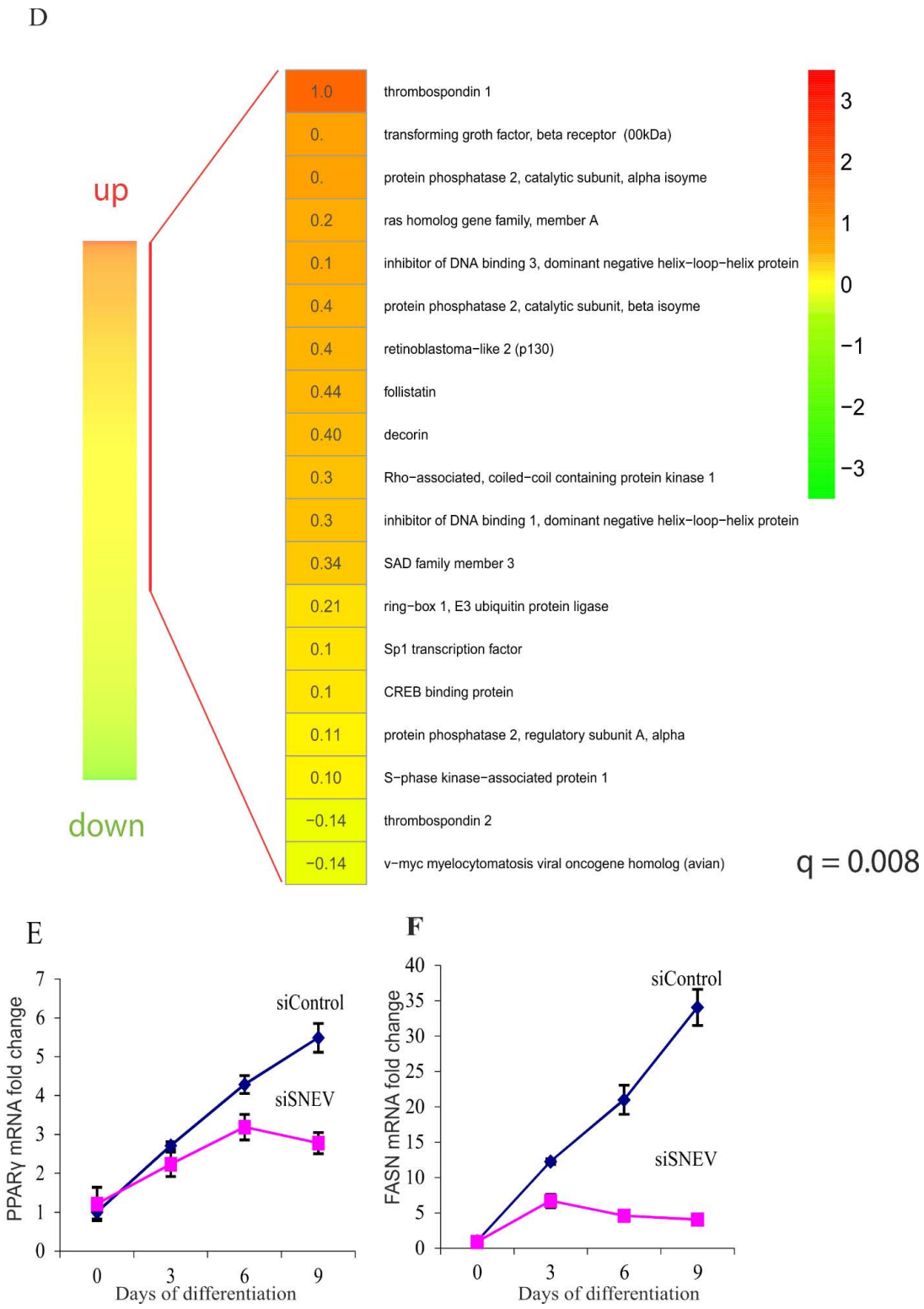

Figure 5.3: Knock-down of SNEV reduces the expression of adipogenic markers. (A) mRNA expression of SNEV in hASCs transfected with siRNA against SNEV (siSNEV) or with control siRNA (siControl) and induced to differentiate for 9 days. Total RNA was isolated and subjected to qPCR. D represent differentiated and U undifferentiated cells and numbers represent day of harvesting. (B) Micro-array based analysis of transcript expression assorted to the KEGG PPARγ signaling pathway is shown as heat map after GSEA. (C) Expression of transcripts assorted to the

KEGG insulin signaling pathway is shown as heat map. (D) Expression of transcripts assorted to the KEGG TGF-β signaling pathway is shown as heat map. Numbers within cells are log2-transformed expression ratios (siSNEV /siControl). The red vertical line denotes the range of this gene set relative to all 3250 transcripts that could be detected (small heat map). FDR q-value obtained from GSEA is depicted bottom right. E) qPCR analysis of PPARγ and (F) FASN confirming the microarray data. The data shown here is a representative of two independent experiments (n=2). (Figure 5.3(B, C, D) are kindly provided by our collaboration partners from medical university Graz)

4.4. *SNEV over-expression accelerates adipogenesis.*

The observation that SNEV knock-down reduced adipogenesis led us to test if its over-expression can lead to its acceleration. Therefore, we transduced hASCs with a lentiviral construct containing SNEV before induction of adipogenesis. hASCs transduced with empty vector were used as a control. Adipogenic differentiation was assessed by qPCR of PPARy and FASN, Oil red O staining and triglyceride quantification as outlined in Fig 5.4A.

Increased expression of SNEV in lentivirally transduced hASCs was confirmed by qPCR and remained elevated during the entire course of differentiation as compared to control (Fig 5.4B). Indeed, SNEV over-expression accelerated adipogenesis as large amounts of lipid droplets appeared already after 6 days as compared to the 10 days necessary under control conditions. In control cells, only very few lipid droplets were present on day 6 (Fig 5.4C). We further quantified intracellular lipid accumulation by triglyceride assay and found a 2-fold increase in SNEV over-expressing hASCs as compared to empty vector control (Fig 5.4D). These results suggest that SNEV over expression indeed accelerates adipogenesis in hASCs. In order to confirm accelerated adipogenesis at a molecular level, we measured mRNA expression of PPARγ and FASN expression by qPCR, showing the expected increases (Fig 5.4E and 5.4F). These results suggest that SNEV is indeed a modulator of adipogenesis as the process is affected both by its knock-down and over-expression.

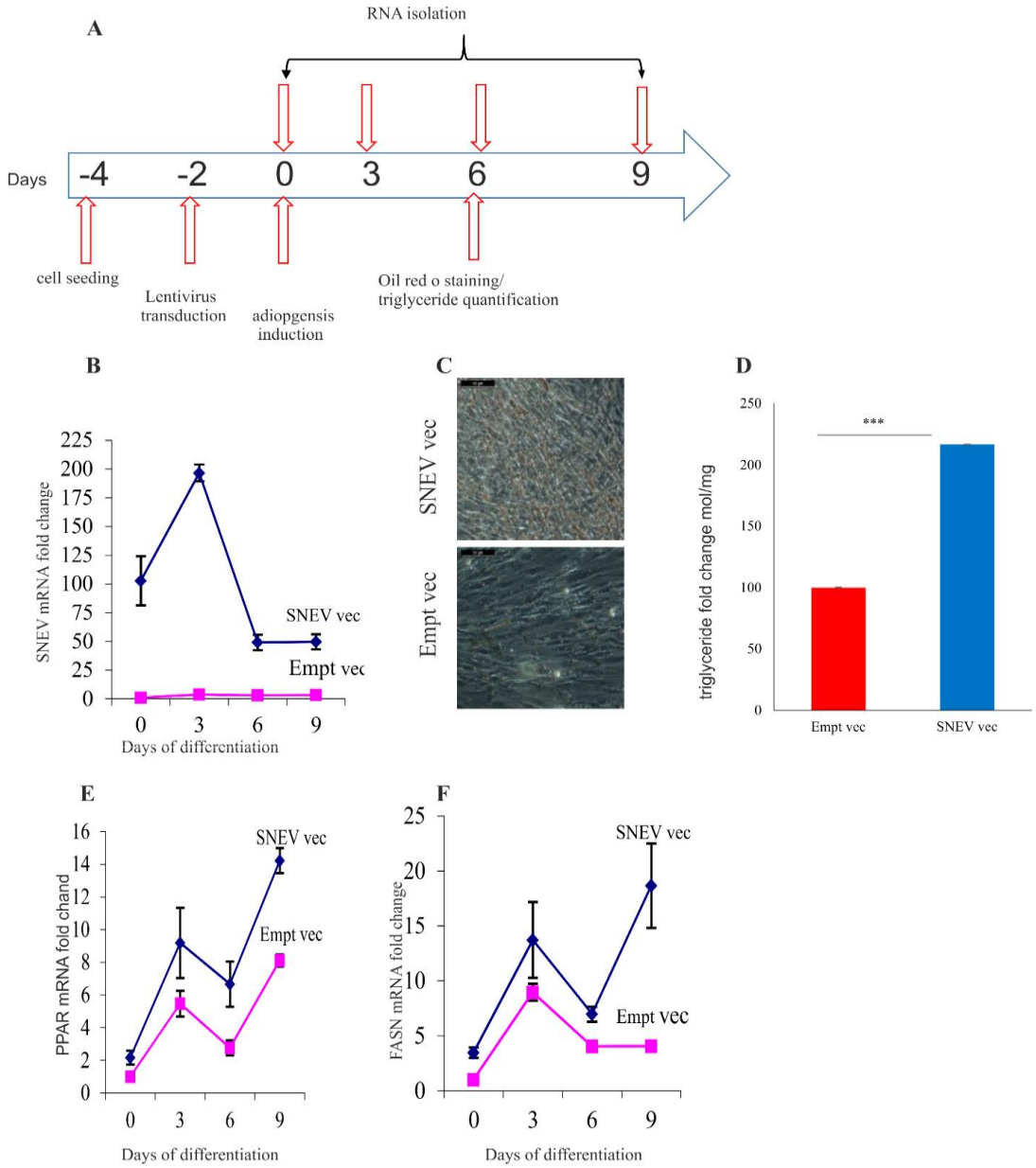

Figure 5.4:SNEV over-expression accelerates adipogenesis in hASCs. (A) Schematic representation of experimental design. hASCs were transduced with SNEV or empty vector and were sequentially differentiated for 10 days. (B) Total RNA isolated at specified time points was subjected to qPCR to analyze SNEV mRNA levels. Data shown here is a representative of 3 independent experiments and was normalized to GAPDH. (C) Oil red O staining of intracellular lipids after 6 days of differentiation. (D) Intracellular triglyceride levels in transduced hASCs after 6 days of differentiation. Triglyceride contents were normalized to total protein contents. (E) Quantitation of PPARγ and (F) FASN mRNA. Data shown is a representative of three independent experiments (*P<0.01; ***P<0.0001).

4.5. *Other DNA repair factors influence adipogenesis in hASCs.*

Since loss of subcutaneous fat is observed in patients suffering from progeroid syndromes, we tested if other DNA repair factors mutated in various segmental progeroid syndromes influence adipogenesis as well. For this purpose, we looked at existing transcriptomic data of an adipogenic differentiation time course experiment (available at Gene Expression Omnibus, accession number GSE64845) and specifically visualized the expression of genes involved in DNA damage repair (data not shown). From these, we selected WRN, CSA and XPE, which are involved in premature aging and are differentially expressed during adipogenesis (Fig. 5A), and confirmed their differential expression by qPCR (Fig. 5.5B, 5.5C, 5.5D). In addition, these genes represent members of different DNA damage repair pathways, CSA being specific for transcription coupled nucleotide excision repair (TC-NER) while XPE is involved in global genome as well as TC-NER and homologous recombination. WRN is a helicase generally required for DNA recombination and repair (reviewed in (Garinis et al., 2008). In order to test if these genes are indeed required for adipogenesis, we knocked down the expression of WRN, CSA, and XPE in hASCs by siRNA transfection, followed by induction of adipogenesis. siRNA knock-down efficiency was confirmed by qPCR (Fig. 5.5E). Adipogenic differentiation was then assessed by intracellular triglyceride accumulation at day 10 of differentiation. Triglyceride quantification data showed slight but significant decrease of adipogenesis of around 20% after CSA and XPE knock-down, while WRN knock-down resulted in a 50% reduction of Triglyceride accumulation in hASCs (Fig. 5.5F).

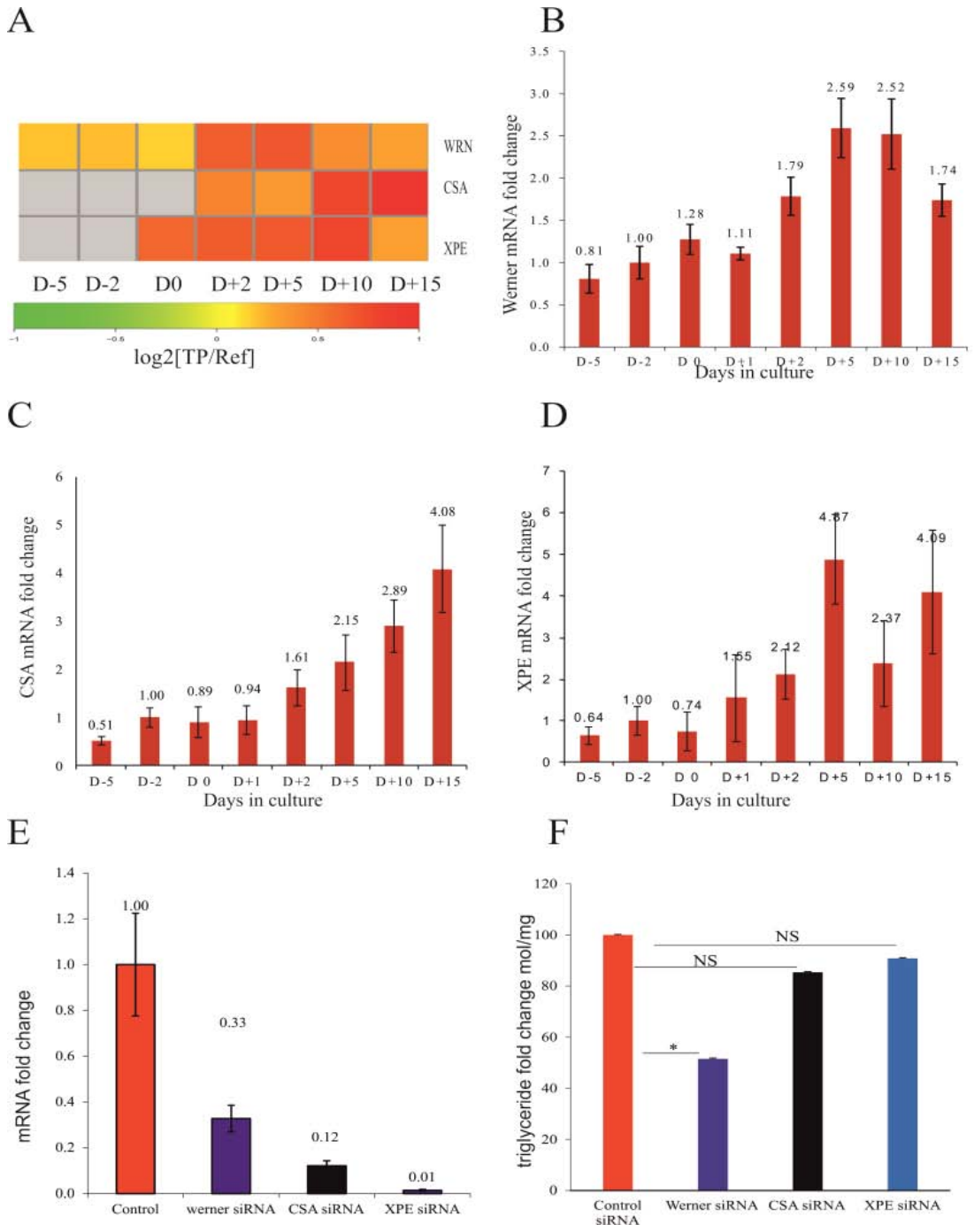

Figure 5.5: Knock-down of WRN, CSA and XPE reduces adipogenic differentiation in hASCs

(A) Heat map of differentially transcribed genes during adipogenesis is shown. Fold changes were calculated at reference day -2. mRNA fold change of (B) WRN, (C) CSA, and (D) XPE, during adipogenic differentiation are shown. (E) Knock-down of WRN, CSA, XPE mRNAs was confirmed by qPCR as compared to siControl and normalized to GAPDH. The data shown here is a representative of two independent experiments. (F) Triglyceride content was quantified at day 10 of adipogenic differentiation and normalized to total protein content. Figure 5.5(A) are kindly provided by our collaboration partners from medical university Graz.

4.6. *Loss of SNEV and WRN leads to reduced fat deposition in C. elegans.*

In order to test the functional conservation of the DNA damage repair factors (SNEV, WRN, CSA, and XPE) in organismal adipogenesis, we assessed their role in fat deposition of *Caenorhabiditis elegans*. For this purpose we selected *prp-19*, *wrn-1*, *xpa-1 and M18.5* as orthologs of the human DNA damage repair factors SNEV, WRN, XPA and DDB1, respectively, and inhibited their expression by RNAi in the N2 wild-type strain. The storage of neutral lipids was measured by Oil Red O staining (Soukas et al., 2009). At the time of planning the experiment, the homolog of human CSA in *C. elegans* was not known until very recently (Babu et al., 2014), therefore we selected *xpa-1* instead of CSA, as a member of NER factors and homologue of human XPA (Park et al., 2002). RNAi treatment was performed already upon hatching, since we did not detect major differences in developmental timing between RNAi-treated and control animals (data not shown). Young adult hermaphrodites (6 days after hatching) were then fixed and subjected to Oil-Red-O staining. Indeed, we found reduced fat mass in *prp-19* and *wrn-1* RNAi animals compared to the RNAi control, while *M18.5* and *xpa-1* RNAi did not show differences (Fig. 5.6A). However, we cannot exclude that slight variances might be missed by Oil Red O staining alone.

We expected to further enhance the observed fat storage phenotype of prp-19 and wrn-1 RNAi by performing the same experiment with the CF1814 strain, which is mutated in *rrf-3 (pk1426)* and *daf-2 (e1370)*. While mutation of *rrf-3* increases RNAi efficiency (Simmer et al., 2002) mutation of *daf-2*, the insulin receptor, results in elevated fat mass (Soukas et al., 2009). Indeed, while the RNAi control group stained positive for Oil Red O throughout the whole body and especially surrounding intestines and pharynx, *prp-19-1* and *wrn-1* RNAi animals stained only weekly positive in close proximity to the pharynx (Fig. 5.6B).

These findings indicate that loss of the conserved DNA damage repair factors *prp-19* and *wrn-1* robustly reduce the accumulation of neutral lipids both in wild-type *C. elegans*, as well as in a mutant strain with a high-fat phenotype.

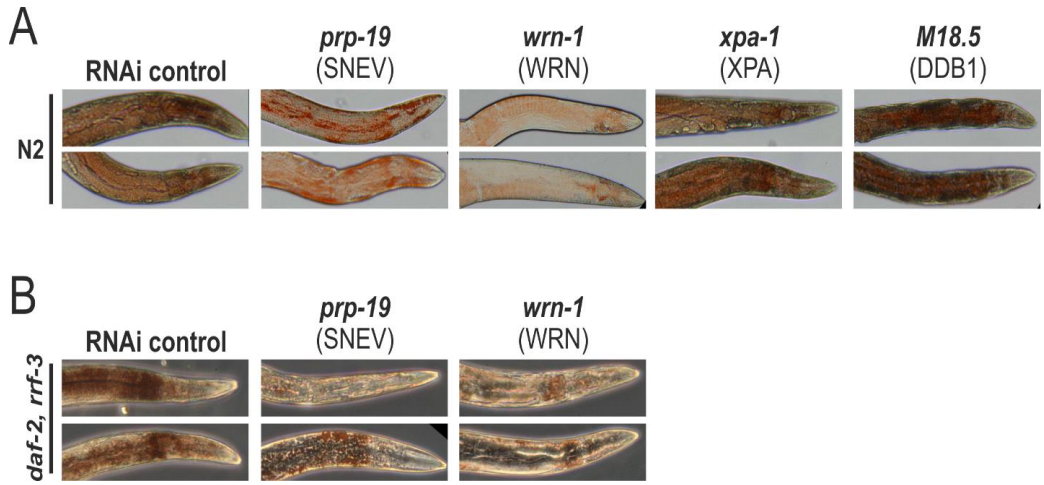

Figure 5.6: Loss of SNEV and WRN reduces fat deposition in *C. elegans*.

(A) Depletion of *prp-19*, *wrn-1*, *xpa-1* and *M18.5* by RNAi in wild-type *C. elegans*, followed by Oil Red O staining demonstrates lower fat deposition upon *prp-19* and *wrn-1*RNAi, compared to the empty vector (HT115) control. Representative images of two biological replicates with at least 20 worms per strain are shown. (B) RNAi to *prp-19* and *wrn-1* in the high-fat and RNAi hypersensitive CF1841strain, followed by Oil Red O staining confirms lower fat deposition compared to the empty vector control. Representative images of two biological replicates with at least 20 worms per strain are shown. (Figure 5.6 is kindly is kindly provided by Markus Schosserer, BOKU).

4.7. *SNEV down regulation does not influence osteogenic differentiation.*

Besides differentiating into adipocytes, hASCs are capable of differentiating into multiple other mesenchymal lineages, including the osteogenic lineage. In fact, an inverse relationship exists between osteogenic and adipogenic commitment and differentiation of mesenchymal stem cells and it is generally thought that differentiation into one of the two lineages comes at the expense of the other (James, 2013). Therefore, we tested if SNEV might influence osteogenic differentiation as well. We induced osteogenic differentiation in SNEV down regulated hASCs, and visualized calcium deposition by Alizarin Red staining as endpoint measurement of osteogenesis.

We first induced osteogenesis by replacing the growth medium with osteogenesis inducing medium and analyzed the expression of SNEV mRNA by qPCR. Figure 5.7A showed that SNEV mRNA expression during osteogenesis.

Next, we knocked down SNEV and induced osteogenesis in hASCs. As an endpoint measurement of osteogenesis, we performed alizarin red staining. siRNA against

SNEV reduced the expression of SNEV nearly 80% as compared to control siRNA(Figure 5.7B), however, we did not see any difference in SNEV down and control cells upon staining them with alizarin red staining(Figure 5.7C). Therefore, we conclude that SNEV may not be required for osteogenesis.

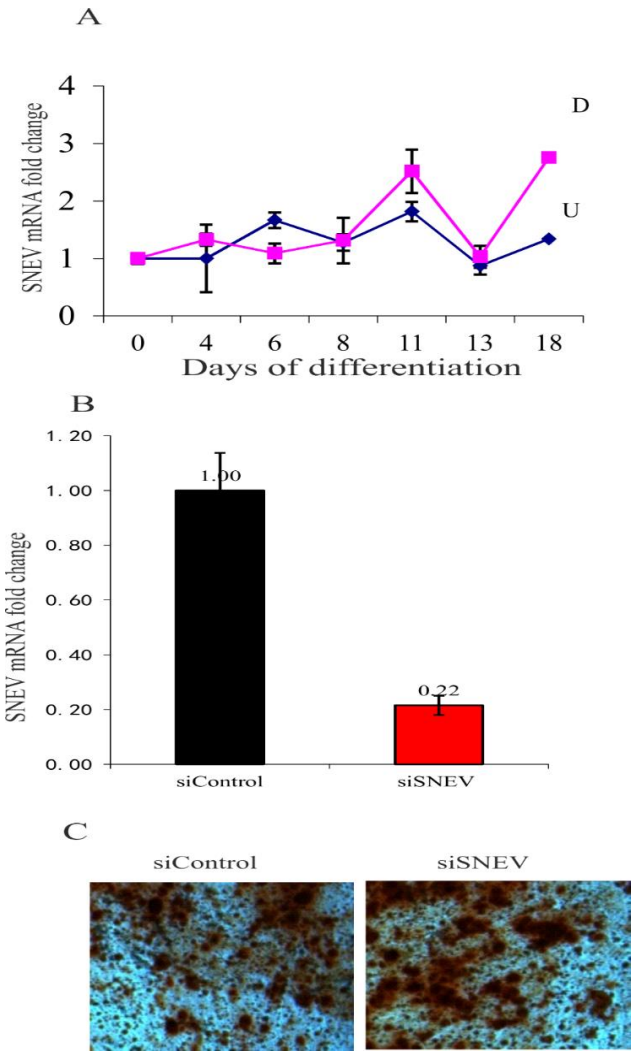

Figure5.7: Down-regulation of SNEV does not influence osteogenic differentiation.
hASCs were seeded 72 hours before initiation of osteogenic differentiation. Total RNA was isolated at indicated time points and subjected to qPCR analysis. (A) SNEV mRNA fold change during osteogenic differentiation. Fold changes were calculated in reference to un-differentiated cells at day 0 and normalized to GAPDH. D and U represent differentiated and undifferentiated cells, respectively. (B) SNEV mRNA fold changes after siRNA SNEV $^{hPrp19/hPso4}$ and control siRNA transfection. Fold changes were calculated in reference to siRNA control transfected cells and normalized to GAPDH. (C) Alizarin red staining of hASCs transfected with siRNA SNEV and control siRNA followed by osteogenic differentiation for 12 days, representative images are shown. Data shown here is performed once.

6. Discussion

6. Discussion

4.8. *How might phosphorylation of SNEV confer life span extension?*

We present SNEV as novel substrate of ATM kinase. SNEV is phosphorylated at S149 by ATM in different cell types in response to oxidative stress and various other DNA damage inducing agent. This modification is essential for suppressing oxidative stress induced apoptosis but dispensable for efficient DNA break repair and accounts for part of cellular life span extension.

We recently showed that multi-talented protein SNEV upon overexpression extends the replicative life span of endothelial cells by reducing basal level of DNA damage and suppresses oxidative stress induced apoptosis (Voglauer et al, 2006b). The multiple talents of SNEV, includes a well documented function in DNA repair (Beck et al, 2008; Lu & Legerski, 2007; Mahajan & Mitchell, 2003; Zhang et al, 2005), in pre-mRNA splicing, ubiquitin E3 ligase activity, adipogenic and neurogenic differentiation (Urano et al, 2006; Urano-Tashiro et al, 2010). However, it is not yet clear which function of SNEV is responsible for the life span extending activity.

We here identified an ATM consensus phosphorylation site on SNEV. although our experimental design does not allow us to be sure that ATM directly phosphorylate SNEV at this site but, Prp19, a SNEV homologue in yeast, is a direct phosphorylation target of Tel1 and/or Mec1, the yeast homologues of ATR and ATM (Smolka et al, 2007), making it more likely that this direct link is also conserved in human.

Since ATM dependent phosphorylation's are key signals of DNA damage and oxidative stress, we hypothesized that ATM dependent phosphorylation of SNEV might activate SNEV's DNA repair activity, which in turn contribute to its cellular life span extension function. In order to test this we overexpressed wild type SNEV and phosphorylation-incompetent point mutant SNEV and found that the DNA damage status of cells in unstressed condition is slightly reduced by point mutation. Surprisingly, oxidative stress mediated induction of apoptosis suppression as seen upon SNEV overexpression was completely abolished by S149A mutation, suggesting an important role of ATM dependent phosphorylation of SNEV in suppression of apoptosis. It is tempting to speculate that at least part of this high susceptibility of

ATM deficient cells to apoptosis (Kamsler et al, 2001; Rotman & Shiloh, 1997a; Takao et al, 2000) is dependent on the inability to phosphorylate SNEV. The question arise here is How might the S149 phosphorylatable form of SNEV suppress apoptosis?

Phosphorylated SNEV localizes under basal conditions exclusively to the cytoplasm, but is detected predominantly in the nucleus after DNA damage. Although it is likely that ATM phosphorylation occurs in the nucleus, but it cannot be ruled out that phosphoSNEV is imported into the nucleus. This would be supported by the notion that amino acids 1-166 of mouse SNEV are necessary for nuclear import (Cho et al, 2007) and the phosphorylation site lies within this portion possibly conferring a nuclear import signal. However, one report suggests that cytoplasmic SNEV is responsible to suppress apoptosis, at least under conditions of hypoxia. Under hypoxic conditions, a particular form of redox stress, SNEV is observed to interact with PHD3 in the cytoplasm (Sato et al, 2010), an interaction that suppresses cell death. In addition, GFP-SNEV, which localized preferentially in the cytoplasm (compared to untagged SNEV), has a stronger anti-apoptotic effect than untagged SNEV, indicating the cytoplasmic localization of SNEV is important for its anti-apoptotic role. We find that upon overexpression, the cytoplasmic portion of SNEV is increased when compared to untransfected HUVEC(Dellago et al., 2012), backing up the importance of cytoplasmic SNEV in preventing apoptosis. On the other hand, also in SNEV S149A HUVEC, the ratio of nuclear versus cytoplasmic SNEV is shifted towards the cytoplasm in a manner similar to SNEV wt HUVEC, but still these cells undergo apotosis upon oxidative stress, indicating that the phosphorylatability of cytoplasmic SNEV is essential for its anti-apoptotic effect. Under normoxic conditions, SNEV interacts with PHD3 via its C-terminus, while under hypoxic conditions, a hypoxia inducible interaction domain comprising amino acids 66-220 stabilizes this interaction (Sato et al, 2010). Since this region covers the S149, it is tempting to speculate that ATM-dependent phosphorylation at S149 is the signal for increased binding to PHD3, leading to apoptosis suppression, while the non phosphorylatable S149A mutant binds PHD3 with lower affinity, allowing for caspase activation by PHD3. It is also unclear, how the phosphoSNEV would accumulate in the cytoplasm, as it is not detected there upon stress with our antibody. It will be interesting to see if a phospho-mimicking S149D point mutant further increases the anti-apoptotic effect of SNEV

overexpression and where it will localize.

It remains to be elucidated how this translates into an extended life span of SNEV overexpressing cells. One of the possibilities is that suppression of apoptosis might reduce the loss of cells during cultivation and thus increase the total replicative life span merely by reducing the replicative exhaustion of the cells. However, the apoptosis competent cells of the S149A mutant overexpression are still markedly longer lived than empty vector control. This would suggest that the full life span extension as observed by wtSNEV overexpression depends on both, apoptosis suppression and the lower basal DNA damage of the cells and thus on SNEV's DNA repair activity.

Taken together, our data support the hypothesis that DNA damage repair and signalling factors can extend the life span of model systems, as in this case the replicative life span of endothelial cells and thus support the idea that a genetically programmed DNA repair ability counteracts and slows down the stochastic accumulation of DNA damage and thus the aging process.

4.9. *How does SNEV regulate adipogenesis of human adipose derived mesenchymal stem cells?*

This thesis also show that SNEV regulates adipogenesis of hASCs. SNEV knockdown inhibits, while its over expression accelerates adipogenesis early after induction of adipogenic differentiation. Furthermore, SNEV regulates fat deposition on the organismal level, as shown using the nematode C. elegans as model system.

SNEV regulates several diverse cellular processes, such as mRNA splicing, transcription (Chanarat et al., 2012), mitosis (Hofmann et al., 2013; Watrin et al., 2014) and apoptosis (Lu et al., 2014)). If, though, it was its DNA repair function that is connected with adipogenesis, then other DNA repair factors might have similar effects on adipogenesis, which would point to a general importance of intact DNA repair capacity for induction of adipogenesis. In fact, knock-down of WRN markedly reduced adipogenesis, while CSA and XPE only slightly inhibit accumulation of lipids in hASCs. In C. elegans, only SNEV and WRN reduced fat storage visibly. This is in accordance to studies that the murine homologues of SNEV and WRN are involved in 3T3 cell adipogenesis (Cho et al., 2007; Turaga et al., 2009), but also are components of an ICL repair complex (Zhang et al 2005a). Still, the species specific

differences in protein function and regulation patterns (Lindroos et al., 2013; Mikkelsen et al., 2010; Qian et al., 2010) make clear that not all molecular regulation steps are indeed conserved from mouse to human. This might explain that in this study human SNEV seems to act upstream of PPARγ and PPARγ induced genes, in contrast to 3T3 where PPARγ remained unchanged but inhibit the expression of SCD and perilipin 1 (Cho et al. 2007). A role upstream or at the level of PPARγ is also supported by findings that SNEV (Grillari et al. 2005) as well as PPARγ tend to cluster at nuclear speckles in adipocytes as compared to undifferentiatied cells (Szczerbal and Bridger, 2010). In addition, SNEV knockdown decreases expression of genes involved in the insulin signaling pathway are known to be pro-adipogenic (Heikkinen et al., 2007; Zhang et al., 2009), while genes involved in TGF-β signaling are increased which have inhibitory effects on adipogenesis (Choy and Derynck, 2003). Altogether, these data point to a regulatory role of SNEV early during adipogenic commitment of hASCs, however, since SNEV is a multifunctional protein, we still cannot rule out the possibility that it regulates adipogenesis via other than its DNA repair function, e.g. via differential pre-mRNA splicing, or via a putative role as a transcription factor, since SNEV has been shown to be required for full transcriptional activity of RNA polymerase II in yeast (Chanarat et al., 2012).

In any case, an interesting possibility is suggested by the fact that not only SNEV but also other DNA repair factors inhibit adipogenesis, supporting the idea that the capacity of repairing DNA damage is a checkpoint for adipogenesis. It is still unclear, however, why the inducibility of DNA damage repair might be such a checkpoint.

One hypothesis might be based on the fact that both adipogenesis and lipolysis are strongly associated with increased generation of reactive oxygen species (ROS)(Kanda et al., 2011; Krawczyk et al., 2012), which might be a driver of increased damage to DNA during adipogenesis, so that differentiating cells are at risk to enter ROS induced premature senescence, concomitant with induction of the senescent/pro-inflammatory phenotype of SASP (senescence associated secretory phenotype) (Monickaraj et al., 2013) . Only if sufficient DNA repair capacity is present in the cells would the cells therefore be allowed to enter adipogenic differentiation. This is supported by the fact that DNA damage repair is induced during early adipogenesis (Meulle et al., 2008) and is even more important, as senescence impair adipogenesis (Mitterberger et al., 2014) and accumulation of

senescent cells in the adipose tissue (Stout et al., 2014) would lead to degeneration of adipose tissue and inflammation. The lack of adipogenic differentiation together with adipose tissue degeneration induced by senescent adipocytes might therefore be one factor why patients suffering from segmental, progeroid syndromes and mouse models of premature aging like e.g. ERCC1 deficient mice, show loss of subcutaneous fat (Jaarsma et al., 2013; Karakasilioti et al., 2013).

In addition to adipogenesis, also neurogenic differentiation is accompanied and modified by ROS (Domenis et al., 2014), and again SNEV knock-down inhibits neurogenic differentiation (Urano-Tashiro et al., 2010). Further, the role of ROS seems different in osteogenic differentiation (Atashi et al., 2015). If the hypothesis that DNA damage repair capacity is a checkpoint for specific differentiation programs is true, the main question to be answer is on what the sensing mechanism for the presence of DNA repair capacity might be. It is tempting to speculate that SNEV, a downstream target of ATM upon oxidative stress (Dellago et al., 2012) might be part of a signaling pathway that senses and repairs DNA damage by a wave of initial ROS produced during early steps of differentiation. It is of interest in this context that during differentiation, mesenchymal stem cells (MSCs) are more susceptible to undergo ROS induced apoptosis than progenitor cells (Oliver et al., 2013), and over-expression of SNEV protects the cell types tested so far against induction of apoptosis (Dellago et al., 2012; Schraml et al., 2008; Voglauer et al., 2006).

Summarized, we suggest that availability of DNA damage repair might represent a checkpoint for cellular differentiation programs, which is of special importance for differentiation processes that involve high levels of ROS, or for long lived cells like adipocytes and neurons.

4.10. *Delineation of the key aspects in the regulation of epithelial monolayer differentiation*

In addition to the above main projects, I also participated in projects aiming at characterization of the transcriptional, metabolic, and functional alterations during epithelial monolayer maturation of proximal tubular epithelial cells(Aschauer et al., 2013) as well as in the face of toxic substances like cisplatin (Fliedl et al., 2014). We showed that proliferating cells have a higher energy demand with both increased glycolysis and oxygen consumption and exhibit an immature cell-to-cell junction

complex with nuclear TJP3 expression and high activity of HIF1A and c-MYC. The matured monolayers have lower energy demands, express TJP3, claudin 2, and claudin 10 at the intercellular junctions, and exhibit high activities of p53 and FOXO1. Given the main role for these processes in physiological function and disease states such as cancer and fibrosis, these data will be of great benefit in the further delineation of these complex cellular pathways and will serve as a reference for the development of differentiation strategies of inducible pluripotent stem cells to a proximal-tubule phenotype. In addition, we showed that the discrepancy in kidney toxicity at organ level versus cell culture level seems to depend exactly on this differentiation and tight layer formation process.

4.11. *Conclusion*

SNEV is a multifunctional protein involved in a diverse array of cellular functions, like pre-mRNA splicing, transcription, DNA repair, apoptosis regulation, life span regulation, lipid droplet biogenesis and neuronal differentiation.

Here, in this thesis we present evidence that SNEV is a novel ATM kinase substrate. ATM phosphorylate SNEV at serine 149(S149) in response to oxidative stress induced DNA damage and this phosphorylation is an important regulator of SNEV in life span regulation, DNA double-strand break repair and apoptosis regulation.

In addition to this, we also demonstrated that SNEV is an important regulator of adipogenesis both, in vitro and in vivo. Its inhibition suppresses while its over expression accelerates adipogenesis in human adipose derived mesenchymal stem cells (hASCs). SNEV inhibition also reduced organismal fat deposition in C. elegans. In addition to SNEV, WRN is also required for adipogenesis in hASCs and in *C.elegans*.

4.12. *Future directions*

4.12.1. **SNEV in brown adipogenesis.**

Murine tissue analysis showed higher level of expression of SNEV both in brown adipose tissue (Cho et al 2007, therefore it will be interesting to know if SNEV is also involved in formation of brown adipose tissue as well.

4.12.2. Super SNEV fly

We have shown that SNEV overexpression accelerate adipogenesis in human adipose derived stem cells. The next logical question is, if these finding is also translated at organismal level. Therefore we generated a SNEV overexpressing Drosophila melanogaster strain in collaboration with Thomas Flatt at the Institute of Population Genetics at the University for Veterinary Medicine. Further characterization of SuperSNEV fly with regard to, adipogenesis, life span and stress resistance will provide a valuable insight into the function of SNEV in fat metabolism at organismal level and into organismal aging.

4.12.3. SNEV Ubiquitination substrate

One crucial point that needs further investigation is the physiological role of SNEV's E3 ligase activity. SNEV modify prp3, required for maturation of spliceosome (reference). SNEV also ubiquitinate RPA, required for activation of ATR (Marchal et al., 2014).

The key question thereby still is: what is the substrate of SNEV's ubiquitin ligase activity? Identification and isolation of new substrate of SNEV E3 activity will give important insights into the physiological functions of SNEV and how splicing, DSB repair and protein degradation might be linked with the extension of cellular life span.

For future efforts to identify SNEV ubiquitination substrates, we plan to use commercially available protein microarrays, which contain thousands of native, purified proteins for identification of SNEV ubiquitination substrates. The candidates obtained by these methods must then be confirmed and further characterized. In order to confirm that the identified candidates are indeed substrates of SNEV, they will be expressed in an E.coli expression strain, purified and tested in an in vitro ubiquitination assay that we have already established according to Hatakeyama (Hatakeyama et al, 2001). In brief, we will reconstitute the ubiquitin ligase cascade by mixing E1, UbcH3 as E2 and SNEV together with recombinant ubiquitin and the putative substrates. Ubiquitination will then be analyzed by Western blotting. As negative control, non-targets will be added to the reaction instead of the candidates or ATP will be omitted from the reaction. In addition the identified candidates will be tested in mammalian cell culture in SNEV knock down/overexpression background

under MG132 treatment. The fraction of the ubiquitinated substrate can be visualized can be visualized by Western blotting. To monitor cellular localization of the substrate(s), we will generate GFP-fusion constructs as well as use (or generate) antibodies for indirect immunofluorescence studies.

Furthermore, we will establish stable, substrate overexpressing HUVECs as done previously with SNEV. Equally, we will inhibit these candidates by siRNA knockdown. Alterations of the cellular phenotype of the various transfected cells will be monitored during the life span by analyzing cell morphology, cell growth kinetics, cell cycle progression and cell type specific markers. The senescent phenotype will be verified by several biomarkers associated with replicative senescence such as senescence associated (SA)-ß-galactosidase staining (Dimri et al, 1995), the senescent morphology and regulation of prominent cell cycle regulators (p21, p16, p27 and p53) will be analyzed by Western blotting. DNA damage will be monitored by the COMET assay like done previously.

4.12.4. Effect of SNEV phosphorylation on life span, DNA repair, ubiquitination, and splicing.

Due to temporal and financial limitations of a doctoral thesis, we were not able to explore all facets of SNEV phosphorylation. However, future research will definitely shed light on the following aspects of SNEV phosphorylation.

In order to test if this ATM dependent phosphorylation is necessary for the life span extending effect of SNEV, we generated lentiviral expression constructs carrying wild type SNEV and site directed mutated SNEV, where the phosphorylated serine is changed to non-phosphorylatable alanine, as well as one construct where serine 149(S149) is replaced with phosphorylation-mimicking aspartic acid(S149D). These cell lines are needed to address the following questions:
Is phosphorylation for efficient splicing? This question can be addressed by in vivo splicing assays using the E1A reporter gene.

Overexpression of SNEV S149D leads to premature senescence. Are these cells arrested in G1, like senescent HUVEC normally are, or in S phase, as suggested by the involvement of SNEV and Cdc5 in ATR-dependent S phase checkpoint (Zhang et al, 2009).

We measured the level of DNA damage by comet assay only under basal conditions; how is the amount of DNA breaks changed by lack of or constitutive presence of S149 phosphorylation?

Finally, we plan to establish stable SNEVwt, S149A and S149D cell lines using HUVEC from different donors and other cell types like fibroblasts.

4.12.5. Confirmation of SNEV as a direct target of ATM kinase

To address the question if SNEV is a direct target of ATM kinase, and not of ATM downstream targets, we plan to perform Invitro kinase assay by using purified SNEV, ATM, and radioactively labeled ATP as a phosphate donor. Similarly we can also identify if SNEV is phosphorylated by any of ATM downstream target.

References.

Abbas, M., Shanmugam, I., Bsaili, M., Hromas, R., Shaheen, M., 2014. The role of the human psoralen 4 (hPso4) protein complex in replication stress and homologous recombination. J. Biol. Chem. 289, 14009–14019. doi:10.1074/jbc.M113.520056

Ahmadian, M., Wang, Y., Sul, H.S., 2010. Lipolysis in adipocytes. Int. J. Biochem. Cell Biol. doi:10.1016/j.biocel.2009.12.009

Ariyoshi, K., Suzuki, K., Goto, M., Watanabe, M., Kodama, S., 2007. Increased chromosome instability and accumulation of DNA double-strand breaks in Werner syndrome cells. J. Radiat. Res. 48, 219–231.

Aschauer, L., Gruber, L.N., Pfaller, W., Limonciel, A., Athersuch, T.J., Cavill, R., Khan, A., Gstraunthaler, G., Grillari, J., Grillari, R., Hewitt, P., Leonard, M.O., Wilmes, A., Jennings, P., 2013. Delineation of the key aspects in the regulation of epithelial monolayer formation. Mol. Cell. Biol. 33, 2535–50. doi:10.1128/MCB.01435-12

Baker, D.J., Dawlaty, M.M., Wijshake, T., Jeganathan, K.B., Malureanu, L., van Ree, J.H., Crespo-Diaz, R., Reyes, S., Seaburg, L., Shapiro, V., Behfar, A., Terzic, A., van de Sluis, B., van Deursen, J.M., 2013. Increased expression of BubR1 protects against aneuploidy and cancer and extends healthy lifespan. Nat. Cell Biol. 15, 96–102. doi:10.1038/ncb2643

Baker, D.J., Jeganathan, K.B., Cameron, J.D., Thompson, M., Juneja, S., Kopecka, A., Kumar, R., Jenkins, R.B., de Groen, P.C., Roche, P., van Deursen, J.M., 2004. BubR1 insufficiency causes early onset of aging-associated phenotypes and infertility in mice. Nat. Genet. 36, 744–749. doi:10.1038/ng1382

Baker, D.J., Wijshake, T., Tchkonia, T., LeBrasseur, N.K., Childs, B.G., van de Sluis, B., Kirkland, J.L., van Deursen, J.M., 2011. Clearance of p16Ink4a-positive senescent cells delays ageing-associated disorders. Nature. doi:10.1038/nature10600

Bernardes de Jesus, B., Vera, E., Schneeberger, K., Tejera, A.M., Ayuso, E., Bosch, F., Blasco, M.A., 2012. Telomerase gene therapy in adult and old mice delays aging and increases longevity without increasing cancer. EMBO Mol. Med. 4, 691–704. doi:10.1002/emmm.201200245

Bertola, D.R., Cao, H., Albano, L.M.J., Oliveira, D.P., Kok, F., Marques-Dias, M.J., Kim, C.A., Hegele, R.A., 2006. Cockayne syndrome type A: Novel mutations in eight typical patients. J. Hum. Genet. 51, 701–705. doi:10.1007/s10038-006-0011-7

Bertrand, H.A., Lynd, F.T., Masoro, E.J., Yu, B.P., 1980. Changes in adipose mass and cellularity through the adult life of rats fed ad libitum or a life-prolonging restricted diet. J. Gerontol. 35, 827–835.

Best, B.P., 2009. Nuclear DNA damage as a direct cause of aging. Rejuvenation Res. 12, 199–208. doi:10.1089/rej.2009.0847

Blalock, E.M., Geddes, J.W., Chen, K.C., Porter, N.M., Markesbery, W.R., Landfield, P.W., 2004. Incipient Alzheimer's disease: microarray correlation analyses reveal major transcriptional and tumor suppressor responses. Proc. Natl. Acad. Sci. U. S. A. 101, 2173–2178. doi:10.1073/pnas.0308512100

Brendel, M., Bonatto, D., Strauss, M., Revers, L.F., Pungartnik, C., Saffi, J., Henriques, J.A.P., 2003. Role of PSO genes in repair of DNA damage of Saccharomyces cerevisiae, in: Mutation Research - Reviews in Mutation Research. pp. 179–193. doi:10.1016/j.mrrev.2003.06.018

Brenner, S., 1974. The genetics of Caenorhabditis elegans. Genetics 77, 71–94. doi:10.1002/cbic.200300625

Campisi, J., 2005. Senescent cells, tumor suppression, and organismal aging: Good citizens, bad neighbors. Cell. doi:10.1016/j.cell.2005.02.003

Campisi, J., 2013. Aging, cellular senescence, and cancer. Annu. Rev. Physiol. 75, 685–705. doi:10.1146/annurev-physiol-030212-183653

Cartwright, M.J., Tchkonia, T., Kirkland, J.L., 2007. Aging in adipocytes: Potential impact of inherent, depot-specific mechanisms. Exp. Gerontol. doi:10.1016/j.exger.2007.03.003

Caso, G., McNurlan, M.A., Mileva, I., Zemlyak, A., Mynarcik, D.C., Gelato, M.C., 2013. Peripheral fat loss and decline in adipogenesis in older humans. Metabolism. 62, 337–340. doi:10.1016/j.metabol.2012.08.007

Chen, Z.J., Sun, L.J., 2009. Nonproteolytic Functions of Ubiquitin in Cell Signaling. Mol. Cell. doi:10.1016/j.molcel.2009.01.014

Cho, S.Y., Shin, E.S., Park, P.J., Shin, D.W., Chang, H.K., Kim, D., Lee, H.H., Lee, J.H., Kim, S.H., Song, M.J., Chang, I.-S., Lee, O.S., Lee, T.R., 2007. Identification of mouse Prp19p as a lipid droplet-associated protein and its possible involvement in the biogenesis of lipid droplets. J. Biol. Chem. 282, 2456–2465. doi:10.1074/jbc.M608042200

Davidovic, M., Sevo, G., Svorcan, P., Milosevic, D.P., Despotovic, N., Erceg, P., 2010. Old age as a privilege of the "selfish ones". Aging Dis. 1, 139–46.

Davy, A., Bello, P., Thierry-Mieg, N., Vaglio, P., Hitti, J., Doucette-Stamm, L., Thierry-Mieg, D., Reboul, J., Boulton, S., Walhout, A.J.M., Coux, O., Vidal, M., 2001. A protein-protein interaction map of the Caenorhabditis elegans 26S proteasome. EMBO Rep. 2, 821–828. doi:10.1093/embo-reports/kve184

Dellago, H., Löscher, M., Ajuh, P., Ryder, U., Kaisermayer, C., Grillari-Voglauer, R., Fortschegger, K., Gross, S., Gstraunthaler, A., Borth, N., Eisenhaber, F., Lamond, A.I., Grillari, J., 2011. Exo70, a subunit of the exocyst complex, interacts with SNEV(hPrp19/hPso4) and is involved in pre-mRNA splicing. Biochem. J. 438, 81–91. doi:10.1042/BJ20110183

Di Leonardo, A., Linke, S.P., Clarkin, K., Wahl, G.M., 1994. DNA damage triggers a prolonged p53-dependent G1 arrest and long-term induction of Cip1 in normal human fibroblasts. Genes Dev. 8, 2540–2551. doi:10.1101/gad.8.21.2540

Fliedl, L., Wieser, M., Manhart, G., Gerstl, M.P., Khan, A., Grillari, J., Grillari-

Voglauer, R., 2014. Controversial role of gamma-glutamyl transferase activity in cisplatin nephrotoxicity. ALTEX 31, 269–278. doi:10.14573/altex.1311152

Fonseca-Alaniz, M.H., Takada, J., Alonso-Vale, M.I.C., Lima, F.B., 2007. Adipose tissue as an endocrine organ: from theory to practice. J. Pediatr. (Rio. J). 83, S192–S203. doi:10.2223/JPED.1709

Garg, A., Agarwal, A.K., 2009. Lipodystrophies: Disorders of adipose tissue biology. Biochim. Biophys. Acta - Mol. Cell Biol. Lipids. doi:10.1016/j.bbalip.2008.12.014

Garinis, G.A., van der Horst, G.T.J., Vijg, J., Hoeijmakers, J.H.J., 2008. DNA damage and ageing: new-age ideas for an age-old problem. Nat. Cell Biol. 10, 1241–1247. doi:10.1038/ncb1108-1241

Goto, M., 2000. Werner's syndrome: From clinics to genetics. Clin. Exp. Rheumatol.

Gotzmann, J., Gerner, C., Meissner, M., Holzmann, K., Grimm, R., Mikulits, W., Sauermann, G., 2000. hNMP 200: a novel human common nuclear matrix protein combining structural and regulatory functions. Exp. Cell Res. 261, 166–179. doi:10.1006/excr.2000.5025

Grey, M., Düsterhöft, A., Henriques, J.A.P., Brendel, M., 1996. Allelism of PSO4 and PRP19 links pre-mRNA processing with recombination and error-prone DNA repair in Saccharomyces cerevisiae. Nucleic Acids Res. 24, 4009–4014. doi:10.1093/nar/24.20.4009

Grillari, J., Ajuh, P., Stadler, G., L??scher, M., Voglauer, R., Ernst, W., Chusainow, J., Eisenhaber, F., Pokar, M., Fortschegger, K., Grey, M., Lamond, A.I., Katinger, H., 2005. SNEV is an evolutionarily conserved splicing factor whose oligomerization is necessary for spliceosome assembly. Nucleic Acids Res. 33, 6868–6883. doi:10.1093/nar/gki986

Grillari, J., Löscher, M., Denegri, M., Lee, K., Fortschegger, K., Eisenhaber, F., Ajuh, P., Lamond, A.I., Katinger, H., Grillari-Voglauer, R., 2009. Blom7alpha is a novel heterogeneous nuclear ribonucleoprotein K homology domain protein

involved in pre-mRNA splicing that interacts with SNEVPrp19-Pso4. J. Biol. Chem. 284, 29193–29204. doi:10.1074/jbc.M109.036632

Hammond, E.M., Giaccia, A.J., 2004. The role of ATM and ATR in the cellular response to hypoxia and re-oxygenation. DNA Repair (Amst). doi:10.1016/j.dnarep.2004.03.035

Harley, C.B., Futcher, A.B., Greider, C.W., 1990. Telomeres shorten during ageing of human fibroblasts. Nature 345, 458–460. doi:10.1038/345458a0

Haslam, D.W., James, W.P.T., 2005. Obesity, in: Lancet. pp. 1197–1209. doi:10.1016/S0140-6736(05)67483-1

Hatakeyama, S., Yada, M., Matsumoto, M., Ishida, N., Nakayama, K.I., 2001. U box proteins as a new family of ubiquitin-protein ligases. J. Biol. Chem. 276, 33111–33120. doi:10.1074/jbc.M102755200

HAYFLICK, L., MOORHEAD, P.S., 1961. The serial cultivation of human diploid cell strains. Exp. Cell Res. 25, 585–621. doi:10.1016/0014-4827(61)90192-6

Heikkinen, S., Auwerx, J., Argmann, C.A., 2007. PPARgamma in human and mouse physiology. Biochim. Biophys. Acta 1771, 999–1013. doi:10.1016/j.bbalip.2007.03.006

Henriques, J.A., Vicente, E.J., Leandro da Silva, K. V, Schenberg, A.C., 1989. PSO4: a novel gene involved in error-prone repair in Saccharomyces cerevisiae. Mutat. Res. 218, 111–124. doi:10.1016/0921-8777(89)90017-7

Herbig, U., Ferreira, M., Condel, L., Carey, D., Sedivy, J.M., 2006. Cellular senescence in aging primates. Science 311, 1257. doi:10.1126/science.1122446

Hickson, I., Zhao, Y., Richardson, C.J., Green, S.J., Martin, N.M.B., Orr, A.I., Reaper, P.M., Jackson, S.P., Curtin, N.J., Smith, G.C.M., 2004. Identification and characterization of a novel and specific inhibitor of the ataxia-telangiectasia mutated kinase ATM. Cancer Res. 64, 9152–9159. doi:10.1158/0008-5472.CAN-04-2727

Hogg, R., McGrail, J.C., O'Keefe, R.T., 2010. The function of the NineTeen Complex (NTC) in regulating spliceosome conformations and fidelity during pre-mRNA splicing. Biochem. Soc. Trans. 38, 1110–1115. doi:10.1042/BST0381110

Hsu, C.S., Li, Y., 2002. Aspirin potently inhibits oxidative DNA strand breaks: implications for cancer chemoprevention. Biochem Biophys Res Commun 293, 705–709. doi:10.1016/S0006-291X(02)00271-1\rS0006-291X(02)00271-1 [pii]

James, A.W., 2013. Review of Signaling Pathways Governing MSC Osteogenic and Adipogenic Differentiation. Scientifica (Cairo). 2013, 684736. doi:10.1155/2013/684736

Jun, J.-I., Lau, L.F., 2010. The matricellular protein CCN1 induces fibroblast senescence and restricts fibrosis in cutaneous wound healing. Nat. Cell Biol. 12, 676–685. doi:10.1038/ncb2070

Kamenisch, Y., Fousteri, M., Knoch, J., von Thaler, A.-K., Fehrenbacher, B., Kato, H., Becker, T., Dollé, M.E.T., Kuiper, R., Majora, M., Schaller, M., van der Horst, G.T.J., van Steeg, H., Röcken, M., Rapaport, D., Krutmann, J., Mullenders, L.H., Berneburg, M., 2010. Proteins of nucleotide and base excision repair pathways interact in mitochondria to protect from loss of subcutaneous fat, a hallmark of aging. J. Exp. Med. 207, 379–390. doi:10.1084/jem.20091834

Karagiannides, I., Tchkonia, T., Dobson, D.E., Steppan, C.M., Cummins, P., Chan, G., Salvatori, K., Hadzopoulou-Cladaras, M., Kirkland, J.L., 2001. Altered expression of C/EBP family members results in decreased adipogenesis with aging. Am. J. Physiol. Regul. Integr. Comp. Physiol. 280, R1772–R1780.

Karakasilioti, I., Kamileri, I., Chatzinikolaou, G., Kosteas, T., Vergadi, E., Robinson, A.R., Tsamardinos, I., Rozgaja, T.A., Siakouli, S., Tsatsanis, C., Niedernhofer, L.J., Garinis, G.A., 2013. DNA damage triggers a chronic autoinflammatory response, leading to fat depletion in NER progeria. Cell Metab. 18, 403–415. doi:10.1016/j.cmet.2013.08.011

Kipling, D., Davis, T., Ostler, E.L., Faragher, R.G.A., 2004. What can progeroid syndromes tell us about human aging? Science 305, 1426–1431.

doi:10.1126/science.1102587

Kirkwood, T.B.L., 1977. Evolution of aging. Nature 270, 301–304. doi:10.1038/270301a0

Krizhanovsky, V., Yon, M., Dickins, R.A., Hearn, S., Simon, J., Miething, C., Yee, H., Zender, L., Lowe, S.W., 2008. Senescence of Activated Stellate Cells Limits Liver Fibrosis. Cell 134, 657–667. doi:10.1016/j.cell.2008.06.049

Kuraoka, I., Ito, S., Wada, T., Hayashida, M., Lee, L., Saijo, M., Nakatsu, Y., Matsumoto, M., Matsunaga, T., Handa, H., Qin, J., Nakatani, Y., Tanaka, K., 2008. Isolation of XAB2 complex involved in pre-mRNA splicing, transcription, and transcription-coupled repair. J. Biol. Chem. 283, 940–950. doi:10.1074/jbc.M706647200

Lee, J.W., Harrigan, J., Opresko, P.L., Bohr, V.A., 2005. Pathways and functions of the Werner syndrome protein, in: Mechanisms of Ageing and Development. pp. 79–86. doi:10.1016/j.mad.2004.09.011

Lindroos, J., Husa, J., Mitterer, G., Haschemi, A., Rauscher, S., Haas, R., Gröger, M., Loewe, R., Kohrgruber, N., Schrögendorfer, K.F., Prager, G., Beck, H., Pospisilik, J.A., Zeyda, M., Stulnig, T.M., Patsch, W., Wagner, O., Esterbauer, H., Bilban, M., 2013. Human but not mouse adipogenesis is critically dependent on LMO3. Cell Metab. 18, 62–74. doi:10.1016/j.cmet.2013.05.020

Lopez, A.D., Mathers, C.D., Ezzati, M., Jamison, D.T., Murray, C.J., 2006. Global and regional burden of disease and risk factors, 2001: systematic analysis of population health data. Lancet 367, 1747–1757. doi:10.1016/S0140-6736(06)68770-9

Löscher, M., Fortschegger, K., Ritter, G., Wostry, M., Voglauer, R., Schmid, J.A., Watters, S., Rivett, A.J., Ajuh, P., Lamond, A.I., Katinger, H., Grillari, J., 2005. Interaction of U-box E3 ligase SNEV with PSMB4, the beta7 subunit of the 20 S proteasome. Biochem. J. 388, 593–603. doi:10.1042/BJ20041517

Lu, S., Wang, R., Cai, C., Liang, J., Xu, L., Miao, S., Wang, L., Song, W., 2014.

Small kinetochore associated protein (SKAP) promotes UV-induced cell apoptosis through negatively regulating Pre-mRNA processing factor 19 (Prp19). PLoS One 9. doi:10.1371/journal.pone.0092712

Lu, X., Legerski, R.J., 2007. The Prp19/Pso4 core complex undergoes ubiquitylation and structural alterations in response to DNA damage. Biochem. Biophys. Res. Commun. 354, 968–974. doi:10.1016/j.bbrc.2007.01.097

Mahajan, K.N., Mitchell, B.S., 2003. Role of human Pso4 in mammalian DNA repair and association with terminal deoxynucleotidyl transferase. Proc. Natl. Acad. Sci. U. S. A. 100, 10746–10751. doi:10.1073/pnas.1631060100

Mangerich, A., Herbach, N., Hanf, B., Fischbach, A., Popp, O., Moreno-Villanueva, M., Bruns, O.T., Bürkle, A., 2010. Inflammatory and age-related pathologies in mice with ectopic expression of human PARP-1. Mech. Ageing Dev. 131, 389–404. doi:10.1016/j.mad.2010.05.005

Mar??chal, A., Li, J.M., Ji, X.Y., Wu, C.S., Yazinski, S.A., Nguyen, H.D., Liu, S., Jim??nez, A.E., Jin, J., Zou, L., 2014. PRP19 Transforms into a Sensor of RPA-ssDNA after DNA Damage and Drives ATR Activation via a Ubiquitin-Mediated Circuitry. Mol. Cell 53, 235–246. doi:10.1016/j.molcel.2013.11.002

Matera, a G., Wang, Z., 2014. A day in the life of the spliceosome. Nat. Rev. Mol. Cell Biol. 15, 108–21. doi:10.1038/nrm3742

Matsuoka, S., Ballif, B.A., Smogorzewska, A., McDonald, E.R., Hurov, K.E., Luo, J., Bakalarski, C.E., Zhao, Z., Solimini, N., Lerenthal, Y., Shiloh, Y., Gygi, S.P., Elledge, S.J., 2007. ATM and ATR substrate analysis reveals extensive protein networks responsive to DNA damage. Science 316, 1160–1166. doi:10.1126/science.1140321

Matyskiela, M.E., Rodrigo-Brenni, M.C., Morgan, D.O., 2009. Mechanisms of ubiquitin transfer by the anaphase-promoting complex. J. Biol. 8, 92. doi:10.1186/jbiol184

Mayas, M.D., Ortega, F.J., Macías-González, M., Bernal, R., Gómez-Huelgas, R.,

Fernández-Real, J.M., Tinahones, F.J., 2010. Inverse relation between FASN expression in human adipose tissue and the insulin resistance level. Nutr. Metab. (Lond). 7, 3. doi:10.1186/1743-7075-7-3

Melk, A., Kittikowit, W., Sandhu, I., Halloran, K.M., Grimm, P., Schmidt, B.M.W., Halloran, P.F., 2003. Cell senescence in rat kidneys in vivo increases with growth and age despite lack of telomere shortening. Kidney Int. 63, 2134–2143. doi:10.1046/j.1523-1755.2003.00032.x

Minamino, T., Miyauchi, H., Yoshida, T., Tateno, K., Kunieda, T., Komuro, I., 2004. Vascular cell senescence and vascular aging. J. Mol. Cell. Cardiol. doi:10.1016/j.yjmcc.2003.11.010

Moore, B.A., Robinson, H.H., Xu, Z., 2007. The Crystal Structure of Mouse Exo70 Reveals Unique Features of the Mammalian Exocyst. J. Mol. Biol. 371, 410–421. doi:10.1016/j.jmb.2007.05.018

Mori, S., Murano, S., Yokote, K., Takemoto, M., Asaumi, S., Take, A., Saito, Y., 2001. Enhanced intra-abdominal visceral fat accumulation in patients with Werner's syndrome., International journal of obesity and related metabolic disorders : journal of the International Association for the Study of Obesity. doi:10.1038/sj.ijo.0801529

Muller-Ohldach, M., Brust, D., Hamann, A., Osiewacz, H.D., 2011. Overexpression of PaParp encoding the poly(ADP-ribose) polymerase of Podospora anserina affects organismal aging. Mech. Ageing Dev. 132, 33–42. doi:10.1016/j.mad.2010.11.003

Muñoz-Espín, D., Cañamero, M., Maraver, A., Gómez-López, G., Contreras, J., Murillo-Cuesta, S., Rodríguez-Baeza, A., Varela-Nieto, I., Ruberte, J., Collado, M., Serrano, M., 2013. Programmed cell senescence during mammalian embryonic development. Cell 155, 1104–18. doi:10.1016/j.cell.2013.10.019

Musi, N., Guardado-Mendoza, R., 2014. Adipose Tissue as an Endocrine Organ, in: Cellular Endocrinology in Health and Disease. pp. 229–237. doi:10.1016/B978-0-12-408134-5.00014-7

Ogryzko, V. V, Hirai, T.H., Russanova, V.R., Barbie, D.A., Howard, B.H., 1996. Human fibroblast commitment to a senescence-like state in response to histone deacetylase inhibitors is cell cycle dependent. Mol. Cell. Biol. 16, 5210–5218.

Ohi, M.D., Vander Kooi, C.W., Rosenberg, J.A., Chazin, W.J., Gould, K.L., 2003. Structural insights into the U-box, a domain associated with multi-ubiquitination. Nat. Struct. Biol. 10, 250–255. doi:10.1038/nsb906

Paleologou, K.E., Schmid, A.W., Rospigliosi, C.C., Kim, H.Y., Lamberto, G.R., Fredenburg, R.A., Lansbury, P.T., Fernandez, C.O., Eliezer, D., Zweckstetter, M., Lashuel, H.A., 2008. Phosphorylation at Ser-129 but not the phosphomimics S129E/D inhibits the fibrillation of α-synuclein. J. Biol. Chem. 283, 16895–16905. doi:10.1074/jbc.M800747200

Park, H.K., Yook, J.-S., Koo, H.-S., Choi, I.S., Ahn, B., 2002. The Caenorhabditis elegans XPA homolog of human XPA. Mol. Cells 14, 50–55.

Pichierri, P., Franchitto, A., Mosesso, P., Palitti, F., 2001. Werner's syndrome protein is required for correct recovery after replication arrest and DNA damage induced in S-phase of cell cycle. Mol. Biol. Cell 12, 2412–2421.

Plyusnina, E.N., Shaposhnikov, M. V., Moskalev, A.A., 2011. Increase of Drosophila melanogaster lifespan due to D-GADD45 overexpression in the nervous system. Biogerontology 12, 211–226. doi:10.1007/s10522-010-9311-6

Poser, I., Sarov, M., Hutchins, J.R.A., Hériché, J.-K., Toyoda, Y., Pozniakovsky, A., Weigl, D., Nitzsche, A., Hegemann, B., Bird, A.W., Pelletier, L., Kittler, R., Hua, S., Naumann, R., Augsburg, M., Sykora, M.M., Hofemeister, H., Zhang, Y., Nasmyth, K., White, K.P., Dietzel, S., Mechtler, K., Durbin, R., Stewart, A.F., Peters, J.-M., Buchholz, F., Hyman, A.A., 2008. BAC TransgeneOmics: a high-throughput method for exploration of protein function in mammals. Nat. Methods 5, 409–415. doi:10.1038/nmeth0808-748b

Qi, M., Zhang, J., Zeng, W., Chen, X., 2014. DNAJB1 stabilizes MDM2 and contributes to cancer cell proliferation in a p53-dependent manner. Biochim. Biophys. Acta - Gene Regul. Mech. 1839, 62–69.

doi:10.1016/j.bbagrm.2013.12.003

Qian, S.-W., Li, X., Zhang, Y.-Y., Huang, H.-Y., Liu, Y., Sun, X., Tang, Q.-Q., 2010. Characterization of adipocyte differentiation from human mesenchymal stem cells in bone marrow. BMC Dev. Biol. 10, 47. doi:10.1186/1471-213X-10-47

Raveche, E., Abbasi, F., Yuan, Y., Salerno, E., Kasar, S., Marti, G.E., 2010. Introduction to Flow Cytometry, in: Flow Cytometry in Drug Discovery and Development. pp. 3–21. doi:10.1002/9780470910085.ch1

Rodriguez, A.M., Elabd, C., Amri, E.Z., Ailhaud, G., Dani, C., 2005. The human adipose tissue is a source of multipotent stem cells, in: Biochimie. pp. 125–128. doi:10.1016/j.biochi.2004.11.007

Rogina, B., Helfand, S.L., 2004. Sir2 mediates longevity in the fly through a pathway related to calorie restriction. Proc. Natl. Acad. Sci. U. S. A. 101, 15998–16003. doi:10.1073/pnas.0404184101

Rose, M.R., 1988. Modern biological theories of aging. Am. J. Hum. Genet. 43, 220–221. doi:10.1016/j.bbi.2008.05.010

Rosen, E.D., Walkey, C.J., Puigserver, P., Spiegelman, B.M., 2000. Transcriptional regulation of adipogenesis. Genes Dev. doi:10.1146/annurev.cellbio.16.1.145

Rossi, D.J., Bryder, D., Seita, J., Nussenzweig, A., Hoeijmakers, J., Weissman, I.L., 2007. Deficiencies in DNA damage repair limit the function of haematopoietic stem cells with age. Nature 447, 725–729. doi:10.1038/nature05862

Ruzankina, Y., Pinzon-Guzman, C., Asare, A., Ong, T., Pontano, L., Cotsarelis, G., Zediak, V.P., Velez, M., Bhandoola, A., Brown, E.J., 2007. Deletion of the Developmentally Essential Gene ATR in Adult Mice Leads to Age-Related Phenotypes and Stem Cell Loss. Cell Stem Cell 1, 113–126. doi:10.1016/j.stem.2007.03.002

Saely, C.H., Geiger, K., Drexel, H., 2011. Brown versus white adipose tissue: A mini-review. Gerontology. doi:10.1159/000321319

Sepe, A., Tchkonia, T., Thomou, T., Zamboni, M., Kirkland, J.L., 2010. Aging and regional differences in fat cell progenitors - A mini-review. Gerontology. doi:10.1159/000279755

Serrano, M., Lin, A.W., McCurrach, M.E., Beach, D., Lowe, S.W., 1997. Oncogenic ras provokes premature cell senescence associated with accumulation of p53 and p16(INK4a). Cell 88, 593–602. doi:10.1016/S0092-8674(00)81902-9

Sihn, C.R., Cho, S.Y., Lee, J.H., Lee, T.R., Kim, S.H., 2007. Mouse homologue of yeast Prp19 interacts with mouse SUG1, the regulatory subunit of 26S proteasome. Biochem. Biophys. Res. Commun. 356, 175–180. doi:10.1016/j.bbrc.2007.02.134

Simmer, F., Tijsterman, M., Parrish, S., Koushika, S.P., Nonet, M.L., Fire, A., Ahringer, J., Plasterk, R.H.A., 2002. Loss of the putative RNA-directed RNA polymerase RRF-3 makes C. elegans hypersensitive to RNAi. Curr. Biol. 12, 1317–1319. doi:10.1016/S0960-9822(02)01041-2

Smolka, M.B., Albuquerque, C.P., Chen, S., Zhou, H., 2007. Proteome-wide identification of in vivo targets of DNA damage checkpoint kinases. Proc. Natl. Acad. Sci. U. S. A. 104, 10364–10369. doi:10.1073/pnas.0701622104

So, S., Davis, A.J., Chen, D.J., 2009. Autophosphorylation at serine 1981 stabilizes ATM at DNA damage sites. J. Cell Biol. 187, 977–990. doi:10.1083/jcb.200906064

Song, E.J., Werner, S.L., Neubauer, J., Stegmeier, F., Aspden, J., Rio, D., Harper, J.W., Elledge, S.J., Kirschner, M.W., Rape, M., 2010. The Prp19 complex and the Usp4Sart3 deubiquitinating enzyme control reversible ubiquitination at the spliceosome. Genes Dev. 24, 1434–1447. doi:10.1101/gad.1925010

Soukas, A.A., Kane, E.A., Carr, C.E., Melo, J.A., Ruvkun, G., 2009. Rictor/TORC2 regulates fat metabolism, feeding, growth, and life span in Caenorhabditis elegans. Genes Dev. 23, 496–511. doi:10.1101/gad.1775409

Stiff, T., O'Driscoll, M., Rief, N., Iwabuchi, K., Löbrich, M., Jeggo, P.A., 2004. ATM

and DNA-PK Function Redundantly to Phosphorylate H2AX after Exposure to Ionizing Radiation. Cancer Res. 64, 2390–2396. doi:10.1158/0008-5472.CAN-03-3207

Strong, R., Miller, R.A., Astle, C.M., Floyd, R.A., Flurkey, K., Hensley, K.L., Javors, M.A., Leeuwenburgh, C., Nelson, J.F., Ongini, E., Nadon, N.L., Warner, H.R., Harrison, D.E., 2008. Nordihydroguaiaretic acid and aspirin increase lifespan of genetically heterogeneous male mice. Aging Cell 7, 641–650. doi:10.1111/j.1474-9726.2008.00414.x

Tang, Q.-Q., Otto, T.C., Lane, M.D., 2003. Mitotic clonal expansion: a synchronous process required for adipogenesis. Proc. Natl. Acad. Sci. U. S. A. 100, 44–49. doi:10.1073/pnas.0137044100

Tchkonia, T., Morbeck, D.E., Von Zglinicki, T., Van Deursen, J., Lustgarten, J., Scrable, H., Khosla, S., Jensen, M.D., Kirkland, J.L., 2010. Fat tissue, aging, and cellular senescence. Aging Cell. doi:10.1111/j.1474-9726.2010.00608.x

Timmons, L., Court, D.L., Fire, A., 2001. Ingestion of bacterially expressed dsRNAs can produce specific and potent genetic interference in Caenorhabditis elegans. Gene 263, 103–112. doi:10.1016/S0378-1119(00)00579-5

Tissenbaum, H.A., Guarente, L., 2001. Increased dosage of a sir-2 gene extends lifespan in Caenorhabditis elegans. Nature 410, 227–230. doi:10.1038/35065638

Turaga, R.V.N., Paquet, E.R., Sild, M., Vignard, J., Garand, C., Johnson, F.B., Masson, J.-Y., Lebel, M., 2009. The Werner syndrome protein affects the expression of genes involved in adipogenesis and inflammation in addition to cell cycle and DNA damage responses. Cell Cycle 8, 2080–2092. doi:10.4161/cc.8.13.8925

Urano, Y., Iiduka, M., Sugiyama, A., Akiyama, H., Uzawa, K., Matsumoto, G., Kawasaki, Y., Tashiro, F., 2006. Involvement of the mouse Prp19 gene in neuronal/astroglial cell fate decisions. J. Biol. Chem. 281, 7498–7514. doi:10.1074/jbc.M510881200

Urano-Tashiro, Y., Sasaki, H., Sugawara-Kawasaki, M., Yamada, T., Sugiyama, A., Akiyama, H., Kawasaki, Y., Tashiro, F., 2010. Implication of Akt-dependent Prp19 alpha/14-3-3beta/Cdc5L complex formation in neuronal differentiation. J. Neurosci. Res. 88, 2787–2797. doi:10.1002/jnr.22455

Vander Kooi, C.W., Ren, L., Xu, P., Ohi, M.D., Gould, K.L., Chazin, W.J., 2010. The Prp19 WD40 domain contains a conserved protein interaction region essential for its function. Structure 18, 584–593. doi:10.1016/j.str.2010.02.015

Voglauer, R., Chang, M.W.F., Dampier, B., Wieser, M., Baumann, K., Sterovsky, T., Schreiber, M., Katinger, H., Grillari, J., 2006. SNEV overexpression extends the life span of human endothelial cells. Exp. Cell Res. 312, 746–759. doi:10.1016/j.yexcr.2005.11.025

Wahl, M.C., Will, C.L., Lührmann, R., 2009. The Spliceosome: Design Principles of a Dynamic RNP Machine. Cell. doi:10.1016/j.cell.2009.02.009

Weissman, A.M., 2001. Themes and variations on ubiquitylation. Nat. Rev. Mol. Cell Biol. 2, 169–178. doi:10.1038/35056563

Wojewódzka, M., Buraczewska, I., Kruszewski, M., 2002. A modified neutral comet assay: Elimination of lysis at high temperature and validation of the assay with anti-single-stranded DNA antibody. Mutat. Res. - Genet. Toxicol. Environ. Mutagen. 518, 9–20. doi:10.1016/S1383-5718(02)00070-0

Wolbank, S., Stadler, G., Peterbauer, A., Gillich, A., Karbiener, M., Streubel, B., Wieser, M., Katinger, H., van Griensven, M., Redl, H., Gabriel, C., Grillari, J., Grillari-Voglauer, R., 2009. Telomerase immortalized human amnion- and adipose-derived mesenchymal stem cells: maintenance of differentiation and immunomodulatory characteristics. Tissue Eng. Part A 15, 1843–1854. doi:10.1089/ten.tea.2008.0205

Zhang, N., Kaur, R., Akhter, S., Legerski, R.J., 2009. Cdc5L interacts with ATR and is required for the S-phase cell-cycle checkpoint. EMBO Rep. 10, 1029–1035. doi:10.1038/embor.2009.122

Zhang, N., Kaur, R., Lu, X., Shen, X., Li, L., Legerski, R.J., 2005. The Pso4 mRNA splicing and DNA repair complex interacts with WRN for processing of DNA interstrand cross-links. J. Biol. Chem. 280, 40559–40567. doi:10.1074/jbc.M50845320

Appendix A

ATM - dependent phosphorylation of SNEV$^{hPrp19/hPso4}$ is involved in extending cellular life span and suppression of apoptosis

Research Paper

ATM-dependent phosphorylation of SNEV$^{hPrp19/hPso4}$ is involved in extending cellular life span and suppression of apoptosis

Hanna Dellago[1], Abdulhameed Khan[1], Monika Nussbacher[1], Anna Gstraunthaler[1], Ingo Lämmermann[1], Markus Schosserer[1], Christoph Mück[2], Dorothea Anrather[3], Annika Scheffold[4], Gustav Ammerer[3], Pidder Jansen-Dürr[2], Karl Lenhard Rudolph[4], Regina Voglauer-Grillari[1,5], Johannes Grillari[1,5]

[1] *Department of Biotechnology, University of Natural Resources and Life Sciences Vienna, Vienna, Austria*
[2] *Institute of Biomedical Aging Research, Austrian Academy of Sciences, Innsbruck, Austria*
[3] *Department of Biochemistry and Cell Biology, Max F. Perutz Laboratories, University of Vienna, Vienna, Austria*
[4] *Institute of Molecular Medicine and Max-Planck-Research Group on Stem Cell Aging, University of Ulm, Germany*
[5] *Evercyte GmbH, Muthgasse 18, 1190 Vienna, Austria*

Key words: *SNEV, Prp19, Pso4, ATM, oxidative stress, endothelial cells, replicative senescence*
Received: *1/31/12; Accepted: 4/18/12; Published: 4/20/12*
Correspondence to: *Johannes Grillari, PhD;* ***E-mail:*** *johannes.grillari@boku.ac.at*

Abstract: Defective DNA repair is widely acknowledged to negatively impact on healthy aging, since mutations in DNA repair factors lead to accelerated and premature aging. However, the opposite, namely if improved DNA repair will also increase the life or health span is less clear, and only few studies have tested if overexpression of DNA repair factors modulates life and health span in cells or organisms. Recently, we identified and characterized SNEV$^{hPrp19/hPso4}$, a protein that plays a role in DNA repair and pre-mRNA splicing, and observed a doubling of the replicative life span upon ectopic overexpression, accompanied by lower basal DNA damage and apoptosis levels as well as an increased resistance to oxidative stress. Here we find that SNEV$^{hPrp19/hPso4}$ is phosphorylated at S149 in an ataxia telangiectasia mutated protein (ATM)-dependent manner in response to oxidative stress and DNA double strand break inducing agents. By overexpressing wild-type SNEV$^{hPrp19/hPso4}$ and a phosphorylation-deficient point-mutant, we found that S149 phosphorylation is necessary for mediating the resistance to apoptosis upon oxidative stress and is partially necessary for elongating the cellular life span. Therefore, ATM dependent phosphorylation of SNEV$^{hPrp19/hPso4}$ upon DNA damage or oxidative stress might represent a novel axis capable of modulating cellular life span.

INTRODUCTION

Accumulation of DNA damage, if not repaired, can lead to premature aging, as indicated by several inherited diseases caused by mutations of DNA damage response factors that show features of premature aging [1], [2]. Furthermore, increased exposure to DNA damage might lead to the development of premature aging characteristics, e.g. in long-term survivors of chemotherapy, for which we proposed to use the term acquired premature progeroid syndrome (APPS; [3]).

One of the proteins orchestrating DNA damage response is ATM (ataxia telangiectasia mutated), which plays a central and multiple role in the cellular stress response by monitoring and maintaining DNA integrity (reviewed by [4]). These crucial functions are mirrored by the disorder caused by its mutations, Ataxia telangiectasia (A-T), which is also classified as a segmental progeroid syndrome [5] and includes symptoms like cerebellar degeneration, immuno-deficency, genomic instability, thymic and gonadal atrophy and cancer predisposition [6].

Biochemically, one of these functions is control of the cell cycle in response to DNA damage. This is exerted by ATM-dependent induction of p53 that leads to activation of the CDK inhibitor p21, resulting in inhibition of the Cyclin-E/CDK2 complex and inhibition of progression from G1 into S-phase [7].as well as a CHK2 phsophorylation dependent G2/M arrest [8].

An equally important function of ATM is in effectively repairing DNA double-strand breaks. Upon DNA damage, ATM is auto-phosphorylated leading to dissociation of the inactive dimer to active monomers, which are rapidly recruited to DNA DSB sites together with the MRN (Mre11, Rad50, NBS1) complex (reviewed by [4]. Then, ATM phosphorylates the histone variant H2AX to γH2AX, which provides a docking station for many repair factors and signal transducers like p53 and BRCA1, which are in turn phosphorylated by ATM [9, 10]. In addition, ATM activity on DNA DSB sites enables the relaxation of heterochromatin, which facilitates access of repair proteins to the damaged DNA [11].

A more recently identified function of ATM has been observed in the response to oxidative stress [12], probably by sensing reactive oxygen species (ROS) [13]. ROS impact on signal transduction, aging/senescence, apoptosis, neuromodulation and antioxidant gene modulation, in addition atherosclerosis and several neurodegenerative diseases [14], and at least part of these effects might involve ATM, as oxidative stress response pathways are constitutively active in A-T cells [13, 15].

Finally, a link between ATM and the pentose phosphate pathway is established (PPP, reviewed in [16]. After DNA damage, ATM stimulates PPP in order to generate nucleotides and NADPH needed for DNA repair. NADPH thereby not only provides the reducing equivalents for biosynthetic reactions but also for regeneration of the major ROS scavenger glutathione [17].

Recently, a consensus phosphorylation motif recognized by ATM and ATR (ATM and Rad3-related; a kinase that shares many substrates with ATM, but responds to distinct types of DNA damage) was identified [18].

To our surprise, the published consensus site is present in the amino acid sequence of SNEV$^{hPrp19/hPso4}$ (for simplicity reasons termed SNEV in the following), a "multi-talented" protein involved in pre-mRNA splicing [19-22], DNA repair [23-25], senescence and extension of life span [26, 27] and neuronal differentiation [28, 29]. SNEV increases replicative resistance to oxidative stress, reduces basal levels of DNA damage and apoptosis and increases cellular life span in vitro [26]. The role of SNEV in the mammalian DNA damage response (DDR) first emerged with the report that it was strongly upregulated by DNA damage in human cells, and that its depletion by siRNA resulted in an accumulation of double-strand breaks (DSBs), apoptosis and reduced survival after exposure to ionizing radiation [23]. Subsequently, Zhang and collaborators (2005) have shown that Cdc5L, a member of the SNEV core complex together with PLRG1 and SPF27/BCAS2, directly interacted with the Werner syndrome protein (WRN) and is involved in early steps of DNA interstrand cross link (ICL) repair. WRN is a DNA helicase that has roles in homologous recombination and the processing of stalled replication forks in response to DNA damage. Mutations of WRN are the cause of Werner's syndrome, one of the segmental progeroid syndromes that most strikingly resemble aging (reviewed by [30]. DNA damage also induces the attachment of ubiquitin to a subfraction of endogenous SNEV via a thiolester linkage, and this modification disrupts the interaction between SNEV and both Cdc5L and PLRG1 demonstrating that DNA damage can profoundly affect the structure of the SNEV core complex [24]. Recently, the SNEV complex has been connected to DNA damage checkpoint signaling pathways. Cdc5L interacts physically with the cell-cycle checkpoint kinase ataxia-telangiectasia and Rad3-related (ATR). Depletion of Cdc5L by RNA-mediated interference methods results in a defective S-phase cell-cycle checkpoint and cellular sensitivity in response to replication-fork blocking agents [31].

While mutations and deletions of several DNA repair factors are known to cause progeroid syndromes, there is very little known on the effects of overexpressing DNA repair factors on the life spans of model systems. As SNEV is known to extend the replicative life span of normal human cells, it would be of some interest to see if this effect is due to its DNA repair function.

Here, we show that indeed SNEV is phosphorylated in response to oxidative stress and different DNA damaging agents, and that phosphoSNEV is located predominantly in the nucleus. Moreover, we examined the impact of the phosphorylation on repair capacity and life span in cultured human cells by overexoressing wt and phosphorylation incompetent SNEV and show that phosphorylation at S149 is essential for mediating the cytoprotective effect of SNEV upon DNA damage/oxidative stress and partially contributes to the life span extension caused by SNEV overexpression.

RESULTS

Oxidative stress induces an additional SNEV protein band in Western blotting

From previous results we know that SNEV expression is induced upon oxidative and DNA DSB damage [23, 26]. To further study the effect of oxidative stress on SNEV, we treated HeLa cells with 1mM hydrogen peroxide for different times and detected additional bands above the expected 56 kDa band in a Western Blot with anti-SNEV antibody, and band intensity increased in a time-dependent manner. These higher bands were removed after dephosphorylation using calf intestinal phosphatase (Fig. 1A). Similarly, this additional SNEV band appeared when we treated human diploid fibroblasts (HDF5) with bleomycin (Fig. 1B).

These results prompted us to ask if these bands might represent a phosphorylated form of SNEV in response to oxidative stress. Therefore, we isolated SNEV as GFP-fusion from stable HeLa cells constitutively expressing GFP-tagged SNEV under the control of the endogenous promoter as described in [32] and submitted it to mass spectrometric analysis. The advantage of using GFP-SNEV-Hela lies in allowing the use of a commercially available GFP-antibody for IP which is covalently coupled to agarose beads, thus avoiding predominant detection of immunglobulins in the mass spectrometric analysis. In order to make sure that GFP-SNEV behaves similarly to SNEV in cells we confirmed its localization to nuclei (Fig. S1A) as well as its ability to integrate into the SNEV/CDC5L complex by co-precipitation of SNEV and CDC5L with GFP-SNEV by GFP antibodies (Fig. S1B).

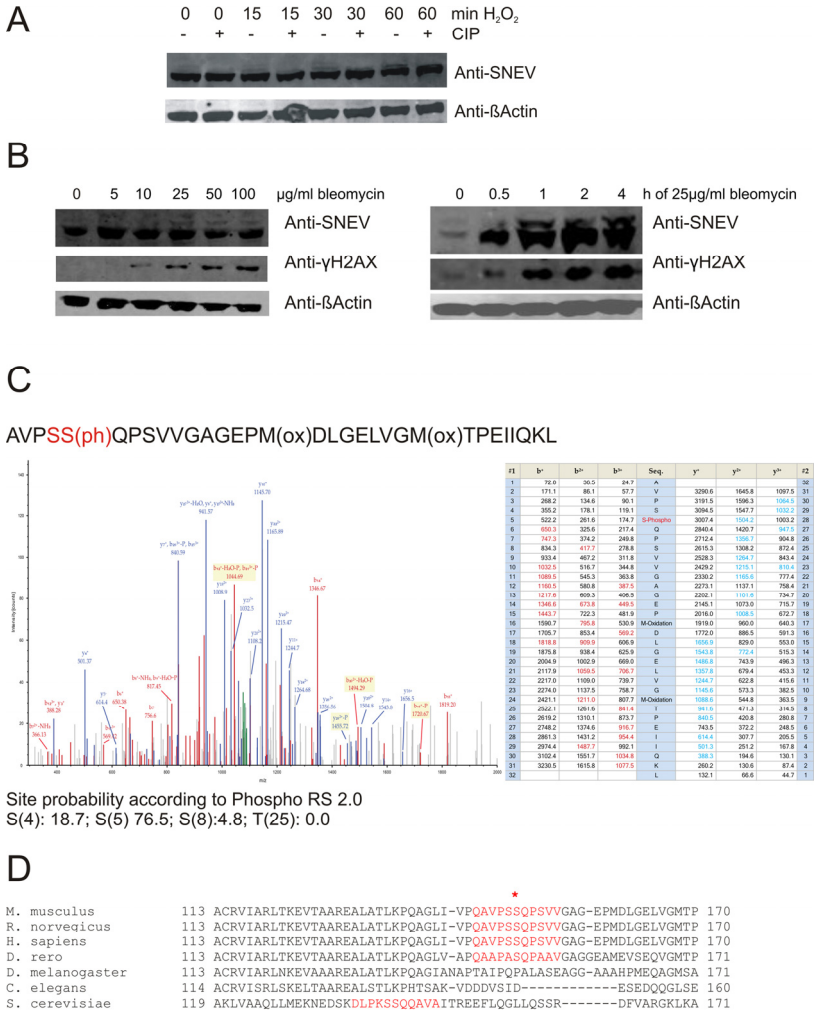

Figure 1. Upon oxidative stress, SNEV is detected as double band, probably representing a phosphorylated species. (**A**) Upon treatment with hydrogen peroxide, additional bands of higher molecular weight were detected with anti-SNEV antibody. These bands disappear upon incubation with phosphatase. (**B**) Similarly, upon bleomycin treatment of fibroblasts, we detected an additional band with anti-SNEV antibody, which increased in a dose-and time-dpendent manner. Fibrolblasts were incubated with 0, 5, 10, 25, 50 or 100µg/ml bleomycin for 1hour (left panels) or with 25µg/ml bleomycin for 0, 0.5, 1, 2, 4 hours (right panels), scraped on ice in 2x SDS loading dye and subjected to Western Blotting with anti-SNEV antibody. Anti-ß-actin was used to ensure equal loading. Anti-γH2AX antibody was used to confirm that the treatment induces DNA damage. (**C**) Collision-induced dissociation spectrum of the SNEV peptide AVPSS(ph)QPSVVGAGEPM(ox)DLGELVGM(ox)TPEIIQKL[3]. GFP-SNEV was isolated by IP from stable GFP-SNEV Hela treated with H_2O_2. Phosphopeptides were enriched by TiO_2 affinity chromatography and analysed on a Velos Orbitrap mass spectrometer. PhosphoRS 2.0 assigns the phospho-rylation to S149 with a probability of 76.5%. (**D**) Sequence comparison of SNEV homologues in the putative ATM target site. The consensus sequence surrounding the phospho-SQ site on ATM substrates that are regulated by DNA damage is conserved in the SNEV amino acid sequences across different vertebrates, but not in non-vertebrates.

Indeed, a phosphorylation was detected and assigned to S149 with a probability of 76.5% (Fig. 1C). While the consistence of three different spectra with different m/z ratios underscores the correct assignment of the phosphorylation to this site, the remaining uncertainty comes from the presence of 3 serine residues within a quite long peptide. Together with the problem of lack of trypsin or chymotrypsin proteolytic sites near these serines, a better proof of S149 as the really phosphorylated serine by mass spectrometry is hampered.

Interestingly, S149 also represents an ATM target site (Fig. 1D). Fig. S2 shows that the signal detected by MS is specific for H_2O_2-treated cells. This is not due to a difference in the efficiency of the IP, since the Western Blot in fig. S1B clearly shows that comparable amounts of GFP-SNEV were precipitated under both conditions. Table S1 gives a list of the identified phosphopeptides of SNEV in the H_2O_2-treated sample with site probability calculated by phosphoRS 2.0.

Taken together, the mass spec spectra, the presence of an ATM kinase consensus site, and ATM's known function as a kinase signaling oxidative stress prompted us to generate an anti-pSNEV(S149) specific antibody.

Phosphorylation of SNEV at S149 is induced by oxidative stress in different cell types

In order to take a closer look at this possible phosphorylation site of SNEV, a phospho-specific antibody was generated. This anti-pSNEV(S149) antibody detects a band at the expected size of SNEV upon oxidative stress treatment of Hela cells, and this signal is abolished upon phosphatase treatment (Fig. 2A). Besides the bands at the expected size, other bands are as well detected by anti-pSNEV(S149) antibody on Western Blot of Hela lysates (Fig. S3), but at higher molecular weights. These bands might represent post-translationally modified SNEV in complexes similar to the ones described in [24].

Based on these results, we were curious to confirm our assumption that SNEV phosphorylation was stimulated by DNA damage in normal cells. Human diploid fibroblasts (HDF5) were exposed to different concentrations of hydrogen peroxide for 1 hour or to 100μM hydrogen peroxide for different times. Total cell lysates were subjected to Western Blot analysis with anti-pSNEV(S149). Indeed, phosphorylation of SNEV was triggered by oxidative stress in a time- and dose-dependent manner (Fig. 2B and C). Phosphorylation was observed as quickly as after 5 minutes of hydrogen peroxide treatment and reached a maximum after 1 hour. To verify that hydrogen peroxide treatment indeed induced the formation of DNA double strand breaks (DSB), we examined the ATM dependent phosphorylation of γH2AX, which occurs in response to DSB [7], and showed a similar kinetic as phosphorylation of SNEV (Fig. 2B and C).

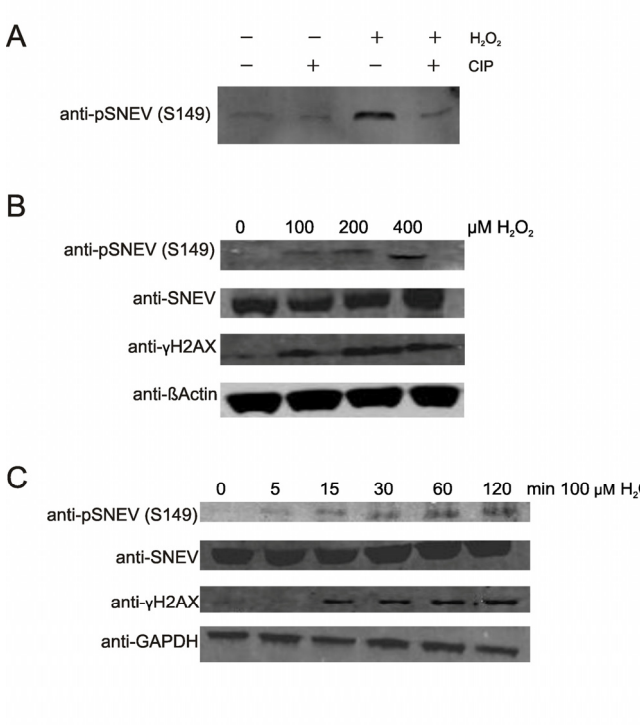

Figure 2. Phosphorylation of SNEV at serine 149 is induced by oxidative stress in a time- and dose dependent manner. (**A**) Upon oxidative stress treatment, the band detected by a phospho-SNEV specific antibody (anti-pSNEV(S149)) increases, and diminishes upon phosphatase treatment. HeLa cells were treated with 1mM H_2O_2 for 1h or left untreated. Lysates were incubated with CIP and subjected to Western Blotting with a specific anti-phosphoSNEV(S149) antibody, that was generated by immunizing rabbits with an artificial SNEV –phosphopeptide. (**B**) Human diploid fibroblasts (HDF) were treated with 0, 100, 200 or 400 μM H_2O_2 for 1h, scraped on ice in 2x SDS loading dye and subjected to SDS PAGE. Western Blot was detected with anti-pSNEV(S149) and anti-SNEV to compare pSNEV to total SNEV levels. anti-γH2AX antibody was used as positive control for stress-dependent phosphorylation. anti-ß-Actin was used as loading control. (**C**) HDF were treated with 100 μM H_2O_2 for 0, 5, 15, 30, 60 or 120 min. Lysis and Western Blot as in **B**.

Different types of DNA damage induce nuclear localization of pSNEV

In order to localize pSNEV within the cells, we first tested for the specificity of the antibody for indirect

immunofluorescence studies. Using either the phospho-peptide that was used for generation of the antibody or a non-phospho-peptide with the same sequence, for pre-blocking the anti-pSNEV antibody, staining was abolished by blocking with the phospho-peptide, while no difference was seen after pre-incubation with the non-phospho-peptide (Fig. S4).

In addition to a strong and predominant nuclear signal upon oxidative stress, the phosphorylated form is also detected in the cytoplasm (Fig, 3A), and it is currently unclear if this phosphorylation is a signal for shuttling of SNEV between nucleus and cytoplasm. In any case, under normal conditions only very few cells stained positive for phosphoSNEV, which seems to localize to the cytoplasm (Fig. 3A).

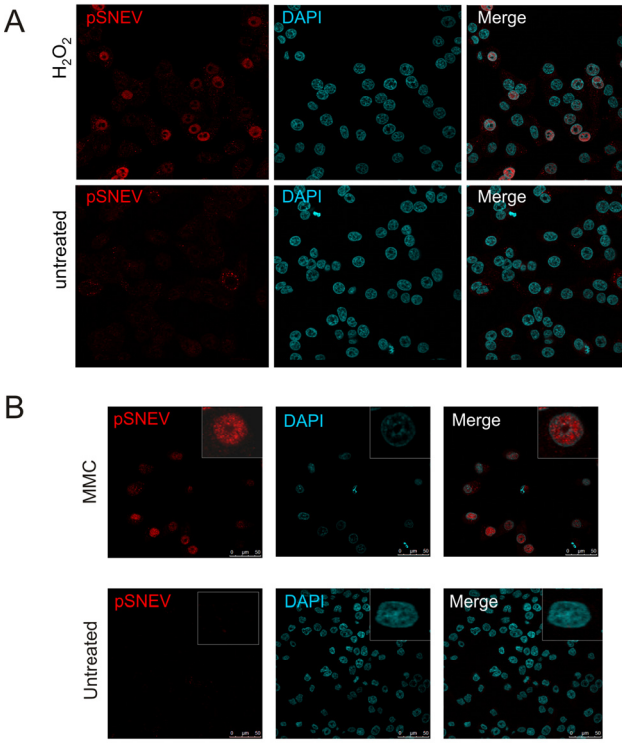

Figure 3. Upon oxidative stress, SNEV is phosphorylated and localizes mainly to the nucleus. (A) Hela cells were seeded on coverslips and treated with 100 µM H_2O_2 for 1 hour. Cells were stained with anti-pSNEV(S149) and DAPI as described in the Materials and Methods section and subjected to fluorescence microscopy. (B) HeLa cells were treated with 25 µg/ml MMC for 24 hours prior to indirect immunofluorescence staining with anti-pSNEV(S149) antibody.

To test if phosphorylation of SNEV is restricted to oxidative stress conditions or if it is a general step in the DNA damage response, we challenged cells with mitomycin C (MMC), a potent DNA crosslinker. HeLa cells were incubated with 25µg/ml MMC for 24 hours and submitted to indirect immunofluorescence staining with anti-pSNEV(S149). As observed for hydrogen proxide, also MMC induces phosphorylation of SNEV, and the phosphorylated species is mainly detected in the nucleus (Fig. 3B).

Thus, we assume that the phosphorylation of SNEV is an integral part of the nuclear DNA damage response.

Phosphorylation of SNEV at serine 149 is ATM-dependent

In order to test if this phosphorylation is dependent on ATM, we took advantage of the reagent 2-(4-Morpholinyl)-6-(1-thianthrenyl)-4*H*-pyran-4-one (KU-55933), a specific inhibitor of ATM kinase activity [33]. Indeed, we observed markedly reduced levels of phosphorylated SNEV upon oxidative stress, when ATM was blocked by Ku-55933. Similarly, upon oxidative stress we detected SNEV as a double band with anti-SNEV antibody, and Ku-55933 treatment abolished the upper band, supporting the idea that this upper band represents phosphoSNEV (Fig. 4A). The fact that the phosphoSNEV bands did not disappear completely could be due to another kinase that backs up ATM function. It is known that both ATM and ATR can phosphorylate H2AX [34], which also explains that H2AX phosphorylation is only slightly reduced upon ATM inhibition.

To confirm that ATM controls SNEV S149 phosphorylation with an independent method, we used mouse embryonic fibroblasts in which ATM was flanked by loxP sites and cut out using Cre recombinase (ATM -/- MEF). As shown in fig. 4B, the induction of pSNEV(S149) upon hydrogen peroxide treatment was reduced to less than half of that observed in wildtype MEF (pSNEV band intensity 0.16 versus 0.38 arbitrary units, normalized to ßActin intensity; data not shown). The lower panel in fig. 4B shows an agarose gel of the genotyping PCR. Using a combination of three primers, three different fragments are amplified according which cells can be genotyped. The 320 bp fragment indicating absence of loxP sites is amplified only in wildtype cells, whereas presence of loxP sites gives rise to a 420 bp fragment. Only after introduction of Cre recombinase is ATM cut out and a fragment of 920 bp is amplified. Since the 420 bp fragment is still present inspite of Cre transfection, there is still residual ATM activity in our ATM -/- MEF, which explains why we still detect some

pSNEV in these cells, although to a lesser extent then in wt MEF.

Taken together, this suggests that SNEV is phosphorylated upon DNA damage in an ATM-dependent manner and the presence of the ATM target motif suggest that it might be a novel direct substrate for ATM.

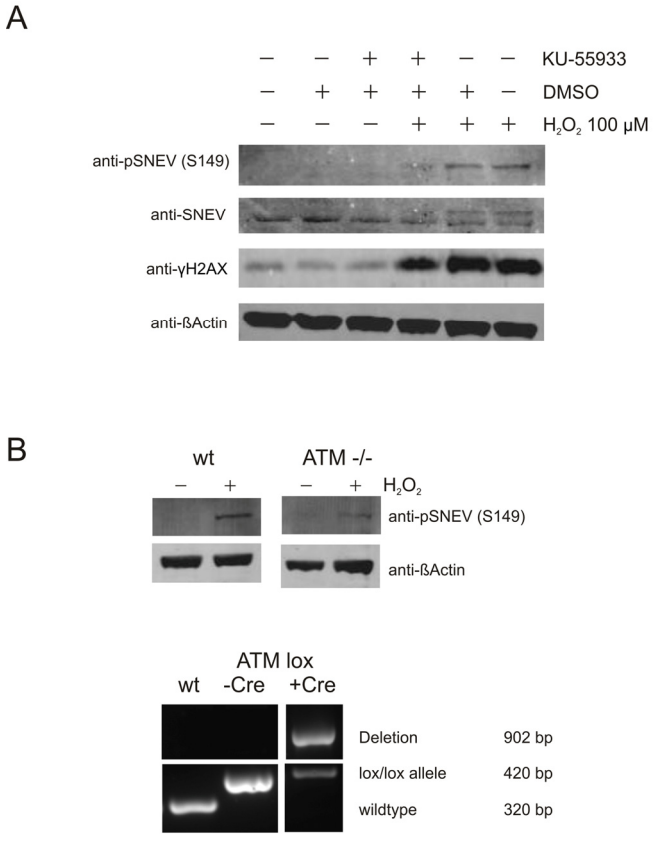

Figure 4. Phosphorylation of SNEV at S149A is ATM-dependent. (**A**) ATM inhibition alleviates phosphorylation of SNEV in response to oxidative stress. HDFs were treated with 100 µM H_2O_2 and the specific ATM inhibitor KU-55933. DMSO, the solvent for Ku-99533, was used as negative control. Phosphorylation of SNEV and known ATM target γH2AX was reduced by inhibition of ATM. (**B**) Phopshorylation of SNEV at S149 is reduced in ATM conditional knockout MEF. Upper panel: wt and ATM -/- MEF were treated with 200 µM H_2O_2 for 1h, harvested, resuspended in 2x SDS loading dye and subjected to SDS PAGE. Western Blot was detected with anti-pSNEV(S149) and anti-ßActin to ensure equael loading. Lower panel: Genomic DNA was isolated from wt and ATM lox/lox MEF before and after transfection with Cre and used in a genotyping PCR. The band for deleted ATM is present only after transfection with Cre, nonetheless the deletion is not quantitative and a small portion of ATM is maintained.

Effect of phosphorylation on life span and stress resistance in HUVEC

To investigate the physiological effect of the phosphorylation at S149 of SNEV, we generated stable HUVEC cell lines overexpressing either wildtype SNEV (wtSNEV HUVEC) or a point mutant SNEV where the ATM target site was abolished by exchanging serine 149 for alanine (SNEV S149A HUVEC). Both recombinant cell lines showed comparable overexpression of SNEV versus untransfected HUVEC (Fig. 5A). Overexpression was additionally confirmed by IF (Fig. S5).

Using these cell lines, we studied how the lack of phosphorylation at S149 affects DNA damage levels, stress resistance and life span.

As described earlier [26], overexpression of wtSNEV had a strong life-span extending effect. Indeed, SNEV wt HUVEC underwent 30 population doublings post transduction, while empty vector control HUVEC reached senescence already upon PD 8 post transduction, thus SNEVwt overexpression more than tripled the replicative life span. Surprisingly, SNEV S149A overexpression did not fully abrogate this effect of SNEV and also extended the replicative life span of HUVEC, albeit to a significantly lower extent of around 18 PD post transduction (Fig. 5B). Replicative senescence at the respective replication end points was confirmed by staining for the widely accepted senescence marker SA ß-galactosidase expression (data not shown).

Since we observed phosphorylation of SNEV upon treatment with DNA damaging agents, we hypothesized that phosphorylation might be necessary to elicit a proper DNA damage response. Therefore we performed comet assays to test for DNA integrity under basal conditions.

Indeed wtSNEV overexpressing cells were mainly assigned to categories I or II, corresponding to no or low levels of DNA damage. In contrast, the SNEV S149 HUVEC have lower levels of DNA damage than empty vector controls, but still increased damage levels compared to wtSNEV HUVEC. We conclude that increased SNEV levels lead to increased DNA maintenance in unstressed conditions, while the full effect of more efficient repair unfolds only if SNEV can be phosphorylated at S149.

In addition to the basal levels of DNA damage, we assessed the cellular response to treatment with genotoxic and/or oxidative stress inducing reagents.

Therefore, we used combined BSO/bleomycin treatment as described earlier [26]. WtSNEV HUVEC did not enter apoptosis upon the treatment in accordance to our earlier results [26], which is also in agreement with findings by the Legerski lab, that GFP-SNEV overexpression in Hela cells reduces MMS induced apoptosis by two-fold [24]. In contrast, in SNEV S149A HUVEC the BSO/bleomycin treatment clearly induced apoptosis/necrosis. The initially low level –when compared to empty vector control cells- of cell death of 10% for SNEV S149A HUVEC more that doubled upon treatment to 22.5 %.

Since SNEV is required for repair of DNA interstrand cross-links [25], we tested if SNEV overexpression protected cells from the deleterious effects of the DNA cross-linking agent cisplatin. Figure 5E shows that cisplatin treatment very strongly induced apoptosis in empty vector control HUVEC as well as in SNEV S149A HUVEC, while wtSNEV HUVEC were clearly more resistant to this treatment. Therefore, we conclude that phosphorylation of SNEV at S149 is necessary for efficient corsslink-repair activity of SNEV.

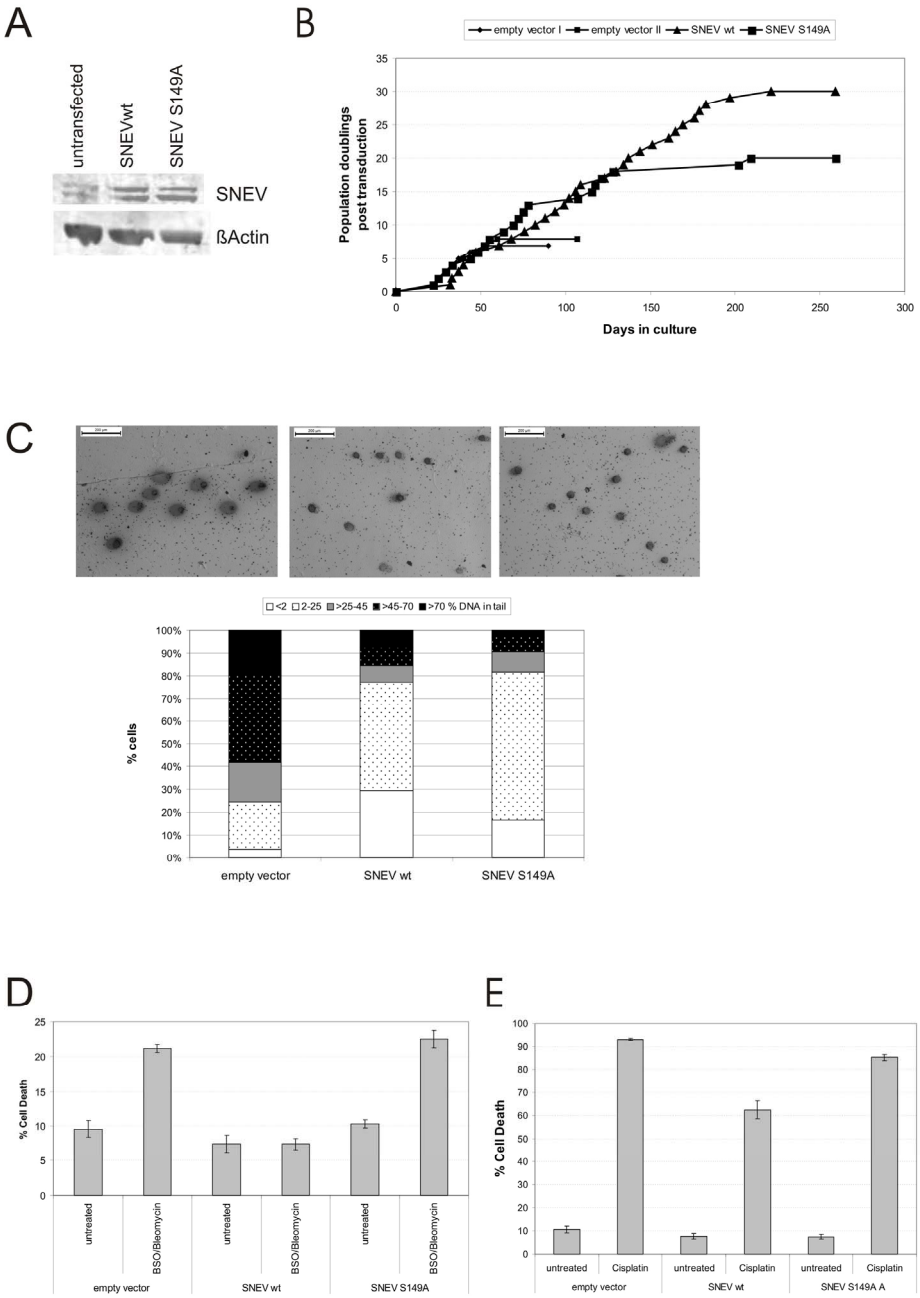

Figure 5. Phosphorylation at S149 is necessary for apoptosis resistance and partially for life span extension conferred by SNEV. (**A**) Normal HUVEC as well as stable HUVEC overexpressing SNEV wt, SNEV S149A or empty vector control cells were lysed and submitted to SDS PAGE. Western Blots were probed with anti-SNEV and anti-ßActin antibodies. SNEV protein expression levels are increased five-fold in SNEV wt and ten-fold in SNEV S149A HUVEC as compared to untransfected HUVEC. (**B**) Growth curves of HUVEC overexpressing SNEV wt, SNEV S149A and empty vector. (**C**) SNEV wt as well as SNEV S149A overexpression reduces the basal level of DNA damage. Upper panel: Representative pictures of Comet assay performed with empty vector, SNEV wt and S149A point mutant overexpressing HUVEC. Lower panel: Comets were classified into 5 categories depending on the percentage of the DNA content in the tail. DNA damage levels of SNEV S149A. (**D**) Cells were pre-incubated with 1 mM BSO for 48h, followed by treatment with 100 µg/ml Bleomycin for 24h. Apoptosis was measured by Annexin-FITC and PI staining and subsequent flow cytometric analysis. (**E**) Cells were incubated with 100µg/ml Cisplatin for 24h. Apoptosis was measured as in **D**.

In summary, we conclude that overexpression of S149-phosphorylation incompetent SNEV does have a small but discernible effect on the DNA damage status under normal culture conditions when compared to wtSNEV overexpression, but does not exert the strong anti-apoptotic effect of wtSNEV after induction of DNA damage by either oxidative stress or interstrans crosslinks.

In any case, the life-span extending and DNA repair functions of SNEV do partially depend on phospho-rylation at S149, most probably in dependence of ATM.

DISCUSSION

Here, we present SNEV as a novel ATM-dependent phosphoryalation substrate in response to oxidative stress induced DNA damage. We show that SNEV is phosphorylated at S149 in an ATM-dependent manner in different cell types in response to various DNA damage. Surprisingly, ATM-dependent phosphorylation at S149 is essential for suppressing oxidative stress induced apoptosis, but dispensable for efficient DNA break repair and accounts for part of the cellular life span extension observed upon SNEV overexpression.

A plethora of mutations in the DNA damage response pathways, specifically in transcription-coupled nucleotide excision repair (TC-NER) is known to be responsible for premature ageing syndromes in humans (reviewed in [35]) Accordingly, gene knock-outs of these factors also show premature aging in mice. However, to the best of our knowledge, only two studies have so far reported that DNA repair factors upon overexpression extend the life span of model systems. One example is overexpression of the repair factor GADD45 in the nervous system of D. melanogaster that increased the life span of these animals [36], while overexpression in the whole animal was lethal [37]. The other example is mice with single extra copies of the tumor suppressor p53 and its stabilizer Arf, which led to an extension of the median life span by 16% compared to controls, while the maximum life span was not increased [38].

We have recently observed that a multi-talented protein, SNEV, extends the replicative life span of endothelial cells upon overexpression, reduces basal levels of DNA damage and suppresses oxidative stress induced apoptosis in these cells [39]. The multiple talents of SNEV, however, include a well documented function in DNA repair [23-25, 40], but also in pre-mRNA splicing, ubiquitination and proteasomal breakdown as well as adipogenic and neurogenic differentiation, where another phosphorylation sites plays a crucial role [28, 29]. Therefore, it is not yet clear which function of SNEV is responsible for the life span extending activity. We here identified an ATM consensus phosphorylation site on SNEV. Our experimental design does not provide direct evidence that ATM phosphorylates SNEV at this site. However, SNEV's highly conserved yeast homologue Prp19 is a direct phosphorylation target of Tel1 and/or Mec1, the yeast homologues of ATR and ATM [41], making it more likely that also in humans this direct link is conserved.

Since ATM dependent phosphorylations are key signals of DNA damage and oxidative stress, we hypothesized that ATM dependent phosphorylation of SNEV might contribute to cellular life span extension as consequence of activating SNEV's DNA repair activity. Therefore, we overexpressed the phosphorylation-incompetent point mutant versus wild type SNEV and found that the DNA damage status of cells in unstressed conditions overexpression is slightly but not dramatically reduced by the point mutation. Surprisingly, suppression of apoptosis upon oxidative stress treatment as seen upon SNEV overexpression was completely abolished by S149A mutation, suggesting an important role of ATM dependent phosphorylation of SNEV for induction of apoptosis. It is tempting to speculate that at least part of this high susceptibility of ATM deficient cells to apoptosis [13, 42, 43] is dependent on the inability to phosphorylate SNEV. Furthermore, the susceptibility of ATM deficient cells to undergo apoptosis is not only dependent on DNA damaging agents, but also on oxidative stress [44], well in accordance with our data.

How might the S149 phosphorylatable form of SNEV suppress apoptosis?

Phosphorylated SNEV localizes under basal conditions exclusively to the cytoplasm, but is detected predominantly in the nucleus after DNA damage. Although it is likely that ATM phosphorylation occurs in the nucleus, it cannot be ruled out that phosphoSNEV is imported into the nucleus. This would be supported by the notion that amino acids 1-166 of mouse SNEV are necessary for nuclear import [45] and the phosphorylation site lies within this portion possibly conferring a nuclear import signal. However, one report suggests that cytoplasmic SNEV is responsible to suppress apoptosis, at least under conditions of hypoxia. Under hypoxic conditions, a particular form of redox stress, SNEV is observed to interact with PHD3 in the cytoplasm [46], an interaction that suppresses cell death. In addition, GFP-SNEV, which locates preferentially in the cytoplasm (compared to untagged SNEV), has a stronger anti-apoptotic effect than untagged SNEV, indicating the cytoplasmic localization

of SNEV is important for its anti-apoptotic role. We find that upon overexpression, the cytoplasmic portion of SNEV is increased when compared to untransfected HUVEC (See Fig. S3), backing up the importance of cytoplasmic SNEV in preventing apoptosis. On the other hand, also in SNEV S149A HUVEC, the ratio of nuclear versus cytoplasmic SNEV is shifted towards the cytoplasm in a manner similar to SNEV wt HUVEC, but still these cells undergo apotosis upon oxidative stress, indicating that the phosphorylatability of cytoplasmic SNEV is essential for its anti-apoptotic effect. Under normoxic conditions, SNEV interacts with PHD3 via its C-terminus, while under hypoxic conditions, a hypoxia inducible interaction domain comprising amino acids 66-220 stabilizes this interaction [46]. Since this region covers the S149, it is tempting to speculate that ATM-dependent phosphorylation at S149 is the signal for increased binding to PHD3, leading to apoptosis suppression, while the non-phosphorylatable S149A mutant binds PHD3 with lower affinity, allowing for caspase activation by PHD3. It is also unclear, how the phosphoSNEV would accumulate in the cytoplasm, as it is not detected there upon stress with our antibody. It will be interesting to see if a phospho-mimicking S149D point mutant further increases the anti-apoptotic effect of SNEV overexpression and where it will localize.

The finding that the point mutant only slightly improves the basal DNA damage status of the cells as visualized by comet assays suggests that the here identified phosphorylation site might be decoupling the DNA repair activity from the apoptosis signalling activity of SNEV.

It remains to be elucidated how this translates into the extended life span of SNEV overexpressing cells. Suppression of apoptosis might reduce the loss of cells during cultivation and thus increase the total replicative life span merely by reducing the replicative exhaustion of the cells. However, the apoptosis competent cells of the S149A mutant overexpression are still markedly longer lived than empty vector controls. This would suggest that the full life span extension as observed by wtSNEV overexpression depends on both, apoptosis suppression and the lower basal DNA damage of the cells and thus on SNEV's DNA repair activity.

Taken together, our data support the hypothesis that DNA damage repair and signalling factors can extend the life span of model systems, as in this case the replicative life span of endothelial cels and thus support the idea that a genetically programmed DNA repair ability counteracts and slows down the stochastic accumulation of DNA damage and thus the aging process.

METHODS

Cells and culture conditions. HeLa cells were grown in RPMI1640 (Biochrom AG, Berlin, Germany) supplemented with 10% fetal calf serum (FCS).
Human diploid fibroblasts (HDF) were grown in DMEM/HAM's F12 1:2 (Biochrom AG, Berlin, Germany) supplemented with 10%FCS.
Human umbilical vein endothelial cells (HUVEC) were cultivated in EBM Basal Medium plus EGM SingleQuot Supplements & Growth Factors (Lonza, Basel, Switzerland) supplemented with FCS to a final 10%. For HUVEC, flasks were precoated with 0.1% gelatine in PBS.
GFP-SNEV-Hela were established by transfecting Hela cells with a SNEV-BAC construct containing all regulatory elements obtained from Ina Poser, Max Planck Institute for Molecular Cell Biology and Genetics, Dresden, Germany. GFP-SNEV-Hela were cultivated in RPMI1640 (Biochrom AG, Berlin, Germany) supplemented with 10% fetal calf serum (FCS) and 800 µg/ml G418 (Gibco, now life technologies, Grand Island, NY, USA).
Confluent adherent cultures were detached using 0.1% trypsin and 0.02% EDTA and were passaged with an appropriate split ratio of 1:2 or 1:4 once or twice a week depending on confluence and population doubling level (PD). Subsequently, cumulative PDs were calculated as a function of passage number and split ratio [47].
Fibroblasts (HDF5) $2x10^5$ /well were seeded in 6 well plates. The next day, cells were treated with H_2O_2 (100, 200, 400 µM/ml) for 1 hour and 100 µM/ml for different time spans (5, 15, 30, 60, 120 minutes).
Fibroblasts (HDF5) were seeded in 6 well plate at a density of $2x10^5$ cells/well 24 hours before treatment with 2.5, 5, 10, 25, 50, 100 µg/ml of Bleomycin for 1 hour and 25µg/ml for (5,15,30,60,120 minutes). For Mitomycin C treatment, fibroblasts cells were exposed to different concentration (2.5, 5, 10, 25, 50 µg/ml) for 24 hours. Cell were scraped directly on ice in 2x SDS loading dye, sonicated and boiled. Proteins were separated by SDS gel electrophoresis in 4-12% BT gel (Invitrogen, now life technologies, Grand Island, NY, USA).
To induce apoptosis, cells were seeded into 12-well cell culture plates at a density of 10000 cells /cm^2. To enhance the sensitivity of cells to bleomycin-induced apoptosis, cells were cultivated in the presence of 1 mM buthionine-sulfoximine (BSO, Sigma-Aldrich, St.Louis, MO, USA) for 48 h before treatment with with 100 µg/ml of bleomycin (Sigma-Aldrich, St.Louis, MO, USA) for further 24 h. Alternatively, cells were treated

with 100 μg/ml of cisplatin (Sigma) for 24h to asssay apoptosis induction by DNA cross-links.

ATM deletion in mouse embryonic fibroblasts. Primary mouse embryonic fibroblasts (MEF) were prepared from E13.5 fetuses (*ATM*$^{flox/flox}$). Cells were cultured in DMEM high glucose medium (Sigma-Aldrich) supplemented with 15% fetal bovine serum (Lonza), 1% L-glutamine (Gibco, now life technologies, Grand Island, NY, USA), 1% penicillin and strepromycin, 1% NEAA (non essential amino acids, Gibco), 1% sodium pyruvate (Gibco) and β-mercaptoethanol (1:140000).
Large T-Antigen was used to immortalize MEFs (*ATM*$^{flox/flox}$). For the generation of retrovirus, Large T-Antigen -MSCVneo plasmid was co-transfected with the packaging plasmid pCL-Eco and the enveloping plasmid VSV-G in 293T cells. Supernatant was collected after 24 and 48 hours. MEFs were transduced using 5 ml of filtered supernatant added to 5 ml cell culture medium in the presence of 8 mg/ml polybrene (Sigma-Aldrich). After 24 hours virus was removed. 14 days selection was started 72 hours after infection using 400μg/ml neomycin (Sigma-Aldrich).
In a second infection step, Large T-Antigen-immortalized MEFs were transduced with the Cre-pBabe-puro retrovirus for the Cre-mediated deletion of *ATM*. Selection was started 72 hours after transduction with 2 μg/ml puromycin for 7 days. Medium was exchanged every Deletion of ATM was verified by PCR of genomic DNA using primer 1 (5' ATC AAA TGT AAA GGC GGC TTC 3'), primer 2 (5'CAT CCT TTA ATG TGC CTC CCT TCG CC 3') and primer 3 (5'GCC CAT CCC GTC CAC AAT ATC TCT GC 3') giving rise to three fragments representing absence or presence of loxP sites or deletion of ATM.

Plasmid construction, generation of recombinant retroviruses and cell line establishment. SNEV cDNA was amplified by PCR and ligated into the retroviral plasmid pLenti6. The SNEV S149A point mutant was generated using the QuikChange Multi Site-Directed Mutagenesis Kit (Agilent, Santa Clara, CA, USA). The negative control vector contained only the blasticidin resistance gene. Retroviral particles were generated according to the manufacturer's protocol (Invitrogen). For cell line establishment, HUVECs (PD14) were infected with retroviral particles according to the manufacturer's protocol (Invitrogen, now life technologies, Grand Island, NY, USA) at a multiplicity of infection (MOI) of 4 in EBM with 10% FCS supplemented with 8 μg/ml Polybrene. Thereafter, transfectants were selected using 5 μg/ml Blasticidin. Arising cell clones (similar number in all experiments) were grown as mass culture. PDs post transfection (pT) were calculated starting with the first passage after selection was completed.

Antibodies. Prp19/Pso4 rabbit polyclonal antibody was from Bethyl Laboratories (Montgomery, TX, USA) #A300-102A. ATM antibody [2C1] mouse monoclonal antibody was from Gene Tex (Irvina, CA, USA) # GTX70103. anti-pSNEV(S149) rabbit polyclonal antibody was generated by Moravian Biotechnology Ltd. (Bratislava, Slovakia). Gamma H2A.X (phospho S139) mouse monoclonal antibody [9F3] was from Abcam (Cambridge, UK) #26350. ß-Actin mouse monoclonal antibody was from Sigma-Aldrich (St.Louis, MO, USA) #A-5441. GAPDH rabbit antibody FL-335 was from Santa Cruz (Santa Cruz, CA, USA) #sc-25778.

SDS PAGE and Western Blotting. For SDS PAGE, protein samples were mixed with 4x SDS loading dye (240 mTris-Cl pH 6.8, 8% SDS, 40 % glycerol, 0.05 % bromophenol blue, 5% ß-Mercaptoethanol) and heated to 75°C for 10min. Samples were separated on a NuPAGE 4–12% Bis/Tris polyacrylamide gel (Invitrogen, Carlsbad, CA; USA) in MOPS buffer at 200V. Electrophoresis and blotting to PVDF membrane (Roth, Karlsruhe, Germany) were performed using the XCell *SureLock*® Mini-Cell (Invitrogen, now life technologies, Grand Island, NY, USA) in accordance to the manufacturer's protocol. After incubating with blocking buffer (3% skim milk powder in PBS with 0.1% Tween-20) on an orbital for 1h at room temperature or overnight at 4°C, the membranes were incubated for 1h or overnight with the primary antibody diluted in blocking buffer, followed by 1h incubation with secondary anti-Rabbit-IR-Dye 800 and/or anti-Mouse-Alexa 680 (Licor), both diluted 1:10000 in blocking buffer. Both antibody incubations were followed by 3 washes with PBS with 0.1% Tween-20. Membranes were scanned using the Odyssey infrared imaging system (LI-COR, Lincoln, NE, USA). Mouse anti-ßActin (Sigma-Aldrich, St.Louis, MO, USA) or rabbit anti-GAPDH (Santa Cruz, Santa Cruz, CA, USA) were used as loading controls.

Dephosphorylation. For dephosphorylation experiments, H_2O_2 treated or untreated HeLa cells were harvested by trypsinization, collected by centrifugation at 170g for 10 min, washed twice with PBS and resuspended in NEB3 Buffer (New England Biolabs, Ipswich, MA, USA), in which Calf intestinal phosphatase (CIP; New England Biolabs, Ipswich, MA, USA) has optimal activity. Cells were lysed by sonication and subsequent centrifugation at maximum speed for 30 min at 4°C. Cleared lysates were split and

one half was incubated with 10U CIP for 30 min at 37°C, whereas the other half was mock treated. Subsequently, samples were submitted to Western Blot analysis.

Anti-GFP Trap IP. GFP-SNEV-Hela were grown to 90% confluence in T175 roux flask and incubated with 100 µM H_2O_2 to induce SNEV phosphorylation or left untreated as negative control. Cells were scraped on ice in 3ml Lysis buffer (50 mM Hepes-KOH pH 7.5, 5 mM EDTA pH8, 150 mM KCl, 10% glycerol, 1% Triton X-100, 20 mM ß-glycerophosphate, 10mM Na-pyrophosphate, 10 mM NaF, 1 mM DTT, 1 mM Na_3VO_4, 0.1mM PMSF, 20 µg/ml Leupeptin, 20 µg/ml Chymostatin, 20 µg/ml Pepstatin, 1µM Okadaic acid) per T175 and sonicated using 3 bursts of 10s. Lysate was cleared by centrifugation for 30 min at full speed. All centrifugation stepy were carried out at 4°C. 30 µl GFP-Trap Beads (ChromoTek, Munich, Germany) were equilibrated by washing thrice in 500 µl ice cold wash buffer (50mM Hepes-KOH pH 7.5, 5mM EDTA pH8, 150mM KCl, 10% glycerol, 0.05% NP-40, 20 mM ß-glycerophosphate, 10 mM Na-pyrophosphate, 10mM NaF, 20 µg/ml Leupeptin, 20 µg/ml Chymostatin, 20 µg/ml Pepstatin) and collected by centrifugation at 2,700 x g for 2 min. 1 ml Lysate corresponding to 1 mg total protein was added to the beads mixed on an overhead shaker for 1h at 4°C. Beads were collected by centrifugation for 2 minutes at 2,000 x g. Discard supernatant and wash beads 5x times with 500µL ice cold wash buffer (ocadaic acid added only for the first two washing steps) and finally resuspended in washing buffer.

Mass spectrometric analysis. Beads were washed five times with ammonium bicarbonate buffer (50mM ABC). Disulfide bonds were reduced by incubation with dithiothreitol (DTT, 5% w/w of the estimated amount of protein) for 30 min at 56°C and Cys-residues were subsequently alkylated with iododacetamide (IAA, 25% w/w of the estimated amount of protein) for 20 min at RT in the dark. DTT (2.5% w/w of the estimated amount of protein) was added to consume excess IAA and proteins were digested with subtilisin for 1 hour at 37°C. Digests were stopped by addition of trifluoro acetic acid (TFA) to approx. pH 3. 10% of the peptide mixture was analysed directly, the remaining 90% were enriched for phosphopeptides by the use of TiO2 as described in [48]. Peptides were separated on a U3000-HPLC-system (Dionex, Sunnyvale, CA, USA). Peptides were loaded on to a the trapping column (PepMAP C18, 0.3 × 5 mm, Dionex) with 0.1 % TFA as loading solvent and then eluted onto an analytical column (PepMAP C18, 75 µm × 150 mm, Dionex) with a flow rate of 300 nl/min and a gradient from 0 % solvent B to 100 % solvent B in 90 min, followed by a washing step of 10 min with 10 % solvent B and 90 % solvent C (solvent B: 40 % acetonitril (ANC), 0.08 % formic acid, solvent C: 80% ACN, 10% trifluorethanol, 0.08 % formic acid). The HPLC system is online coupled to a Velos Orbitrap mass spectrometer (Thermo Scientific, Waltham, MA, USA) equipped with an ESI-source (Proxeon, now Thermo Scientific). A full scan (scan range 400-1800 Th, resolution 60.000) was followed by MS2 analysis by collision-induced dissociation (CID) of the 20 most intense precursors in the linear iontrap. Normalized collision energy was set to 35%, activation Q at 25 and activation time at 30 ms. Peptide identification was performed using the SEQUEST algorithm in the ProteomeDiscoverer 1.3.0.339 software package (Thermo Scientific). Carbamidomethylation of Cys was set as static modifications, phosphorylation of Ser/Thr/Tyr and oxidation of Met were set as variable modifications. Spectra were searched against a small database plus contaminants for a fast PTM analysis. Search parameters were no protease specificity, a peptide tolerance of 2 ppm, a fragment ions tolerance of 0.8 Da. The results were filtered at the XCorr values to an FDR of 1% on the peptide level. The probability of phosphosite localization was calculated using the phosphoRS 2.0 software [49] implemented into the Proteome Discoverer.

Indirect immunofuorescence staining. Cells were seeded on coverslips one day prior to immunofluorescence staining. The next day, cells were washed with PBS and fixed with 3.7% (w/v) for 20 min at room temperature. Permeabilization was performed with 0.1% Triton X-100 in PBS for 10 min at room temperature. Cells were incubated with primary antibodies diluted in PBS with 10% FCS for 1 h, washed 3 times for 10 min with PBS, incubated for 1 h with the appropriate secondary antibodies diluted in PBS with 10% FCS, and washed 3 times for 10 min with PBS. Anti-pSNEV (S149) was diluted 1:250. As secondary antibodies, anti mouse dyelight488 1:1000 and dyelight649 1:1000 anti-rabbit or anti-mouse antibodies were used. Microscope as described previously.

To visualize the nuclei, cells were counterstained with 4',6-diamidino-2-phenylindole (DAPI). Cells were washed and fixed as above and subsequently incubated with 100ng/ml DAPI in PBS for 10 min at room temperature.

After staining, slides were mounted on cover slips using slow fade gold Mounting Medium for Fluorescence (life technologie, Grand Island, NY, USA) and sealed with nail polish.

Microscopy and image analysis were carried out using a Leica SP5 II laser scanning confocal microscope (Leica Microsystems CMS, Mannheim, Germany).

Comet assay. Single- and double-stranded DNA damage in SNEVwt and SNEV S149A overexpressing HUVEC under basal conditions was measured by single-cell gel electrophoresis (comet assay) under alkaline conditions as described previously [50]. At least 100 randomly selected cells per slide were examined for the presence or absence of comets using fluorescence microscopy. The cells were assigned to five different categories according to their DNA content in tail using the TriTek CometScore software. Percentage of cells in each category was calculated.

Apoptosis staining. Cells were detached using 0.1% Trypsin/0,02%EDTA and stained with Annexin V–Bacific Blue (Invitrogen, now life technologies) and PI (Roche, Basel, Switzerland) according to the manufacturer's instructions. Analysis of the percentages of apoptotic and necrotic/late-apoptotic cells was performed using a BD FACS Canto II flow cytometer (Becton Dickinson, Franklin Lakes, NJ, USA) and the FCS Express V3 software (De Novo Software, Los Angeles, CA, USA).

ACKNOWLEDGMENTS

Conditional ATM knockout mice were a generous gift from Fred Alt, Harvard Medical School. KU-55933 reagent was a kind gift of KuDOS Pharmaceuticals. We thank Ina Poser for providing the SNEV-BAC construct. We thank the Imaging center of BOKU and especially Monika Debreczeny for excellent technical support with microscopy. We thank Rita Reynoso for help with Comet assay and Matthias Wieser for help with flow cytometry. We thank Ilija Bilic and Luci Terlecki for technical assistance.
This work was supported by the Austrian Science Fund [P 24498-B20]; Genome Research Autria GEN-AU [Project 820982 „Non-coding RNAs"]; and grants by the Herzfelder'sche Familienstiftung and CE.R.I.E.S. HD is a recipient of a DOC-fFORTE-fellowship of the Austrian Academy of Sciences.

CONFLICT OF INTERESTS STATEMENT

JG and RGV are co-founders of Evercyte GmbH.

REFERENCES

1. Burtner C, and Kennedy B. Progeria syndromes and ageing: what is the connection? Nat Rev Mol Cell Biol. 2010; 11:567-578.
2. Schumacher B, Hoeijmakers J, and Garinis G. Sealing the gap between nuclear DNA damage and longevity. Mol Cell Endocrinol. 2009; 299:112-117.
3. Grillari J, Katinger H, and Voglauer R. Contributions of DNA interstrand cross-links to aging of cells and organisms. Nucleic Acids Res. 2007;.35:7566-7576.
4. Derheimer FA and Kastan MB. Multiple roles of ATM in monitoring and maintaining DNA integrity. FEBS Lett. 2010; 584:3675-3681.
5. Martin GM. Genetic modulation of senescent phenotypes in Homo sapiens. Cell. 2005; 120:523-532.
6. Gatti RA, Becker-Catania S, Chun HH, Sun X, Mitui M, Lai CH, Khanlou N, Babaei M, Cheng R, Clark C, Huo Y, Udar NC, and Iyer RK. The pathogenesis of ataxia-telangiectasia. Learning from a Rosetta Stone. Clin Rev Allergy Immunol. 2001; 20:87-108.
7. Kastan MB, and Lim DS. The many substrates and functions of ATM. Nat Rev Mol Cell Biol. 2000; 1:179-186.
8. Garg R, Callens S, Lim DS, Canman CE, Kastan MB, and Xu B. Chromatin association of rad17 is required for an ataxia telangiectasia and rad-related kinase-mediated S-phase checkpoint in response to low-dose ultraviolet radiation. Mol Cancer Res. 2004; 2:362-369.
9. Rogakou EP, Pilch DR, Orr AH, Ivanova VS, and Bonner WM. DNA double-stranded breaks induce histone H2AX phosphorylation on serine 139. J Biol Chem. 1998; 273:5858-5868.
10. Burma S, Chen BP, Murphy M, Kurimasa A, and Chen DJ. ATM phosphorylates histone H2AX in response to DNA double-strand breaks. J Biol Chem. 2001; 276:42462-42467.
11. Berkovich E, Monnat RJ, and Kastan MB. Roles of ATM and NBS1 in chromatin structure modulation and DNA double-strand break repair. Nat Cell Biol. 2007; 9:683-690.
12. Shackelford RE, Innes CL, Sieber SO, Heinloth AN, Leadon SA, and Paules RS. The Ataxia telangiectasia gene product is required for oxidative stress-induced G1 and G2 checkpoint function in human fibroblasts. J Biol Chem. 2001; 276:21951-21959.
13. Rotman G and Shiloh Y. Ataxia-telangiectasia: is ATM a sensor of oxidative damage and stress? Bioessays. 1997; 19:911-917.
14. Droge W. Free radicals in the physiological control of cell function. Physiol Rev. 2002;.82:47-95.
15. Rotman G, and Shiloh Y. The ATM gene and protein: possible roles in genome surveillance, checkpoint controls and cellular defence against oxidative stress. Cancer Surv. 1997; 29:285-304.
16. Krüger A and Ralser M. ATM is a redox sensor linking genome stability and carbon metabolism. Sci Signal. 2011; 4:pe17.
17. Kehrer JP and Lund LG. Cellular reducing equivalents and oxidative stress. Free Radic Biol Med. 1994; 17:65-75.
18. Matsuoka S, Ballif BA, Smogorzewska A, McDonald ER 3rd, Hurov KE, Luo J, Bakalarski CE, Zhao Z, Solimini N, Lerenthal Y, Shiloh Y, Gygi SP, and Elledge SJ. ATM and ATR substrate analysis reveals extensive protein networks responsive to DNA damage. Science. 2007;.316:1160-1166.
19. Ajuh P, Kuster B, Panov K, Zomerdijk JC, Mann M, and Lamond AI. Functional analysis of the human CDC5L complex and identification of its components by mass spectrometry. Embo J. 2000; 19:6569-6581.
20. Grillari J, Ajuh P, Stadler G, Löscher M, Voglauer R, Ernst W, Chusainow J, Eisenhaber F, Pokar M, Fortschegger K, Grey M, Lamond AI, Katinger H. SNEV is an evolutionarily conserved splicing factor whose oligomerization is necessary for spliceosome assembly. Nucleic Acids Res. 2005;.33:6868-6883.
21. Löscher M, Fortschegger K, Ritter G, Wostry M, Voglauer R, Schmid JA, Watters S, Rivett AJ, Ajuh P, Lamond AI, Katinger H, Grillari J. The U-box E3 ligase SNEV interacts with the 7 subunit of the 20S proteasome. Biochem J. 2005; 388:593-603.

22. Llères D, Denegri M, Biggiogera M, Ajuh P, and Lamond AI. Direct interaction between hnRNP-M and CDC5L/PLRG1 proteins affects alternative splice site choice. EMBO Rep. 2010; 11:445-451.

23. Mahajan KN and Mitchell BS. Role of human Pso4 in mammalian DNA repair and association with terminal deoxynucleotidyl transferase. Proc Natl Acad Sci U S A. 2003; 100:10746-10751.

24. Lu X and Legerski R. The Prp19/Pso4 core complex undergoes ubiquitylation and structural alterations in response to DNA damage. Biochem Biophys Res Commun. 2007; 354:968-974.

25. Zhang N, Kaur R, Lu X, Shen X, Li L, and Legerski RJ. The Pso4 mRNA splicing and DNA repair complex interacts with WRN for processing of DNA interstrand cross-links. J Biol Chem. 2005; 280:40559-40567.

26. Voglauer R, Chang MW, Dampier B, Wieser M, Baumann K, Sterovsky T, Schreiber M, Katinger H, and Grillari J. SNEV overexpression extends the life span of human endothelial cells. Exp Cell Res. 2006; 312:746-759.

27. Grillari J, Hohenwarter O, Grabherr RM, and Katinger H. Subtractive hybridization of mRNA from early passage and senescent endothelial cells. Exp Gerontol. 2000; 35:187-197.

28. Urano Y, Iiduka M, Sugiyama A, Akiyama H, Uzawa K, Matsumoto G, Kawasaki Y, and Tashiro F. Involvement of the mouse Prp19 gene in neuronal/astroglial cell fate decisions. J Biol Chem. 2006; 281:7498-7514.

29. Urano-Tashiro Y, Sasaki H, Sugawara-Kawasaki M, Yamada T, Sugiyama A, Akiyama H, Kawasaki Y, Tashiro F. Implication of Akt-dependent Prp19 alpha/14-3-3beta/Cdc5L complex formation in neuronal differentiation. J Neurosci Res. 2010; 88:2787-2797.

30. Lee JW, Harrigan J, Opresko PL, and Bohr VA. Pathways and functions of the Werner syndrome protein. Mech Ageing Dev. 2005; 126:79-86.

31. Zhang N, Kaur R, Akhter S, and Legerski RJ. Cdc5L interacts with ATR and is required for the S-phase cell-cycle checkpoint. EMBO Rep. 2009; 10:1029-1035.

32. Poser I, Sarov M, Hutchins JR, Hériché JK, Toyoda Y, Pozniakovsky A, Weigl D, Nitzsche A, Hegemann B, Bird AW, Pelletier L, Kittler R, Hua S, Naumann R, Augsburg M, Sykora MM, Hofemeister H, Zhang Y, Nasmyth K, White KP, Dietzel S, Mechtler K, Durbin R, Stewart AF, Peters JM, Buchholz F, and Hyman AA. BAC TransgeneOmics: a high-throughput method for exploration of protein function in mammals. Nat Methods. 2008; 5:409-415.

33. Hickson I, Zhao Y, Richardson CJ, Green SJ, Martin NM, Orr AI, Reaper PM, Jackson SP, Curtin NJ, Smith GC. Identification and characterization of a novel and specific inhibitor of the ataxia-telangiectasia mutated kinase ATM. Cancer Res. 2004; 64:9152-9159.

34. Stiff T, O'Driscoll M, Rief N, Iwabuchi K, Löbrich M, and Jeggo PA. ATM and DNA-PK function redundantly to phosphorylate H2AX after exposure to ionizing radiation. Cancer Res. 2004; 64:2390-2396.

35. Garinis GA, van der Horst GT, Vijg J, and Hoeijmakers JH. DNA damage and ageing: new-age ideas for an age-old problem. Nat Cell Biol. 2008; 10:1241-1247.

36. Xu B, Kim St, and Kastan MB. Involvement of Brca1 in S-phase and G(2)-phase checkpoints after ionizing irradiation. Mol Cell Biol. 2001; 21:3445-3450.

37. Plyusnina EN, Shaposhnikov MV, and Moskalev AA. Increase of Drosophila melanogaster lifespan due to D-GADD45 overexpression in the nervous system. Biogerontology. 2011; 12:211-226.

38. Matheu A, Maraver A, Klatt P, Flores I, Garcia-Cao I, Borras C, Flores JM, Viña J, Blasco MA, and Serrano M. Delayed ageing through damage protection by the Arf/p53 pathway. Nature. 2007; 448:375-379.

39. Voglauer R, Chang MW, Dampier B, Wieser M, Baumann K, Sterovsky T, Schreiber M, Katinger H, and Grillari J. SNEV overexpression extends the life span of human endothelial cells. Exp Cell Res. 2006; 312:746-759.

40. Beck B, Park S, Lee Y, Roman Y, Hromas RA, and Lee SH. Human Pso4 is a metnase (SETMAR)-binding partner that regulates metnase function in DNA repair. J Biol Chem. 2008; 283:9023-9030.

41. Smolka MB, Albuquerque CP, Chen SH, and Zhou H. Proteome-wide identification of in vivo targets of DNA damage checkpoint kinases. Proc Natl Acad Sci U S A. 2007; 104:10364-10369.

42. Takao N, Li Y, and Yamamoto K. Protective roles for ATM in cellular response to oxidative stress. FEBS Lett. 2000; 472:133-136.

43. Kamsler A, Daily D, Hochman A, , Stern N, Shiloh Y, Rotman G, Barzilai A. Increased oxidative stress in ataxia telangiectasia evidenced by alterations in redox state of brains from Atm-deficient mice. Cancer Res. 2001; 61:1849-1854.

44. Reichenbach J, Schubert R, Schwan C, Müller K, Böhles HJ, and Zielen S. l. Anti-oxidative capacity in patients with ataxia telangiectasia. Clin Exp Immunol. 1999; 117:535-539.

45. Cho SY, Park PJ, Lee JH, Kim JJ, and Lee TR. Identification of the domains required for the localization of Prp19p to lipid droplets or the nucleus. Biochem Biophys Res Commun. 2007; 364:844-849.

46. Sato M, Sakota M, and Nakayama K. Human PRP19 interacts with prolyl-hydroxylase PHD3 and inhibits cell death in hypoxia. Exp Cell Res. 2010; 316:2871-2882.

47. Chang M, Grillari J, Mayrhofer C, Fortschegger K, Allmaier G, Marzban G, Katinger H, and Voglauer R. Comparison of early passage, senescent and hTERT immortalized endothelial cells. Exp Cell Res. 2005; 309:121-136.

48. Mazanek M, Mituloviae G, Herzog F, Stingl C, Hutchins JR, Peters JM, and Mechtler K. Titanium dioxide as a chemo-affinity solid phase in offline phosphopeptide chromatography prior to HPLC-MS/MS analysis. Nat Protoc. 2007; 2:1059-1069.

49. Taus T, Kocher T, Pichler P, Paschke C, Schmidt A, Henrich C, and Mechtler K. Universal and Confident Phosphorylation Site Localization Using phosphoRS. J Proteome Res. 2011; 10:5354-5362.

50. Wojewodzka M, Buraczewska I, and Kruszewski M. A modified neutral comet assay: elimination of lysis at high temperature and validation of the assay with anti-single-stranded DNA antibody. Mutat Res. 2002; 518:9-20.

SUPPLEMENTAL FIGURES

Fig. S1 The GFP-SNEV fusion protein is functional

A

GFP-SNEV is predominantly localized to the nucleus (left panel), in contrast the GFP alone, which localizes throughout the cell (right panel).

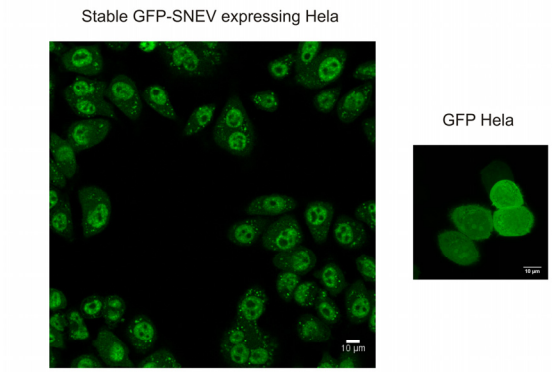

B

Endogenous SNEV and the known SNEV interactor CDC5L co-precipitate with GFP-SNEV, indicating that GFP-SNEV is incorporated in complexes similar to endogenous SNEV. No bands were detected in the control IP. The membrane was first detected with anti-SNEV, which gave rise to the 55kDa and 82kDa bands. Subsequent detection with anti-CDC5L antibody gave rise to the additional 105kDa band for CDC5L.

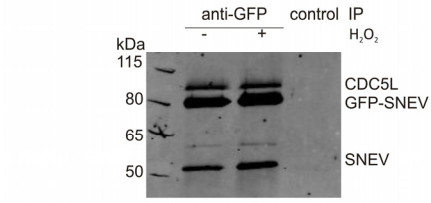

Fig. S2 SNEV is found to be phosphorylated in H_2O_2-treated cells only

A

Extracted ion chromatograms with a mass window of 3 ppm of the m/z of the phosphopeptide AVPS(ph)SQPSVVGAGEPM(ox)DLGELVGM(ox) (doubly and triply charged) show a signal in H_2O_2-treated cells and none in the control sample.

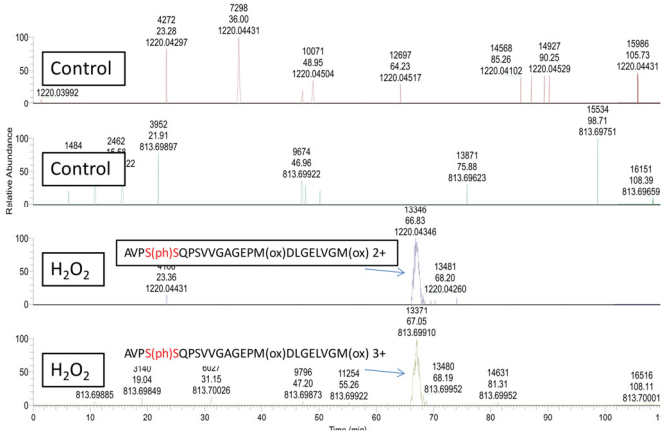

B

The extracted ion chromatogram of the m/z of the AVPS(ph)SQPSVVGAGEPM(ox)DLGELVGM(ox)TPEIIQKL phosphopeptide (triply charged) show signal in the H_2O_2-treated cells and none in the control sample.

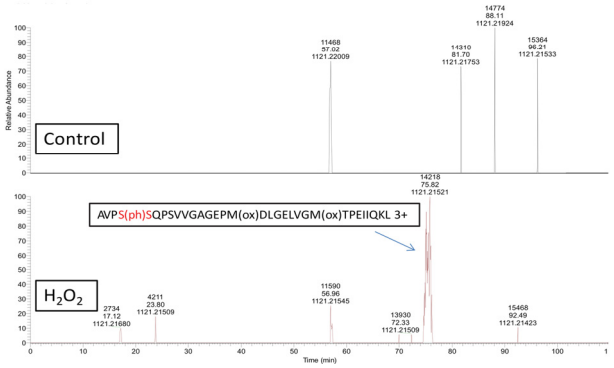

Fig. S3 Characterization of the pSNEV(S149)-antibody by Western Blot

The antibody detects a number of unspecific bands which show that equal protein amounts have been loaded.

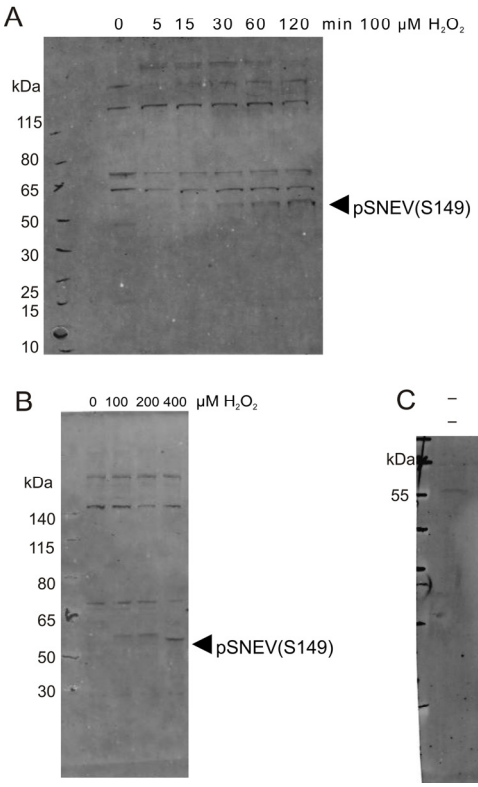

Fig.S4 Pre-incubation of pSNEV(S149)-antibody with synthetic phoshoSNEV peptides abolishes signal, indicating that the antibody is specific for pSNEV(S149).

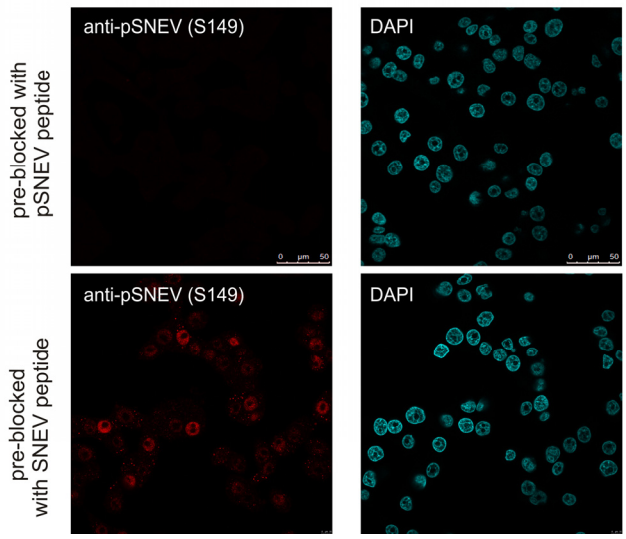

Fig. S5

A

Immunofluorescence of untransfected HUVEC, stable SNEV wt and SNEV S149A HUVEC using anti-SNEV antibody.

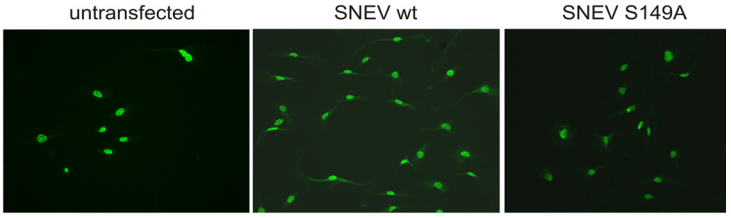

B

SNEV overexpression shifts the protein's subcellular distribution, leading to an increase of the cytoplasmic portion.
Mean pixel intensity was calculated using the Image J software.

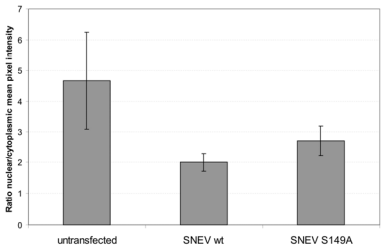

SUPPLEMENTAL TABLE

For Supplemental Table please see the full version of this manuscript on AGING web.

Appendix B

$SNEV^{hPrp19/hPSO4}$ regulates adipogenesis of human adipose derived mesenchymal stem cells

SNEV$^{hPrp19/hPSO4}$ regulates adipogenesis of human adipose derived mesenchymal stem cells

Abdulhameed Khan[1], Markus Schosserer[1], Hanna Dellago[1,9], Michael Karbiener[4], Sylvia Weilner[1], Florian Hildner[2], Christian Gabriel[2,9,10], Christoph Mück[3], Pidder Jansen-Dürr[3], Marcel Scheideler[5,6], Regina Grillari-Voglauer[1, 7,8], and Johannes Grillari[1, 7,8,9*]

[1] Department of Biotechnology, BOKU - University of Natural Resources and Life Sciences Vienna, Austria

[2] Red Cross Blood Transfusion Service of Upper Austria, Austrian, Cluster for Tissue Regeneration, Linz, Austria

[3] Institut für Biomedizinische Alternsforschung and Center for Molecular Biosciences (CMBI), Universität Innsbruck, Innsbruck, Austria

[4] RNA Biology Group, Institute for Molecular Biotechnology, Graz University of Technology, 8010 Graz, Austria

[5] Institute for Diabetes and Cancer (IDC), Helmholtz Center Munich, Neuherberg, Germany

[6] German Center for Diabetes Research (DZD), Neuherberg, Germany

[7] Evercyte GmbH, 1190 Vienna, Austria

[8] Austrian Cluster for Tissue Regeneration

[9]Christian Doppler Laboratory on Biotechnology of Skin Aging, Vienna, Austria

[10] Ludwig Boltzmann Institute for experimental and clinical traumatology, 1220 Vienna, Austria

Running title: SNEV $^{hPrp19/hPSO4}$ and adipogenesis

Correspondence to:

[*]Johannes Grillari

Department of Biotechnology, BOKU - University for Natural Resources and Life Sciences Vienna Vienna, Muthgasse 18, A-1190 Vienna, Austria,

Phone: +43(0)1-47654-6230

E-mail: johannes.grillari@boku.ac.at

ABSTRACT.

Aging and premature aging, are both accompanied by loss of subcutaneous adipose tissue mass in human and in mouse models of progeria. This may be due to reduced differentiation capacity or deficiency in DNA damage repair (DDR) factors. Here we investigated the role of SNEV (Senescent Evasion factor) which was implicated in DDR and senescence evasion, in adipogenic differentiation of human adipose derived stem cells (hASCs). We showed that expression of SNEV$^{hPrp19/hPso4}$ is induced during adipogenesis, and localized both in the nucleus and in the cytoplasm. SiRNA mediated down regulation of SNEV$^{hPrp19/hPso4}$ drastically perturbed adipogenic differentiation of hASCs while its over expression accelerated adipogenesis by regulating the expression of PPARγ. In addition, we demonstrated that SNEV$^{hPrp19/hPso4}$ is required for organismal fat deposition in vivo, in *C. elegans*. Moreover, we tested other DDR factors and found that, in addition to SNEV$^{hPrp19/hPso4}$, Werner (WRN), gene mutated in Werner syndrome is also required for adipogenesis in hASCs and in *C. elegans*.

These results firmly show that SNEV$^{hPrp19/hPso4}$ regulates adipogenesis in hASCs. Since adipogenesis is associated with high levels of reactive oxygen species, these data suggest that DDR capacity might be a pre-requisite for allowing differentiation into a lineage of long-lived cells.

Key words. SNEV $^{hPrp19/hPSO4}$, adipogenesis.

1-Introduction.

Adipose tissue is the largest organ in many organisms and is formed at specific times and locations in a wide variety of species as one of the major energy storage compartments, but also as an important source of signaling activity However, its functional connection with aging and senescence on a cellular and molecular level has come into focus only recently (Tchkonia et al., 2010), although it has been observed a long time ago that during aging profound alteration in mass and distribution of adipose tissue occur. Adipose tissue expands until early or mid-old age followed by a decline in very old age (Cartwright et al., 2007). In addition to increased fat mass, the distribution pattern of fat also changes with age, with a relative decrease in subcutaneous adipose reservoir and increase in visceral adipose mass (Caso et al., 2013). Such abnormal distribution of fat not only reduces mammalian life span (Muzumdar et al., 2008), but is also associated with an increased risk of various health complications such as atherosclerosis, type 2 diabetes, dyslipidemia, cardiovascular disease, thermal dysregulation, skin ulcers, and impaired wound healing (Ibrahim, 2010; Shuster et al., 2012). Loss of subcutaneous fat and increase in visceral adiposity, a hallmark of physiological aging, is also observed at younger ages in patients suffering from premature aging syndromes such as Werner syndrome (Caso et al., 2013; Mori et al., 2001), Cockayne syndrome, or Trichothiodystrophy (TTD). One of the common denominators of these premature aging syndromes are mutations in DNA damage repair (DDR) factors and in consequence also accumulation of DNA damage over time. The reasons for this observed loss of subcutaneous fat might lie in a reduced proliferation, differentiation or even senescence of pre-adipocytes, but could also be due to loss of signaling balance between these cells, e.g. by an increase in secretion of pro-inflammatory factors, a cell status resembling again cellular senescence (Caso et al., 2013; Karakasilioti et al., 2013; Kirkland et al., 1994; Tchkonia et al., 2010).

Indeed, mouse models that are deficient in DNA repair and high in senescent cells show a persistent inflammatory response resulting in adipose tissue degeneration, as observed in ERCC1 knock-out mice (Karakasilioti et al., 2013) as well as in BubR1 deficient mice (Baker et al., 2004). However, it remains unclear, if DNA repair factors themselves might have an impact on adipogenic differentiation of human hASCs. During adipogenesis (Kanda et al., 2011) as well as during beta oxidation reactive oxygen species (ROS) (Krawczyk et al., 2012) are formed that can damage the DNA. It could therefore be imagined that such a suppression of adipogenesis in the absence of DNA damage repair might represent a failsafe mechanism preventing cells to differentiate into adipocytes, unless they do have the capacity to repair a certain threshold of DNA damage. In addition, the DNA repair proficiency will reduce the risk of induction of cellular senescence by ROS, reducing the risk of accumulating DNA damaged and / or senescent cells with a strong pro-inflammatory phenotype (Tchkonia et al., 2013). Indeed, using the 3T3-L1 mouse cell

line, two DNA repair factors, WRN protein and SNEV$^{hPrp19/hPSO4}$ are involved in adipogenesis (Cho et al., 2007; Turaga et al., 2009), and both, WRN and SNEV$^{hPrp19/hPSO4}$ are members of one protein complex necessary for DNA damage repair (Zhang et al., 2005a). However, due to differences in the adipogenic differentiation processes of mice and men (Lindroos et al., 2013; Mikkelsen et al., 2010; Qian et al., 2010), the impact of the human homologues is still unclear.

The protein SNEV$^{hPrp19/hPSO4}$ is highly conserved from yeast to human cells and plays a role in numerous cellular pathways, reflected by the existence of different synonyms in the literature, such as Prp19, hNMP200, and Pso4. It is an essential splicing factor (Grillari et al., 2005) and an integral member of the human CDC5L complex. SNEV$^{hPrp19/hPSO4}$ possesses E3 ubiquitin ligase activity, it decorates itself and its substrate with ubiquitin chains (Hatakeyama et al., 2001; Mar et al., 2014; Song et al., 2010) and also directly interacts with the proteasome (Löscher et al., 2005). In addition, SNEV$^{hPrp19/hPSO4}$ is involved in various types of DNA damage repair like DNA double strand break repair (Mahajan et al., 2003; Sato et al., 2010; Yin et al., 2014) and interstrand cross link (ICL) repair (Zhang et al., 2005b). Importantly, SNEV$^{hPrp19/hPSO4}$ interacts with two major DNA damage response (DDR) regulators. Ataxia telangiectasia-mutated (ATM) phosphorylates SNEV after exposure to reactive oxygen species (Dellago et al., 2012) and SNEV contributes to the activation of ataxia telangiectasia-mutated and Rad3-related (ATR) (Marechal et al., 2014; Wan and Huang, 2014) .

We found that SNEV$^{hPrp19/hPSO4}$ is also linked to cellular senescence, as it is down regulated in a variety of senescent cells and its over-expression postpones entry into replicative senescence in human endothelial cells (Voglauer et al., 2006). Moreover, mouse embryonic fibroblasts (MEFs) from heterozygous knock-out mice enter senescence earlier than wild type litter mate controls (Fortschegger et al., 2007)

The link between DNA repair, cellular senescence and its association with lipid droplet biogenesis in mouse 3T3-L1 cells prompted us to investigate if SNEV$^{hPrp19/hPSO4}$ also regulates adipogenesis in human adipose derived stem cells (hASCs). Indeed, we find that SNEV modulates the kinetics and amount of lipid storage of differentiated human adipocytes via modulating the expression of genes involved in the PPARγ signaling axis. In addition, we also demonstrate that SNEV$^{hPrp19/hPSO4}$ is required for in vivo adipogenesis in C. elegans. Beside this, we also tested several other DNA repair factors that are differentially transcribed during adipogenesis and found that knock-down of Cockayne syndrome A (CSA), and Xeroderma pigmentosa E (XPE) slightly reduce adipogenesis of hASCs. Therefore, we speculate that the ability to repair DNA is an important checkpoint for adipogenesis, during which potentially damaging ROS are produced, and acts as a failsafe mechanism to reduce the risk of accumulation of DNA damaged and / or senescent cells with a large pro-inflammatory phenotype.

2. Material and Methods.

2.1. hASCs isolation and maintenance.

hASCs were isolated according to the protocol of Wolbank et al., 2009 and maintained in DMEM (4.5 g/l glucose) supplemented with 4 mM L-Glutamine (VWR #1.00286.1000) , 10% FCS, 1 ng/ml βFGF(Sigma # F0291-25UG), 1x Primocin (Eubio # ant-pm-1) at 37°C and 5% CO_2.

2.2. C. elegans maintenance.

C. elegans strains were cultured under standard laboratory conditions on NGM agar as described previously (Brenner, 1974). Strains used in this work include N2 (provided by V. Jantsch) and CF1814 [rrf-3(pk1426) II and daf-2(e1370) III]. All strains are available through the Caenorhabditis Genetics Center (CGC). Worms were synchronized by timed-egg lay on fresh RNAi plates and transferred to FuDR containing plates upon adulthood (usually on day 4 after hatching).

2.3. Adipogenic differentiation.

14000 hASCs were seeded in 1.9 cm^2 plates in growth medium (DMEM) for two days prior to adipogenic induction. Adipogenesis was induced by replacing the growth medium with fresh DMEM supplemented with 549µM 3-Isobutyl-1-methylxanthine (#I5879-100MG Sigma), 1µM Dexamethasone (Sigma), 549µM hydrocortisone (Sigma, #H-0396) and 66µM Indomethacin (Sigma, # I7378-5G), 100 µg/ml Primocin (Life Technologies, # ant-pm-1). Medium was exchanged twice a week until day 10, followed by Oil Red O staining. hASCs grown in DMEM low glucose/Ham`s F12,1:1(PAA # E15-012) supplemented with 10% FCS, 4 mM L-Glutamine, 100 µg/ml Primocin(Invivogen) were used as control. Total RNA and protein were isolated at specified time points during differentiation. Triglycerides contents were quantified by infinity T^m triglyceride quantification kit (ThermoScientific, #TR 22421) according to the manufacturer's recommended protocol and normalized to total protein concentration, measured using the BCA kit (ThermoScientific).

Oil red O staining of hASCs was performed on day 10 of differentiation. Differentiation medium was removed and cells were washed briefly with PBS twice and fixed by incubating in 3.6% formaldehyde in PBS for 1 hour at room temperature. Cells were then washed twice for 5 minutes each with PBS and incubated with 70% ethanol for 2 minutes, followed by 10 minutes incubation in Oil red O working solution (1.8mg/ml, Sigma). Cells were washed with PBS until all visible traces of remaining dye were removed.

Pictures were taken by Leica DM IL LED Inverted Microscope with a 10x dry objective (Leica Microsystems CMS, Mannheim, Germany).

Oil-Red-O staining in *C. elegans* was performed on day 6 after hatching as previously described (Soukas et al., 2009). Stained worms were embedded in Mowiol and pictures were taken on the next day on a Leica DM IL LED Inverted Microscope with a 10x dry objective.

2.4. Osteogenic differentiation.

2000 hASCs were seeded in 1.9 cm^2 plate 72 hours prior to induction of osteogenesis. Osteogenesis was induced by replacing the growth medium with fresh DMEM (low glucose GE Healthcare) supplemented with 10% FCS, 4 mM L-Glutamine (Sigma), 10mM L-Glycerophosphate (sigma), 150 µM Ascorbate-2-phosphate, 10nM vitamin-D3 (Sigma), 10nM Dexamethasone (Sigma), 100 µg/ml Primocin. hASCs grown in DMEM low glucose/Ham`s F12, 1:1(PAA # E15-012) supplemented with 10% FCS, 4 mM L-Glutamine, 1x Primocin were used as control. The medium was replaced every third day with fresh medium until day 12. Osteogenic differentiation was assessed by Alizarin Red staining. To perform Alizarin Red staining, osteogenesis inducing medium was removed and cells were washed three times briefly with PBS, incubated with 70% ethanol for 1 hour at -20°C, and washed 3 times with PBS. Cells were then incubated for 10 minutes with gentle shaking with alizarin Red solution (200mg/ml)(Applichem # A2306,0025) followed by thorough washing with PBS until all visible traces of the remaining dye were removed. Pictures were taken on a Leica DM IL LED Inverted Microscope with a 10x dry objective .

2.5. siRNA transfection in ASCs.

$SNEV^{Prp19/Pso4}$ siRNA and control siRNA (Dharmacon, D-001810-10-20) was purchased from Dharmacon (Thermo Scientific, J-004668-05). siRNAs against Werner, CSA, XPE and control were purchased from riboxx (Radebeul, Germany, D-00101-IBONI first). 14000 hASCs were seeded in 1.9 cm^2 well plates 48 hours prior to siRNA transfections using 50 nM of the respective siRNAs. The siRNAs were introduced into cells using DharmaFECT1 transfection reagent (Dharmacon) according to the manufacturer instructions. Knock-down efficiency of siRNAs was determined 48 hours after transfection by qPCR. Primer sequences are provided in Supplementary table 1.

2.6 SNEV$^{hPrp19/hPSO4}$ over-expression.

SNEV cDNA was amplified by PCR and cloned into the retroviral plasmid pLenti6. The negative control vector contained only the Blasticidin resistance gene. Retroviral particles were generated according to the manufacturer's protocol (Life Technologies). For SNEV over-expression 14000/1.9cm^2 hASCs were seeded in growth medium 48 hours prior to transduction and infected with retroviral particles according to the manufacturer's protocol (Life Technologies) at a multiplicity of infection (MOI) of 2 in DMEM (4.5 g/l glucose), supplemented with 4 mM L-Glutamine, 10% FCS, 1 ng/ml βFGF, 8 µg/ml Polybrene. The medium was replaced with adipogenesis inducing medium 48 hours post transduction.

2.7. RNA interference assays in *C. elegans*.

For the inactivation of DNA repair factors, feeding of double-stranded RNA expressed in bacteria was used as previously described (Timmons et al., 2001). RNAi constructs against *prp-19*, *wrn-1*, *xpe-1* and *M18.5*, derived from J. Ahringer's RNAi library, were distributed by Source BioScience. The HT115 strain of *E. coli* carrying the RNAi-construct, or the empty vector (L4440) as control, was cultured overnight in liquid LB medium with ampicillin and tetracyclin at 37°C. The bacteria were harvested by centrifugation, re-suspended in LB to a concentration of 60 mg/ml and 200 µl of this suspension was seeded on NGM plates containing 1 mM IPTG and 25 µg/ml Carbenicillin. The plates were incubated at 37°C overnight and used within one week.

2.8. qPCR analysis.

Total RNA from cells isolated at various time points was extracted using Trizol reagent (Life Technologies) according to the manufacturer's protocol. cDNA was synthesized from 500 ng of total RNA with the Dynamo cDNA synthesis kit (Thermo scientific) according to manufacturer instructions. qPCR analysis was performed using 5x Hot Firepol Eva green qPCR mix (MEDIBENA). Primers designed for qPCR are listed in Supplementary Table 1. mRNA expression was normalized to GAPDH.

2.9. Microarray analysis.

Global gene expression analysis was performed by two-color microarrays for hASCs upon SNEV knock-down, as well as for hMADS cells at various stages of adipocyte differentiation. Metadata (experimental parameters and detailed procedures), raw data files and final (filtered and normalized) data are accessible via Gene Expression Omnibus (GEO, series records GSE64937 and GSE64845).

2.10. Protein extraction and western blotting.

hASCs were harvested at different time points of differentiations using RIPA buffer (25 mM Tris.HCl pH 7.6, 150mM NaCl, 1% NP40, 1% sodium deoxycholate, 0.1% SDS, Roche 1x protease and phosphatase inhibitor(Roche)), sonicated for 30 cycles (30 s on and 30 s off) at 4°C in a Bioruptor sonicator (Diagenode) and centrifuged for 30 minutes at 10000 RPM. The pellet was discarded and protein concentration in the supernatant was determined with BCA kit (ThermoScientific). 30 µg of protein were mixed with 4xSDS loading dye (240 mM Tris-Cl pH 6.8, 8% SDS, 40 % glycerol, 0.05% bromophenol blue, 5% ß-Mercaptoethanol) and boiled for 95°C for 10 min and separated on a NuPAGE 4–12% Bis/Tris polyacrylamide gel (Life Technologies) in MOPS buffer at 200 V. Proteins from the gel were transferred to PVDF membranes (Roth) by using XCell SureLock® Mini-Cell (Life Technologies) at 180 mA for 1.5 hours. The membrane was blocked in PBS containing 3% skim milk and 0.1% tween for 1 hour on an orbital shaker at room temperature followed by overnight incubation with anti Prp19 antibody (Bethyl #A300-102A) diluted 1:2000 in PBS containing 3% skim milk at 4°C. the membrane was washed 3 times for 5 minutes each with PBS containing 0.1% tween and incubated with anti-Rabbit-IR-Dye 800 antibody (Licor, # 926-32211), diluted 1.5000 in PBS containing 3% milk and washed three times for 5minutes each with PBS containing 0.1% Tween. Membranes were scanned using the Odyssey infrared imaging system (LI-COR, Lincoln, NE, USA). The same membrane was then incubated with rabbit anti-GAPDH, 1:5000 dilution (Santa Cruz, # sc25778) for 1 hour at room temperature and stained with anti-Rabbit-IR-Dye 800 antibody (Licor, # 926-32211), diluted 1:5000 according to the procedure as mentioned above. GAPDH was used as loading control.

2.11. Indirect immuno-fluorescence.

60000 hASCs were grown in DMEM medium (4.5 g/l glucose) on coverslips in a six well plate. 48 hours after seeding growth medium was replaced by adipogenic differentiation media containing Indomethacin, Dexamethasone, and IBMX. Medium was changed after each 3 days until day 10. At day-10, cells were washed twice with PBS and fixed in 4% formaldehyde for 20 minutes at room temperature. After subsequent three times washing with PBS, cells were permeabilized in 0.25% Triton in PBS for 20 minutes and blocked in 20% FCS (in PBS) for 1 hour. Cells were washed with PBS three times for 5 minutes each and stained with anti-Prp19 antibody (Bethyllab #A300-102A) diluted 1: 500 in PBS containing 20% FCS for 1 hour. Cells were again washed with PBS for 3 x 5 minutes each prior to application of Dyelight 649 anti-rabbit antibody (Jackson Immunoresearch, # 111-495-144) diluted 1:500 in PBS containing 20% FCS for 1 hour. Cells were washed again with PBS for 3 x 5 minutes each. For nuclear DNA staining DAPI at 200 ng/ml was applied for 10 minutes and then washed with PBS for 1 x 5 minutes. Slides were mounted

with Vectashield mounting medium (Vector Laboratories, Burlingame, U.S.A) and sealed with nail polish. Microscopy and image analysis were done by using Leica SP5 II laser scanning confocal microscope (Leica Microsystems CMS, Mannheim, Germany).

2.12. Statistical analysis.

Differences between data sets were tested for statistical significance using Student's *t*-test wih Prism Graphpad QuickCalcs and $P < 0.05$ considered statistically significant.

3. Results.

3.1. SNEV $^{hPrp19/hPso4}$ expression is induced at both mRNA and Protein level during adipogenesis.

In order to investigate the role of SNEV $^{hPrp19/hPso4}$ in adipogenesis we first analyzed its expression during adipogenesis in a time course dependent manner. Human ASCs were induced to differentiate into adipocytes by medium supplemented with a cocktail of known adipogenesis inducing agents and total RNA and protein were isolated at indicated time points during differentiation. Non-differentiated hASCs were used as control. Indeed, SNEV$^{hPrp19/hPso4}$ mRNA (Fig. 1A) as well as protein levels (Fig. 1B) increased in a time course dependent manner over 9 days. As SNEV $^{hPrp19/hPso4}$ is mainly a nuclear protein (Gotzmann et al., 2000), we used indirect immunofluorescence to monitor SNEV $^{hPrp19/hPso4}$ localization during adipogenesis. SNEV$^{hPrp19/hPso4}$ was detected both in the nucleus and in the cytoplasm of differentiated cells, while only nuclear staining was observed in the undifferentiated controls (Fig. 1C). Adipogenic differentiation was confirmed by quantitation of PPARγ and FASN mRNA (Fig. 1D& 1E), both well accepted markers of adipogenesis (Heikkinen et al., 2007; Mayas et al., 2010). Oil Red O staining after 10 days also confirmed extensive lipid droplet formation in the differentiated culture, whereas no lipid droplets were observed in the control (data not shown).

These results show that SNEV$^{hPrp19/hPso4}$ expression is induced during adipogenesis and that its localization is not restricted to the nucleus, similar to the observation in mouse 3T3 cell line (Cho et al., 2007).

3.2. SNEV$^{hPrp19/hPso4}$ is required for adipogenic differentiation in human ASCs.

In order to determine whether SNEV$^{hPrp19/hPso4}$ is not only regulated during but also necessary for adipogenesis of hASCs, we performed siRNA mediated knock-down of SNEV$^{hPrp19/hPso4}$ followed by adipogenic induction. hASCs were transfected with siSNEV and control siRNA and were induced to differentiate 48 hours after transfection. Adipogenic differentiation was assessed by Oil red O staining and measurement of intracellular triglyceride content 10 days after start of differentiation according to the experimental design shown in figure 2A (Fig. 2A). siSNEV transfection resulted in around 90% knock-down efficiency on mRNA level over the 9 day period of differentiation tested (Fig. 2B). Non-targeting control siRNA transfected cells underwent normal lipid droplet formation, whereas SNEV$^{hPrp19/hPso4}$ knock-down resulted in formation of fewer lipid droplets as shown by Oil Red O staining (Fig. 2C). Accordingly,

intracellular triglyceride content was also 5-fold reduced after SNEV $^{hPrp19/hPso4}$ knock-down as compared to control (Fig. 2D).

3.3. Reduced adipogenesis by SNEV$^{hPrp19/hPso4}$ knock-down is accompanied by down regulated PPARγ and insulin signaling axis.

We next sought to investigate how SNEV$^{hPrp19/hPso4}$ might inhibit the early steps of adipogenesis. Thus, we performed microarray analysis to visualize profile changes in gene expression in response to SNEV$^{hPrp19/hPso4}$ down regulation during adipogenesis. hASCs transfected with siSNEV and siControl were induced to differentiate. Total RNA was collected at day 3 of differentiation (see material & methods) and subjected to microarray analysis. SNEV $^{hPrp19/hPso4}$ mRNA expression is efficiently down regulated in response to siSNEV transfection (Fig. 3A). The microarray data identified 163 genes that showed at least two fold differential expression in siSNEV vs siControl culture. In order to identify the pathways that might be addressed by SNEV$^{hPrp19/hPso4}$ knock-down, we performed gene set enrichment analysis (GSEA). In accordance to the observed inhibition in adipogenesis, genes involved in the pro-adipogenic PPARγ (Fig. 3B) and insulin signaling (Fig. 3C) pathways were down-regulated by siSNEV, whereas genes involved in the anti-adipogenic TGFβ signaling (Fig. 3D) pathway were up regulated. We further confirmed our microarray data by qPCR of PPARγ (Fig. 3E) and FASN (Fig. 3F) during the entire course of adipogenesis. Collectively, these data suggest that SNEV$^{hPrp19/hPso4}$ is necessary in an early step as it inhibits the global changes of the transcriptome towards adipogenesis induced by starting the differentiation process.

Besides differentiating into adipocytes, hASCs are capable of differentiating into multiple other mesenchymal lineages, including the osteogenic lineage. In fact, an inverse relationship exists between osteogenic and adipogenic commitment and differentiation of mesenchymal stem cells and it is generally thought that differentiation into one of the two lineages comes at the expense of the other (James, 2013). Therefore, we tested if SNEV$^{hPrp19/hPso4}$ might influence osteogenic differentiation as well. We induced osteogenic differentiation in SNEV$^{hPrp19/hPso4}$ down regulated hASCs, and visualized calcium deposition by Alizarin Red staining as endpoint measurement of osteogenesis. However, we did not find any significant differences in osteogenic differentiation between SNEV$^{hPrp19/hPso4}$ knock-down and control hASCs (Supplemental Figure 1) as quantitated using Alizarin Red staining for calcium deposition as end-point measurement.

3.4. SNEV$^{hPrp19/hPso4}$ over-expression accelerates adipogenesis.

The observation that SNEV$^{hPrp19/hPso4}$ knock-down reduced adipogenesis led us to test if its over-expression can lead to its acceleration. Therefore, we transduced hASCs with a lentiviral construct containing SNEV$^{hPrp19/hPso4}$ before induction of adipogenesis. ASCs transduced with empty vector were used as a control. Adipogenic differentiation was assessed by qPCR of PPARy and FASN, Oil red O staining and triglyceride quantification as outlined in Fig. 4A.

Increased expression of SNEV$^{hPrp19/hPso4}$ in lentivirally transduced hASCs was confirmed by qPCR and remained elevated during the entire course of differentiation as compared to control (Fig. 4B). Indeed, SNEV$^{hPrp19/hPso4}$ over-expression accelerated adipogenesis as large amounts of lipid droplets appeared already after 6 days as compared to the 10 days necessary under control conditions (Fig. 1). In control cells, only very few lipid droplets were present on day 6 (Fig. 4C). We further quantified intracellular lipid accumulation by triglyceride assay and found a 2-fold increase in SNEV$^{hPrp19/hPso4}$ over-expressing hASCs as compared to empty vector control (Fig. 4D). These results suggest that SNEV$^{hPrp19/hPso4}$ over expression indeed accelerates adipogenesis in hASCs. In order to confirm accelerated adipogenesis at a molecular level, we measured mRNA expression of PPARγ and FASN expression by qPCR, showing the expected increases (Fig. 4E and 4F). These results suggest that SNEV$^{hPrp19/hPso4}$ is indeed a modulator of adipogenesis as the process is affected both by its knock-down and over-expression.

3.5. Other DNA repair factors influence adipogenesis in hASCs.

Since loss of subcutaneous fat is observed in patients suffering from progeroid syndromes, we tested if other DNA repair factors mutated in various segmental progeroid syndromes influence adipogenesis as well. For this purpose, we looked at existing transcriptomic data of an adipogenic differentiation time course experiment (available at Gene Expression Omnibus, accession number GSE64845) and specifically visualized the expression of genes involved in DNA damage repair (data not shown). From these, we selected WRN, CSA and XPE, which are involved in premature aging and are differentially expressed during adipogenesis (Fig. 5A), and confirmed their differential expression by qPCR (Fig. 5B, 5C, 5D). In addition, these genes represent members of different DNA damage repair pathways, CSA being specific for transcription coupled nucleotide excision repair (TC-NER) while XPE is involved in global genome- as well as TC-NER and homologous recombination. WRN is a helicase generally required for DNA recombination and repair (reviewed in(Garinis et al., 2008). In order to test if these genes are indeed required for adipogenesis, we knocked down the expression of WRN, CSA, and XPE in hASCs by siRNA transfection, followed by induction of adipogenesis. siRNA knock-down efficiency was confirmed by

qPCR (Fig. 5E). Adipogenic differentiation was then assessed by intracellular triglyceride accumulation at day 10 of differentiation. Triglyceride quantification data showed slight but significant decrease of adipogenesis of around 20% after CSA and XPE knock-down, while WRN knock-down resulted in a 50% reduction of Triglyceride accumulation in hASCs (Fig. 5F).

3.6. Loss of SNEV$^{hPrp19/hPso4}$ and WRN leads to reduced fat deposition in C. elegans.

In order to test the functional conservation of the DNA damage repair factors (SNEV$^{hPrp19/hPso4}$, WRN, CSA, and XPE) in organismal adipogenesis, we assessed their role in fat deposition of *Caenorhabiditis elegans*. For this purpose we selected *prp-19, wrn-1, xpa-1 and M18.5* as orthologs of the human DNA damage repair factors SNEV, WRN, XPA and DDB1, respectively, and inhibited their expression by RNAi in the N2 wild-type strain. The storage of neutral lipids was measured by Oil Red O staining (Soukas et al., 2009). At the time of planning the experiment, the homolog of human CSA in *C. elegans* was not known until very recently (Babu et al., 2014), therefore we selected *xpa-1* instead of CSA, as a member of NER factors and homologue of human XPA (Park et al., 2002). RNAi treatment was performed already upon hatching, since we did not detect major differences in developmental timing between RNAi-treated and control animals (data not shown). Young adult hermaphrodites (6 days after hatching) were then fixed and subjected to Oil-Red-O staining. Indeed, we found reduced fat mass in *prp-19* and *wrn-1* RNAi animals compared to the RNAi control, while *M18.5* and *xpa-1* RNAi did not show differences (Fig. 6A). However, we cannot exclude that slight variances might be missed by Oil Red O staining alone.

We expected to further enhance the observed fat storage phenotype of prp-19 and wrn-1 RNAi by performing the same experiment with the CF1814 strain, which is mutated in *rrf-3 (pk1426)* and *daf-2 (e1370)*. While mutation of *rrf-3* increases RNAi efficiency (Simmer et al., 2002) mutation of *daf-2*, the insulin receptor, results in elevated fat mass (Soukas et al., 2009). Indeed, while the RNAi control group stained positive for Oil Red O throughout the whole body and especially surrounding intestines and pharynx, *prp-19-1* and *wrn-1* RNAi animals stained only weekly positive in close proximity to the pharynx (Fig. 6B).

These findings indicate that loss of the conserved DNA damage repair factors *prp-19* and *wrn-1* robustly reduce the accumulation of neutral lipids both in wild-type *C. elegans*, as well as in a mutant strain with a high-fat phenotype.

4. Discussion.

Here, we show that SNEV$^{hPrp19/hPso4}$ regulates adipogenesis of hASCs. We found that SNEV$^{hPrp19/hPso4}$ knock-down inhibits, while its over expression accelerates adipogenesis early after induction of adipogenic differentiation. Furthermore, SNEV$^{hPrp19/hPso4}$ regulates fat deposition on the organismal level, as shown using the nematode C. elegans as model system.

SNEV$^{hPrp19/hPso4}$ regulates several diverse cellular processes, such as mRNA splicing, transcription (Chanarat et al., 2012), mitosis (Hofmann et al., 2013; Watrin et al., 2014) and apoptosis (Lu et al., 2014)). If, though, it was its DNA repair function that is connected with adipogenesis, then other DNA repair factors might have similar effects on adipogenesis, which would point to a general importance of intact DNA repair capacity for induction of adipogenesis. In fact, knock-down of WRN markedly reduced adipogenesis, while CSA and XPE only slightly but significantly inhibited accumulation of lipids in hASCs. In C. elegans, only SNEV$^{hPrp19/hPso4}$ and WRN reduced fat storage visibly. This is in accordance to studies that the murine homologues of SNEV$^{hPrp19/hPso4}$ and WRN are involved in 3T3 cell adipogenesis (Cho et al., 2007; Turaga et al., 2009), but also are components of an ICL repair complex (Zhang et al 2005a). Still, the species-specific differences in protein function and regulation patterns (Lindroos et al., 2013; Mikkelsen et al., 2010; Qian et al., 2010) make clear that not all molecular regulation steps are indeed conserved from mouse to human. This might explain that in this study human SNEV$^{hPrp19/hPso4}$ seems to act upstream of PPARγ and PPARγ induced genes, in contrast to 3T3 where PPARγ remained unchanged but inhibited increase of SCD and perilipin 1 (Cho et al. 2007). A role upstream or at the level of PPARγ is also supported by findings that SNEV$^{hPrp19/hPso4}$ (Grillari et al. 2005) as well as PPARγ tend to cluster at nuclear speckles in adipocytes as compared to undifferentiatied cells (Szczerbal and Bridger, 2010). In addition, SNEV$^{hPrp19/hPso4}$ knock-down decreases expression of genes involved in the insulin signaling pathway known to be pro-adipogenic (Heikkinen et al., 2007; Zhang et al., 2009), while genes involved in TGF-β signaling are increased and known to have inhibitory effects on adipogenesis (Choy and Derynck, 2003). Altogether, these data point to a regulatory role of SNEV$^{hPrp19/hPso4}$ early during adipogenic commitment of hASCs, however, since SNEV $^{hPrp19/hPso4}$ is a multifunctional protein, we still cannot rule out the possibility that it regulates adipogenesis via other than its DNA repair function, e.g. via differential pre-mRNA splicing, or via a putative role as a transcription factor, since SNEV $^{hPrp19/hPso4}$ has been shown to be required for full transcriptional activity of RNA polymerase II in yeast (Chanarat et al., 2012).

In any case, an interesting possibility is suggested by the fact that not only SNEV$^{hPrp19/hPso4}$, but also other DNA repair factors inhibit adipogenesis, supporting the idea that the capacity of repairing DNA damage is

a checkpoint for adipogenesis. It is still unclear, however, why the inducibility of DNA damage repair might be such a checkpoint.

One hypothesis might be based on the fact that both adipogenesis and lipolysis are strongly associated with increased generation of reactive oxygen species (ROS)(Kanda et al., 2011; Krawczyk et al., 2012), which might be a driver of increased damage to DNA during adipogenesis, so that differentiating cells are at risk to enter ROS induced premature senescence, concomitant with induction of the senescent/pro-inflammatory phenotype of SASP (senescence associated secretory phenotype) (Monickaraj et al., 2013) . Only if sufficient DNA repair capacity is present in the cells would the cells therefore be allowed to enter adipogenic differentiation. This is supported by the fact that DNA damage repair is induced during early adipogenesis (Meulle et al., 2008) and is even more important, as senescence impair adipogenesis (Mitterberger et al., 2014) and accumulation of senescent cells in the adipose tissue (Stout et al., 2014) would lead to degeneration of adipose tissue and inflammation. The lack of adipogenic differentiation together with adipose tissue degeneration induced by senescent adipocytes might therefore be one factor why patients suffering from segmental, progeroid syndromes and mouse models of premature aging like e.g. ERCC1 deficient mice, show loss of subcutaneous fat (Jaarsma et al., 2013; Karakasilioti et al., 2013).

In addition to adipogenesis, also neurogenic differentiation is accompanied and modified by ROS (Domenis et al., 2014), and again SNEV$^{hPrp19/hPso4}$ knock-down inhibits neurogenic differentiation (Urano-Tashiro et al., 2010). Further, the role of ROS seems different in osteogenic differentiation (Atashi et al., 2015). If the hypothesis that DNA damage repair capacity is a checkpoint for specific differentiation programs is true, the main question to be answer is on what the sensing mechanism for the presence of DNA repair capacity might be. It is tempting to speculate that SNEV$^{hPrp19/hPso4}$ - a downstream target of ATM upon oxidative stress (Dellago et al., 2012) - might be part of a signaling pathway that senses and repairs DNA damage by a wave of initial ROS produced during early steps of differentiation. It is of interest in this context that during differentiation, mesenchymal stem cells (MSCs) are more susceptible to undergo ROS induced apoptosis than progenitor cells (Oliver et al., 2013), and over-expression of SNEV$^{hPrp19/hPso4}$ protects the cell types tested so far against induction of apoptosis (Dellago et al., 2012; Schraml et al., 2008; Voglauer et al., 2006).

Summarized, we suggest that availability of DNA damage repair might represent a checkpoint for cellular differentiation programs, which is of special importance for differentiation processes that involve high levels of ROS, or for long lived cells like adipocytes and neurons.

5. Acknowledgements.

We are grateful to M.Mur for technical assistance. Some strains were provided by the CGC, which is funded by NIH Office of Research Infrastructure Programs (P40 OD010440). We thank the imaging center of BOKU and especially Monika Debreczeny for excellent technical support with microscopy.This work was supported by FWF Project P24498, by the Austrian Federal Ministry of Economy, Family and Youth and the National Foundation for Research, Technology and Development, as well as by CERIES.

6. Conflict of interest.

JG and RGV are co-founders of Evercyte GmbH.

References.

Atashi, F., Modarressi, A., Pepper, M.S., 2015. The role of reactive oxygen species in mesenchymal stem cell adipogenic and osteogenic differentiation: a review. Stem Cells Dev. doi:10.1089/scd.2014.0484

Baker, D.J., Jeganathan, K.B., Cameron, J.D., Thompson, M., Juneja, S., Kopecka, A., Kumar, R., Jenkins, R.B., de Groen, P.C., Roche, P., van Deursen, J.M., 2004. BubR1 insufficiency causes early onset of aging-associated phenotypes and infertility in mice. Nat. Genet. 36, 744–749. doi:10.1038/ng1382

Brenner, S., 1974. The genetics of Caenorhabditis elegans. Genetics 77, 71–94. doi:10.1002/cbic.200300625

Cartwright, M.J., Tchkonia, T., Kirkland, J.L., 2007. Aging in adipocytes: Potential impact of inherent, depot-specific mechanisms. Exp. Gerontol. doi:10.1016/j.exger.2007.03.003

Caso, G., McNurlan, M.A., Mileva, I., Zemlyak, A., Mynarcik, D.C., Gelato, M.C., 2013. Peripheral fat loss and decline in adipogenesis in older humans. Metabolism. 62, 337–340. doi:10.1016/j.metabol.2012.08.007

Chanarat, S., Burkert-Kautzsch, C., Meinel, D.M., Sträßer, K., 2012. Prp19C and TREX: Interacting to promote transcription elongation and mRNA export. Transcription. doi:10.4161/trns.3.1.19078

Cho, S.Y., Shin, E.S., Park, P.J., Shin, D.W., Chang, H.K., Kim, D., Lee, H.H., Lee, J.H., Kim, S.H., Song, M.J., Chang, I.-S., Lee, O.S., Lee, T.R., 2007. Identification of mouse Prp19p as a lipid droplet-associated protein and its possible involvement in the biogenesis of lipid droplets. J. Biol. Chem. 282, 2456–2465. doi:10.1074/jbc.M608042200

Choy, L., Derynck, R., 2003. Transforming growth factor-beta inhibits adipocyte differentiation by Smad3 interacting with CCAAT/enhancer-binding protein (C/EBP) and repressing C/EBP transactivation function. J. Biol. Chem. 278, 9609–9619. doi:10.1074/jbc.M212259200

Dellago, H., Khan, A., Nussbacher, M., Gstraunthaler, A., Lämmermann, I., Schosserer, M., Mück, C., Anrather, D., Scheffold, A., Ammerer, G., Jansen-Dürr, P., Rudolph, K.L., Voglauer-Grillari, R., Grillari, J., Lammermann, I., Muck, C., Jansen-Durr, P., 2012. ATM-dependent phosphorylation of SNEVhPrp19/hPso4 is involved in extending cellular life span and suppression of apoptosis. Aging (Albany NY) 4, 290–304.

Domenis, R., Bergamin, N., Gianfranceschi, G., Vascotto, C., Romanello, M., Rigo, S., Vagnarelli, G., Faggiani, M., Parodi, P., Kelley, M.R., Beltrami, C.A., Cesselli, D., Tell, G., Beltrami, A.P., 2014. The redox function of APE1 is involved in the differentiation process of stem cells toward a neuronal cell fate. PLoS One 9. doi:10.1371/journal.pone.0089232

Fortschegger, K., Wagner, B., Voglauer, R., Katinger, H., Sibilia, M., Grillari, J., 2007. Early embryonic lethality of mice lacking the essential protein SNEV. Mol. Cell. Biol. 27, 3123–3130. doi:10.1128/MCB.01188-06

Garinis, G.A., van der Horst, G.T.J., Vijg, J., Hoeijmakers, J.H.J., 2008. DNA damage and ageing: new-age ideas for an age-old problem. Nat. Cell Biol. 10, 1241–1247. doi:10.1038/ncb1108-1241

Gotzmann, J., Gerner, C., Meissner, M., Holzmann, K., Grimm, R., Mikulits, W., Sauermann, G., 2000. hNMP 200: a novel human common nuclear matrix protein combining structural and regulatory functions. Exp. Cell Res. 261, 166–179. doi:10.1006/excr.2000.5025

Grillari, J., Ajuh, P., Stadler, G., L??scher, M., Voglauer, R., Ernst, W., Chusainow, J., Eisenhaber, F., Pokar, M., Fortschegger, K., Grey, M., Lamond, A.I., Katinger, H., 2005. SNEV is an evolutionarily conserved splicing factor whose oligomerization is necessary for spliceosome assembly. Nucleic Acids Res. 33, 6868–6883. doi:10.1093/nar/gki986

Hatakeyama, S., Yada, M., Matsumoto, M., Ishida, N., Nakayama, K.I., 2001. U box proteins as a new family of ubiquitin-protein ligases. J. Biol. Chem. 276, 33111–33120. doi:10.1074/jbc.M102755200

Heikkinen, S., Auwerx, J., Argmann, C.A., 2007. PPARgamma in human and mouse physiology. Biochim. Biophys. Acta 1771, 999–1013. doi:10.1016/j.bbalip.2007.03.006

Hofmann, J.C., Tegha-Dunghu, J., Dräger, S., Will, C.L., Lührmann, R., Gruss, O.J., 2013. The Prp19 Complex Directly Functions in Mitotic Spindle Assembly. PLoS One 8. doi:10.1371/journal.pone.0074851

Ibrahim, M.M., 2010. Subcutaneous and visceral adipose tissue: structural and functional differences. Obes. Rev. 11, 11–18. doi:10.1111/j.1467-789X.2009.00623.x

Jaarsma, D., van der Pluijm, I., van der Horst, G.T.J., Hoeijmakers, J.H.J., 2013. Cockayne syndrome pathogenesis: Lessons from mouse models. Mech. Ageing Dev. 134, 180–195. doi:10.1016/j.mad.2013.04.003

James, A.W., 2013. Review of Signaling Pathways Governing MSC Osteogenic and Adipogenic Differentiation. Scientifica (Cairo). 2013, 684736. doi:10.1155/2013/684736

Kanda, Y., Hinata, T., Kang, S.W., Watanabe, Y., 2011. Reactive oxygen species mediate adipocyte differentiation in mesenchymal stem cells. Life Sci 89, 250–258. doi:10.1016/j.lfs.2011.06.007

Karakasilioti, I., Kamileri, I., Chatzinikolaou, G., Kosteas, T., Vergadi, E., Robinson, A.R., Tsamardinos, I., Rozgaja, T.A., Siakouli, S., Tsatsanis, C., Niedernhofer, L.J., Garinis, G.A., 2013. DNA damage triggers a chronic autoinflammatory response, leading to fat depletion in NER progeria. Cell Metab. 18, 403–415. doi:10.1016/j.cmet.2013.08.011

Kirkland, J.L., Hollenberg, C.H., Kindler, S., Gillon, W.S., 1994. Effects of age and anatomic site on preadipocyte number in rat fat depots. J. Gerontol. 49, B31–B35.

Krawczyk, S.A., Haller, J.F., Ferrante, T., Zoeller, R.A., Corkey, B.E., 2012. Reactive oxygen species facilitate translocation of hormone sensitive lipase to the lipid droplet during lipolysis in human differentiated adipocytes. PLoS One 7. doi:10.1371/journal.pone.0034904

Lindroos, J., Husa, J., Mitterer, G., Haschemi, A., Rauscher, S., Haas, R., Gröger, M., Loewe, R., Kohrgruber, N., Schrögendorfer, K.F., Prager, G., Beck, H., Pospisilik, J.A., Zeyda, M., Stulnig,

T.M., Patsch, W., Wagner, O., Esterbauer, H., Bilban, M., 2013. Human but not mouse adipogenesis is critically dependent on LMO3. Cell Metab. 18, 62–74. doi:10.1016/j.cmet.2013.05.020

Löscher, M., Fortschegger, K., Ritter, G., Wostry, M., Voglauer, R., Schmid, J.A., Watters, S., Rivett, A.J., Ajuh, P., Lamond, A.I., Katinger, H., Grillari, J., 2005. Interaction of U-box E3 ligase SNEV with PSMB4, the beta7 subunit of the 20 S proteasome. Biochem. J. 388, 593–603. doi:10.1042/BJ20041517

Lu, S., Wang, R., Cai, C., Liang, J., Xu, L., Miao, S., Wang, L., Song, W., 2014. Small kinetochore associated protein (SKAP) promotes UV-induced cell apoptosis through negatively regulating Pre-mRNA processing factor 19 (Prp19). PLoS One 9. doi:10.1371/journal.pone.0092712

Mahajan, K.N., Mitchell, B.S., 2003. Role of human Pso4 in mammalian DNA repair and association with terminal deoxynucleotidyl transferase. Proc. Natl. Acad. Sci. U. S. A. 100, 10746–10751. doi:10.1073/pnas.1631060100

Mar??chal, A., Li, J.M., Ji, X.Y., Wu, C.S., Yazinski, S.A., Nguyen, H.D., Liu, S., Jim??nez, A.E., Jin, J., Zou, L., 2014. PRP19 Transforms into a Sensor of RPA-ssDNA after DNA Damage and Drives ATR Activation via a Ubiquitin-Mediated Circuitry. Mol. Cell 53, 235–246. doi:10.1016/j.molcel.2013.11.002

Mayas, M.D., Ortega, F.J., Macías-González, M., Bernal, R., Gómez-Huelgas, R., Fernández-Real, J.M., Tinahones, F.J., 2010. Inverse relation between FASN expression in human adipose tissue and the insulin resistance level. Nutr. Metab. (Lond). 7, 3. doi:10.1186/1743-7075-7-3

Meulle, A., Salles, B., Daviaud, D., Valet, P., Muller, C., 2008. Positive regulation of DNA double strand break repair activity during differentiation of long life span cells: The example of adipogenesis. PLoS One 3. doi:10.1371/journal.pone.0003345

Mikkelsen, T.S., Xu, Z., Zhang, X., Wang, L., Gimble, J.M., Lander, E.S., Rosen, E.D., 2010. Comparative epigenomic analysis of murine and human adipogenesis. Cell 143, 156–169. doi:10.1016/j.cell.2010.09.006

Mitterberger, M.C., Lechner, S., Mattesich, M., Zwerschke, W., 2014. Adipogenic differentiation is impaired in replicative senescent human subcutaneous adipose-derived stromal/progenitor cells. Journals Gerontol. - Ser. A Biol. Sci. Med. Sci. 69, 13–24. doi:10.1093/gerona/glt043

Monickaraj, F., Aravind, S., Nandhini, P., Prabu, P., Sathishkumar, C., Mohan, V., Balasubramanyam, M., 2013. Accelerated fat cell aging links oxidative stress and insulin resistance in adipocytes. J. Biosci. 38, 113–122. doi:10.1007/s12038-012-9289-0

Mori, S., Murano, S., Yokote, K., Takemoto, M., Asaumi, S., Take, A., Saito, Y., 2001. Enhanced intra-abdominal visceral fat accumulation in patients with Werner's syndrome., International journal of obesity and related metabolic disorders : journal of the International Association for the Study of Obesity. doi:10.1038/sj.ijo.0801529

Muzumdar, R., Allison, D.B., Huffman, D.M., Ma, X., Atzmon, G., Einstein, F.H., Fishman, S., Poduval, A.D., McVei, T., Keith, S.W., Barzilai, N., 2008. Visceral adipose tissue modulates mammalian longevity. Aging Cell 7, 438–440. doi:10.1111/j.1474-9726.2008.00391.x

Oliver, L., Hue, E., Séry, Q., Lafargue, A., Pecqueur, C., Paris, F., Vallette, F.M., 2013. Differentiation-related response to DNA breaks in human mesenchymal stem cells. Stem Cells 31, 800–7. doi:10.1002/stem.1336

Park, H.K., Yook, J.-S., Koo, H.-S., Choi, I.S., Ahn, B., 2002. The Caenorhabditis elegans XPA homolog of human XPA. Mol. Cells 14, 50–55.

Qian, S.-W., Li, X., Zhang, Y.-Y., Huang, H.-Y., Liu, Y., Sun, X., Tang, Q.-Q., 2010. Characterization of adipocyte differentiation from human mesenchymal stem cells in bone marrow. BMC Dev. Biol. 10, 47. doi:10.1186/1471-213X-10-47

Ross, S.E., Hemati, N., Longo, K.A., Bennett, C.N., Lucas, P.C., Erickson, R.L., MacDougald, O.A., 2000. Inhibition of adipogenesis by Wnt signaling. Science 289, 950–953. doi:10.1126/science.289.5481.950

Sato, M., Sakota, M., Nakayama, K., 2010. Human PRP19 interacts with prolyl-hydroxylase PHD3 and inhibits cell death in hypoxia. Exp. Cell Res. 316, 2871–2882. doi:10.1016/j.yexcr.2010.06.018

Schraml, E., Voglauer, R., Fortschegger, K., Sibilia, M., Stelzer, I., Grillari, J., Schauenstein, K., 2008. Haploinsufficiency of senescence evasion factor causes defects of hematopoietic stem cells functions. Stem Cells Dev. 17, 355–366. doi:10.1089/scd.2007.0107

Shuster, a, Patlas, M., Pinthus, J.H., Mourtzakis, M., 2012. The clinical importance of visceral adiposity: a critical review of methods for visceral adipose tissue analysis. Br. J. Radiol. 85, 1–10. doi:10.1259/bjr/38447238

Simmer, F., Tijsterman, M., Parrish, S., Koushika, S.P., Nonet, M.L., Fire, A., Ahringer, J., Plasterk, R.H.A., 2002. Loss of the putative RNA-directed RNA polymerase RRF-3 makes C. elegans hypersensitive to RNAi. Curr. Biol. 12, 1317–1319. doi:10.1016/S0960-9822(02)01041-2

Song, E.J., Werner, S.L., Neubauer, J., Stegmeier, F., Aspden, J., Rio, D., Harper, J.W., Elledge, S.J., Kirschner, M.W., Rape, M., 2010. The Prp19 complex and the Usp4Sart3 deubiquitinating enzyme control reversible ubiquitination at the spliceosome. Genes Dev. 24, 1434–1447. doi:10.1101/gad.1925010

Soukas, A.A., Kane, E.A., Carr, C.E., Melo, J.A., Ruvkun, G., 2009. Rictor/TORC2 regulates fat metabolism, feeding, growth, and life span in Caenorhabditis elegans. Genes Dev. 23, 496–511. doi:10.1101/gad.1775409

Stout, M.B., Tchkonia, T., Pirtskhalava, T., Palmer, A.K., List, E.O., Berryman, D.E., Lubbers, E.R., Escande, C., Spong, A., Masternak, M.M., Oberg, A.L., LeBrasseur, N.K., Miller, R.A., Kopchick, J.J., Bartke, A., Kirkland, J.L., 2014. Growth hormone action predicts age-related white adipose tissue dysfunction and senescent cell burden in mice. Aging (Albany. NY). 6, 575–586.

Szczerbal, I., Bridger, J.M., 2010. Association of adipogenic genes with SC-35 domains during porcine adipogenesis. Chromosom. Res. 18, 887–895. doi:10.1007/s10577-010-9176-1

Tchkonia, T., Morbeck, D.E., Von Zglinicki, T., Van Deursen, J., Lustgarten, J., Scrable, H., Khosla, S., Jensen, M.D., Kirkland, J.L., 2010. Fat tissue, aging, and cellular senescence. Aging Cell. doi:10.1111/j.1474-9726.2010.00608.x

Tchkonia, T., Zhu, Y., Van Deursen, J., Campisi, J., Kirkland, J.L., 2013. Cellular senescence and the senescent secretory phenotype: Therapeutic opportunities. J. Clin. Invest. doi:10.1172/JCI64098

Timmons, L., Court, D.L., Fire, A., 2001. Ingestion of bacterially expressed dsRNAs can produce specific and potent genetic interference in Caenorhabditis elegans. Gene 263, 103–112. doi:10.1016/S0378-1119(00)00579-5

Turaga, R.V.N., Paquet, E.R., Sild, M., Vignard, J., Garand, C., Johnson, F.B., Masson, J.-Y., Lebel, M., 2009. The Werner syndrome protein affects the expression of genes involved in adipogenesis and inflammation in addition to cell cycle and DNA damage responses. Cell Cycle 8, 2080–2092. doi:10.4161/cc.8.13.8925

Urano-Tashiro, Y., Sasaki, H., Sugawara-Kawasaki, M., Yamada, T., Sugiyama, A., Akiyama, H., Kawasaki, Y., Tashiro, F., 2010. Implication of Akt-dependent Prp19 alpha/14-3-3beta/Cdc5L complex formation in neuronal differentiation. J. Neurosci. Res. 88, 2787–2797. doi:10.1002/jnr.22455

Voglauer, R., Chang, M.W.F., Dampier, B., Wieser, M., Baumann, K., Sterovsky, T., Schreiber, M., Katinger, H., Grillari, J., 2006. SNEV overexpression extends the life span of human endothelial cells. Exp. Cell Res. 312, 746–759. doi:10.1016/j.yexcr.2005.11.025

Wan, L., Huang, J., 2014. The PSO4 protein complex associates with replication protein a (RPA) and modulates the activation of ataxia telangiectasia-mutated and RAD3-related (ATR). J. Biol. Chem. 289, 6619–6626. doi:10.1074/jbc.M113.543439

Watrin, E., Demidova, M., Watrin, T., Hu, Z., Prigent, C., 2014. Sororin pre-mRNA splicing is required for proper sister chromatid cohesion in human cells. EMBO Rep. 1–8. doi:10.15252/embr.201438640

Wolbank, S., Stadler, G., Peterbauer, A., Gillich, A., Karbiener, M., Streubel, B., Wieser, M., Katinger, H., van Griensven, M., Redl, H., Gabriel, C., Grillari, J., Grillari-Voglauer, R., 2009. Telomerase immortalized human amnion- and adipose-derived mesenchymal stem cells: maintenance of differentiation and immunomodulatory characteristics. Tissue Eng. Part A 15, 1843–1854. doi:10.1089/ten.tea.2008.0205

Yin, J., Zhang, Y.A., Liu, T.T., Zhu, J.M., Shen, X.Z., 2014. DNA damage induces down-regulation of prp19 via impairing prp19 stability in hepatocellular carcinoma cells. PLoS One 9. doi:10.1371/journal.pone.0089976

Zhang, H.H., Huang, J., D??vel, K., Boback, B., Wu, S., Squillance, R.M., Wu, C.L., Manning, B.D., 2009. Insulin stimulates adipogenesis through the Akt-TSC2-mTORC1 pathway. PLoS One 4. doi:10.1371/journal.pone.0006189

Zhang, N., Kaur, R., Lu, X., Shen, X., Li, L., Legerski, R.J., 2005a. The Pso4 mRNA splicing and DNA repair complex interacts with WRN for processing of DNA interstrand cross-links. J. Biol. Chem. 280, 40559–40567. doi:10.1074/jbc.M508453200

Zhang, N., Kaur, R., Lu, X., Shen, X., Li, L., Legerski, R.J., 2005b. The Pso4 mRNA splicing and DNA repair complex interacts with WRN for processing of DNA interstrand cross-links. J. Biol. Chem. 280, 40559–40567. doi:10.1074/jbc.M508453200

7. Figures and legends.

Figure 1. Expression of SNEV $^{hPrp19/hPso4}$ is induced during adipogenesis

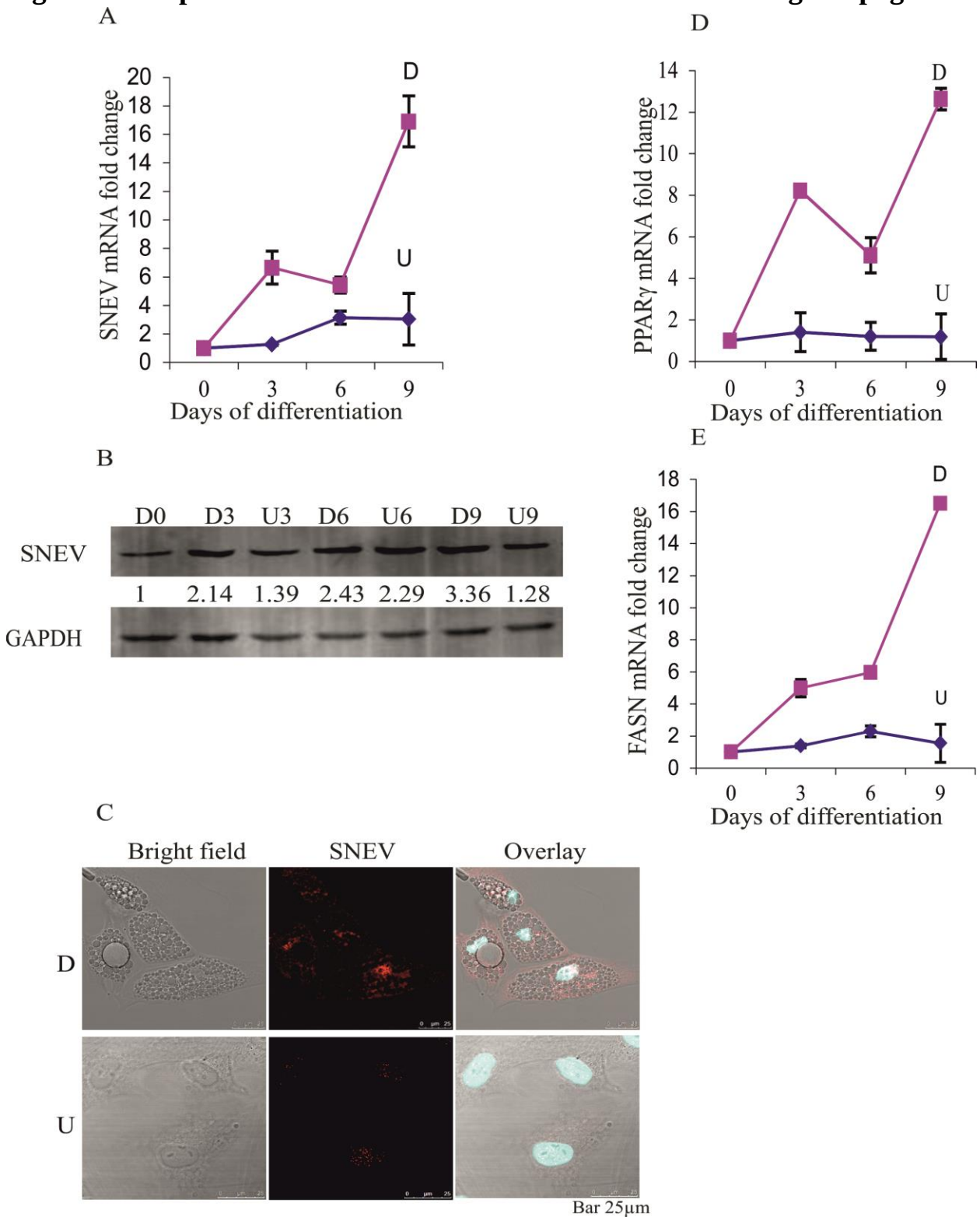

Figure 1. Expression of SNEV $^{hPrp19/hPso4}$ is induced during adipogenesis.

(A) Total RNA isolated from differentiated and undifferentiated hASCs were subjected to qPCR for quantitation of SNEV$^{hPrp19/hPso4}$. The data were normalized to GAPDH. D represents differentiated and U undifferentiated cells and numbers represent the day of harvesting RNA. (B) hASCs differentiated (D) and undifferentiated (U) at various time points were harvested and whole cell lysate were prepared for Western blotting. GAPDH was used to ensure equal amount of protein loading. Numbers represent intensities of bands, normalized to GAPDH. (C) Differentiated and (D) undifferentiated (U) hASCs were fixed on day 10 and stained with anti SNEV $^{hPrp19/hPso4}$ antibody (red) and DAPI (blue). Images were taken by Leica SP5 II laser scanning confocal microscope. Scale bar = 25μM. (D, E) Quantification of adipogenic differentiation was performed using PPARγ (D) and FASN (E) as marker mRNAs. Data shown here is a representative of three independent experiments from 3 different donors (n=3).

Figure 2. Knock-down of SNEV $^{hPrp19/hPso4}$ inhibit adipogenic differentiation in hASCs.

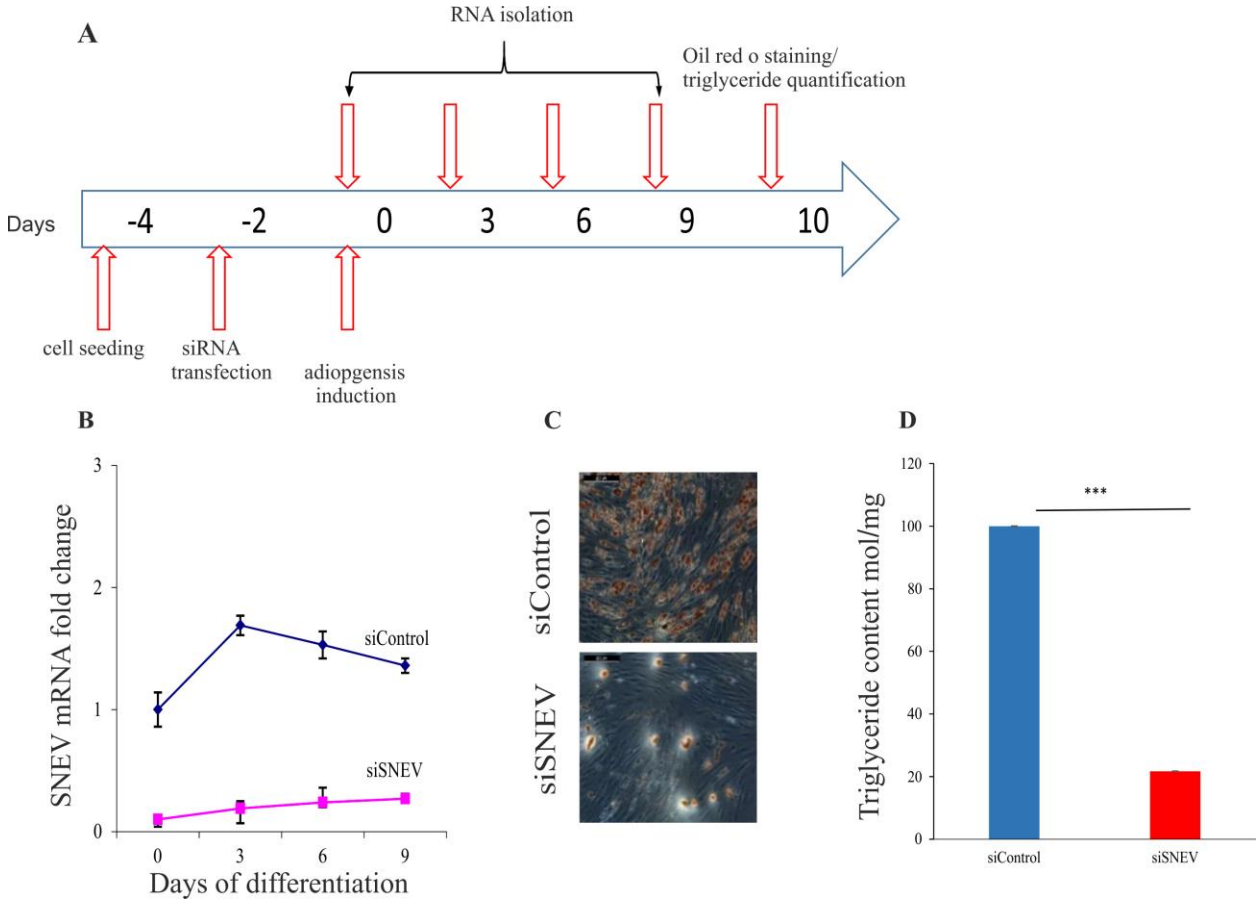

Figure 2. Knock-down of SNEV $^{hPrp19/hPso4}$ inhibits adipogenic differentiation in hASCs.

(A) Schematic representation of experimental design, where hASCs were transfected with siRNA against SNEV$^{hPrp19/hPso4}$ (siSNEV) or with control siRNA (siControl) to down-regulate SNEV$^{hPrp19/hPso4}$ and then induced to differentiate. Total RNA isolated at specified time points was subjected to qPCR analysis. (B) mRNA expression of SNEV$^{hPrp19/hPso4}$ during adipogenic differentiation. Data shown are representative of three independent experiments and were normalized to GAPDH mRNA (*P<0.01; **P<0.001). (C) Oil red O staining for triglyceride content in transfected hASCs after 10 days of differentiation. (D) Intracellular triglyceride levels in transfected hASCs after 10 days of differentiation. Triglyceride content was normalized to total protein content. Data shown is a representative of two independent experiments performed in quadruplicates (*P<0.01; ***P<0.0001).

Figure 3. Knock-down of SNEV $^{hPrp19/hPso4}$ reduces the mRNA expression levels of pro-adipogenic and increases anti-adipogenic pathways.

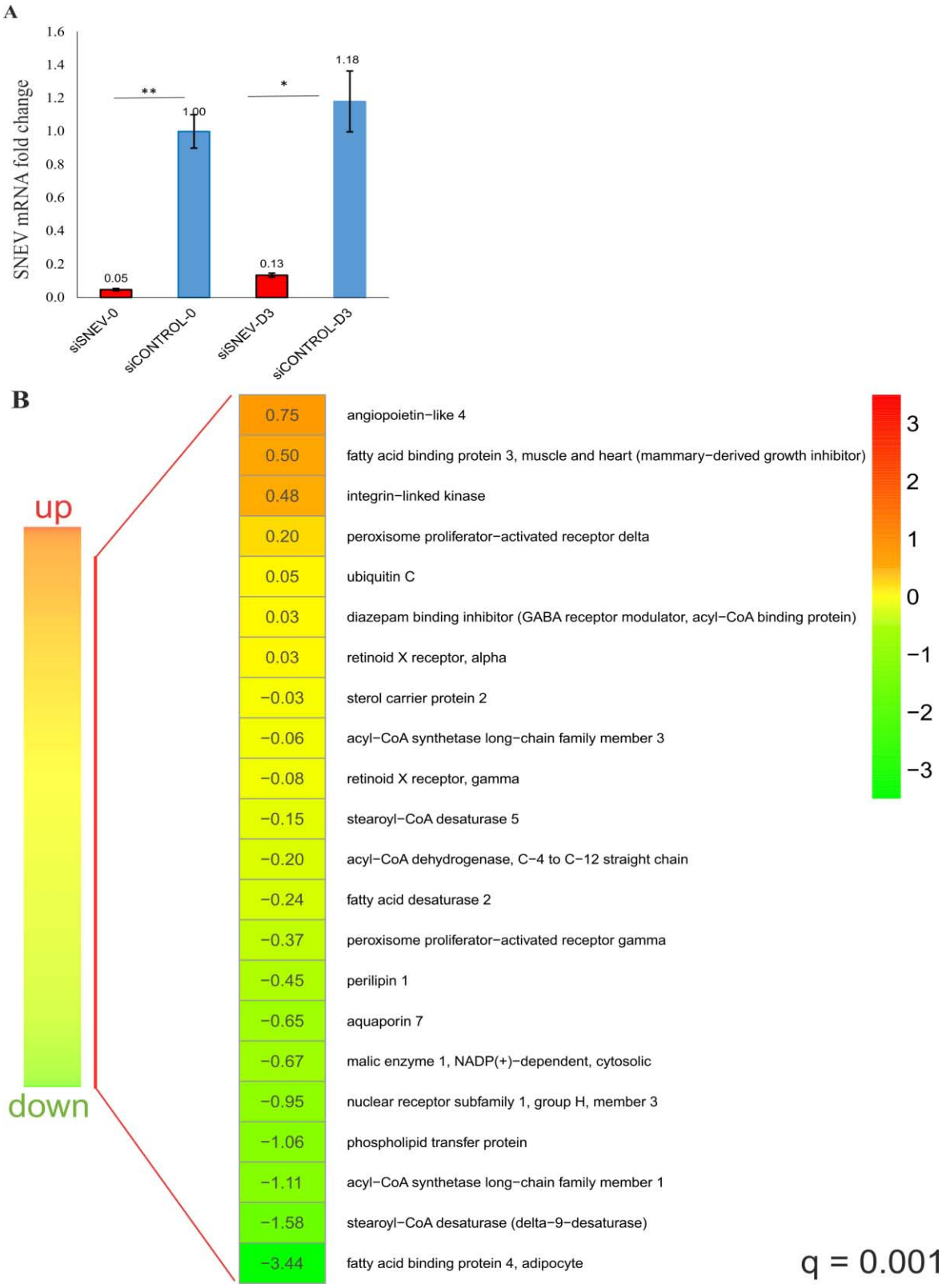

C


up
down
0.56 thyroid hormone receptor interactor 10
0.55 protein phosphatase 1, catalytic subunit, alpha isoyme
0.51 glycogen synthase kinase 3 beta
0.47 calmodulin 3 (phosphorylase kinase, delta)
0.46 v−akt murine thymoma viral oncogene homolog 1
0.44 mitogen−activated protein kinase 9
0.41 insulin receptor substrate 1
0.36 protein phosphatase 1, regulatory (inhibitor) subunit 3D
0.26 protein kinase, cAMP−dependent, regulatory, type I, alpha (tissue specific extinguisher 1)
0.22 protein kinase, AMP−activated, gamma 1 non−catalytic subunit
0.20 flotillin 1
0.18 protein kinase, AMP−activated, alpha 1 catalytic subunit
0.06 as homolog enriched in brain
0.05 protein kinase, cAMP−dependent, catalytic, gamma
0.03 phosphoinositide−3−kinase, regulatory subunit 1 (alpha)
0.00 hexokinase 2
−0.04 inositol polyphosphate−5−phosphatase K
−0.11 son of sevenless homolog 1 (Drosophila)
−0.12 glycogen synthase 1 (muscle)
−0.13 protein kinase, X−linked
−0.14 mitogen−activated protein kinase kinase 2
−0.14 protein kinase, AMP−activated, gamma 3 non−catalytic subunit
−0.14 eukaryotic translation initiation factor 4E
−0.16 mitogen−activated protein kinase 8
−0.21 inositol polyphosphate−5−phosphatase, 145kDa
−0.29 phosphorylase, glycogen, liver
−0.39 eukaryotic translation initiation factor 4E binding protein 1
−0.58 SHC (Src homology 2 domain containing) transforming protein 1
−0.60 ras homolog gene family, member Q
−0.62 acetyl−CoA carboxylase beta
−0.69 insulin
−0.72 protein phosphatase 1, catalytic subunit, gamma isoyme
−0.76 sterol regulatory element binding transcription factor 1
−0.88 sterol regulatory element binding transcription factor 1
−1.01 ribosomal protein S6
−1.93 phosphorylase, glycogen brain
−2.21 fatty acid synthase
3
2
1
0
−1
−2
−3
q = 0.025

D

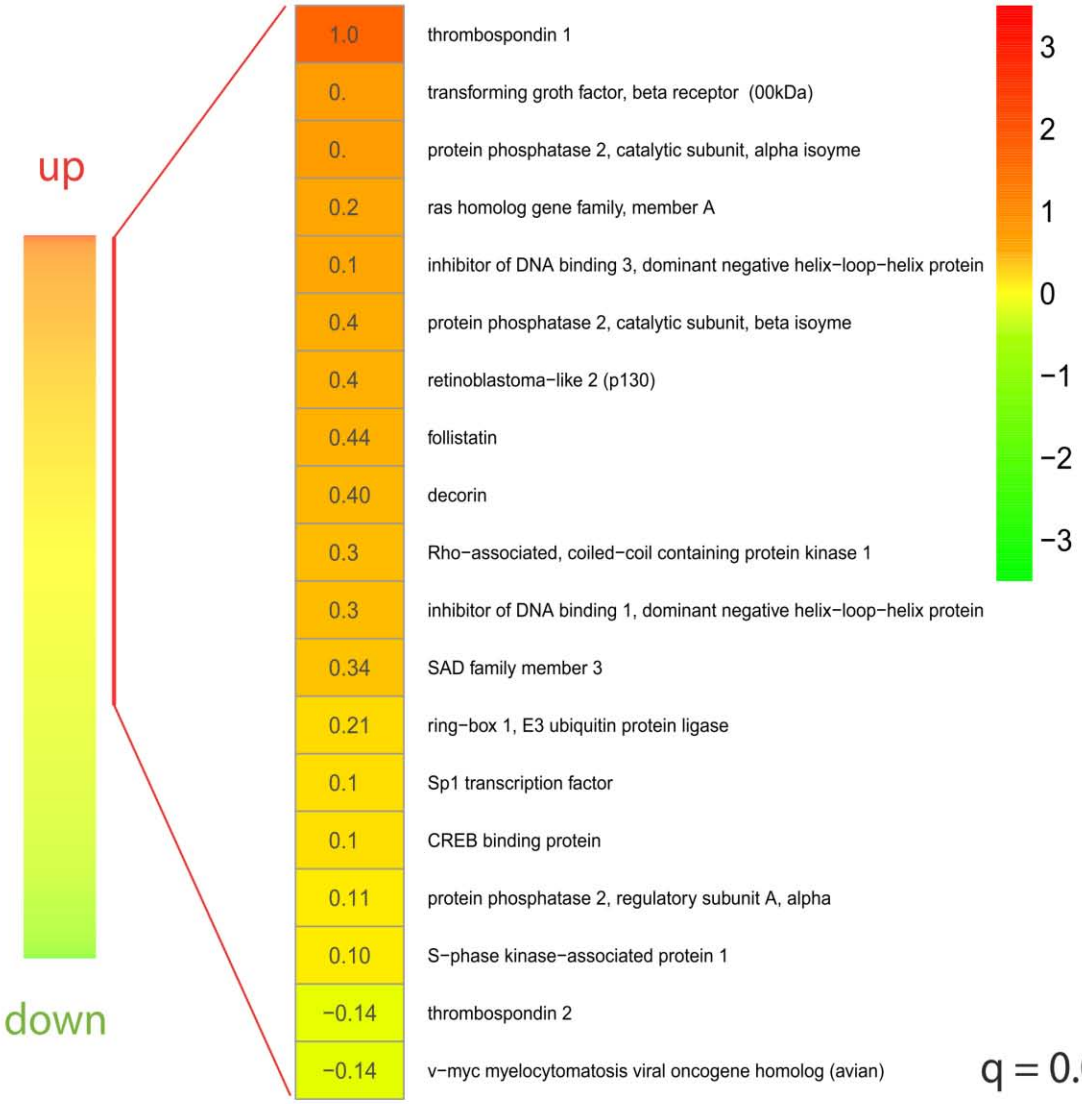
up
down
1.0
0.
0.
0.2
0.1
0.4
0.4
0.44
0.40
0.3
0.3
0.34
0.21
0.1
0.1
0.11
0.10
−0.14
−0.14
thrombospondin 1
transforming groth factor, beta receptor (00kDa)
protein phosphatase 2, catalytic subunit, alpha isoyme
ras homolog gene family, member A
inhibitor of DNA binding 3, dominant negative helix−loop−helix protein
protein phosphatase 2, catalytic subunit, beta isoyme
retinoblastoma−like 2 (p130)
follistatin
decorin
Rho−associated, coiled−coil containing protein kinase 1
inhibitor of DNA binding 1, dominant negative helix−loop−helix protein
SAD family member 3
ring−box 1, E3 ubiquitin protein ligase
Sp1 transcription factor
CREB binding protein
protein phosphatase 2, regulatory subunit A, alpha
S−phase kinase−associated protein 1
thrombospondin 2
v−myc myelocytomatosis viral oncogene homolog (avian)
3
2
1
0
−1
−2
−3

q = 0.008

E

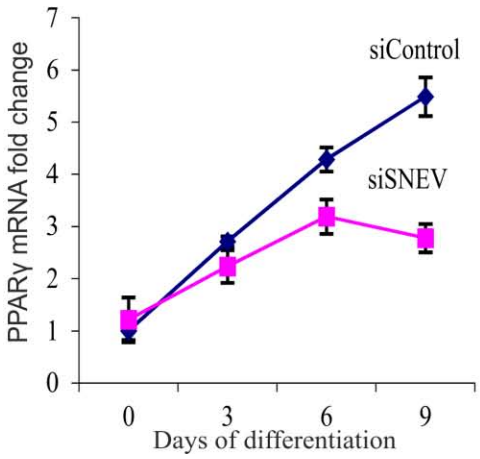
PPARγ mRNA fold change
siControl
siSNEV
Days of differentiation
0
1
2
3
4
5
6
7
0
3
6
9

F

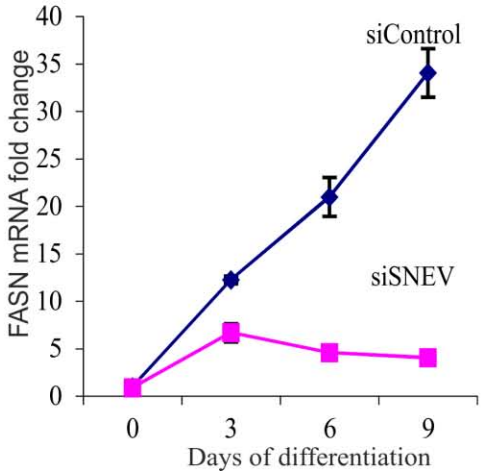
FASN mRNA fold change
siControl
siSNEV
Days of differentiation
0
5
10
15
20
25
30
35
40
0
3
6
9

Figure 3. Knock-down of SNEV$^{hPrp19/hPso4}$ reduces the expression of adipogenic markers.

(A) mRNA expression of SNEV$^{hPrp19/hPso4}$ in hASCs transfected with siRNA against SNEV$^{hPrp19/hPso4}$ (siSNEV) or with control siRNA (siControl) and induced to differentiate for 9 days. Total RNA was isolated and subjected to qPCR. D represent differentiated and U undifferentiated cells and numbers represent day of harvesting. (B) Micro-array based analysis of transcript expression assorted to the KEGG PPARγ signaling pathway is shown as heat map after GSEA. (C) Expression of transcripts assorted to the KEGG insulin signaling pathway is shown as heat map. (D) Expression of transcripts assorted to the KEGG TGF-β signaling pathway is shown as heat map. Numbers within cells are log2-transformed expression ratios (siSNEV /siControl). The red vertical line denotes the range of this gene set relative to all 3250 transcripts that could be detected (small heat map). FDR q-value obtained from GSEA is depicted bottom right. (E) qPCR analysis of PPARγ and (F) FASN confirming the microarray data. The data shown here is a representative of two independent experiments (n=2).

Figure 4. SNEV $^{hPrp19/hPso4}$ over expression accelerate adipogenesis in hASCs.

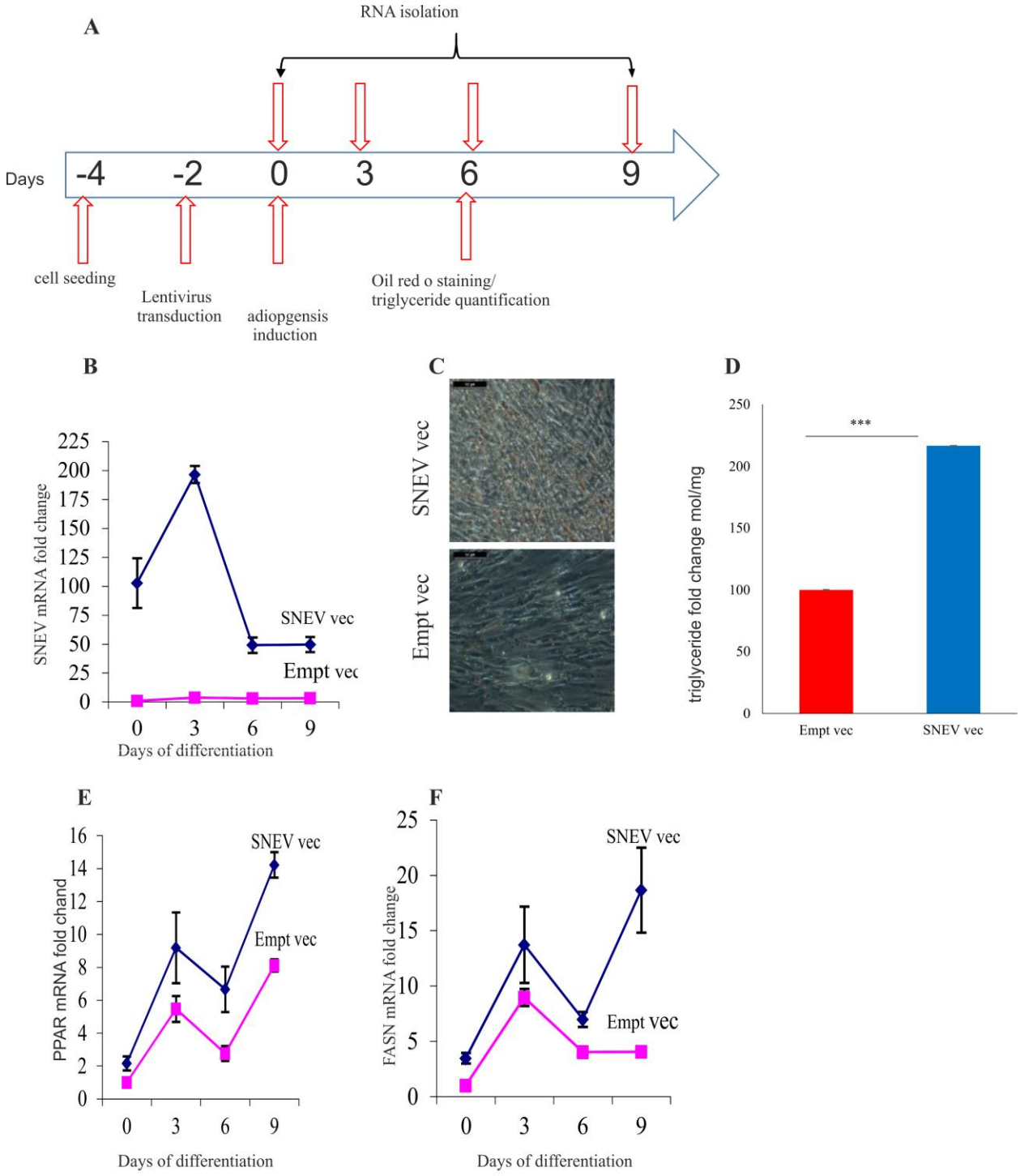

Figure 4. SNEV $^{hPrp19/hPso4}$ over-expression accelerates adipogenesis in hASCs.

(A) Schematic representation of experimental design. hASCs were transduced with SNEV$^{hPrp19/hPso4}$ or empty vector and were sequentially differentiated for 10 days. (B) Total RNA isolated at specified time points was subjected to qPCR to analyze SNEV$^{hPrp19/hPso4}$ mRNA levels. Data shown here is a representative of 3 independent experiments and was normalized to GAPDH. (C) Oil red O staining of intracellular lipids after 6 days of differentiation. (D) Intracellular triglyceride levels in transduced hASCs after 6 days of differentiation. Triglyceride contents were normalized to total protein contents. (E) Quantitation of PPARγ and (F) FASN mRNA. Data shown is a representative of three independent experiments (*P<0.01; ***P<0.0001).

Figure 5. Loss of Werner (WRN) reduced adipogenic differentiation in hASCs.

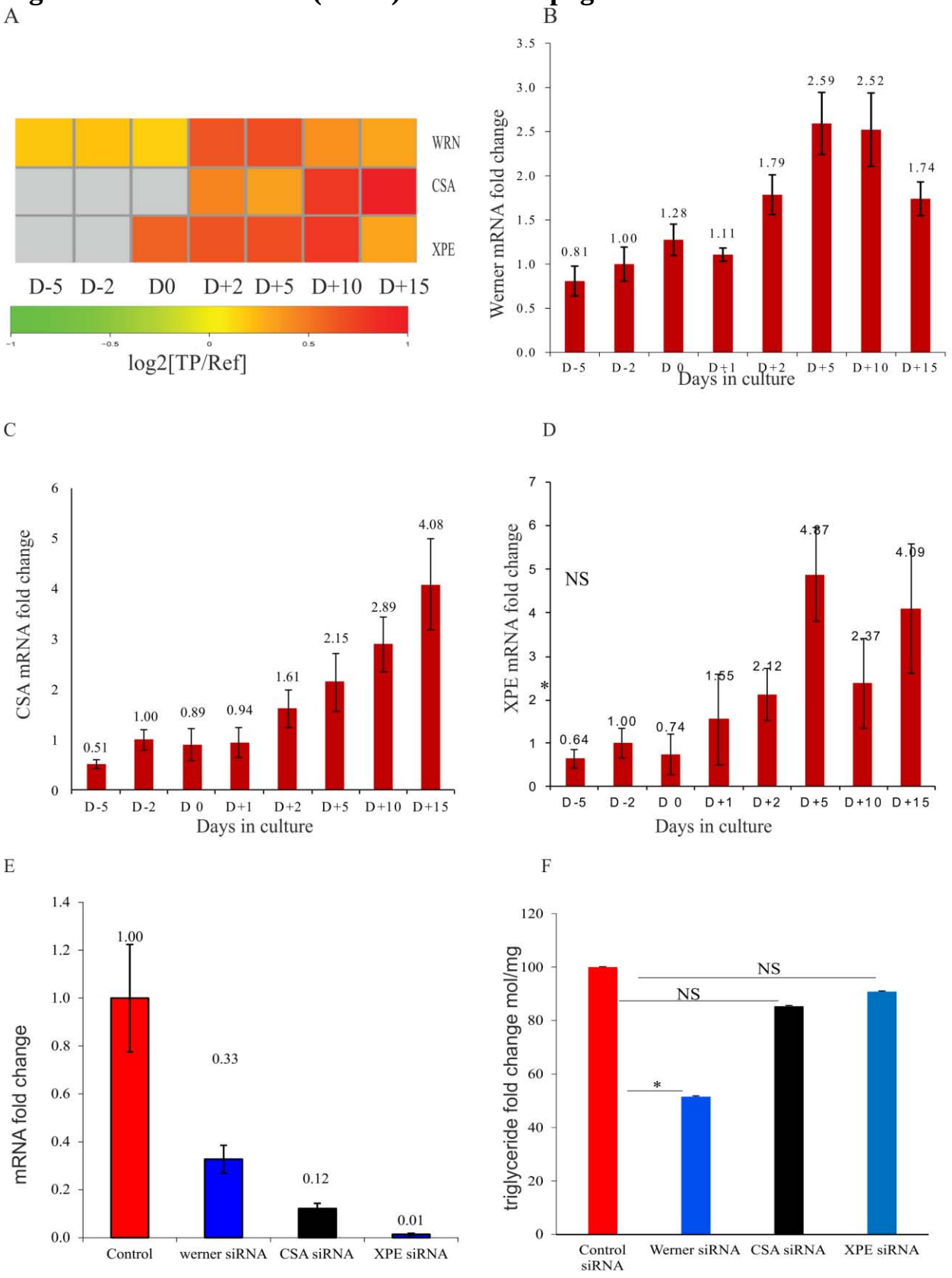

Figure 5. Knock-down of WRN, CSA and XPE reduces adipogenic differentiation in hASCs.

(A) Heat map of differentially transcribed genes during adipogenesis is shown. Fold changes were calculated at reference day -2. mRNA fold change of (B) WRN, (C) CSA, and (D) XPE, during adipogenic differentiation are shown. (E) Knock-down of WRN, CSA, XPE mRNAs was confirmed by qPCR as compared to siControl and normalized to GAPDH. The data shown here is a representative of two independent experiments. (F) Triglyceride content was quantified at day 10 of adipogenic differentiation and normalized to total protein content.

Figure 6.

Loss of SNEV$^{hPrp19/hPso4}$ reduced and Werner Fat deposition in C. elegans.

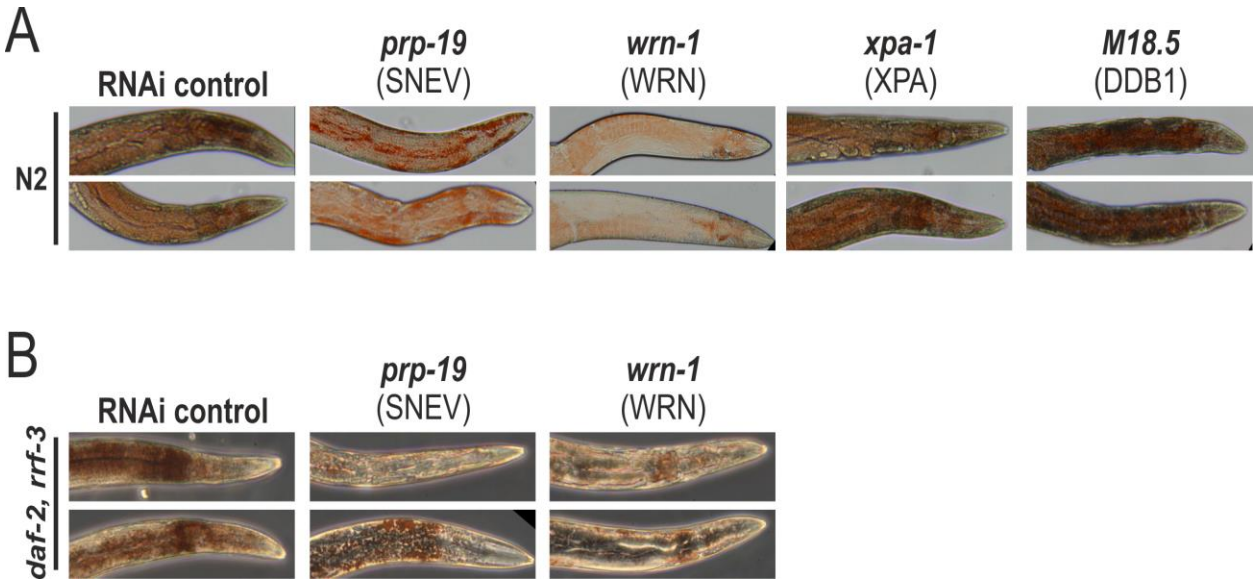

Figure 6. Loss of SNEV$^{hPrp19/hPso4}$ and WRN reduces fat deposition in *C. elegans*.

(A) Depletion of *prp-19*, *wrn-1*, *xpa-1* and *M18.5* by RNAi in wild-type *C. elegans*, followed by Oil Red O staining demonstrates lower fat deposition upon *prp-19* and *wrn-1*RNAi, compared to the empty vector (HT115) control. Representative images of two biological replicates with at least 20 worms per strain are shown. (B) RNAi to *prp-19* and *wrn-1* in the high-fat and RNAi hypersensitive CF1841strain, followed by Oil Red O staining confirms lower fat deposition compared to the empty vector control. Representative images of two biological replicates with at least 20 worms per strain are shown.

Supplementary figure.

Supplementary Figure 1. Down regulation of SNEV$^{hPrp19/hPso4}$ does not influence osteogenic differentiation.

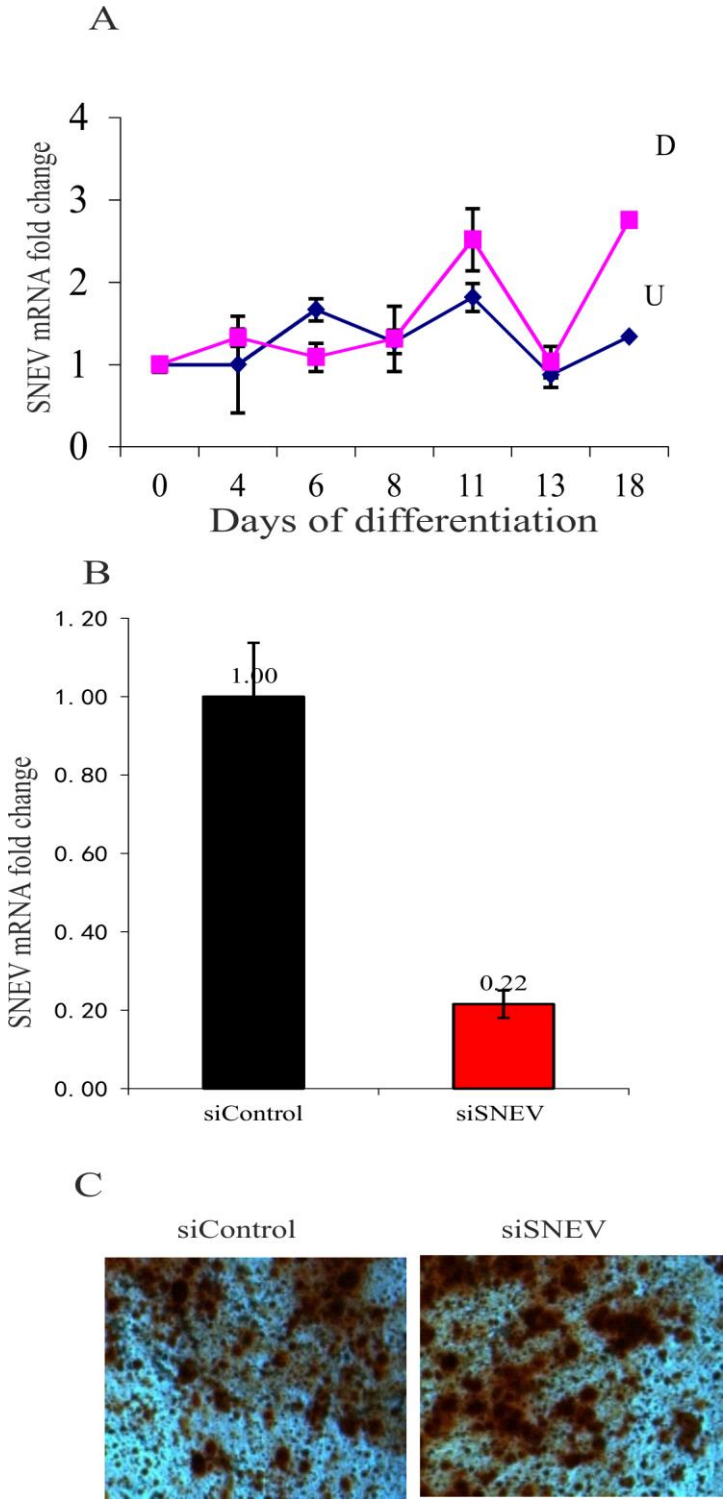

Supplementary figure 1. Down-regulation of SNEV$^{hPrp19/hPso4}$ does not influence osteogenic differentiation.

hASCs were seeded 72 hours before initiation of osteogenic differentiation. Total RNA was isolated at indicated time points and subjected to qPCR analysis. (A) SNEV$^{hPrp19/hPso4}$ mRNA fold change during osteogenic differentiation. Fold changes were calculated in reference to un-differentiated cells at day 0 and normalized to GAPDH. D and U represent differentiated and undifferentiated cells, respectively. (B) SNEV $^{hPrp19/hPso4}$ mRNA fold changes after siRNA SNEV $^{hPrp19/hPso4}$ and control siRNA transfection. Fold changes were calculated in reference to siRNA control transfected cells and normalized to GAPDH. (C) Alizarin red staining of hASCs transfected with siRNA SNEV and control siRNA followed by osteogenic differentiation for 12 days, representative images are shown. Data shown here is performed once.

Supplementary table 1.

Primers pairs used for mRNA expression analysis by qPCR.

Supplementary Table 1- primer pairs used for mRNA analysis by qPCR.

Gene name	Forward primer	Reverse primer
SNEV	TCATTGCCCGTCTCACCAAG	GGCACAGTCTTCCCTCTCTTC
PPARγ	AGCCTGCGAAAGCCTTTTGGTGA	GCAGTAGCTGCACGTGTTCCGT
FASN	AACTTGCAGGAGTTCTGGGAC	TGAATCTGGGTTGATGCCTCCG
GAPDH	TGTGAGGAGGGGAGATTCAG	CGACCACTTTGTCAAGCTCA
Werner	GTGGCGCTCCACAGTCAT	TCTTCCGAACACATGCCTTTC
CSA	GAGGACACGATATGCTGGGG	CCAGTCCCAAAACTCTCCGT
XPE	AAGAAACGCCCAGAAACCCA	ACATCTTCTGCTAGGACCGGA

Appendix C

Delineation of the Key Aspects in the Regulation of Epithelial Monolayer Formation

MCB
Journals.ASM.org

Delineation of the Key Aspects in the Regulation of Epithelial Monolayer Formation

Lydia Aschauer,[a] Leonhard N. Gruber,[a] Walter Pfaller,[a] Alice Limonciel,[a] Toby J. Athersuch,[b,c] Rachel Cavill,[b] Abdulhameed Khan,[d] Gerhard Gstraunthaler,[a] Johannes Grillari,[d,f] Regina Grillari,[d,f] Philip Hewitt,[e] Martin O. Leonard,[g] Anja Wilmes,[a] Paul Jennings[a]

Division of Physiology, Department of Physiology and Medical Physics, Innsbruck Medical University, Innsbruck, Austria[a]; Section of Biomolecular Medicine, Department of Surgery and Cancer, Faculty of Medicine, Imperial College London, London, United Kingdom[b]; MRC-HPA Centre for Environment and Health, Department of Epidemiology and Biostatistics, School of Public Health, Faculty of Medicine, Imperial College London, London, United Kingdom[c]; Institute of Applied Microbiology, Department of Biotechnology, University of Natural Resources and Life Sciences Vienna, Vienna, Austria[d]; Merck KGaA, Merck Serono, Toxicology, Darmstadt, Germany[e]; Evercyte GmbH, Vienna, Austria[f]; School of Medicine and Medical Science, and Conway Institute of Biomolecular and Biomedical Research, University College Dublin, Belfield, Dublin, Ireland[g]

The formation, maintenance, and repair of epithelial barriers are of critical importance for whole-body homeostasis. However, the molecular events involved in epithelial tissue maturation are not fully established. To this end, we investigated the molecular processes involved in renal epithelial proximal-tubule monolayer maturation utilizing transcriptomic, metabolomic, and functional parameters. We uncovered profound dynamic alterations in transcriptional regulation, energy metabolism, and nutrient utilization over the maturation process. Proliferating cells exhibited high glycolytic rates and high transcript levels for fatty acid synthesis genes (*FASN*), whereas matured cells had low glycolytic rates, increased oxidative capacity, and preferentially expressed genes for beta oxidation. There were dynamic alterations in the expression and localization of several adherens (CDH1, -4, and -16) and tight junction (TJP3 and CLDN2 and -10) proteins. Genes involved in differentiated proximal-tubule function, cilium biogenesis (*BBS1*), and transport (*ATP1A1* and *ATP1B1*) exhibited increased expression during epithelial maturation. Using TransAM transcription factor activity assays, we could demonstrate that p53 and FOXO1 were highly active in matured cells, whereas HIF1A and c-MYC were highly active in proliferating cells. The data presented here will be invaluable in the further delineation of the complex dynamic cellular processes involved in epithelial cell regulation.

The primary function of epithelial cells is to form a selective barrier between two adjacent compartments. However, epithelial cells are not merely barriers but possess many other functions qualifying them as one of the most diverse group of cells in the human body. Epithelial cells can be considered the body's regulators, functioning in concert to allow precise homeostatic regulation. The loss of regulated epithelial function gives rise to many disease states, including chronic inflammation, fibrosis (leading to end-stage organ failure), and cancer. Indeed, the vast majority of all diagnosed cancers are of epithelial origin (termed carcinomas). In recent years, the use of epithelial cell cultures has allowed detailed studies of many cellular and molecular aspects of epithelial cell physiology and pathophysiology.

In the kidney alone, more than 12 morphologically distinct types of epithelial cells have been described (1). The proximal tubule is the main site of reabsorption in the nephron and is considered a "leaky" epithelium due to the expression of pore-forming claudins 2 and 10 in the tight junctions (2). The high transport rates of the proximal tubule are driven primarily by the Na^+/K^+ ATPase, creating a high energy demand that is predominantly fulfilled by oxidative metabolism (3). In addition, this part of the nephron is one of the areas most sensitive to chemical and ischemic injury (4–6).

The formation, maintenance, and repair of epithelial barriers are of critical importance for the maintenance of whole-body homeostasis and thus are very tightly regulated processes. Generally, the processes involved in epithelial proliferation are the opposite of those required for cell differentiation (7). Both states involve the sensing of the external environment, providing the cell with critical information pertaining to orientation, neighboring cells, and tissue density. These signals are relayed to the nucleus to activate transcription and alter processes involved in energy metabolism (8), differentiated function (7), proliferation (9), and motility (10). Tight and adherens junctions exert central control in the regulation of cell-to-cell contact and tissue density (11, 12). A low number of intercellular interactions favors epithelial cell proliferation, whereas a high density of intercellular contacts halts proliferation and promotes differentiation, allowing the establishment of specific tissue functions.

The transition of epithelial cells from proliferating, highly energy-consuming cells to a mature transporting epithelium is complex, involving the simultaneous activation and inactivation of several distinct pathways. In order to characterize these processes at a molecular level, we used a simple cell culture system where renal epithelial cells were seeded at low density in culture dishes. Primary human proximal-tubule cells and a telomerase-immortalized human proximal-tubule cell line (RPTEC/TERT1) were studied over a maturation process of 16 days. Transcriptomics and metabolomics were used to investigate the processes involved in epithelial monolayer maturation.

Received 23 October 2012 **Returned for modification** 24 December 2012
Accepted 10 April 2013
Published ahead of print 22 April 2013
Address correspondence to Paul Jennings, paul.jennings@i-med.ac.at.

doi:10.1128/MCB.01435-12

MATERIALS AND METHODS

All chemicals were purchased from Sigma-Aldrich unless otherwise stated.

Cell culture. Human primary proximal-tubule cells were prepared as previously described (13). Both primary and RPTEC/TERT1 (14) cells were cultured in hormonally defined medium that consisted of a 1:1 mixture of Dulbecco's modified Eagle's medium (DMEM; catalog no. 11966; Invitrogen) and Ham's F-12 nutrient mix (catalog no. 21765; Invitrogen) supplemented with 2 mM Glutamax (Invitrogen), 5 μg/ml insulin, 5 μg/ml transferrin, 5 ng/ml sodium selenite, 100 U/ml penicillin, 100 μg/ml streptomycin, 10 ng/ml epithelial growth factor, and 36 ng/ml hydrocortisone. Routinely, cells were cultured in 10-cm dishes (Sarstedt) at 37°C in a 5% CO_2 humidified atmosphere and subcultured by trypsinization. Medium was replaced three times per week, and the volumes were 2 ml for 6 wells, 10 ml for 10-cm dishes, and 1 ml for coverslips. RPTEC/TERT1 cells were used at passages 76 to 100. Primary cells were used at passage 3.

For studying epithelial monolayer formation, cells were freshly seeded to a density of 30% surface area and followed over the following 16-day interval. Medium was replaced every day.

Transcriptomic and array analysis. Cells were cultured on 6-well plates, and RNA was isolated by cell lysis in RLT buffer (Qiagen) containing 1% (vol/vol) β-mercaptoethanol and further processed with a Qiagen RNeasy Protect cell minikit. For the synthesis of biotinylated cRNA, a MessageAmp II aRNA amplification kit (Ambion Inc.) with several modifications (15) was applied using the Theonyx automatic pipetting robot (Aviso GmbH). To optimize the cleanup, the Agencourt RNAClean (Beckman Coulter) method was used instead of a column-based method. RNA quality was controlled using a 28S/18S ratio with an Agilent Bioanalyzer 2100, and the RNA quantity was assessed with a NanoDrop (Thermo Fisher Scientific) ND-1000 photometer before processing. Amplified biotin-labeled cRNA (750 ng) was hybridized in a hybridization chamber for 20 h at 58°C on Illumina human HT12 v3 BeadChips, which assay 48,802 probes per sample. Afterwards, the chips were washed and stained with 1 μg/ml streptavidin-conjugated Cy3 (Amersham Biosciences). Chips were then dried by centrifugation, and fluorescence was detected by confocal laser scanning with an Illumina bead array reader (Illumina) at 532 nm and a 0.8-μm resolution. Using Illumina BeadStudio software, the data from all beads with the same probe were condensed to one value and further to ensure array quality based on different control bead parameters. Quantile normalization was applied to remove nonbiological variance between arrays (16).

Selection of significantly deregulated genes and cluster analysis of the unsupervised samples were performed using BRB ArrayTools (version 4) (17). Hierarchical clustering of samples using centered correlation and average linkage was carried out, and samples demonstrating a correlation lower than 0.5 to their biological replicates were considered outliers and excluded from further analysis (three primary-cell samples). A class comparison was conducted between all time points within each cell model with a cutoff of 1.5-fold change and a significance level for P of <0.001 for the univariate test. The $\log_2$ fold change value of the differentially expressed probes (DEP) is represented here as the ratio of the value at the later time point to that at the earlier time point. DEPs from the RPTEC/TERT1 and primary-cell data sets were intersected according to direction of change. Thus, only DEPs that changed in the same direction in both cell models were used for further analysis. The combined list (1,630 DEPs) was then subjected to a time course analysis in BRB ArrayTools with a threshold false discovery rate of 0.01. The expression values of the resulting 1390 DEPs were normalized by "mean centering" (expression values of each probe were divided by the mean expression of that probe over all time points within each cell model). Heat maps were generated using TreeView (http://rana.lbl.gov/EisenSoftware.htm). Where multiple probes existed for the same gene, the probe with the highest variance across the RPTEC/TERT1 time course was chosen. Finally, a list of 1,238 differently expressed genes (DEG) reflecting gene alterations during the time course of monolayer formation was generated.

TABLE 1 qPCR primer sequences

Gene symbol	Forward primer	Reverse primer
ATP1A1	GGGAGCTGCTCTGTGCTTTT	CTTATCACGTCCAACCCCCT
ATP1B1	GCTTATCACGTCCAACCCCCT	GGCACATCGCCACAATCTTC
BBOX1	ACCTTCAAGATGAATCCAGGTGA	GACCACATCCCAGTCAGCAT
BBS1	GTCCCCGTCTTCCTAGAGGT	GGGGTGCTTGGAGTCTCTTC
CDKN1A	GGCGGCAGACCAGCATGACAGATT	GCAGGGGGCGGCCAGGGTAT
CDC25A	TCGTCTGAAGAAGCTCTGAGG	CCCTCTCCAAATGTCACACA
FASN	GATGACCGTCGCTGGAAGG	AATCTGGGTTGATGCCTCCG

Quantitative real-time PCR (qPCR). At 1, 7, and 16 days after seeding, RNA was harvested from RPTEC/TERT1 cells on 10-cm dishes as described above. cDNA was synthesized from 500 ng of total RNA using a Dynamo cDNA synthesis kit (Biozyme). qPCRs were performed using 5× HOT FIREPol EvaGreen qPCR Mix Plus (Medibena) on a Rotor-Gene Q (Qiagen) according to the manufacturer's protocol. Three biological samples were analyzed with 4 technical replicates each. A standard curve was generated using a dilution series of a reference RPTEC/TERT1 sample. Primer pairs used for amplification of the target genes are given in Table 1.

Transcription factor (TF) prediction analysis. The complete list of 1,390 DEPs and their mean-centered expression values were uploaded into Ingenuity Pathway Analysis (IPA) version 9.0 (1,353 mapped genes; in cases of multiple probes for one gene, the probe with the maximum absolute $\log_2$ ratio was used, and for prediction of TF activation, direct and indirect relationships were considered where confidence at an experimental level was available), which includes a TF analysis feature. TF analysis computes an overlap P value (Fisher's exact test) assessing whether there is a statistically significant overlap between the genes in the data set and the genes that are regulated by a TF. The activation state of the TF is predicted by a second parameter, the z score, that reflects the expected causal effects between a TF and its targets based on the expression direction of the genes in the data set regulated by the given TF. A z score greater than 2 predicts significant activation and a score lower than -2 points to an inhibition of the given TF. For the refined selection of TFs, only TFs with an overlap P value of ≤ 0.001, a z score of ≥ 2 or ≤ -2 at least at one time point in both cell models and more than 10 altered target molecules were considered.

Transcription factor activity assays. Nuclear extracts from RPTEC/TERT1 cells cultured in 10-cm dishes at 1 day (subconfluent) and 16 days (matured) after seeding were washed and scraped into ice-cold hypotonic buffer [10 mM HEPES-NaOH, pH 7.9, containing 10 mM KCl, 0.1 mM EDTA, 0.1 mM EGTA, 1 mM dithiothreitol (DTT), 1 mM phenylmethylsulfonyl fluoride (PMSF), protease inhibitor cocktail (catalog no. P8340; Sigma), phosphatase inhibitor cocktail (catalog no. P0044; Sigma), and 2 mM activated Na_3VO_4]. The cell suspensions were incubated for 20 min on ice, and then 10% (vol/vol; final concentration, 0.58%) Igepal CA-630 was added to lyse the cells. Samples were centrifuged at 21,000 × g for 1 min, and the resulting pellets were resuspended in high-salt buffer [20 mM HEPES-NaOH, pH 7.9, containing 400 mM NaCl, 1 mM EDTA, 1 mM EGTA, 10% (vol/vol) glycerol, 1 mM DTT, 1 mM PMSF, protease inhibitor cocktail, phosphatase inhibitor cocktail and 2 mM activated Na_3VO_4]. Samples were incubated for 30 min on ice with periodic vortexing and were subsequently centrifuged at 21,000 × g for 10 min at 4°C. The resulting supernatants were removed as the nuclear extracts. The protein content of nuclear extracts of RPTEC/TERT1 cells was measured using the bicinchoninic acid (BCA) method according to the manufacturer's protocol (Pierce, Thermo Scientific). For the assays of TP53, FOXO1, and c-MYC, 20 μg nuclear extract per well was used, and for HIF1A, 30 μg nuclear extract per well was used. Levels of transcriptionally active TP53, HIF1A, FOXO1, and c-MYC were determined by using TransAM transcription factor enzyme-linked immunosorbent assays (ELISAs) (Active Motif) according to the manufacturer's protocol.

Cell cycle analysis. At indicated time points, RPTEC/TERT1 cells cultured on 6-well plates, were washed twice in phosphate-buffered saline (PBS) and harvested using 1 ml phenol red-free 5% (wt/vol) trypsin–2% (wt/vol) EDTA solution per well after prolonged incubation at 37°C. Cell pellets were washed three times with ice-cold PBS and fixed in 100% ice-cold methanol. The fixed cells were stored at 4°C until analysis. On the day of analysis, cells were washed thrice with ice-cold PBS and stained with propidium iodide (PI)-RNase staining buffer (5 μg/ml PI, 200 μg/ml RNase) (Becton, Dickinson Biosciences). Cell cycle distribution was assessed using a Becton, Dickinson FACScan (Becton, Dickinson Biosciences) and BD Cell Quest Pro 4.0.2 software (25 000 positive hits, custom inclusion criteria). The data were then analyzed using BD ModFit.

Glycolysis and glycogen measurements. Lactate was measured in the supernatant medium with a colorimetric assay, as previously described (18). Glucose was measured in the supernatant medium from the same samples using a colorimetric hexokinase-based assay, as previously described (19). Glycogen was measured in methanol extracts by boiling the insoluble fractions in 0.03 N HCl, followed by addition of 10 mM sodium acetate (pH 4.9), incubation of samples with or without amyloglucosidase (24 U/ml, from *Aspergillus niger*; catalog no. 10115; Sigma), and subsequent determination of glucose. Glycogen content was calculated as the difference between glucose levels with and without amyloglucosidase conversion.

^{1}H nuclear magnetic resonance (NMR) spectroscopy and metabolic profile data processing. For ^{1}H NMR spectroscopy, 1 ml of cell culture medium (supernatant) was centrifuged for 5 min at 150 × *g* to remove dead cells and subsequently stored at −80°C to await NMR analysis. ^{1}H NMR spectroscopy and data processing for metabolomic investigation were performed as described by Ellis et al. (20). Briefly, to 550 μl supernatant, 50 μl of D_2O [containing 0.2% (wt/vol) TSP (trimethylsilyl propionate] was added, vortexed, and then centrifuged (13,000 × *g*, 10 min) to remove insoluble material before the mixture was transferred to a clean NMR tube. All reagents were checked prior to sample preparation by obtaining a one-dimensional ^{1}H NMR spectrum to ensure that they contained no contaminants that may interfere with the downstream spectroscopic analysis. CPMG (Carr-Purcell-Meiboom-Gill) spectra were acquired on a 600-MHz Bruker spectrometer for each sample to suppress broad protein peaks. NMR spectroscopic data were imported and manipulated in Matlab (Mathworks) using in-house software written and compiled by T. M. D. Ebbels, H. C. Keun, J. T. Pearce, and R. Cavill. Using this software, the ^{1}H NMR spectra were automatically phased, baseline corrected, and referenced and normalized to the TSP resonance at δ 0.

Immunofluorescence analysis. RPTEC/TERT1 cells were cultured on 18-mm glass coverslips in 24-well plates and fixed in 100% ice-cold methanol for 10 min at −20°C at three states: subconfluent, newly confluent, and as a matured monolayer. Fixed cells were incubated at room temperature in blocking buffer (5% [wt/vol] bovine serum albumin [BSA; Calbiochem, Merck], 1% [vol/vol] Triton X-100 in PBS) for 30 min followed by incubation with primary antibody for 1 h. All antibodies were diluted in antibody diluent in a 1% BSA, 0.2% Triton X-100 PBS solution. Mouse anti-E-cadherin (no. 610182; BD Transduction Laboratories) was used at 0.31 μg/ml, rabbit anti-cadherin 4 (HPA015613; Sigma) at 0.44 μg/ml, rabbit anti-cadherin 16 (Abcam, ab80320) at 10 μg/ml, mouse anti-claudin 2 (no. 32-5600; Invitrogen) at 1.6 μg/ml, rabbit anti-claudin 3 (SAB4500435; Sigma) at 2 μg/ml, rabbit anti-claudin 10 (ab52234; Abcam) at 3.3 μg/ml and rabbit anti-ZO3 (no. 36-4000; Zymed, Invitrogen) at 1.25 μg/ml. Cells were incubated with 2.5 μg/ml of the appropriate Alexa 488-conjugated secondary antibody (no. A11059 and A21206; Invitrogen) for 35 min. Repeated washing with PBS was performed between the incubation steps. Cells were mounted in 3 mg/ml *p*-phenylene-diamine glycerol on a microscope slide and sealed with nail varnish. Fluorescence images were obtained using a Zeiss Axiophot fluorescence microscope mounted with a 63× oil immersion objective (1.4 numerical aperture; Zeiss). Images were captured with a cooled charge-coupled device (CCD) camera (Spot Diagnostics) using Metavue image processing software (Molecular Devices).

Western blot analysis. RPTEC/TERT1 cells were lysed in RIPA buffer including protease inhibitor cocktail (catalog no. 8340; Sigma) and 10 μl/ml phosphatase inhibitor (catalog no. P0044; Sigma) at various time points. Samples were incubated for 30 min on ice and then centrifuged at 8,000 × *g* for 5 min to separate RIPA buffer-soluble and -insoluble fractions. Protein concentrations of the soluble fraction samples were determined by the BCA method according to the manufacturer's protocol (Pierce). The insoluble fraction was resuspended directly in 90 μl Laemmli buffer. Soluble (35 to 40 μg total protein in Laemmli buffer) and insoluble (15 μl of the resuspended pellet) samples were run on 4 to 12% bis-Tris minigels (Invitrogen). Gels for blots of proteins of <40 kDa were run in NuPage MES (morpholineethanesulfonic acid) SDS running buffer and those of proteins of >40 kDa in NuPage MOPS (morpholinepropanesulfonic acid) SDS running buffer (Invitrogen) at 200 V for 35 min and 50 min, respectively. Proteins were transferred onto methanol-activated low-fluorescence Immobilon-P membranes (Millipore, Merck) in 2× NuPage transfer buffer (Invitrogen) containing 20% methanol (for proteins of <40 kDa) or 10% methanol (for proteins of 40 to 110 kDa) for 30 or 60 min, respectively (maximum, 20 V) using a semidry transfer system (Invitrogen). Membranes were blocked in 5% (wt/vol) BSA (Calbiochem)–Tris-buffered saline-Tween (TBST) for 1 h and probed with primary antibodies (2 h at room temperature [RT] or overnight at 4°C). All antibodies were diluted in TBST, except for anti-cadherin 4, anti-cadherin 16, and anti-ZO3, which were diluted in 5% BSA-TBST. Mouse anti-E-cadherin (no. 610182; BD Transduction) was used at 0.1 μg/ml, rabbit anti-cadherin 4 (HPA015613; Sigma) at 0.44 μg/ml, rabbit anti-cadherin 16 (ab80320; Abcam) at 1 μg/ml, mouse anti-claudin 2 (no. 32-5600; Invitrogen) at 0.8 μg/ml, rabbit anti-claudin 3 (SAB4500435; Sigma) at 2 μg/ml, rabbit anti-claudin 10 (ab52234; Abcam) at 2 μg/ml, and rabbit anti-ZO3 (no. 36-4000; Zymed, Invitrogen) at 2.5 μg/ml. Mouse anti-beta actin (no. A2228; Sigma) at 0.1 μg/ml was used as an internal control. Blots were incubated with the appropriate secondary antibody conjugated to Cy3 or Cy5 (1:5,000; no. PA45011V and PA443009V; GE Healthcare) for 1 h at RT. Bands were detected using an Image Quant Las 4000 imager (GE Healthcare) and visualized and quantified with Image Quant TL image analysis software (GE Healthcare). For graphical representation, target values were normalized to the respective beta-actin band and expressed as the increase (fold) over maximum intensity.

Oxygen consumption analysis. Oxygen was measured using oxygen sensor spots (PreSens) mounted on the inside of the upper lid of 10-cm dishes, connected on the outside to the accompanying fiber optic AD system Fibox 3 (PreSens). One hour before initiation of measurement, medium was renewed and equilibrated to 21% oxygen and 37°C in a 5% CO_2 humidified atmosphere. Dishes were sealed with PetriSeal adhesive tape, and oxygen in the headspace was measured over a 15-min period at 3, 6, and 24 h after sealing. The measurement cycle was repeated every second day from day 1 to day 18 after seeding. Oxygen consumption was determined using an exponential decline fitting for greatest correlation and then integrated for the area over the curve (AOC). To adjust for cell number, 10 or more randomly spaced microscope images per dish were taken with a Zeiss Axiovert 100 microscope at a magnification of 320× before and after each measurement cycle, and cells were counted in an area of 0.08 mm^2 using the Image J cell counting tool (National Institutes of Health). Average total cell number of a 10-cm dish was then calculated at the respective time points.

In addition, oxygen consumption measurements were performed in the presence of a 10 μM concentration of the oxidative phosphorylation uncoupler carbonyl cyanide 4-(trifluoromethoxy)phenylhydrazone (FCCP) in order to elucidate the maximum oxygen consumption capacity. Measurements were conducted as described above for a maximum of 8 h. FCCP treatment was conducted in three states: subconfluent (day 1), newly confluent (day 6), and matured (days 25 to 30).

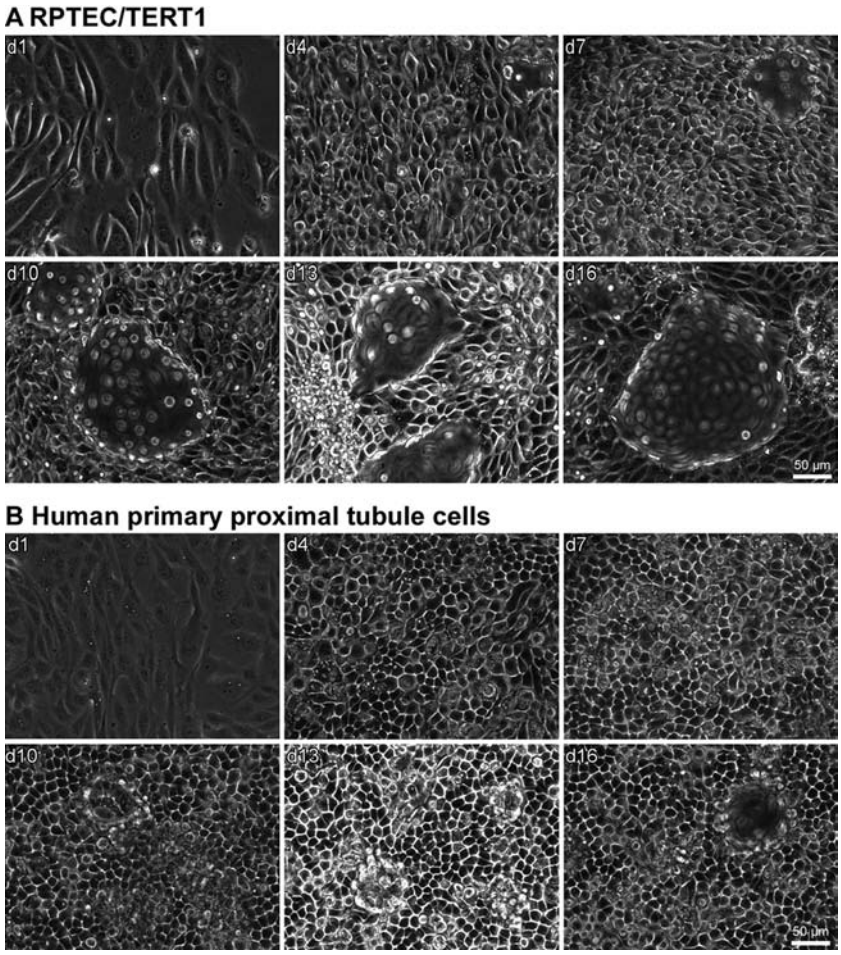

FIG 1 Morphology of RPTEC/TERT1 (A) and primary cells (B) over the experimental time course. Phase-contrast images were captured at the indicated time points after seeding. Domes are visible as structures that are out of focus. Micrographs were obtained with a Zeiss Axiovert 100 microscope at a magnification of ×320.

Stereology. Total RPTEC/TERT1 cell volume was estimated by a stereology approach using light and electron microscopy, as previously described in detail (21). Briefly, newly confluent and matured RPTEC/TERT1 cells were washed with PBS, fixed in 1% (vol/vol) glutaraldehyde, and then postfixed in 1% (wt/vol) OsO_4. Monolayers were dehydrated and embedded in Polybed (Polysciences) for transmission electron microscopy (TEM). Relative volume values (V_V) of nuclei, mitochondria, and other subcellular structures (e.g., agglomerates of glycogen) were estimated at a magnification of ×5,000 by point counting (22) utilizing a square lattice and the relationship $V_v = P_i/P_r \times d$, where P_i is the number of lattice cross points overlying the structure of interest i, P_r is the total number of lattice cross points over the reference structure r, and d is the lattice square length. Absolute values can be obtained by referring the relative values to the mean average cell volume of RPTEC/TERT1 cells. The latter value was obtained from the number of cells per unit area of culture dish and the mean thickness of the monolayer assessed from electron micrographs of strictly perpendicularly cut cell monolayers.

Statistics. Statistical tests were applied to data in GraphPad Prism 5.02 and are specified in the legends. The error bars in the figures represent standard deviation (SD), and the n values are given in the legends.

RESULTS

Cells transition from mesenchymal to cobblestone epithelial morphology during the maturation process. Phase-contrast images at different times of monolayer maturation showed that both primary and RPTEC/TERT1 cells matured from spindle-shaped subconfluent cells to cobblestone-shaped epithelial cells (Fig. 1). In addition, both cell types developed extensive dome formation at the later time points that are indicative of unidirectional transport of water and solutes and thus of a matured epithelium.

The number of transcriptomic alterations decreased over the time course of the experiment. At 3-day intervals over the 16-day monolayer maturation process, RNA was harvested for whole-genome microarray analysis. Hierarchical clustering of the unsupervised samples revealed a high correlation (≥0.5) among the time-matched replicates (Fig. 2A). RPTEC/TERT1 and primary cells clustered separately from each other. In both cell types, two time-dependent clusters appeared (correlation ≥ 0.4), grouping early time points (days 1 and 4) away from later time points (days 7 to 16) (Fig. 2A). Class comparisons (1.5-fold change; $P < 0.001$) conducted between two time points uncovered a decreasing number of differentially expressed probes (DEPs) over the time of monolayer maturation, indicating a stabilization of the transcriptome as the monolayer matured (Fig. 2B).

Adherens junction proteins mediating cell adhesion increased during epithelial maturation, whereas those that support cell migration decreased. Since adherens junction (AJ) proteins are key players in mediating cell-cell contacts (23), we

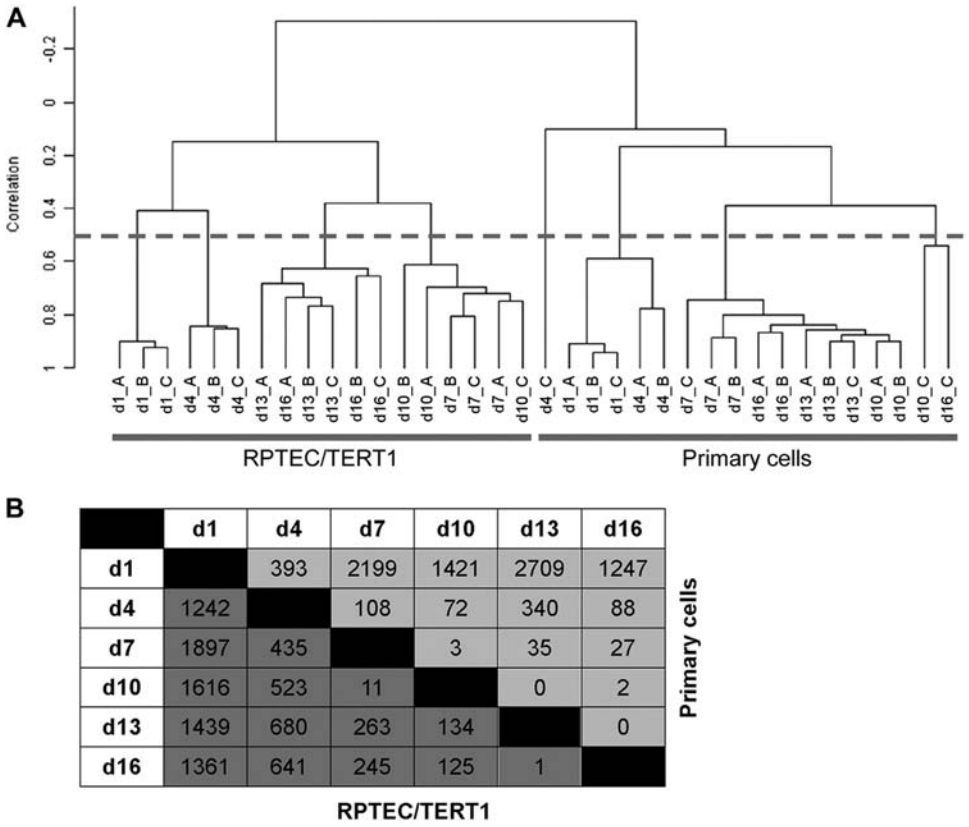

FIG 2 Overview of gene alterations over monolayer formation. (A) Hierarchical clustering. Dendrogram of the hierarchical clustering (centered correlation and average linkage) of the unsupervised samples. The dashed line indicates a correlation of 0.5. Samples that had a correlation of <0.5 with their biological replicates were excluded from further analysis ($n = 3$). (B) Matrix showing the number of delta differentially expressed probes (DEP) (1.5-fold change; $P < 0.001$) between two time points for each cell model. Dark and light gray boxes indicate the numbers of DEPs for RPTEC/TERT1 and primary cells, respectively.

investigated the protein expression and localization of cadherins that were altered in the transcriptomic data. mRNA levels for cadherin 1 (encoded by *CDH1*; also known as E-cadherin) increased, whereas levels of the cadherin 4 gene (*CDH4*) decreased over time, exhibiting the highest expression on days 1 and 4 (Fig. 3A). Cadherin 16 (*CDH16*) mRNA and protein levels were highest at intermediate time points. CDH1 exhibited increased junctional targeting and abundance during maturation, whereas the opposite was true for CDH4 (Fig. 3A). CDH16, on the other hand, exhibited maximal junctional expression at confluence and became more diffuse after monolayer maturation (Fig. 3A). In the matured epithelium, CDH16 was junctionally expressed in a very small subset of the population which corresponded to cells at the apex of some domes (Fig. 3A).

Tissue-specific tight junction proteins exhibited enhanced expression in the matured monolayer. The tight junction (TJ) complex is one of the main regulators of cell density and contact inhibition (24) and also plays a role in the maintenance and regulation of the epithelial barrier. The transcript levels of genes for the TJ proteins claudin (*CLDN-2*, *-3*, and *-10*) and tight junction protein 3 (*TJP3*; also known as ZO3) increased over the time course (Fig. 3B). A similar expression pattern was observed at protein level (Fig. 3B). Additionally, CLDN2, -3, and -10 exhibited increased junctional expression over the maturation period. TJP3 exhibited predominant nuclear expression in proliferating cells but was exclusively junctionally expressed after confluence was reached (Fig. 3B). Additionally, TJP3 increased in protein abundance over the maturation period.

Transcriptome alterations associated with arrest in G_0/G_1 cell cycle phase. As expected, a large number of the differentially expressed genes are associated with cell cycle (Fig. 4A). For the most part, the expression levels of these genes were higher at early time points (day 1 and 4) and lower at the later time points (day 7 to 16). Many of the G_1/S-phase genes exhibited the opposite expression pattern, however. This was observed for *B-cell translocation gene 1*, *anti-proliferative* (*BTG1*), *cyclin-dependent kinase inhibitor 1B* (*CDKN1B*, encoding a protein also known as p27), *cyclin G2* (*CCNG2*), *inhibitor of growth family*, *member 4* (*ING4*), *CDC14 cell division cycle 14 homolog B* (*CDC14B*), *lysine* (K)*-specific demethylase 5B* (*JARID1B*), *leucine zipper*, *putative tumor suppressor 1* (*LZTS1*), *polo-like kinase 1 substrate 1* (*C20ORF19*, encoding a protein also known as PLK1S1), *cell cycle progression 1* (*CCPG1*), and *kelch-like 9* (*KLHL9*).

The gene expression pattern of these cell cycle-associated genes points to a highly proliferating status until day 4, followed by arrest in the G_0/G_1 phase. This was confirmed by cell cycle analysis using flow cytometry (Fig. 4B), which indicated that at a subconfluent state (day 1), 53.8% (±8.0%) of the cells were in G_0/G_1 phase, 33.3% (±5.0%) in S phase and 12.8% (±4.9%) in G_2/M phase. Cell cycle distribution was similar on day 3 and shifted at day 5, with most cells being in G_0/G_1 phase (84.5% ± 0.7%), whereas the fractions in S phase (11.8% ± 0.7%) and G_2/M phase

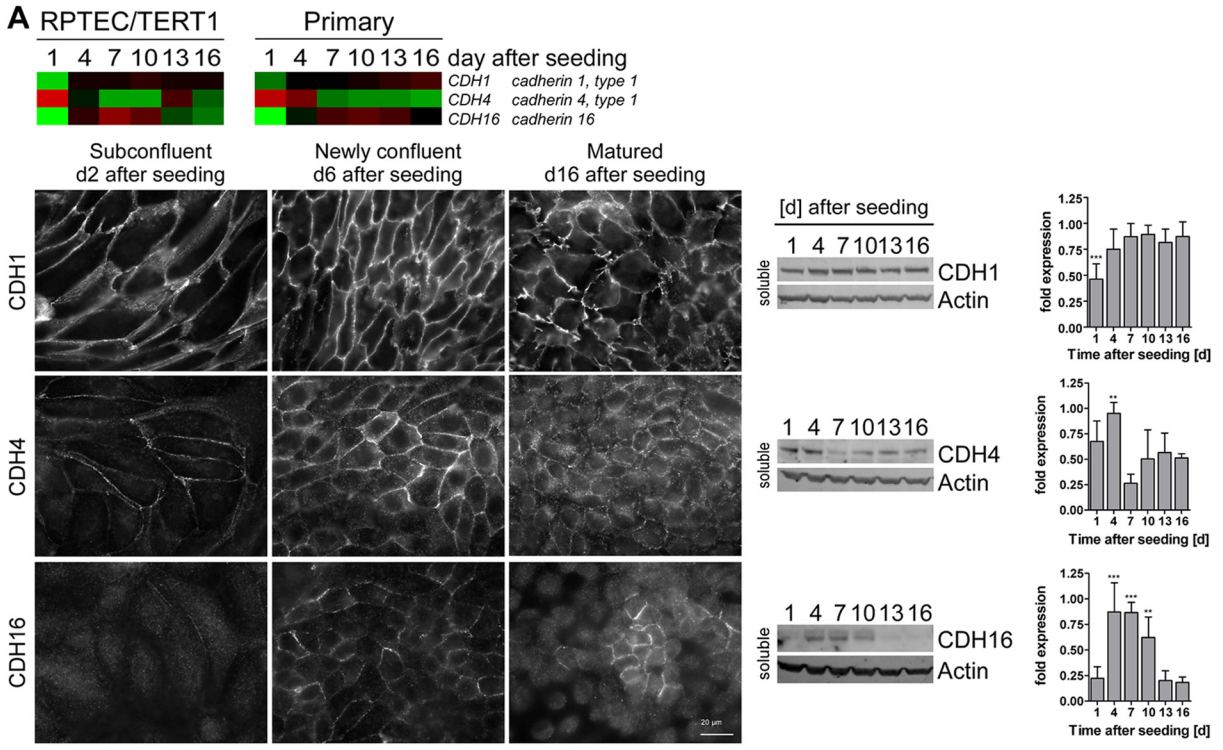
A
RPTEC/TERT1
1 4 7 10 13 16
Primary
1 4 7 10 13 16 day after seeding
CDH1 cadherin 1, type 1
CDH4 cadherin 4, type 1
CDH16 cadherin 16
Subconfluent d2 after seeding
Newly confluent d6 after seeding
Matured d16 after seeding
CDH1
CDH4
CDH16
[d] after seeding
1 4 7 10 13 16
soluble
CDH1
Actin
CDH4
Actin
CDH16
Actin
fold expression
Time after seeding [d]

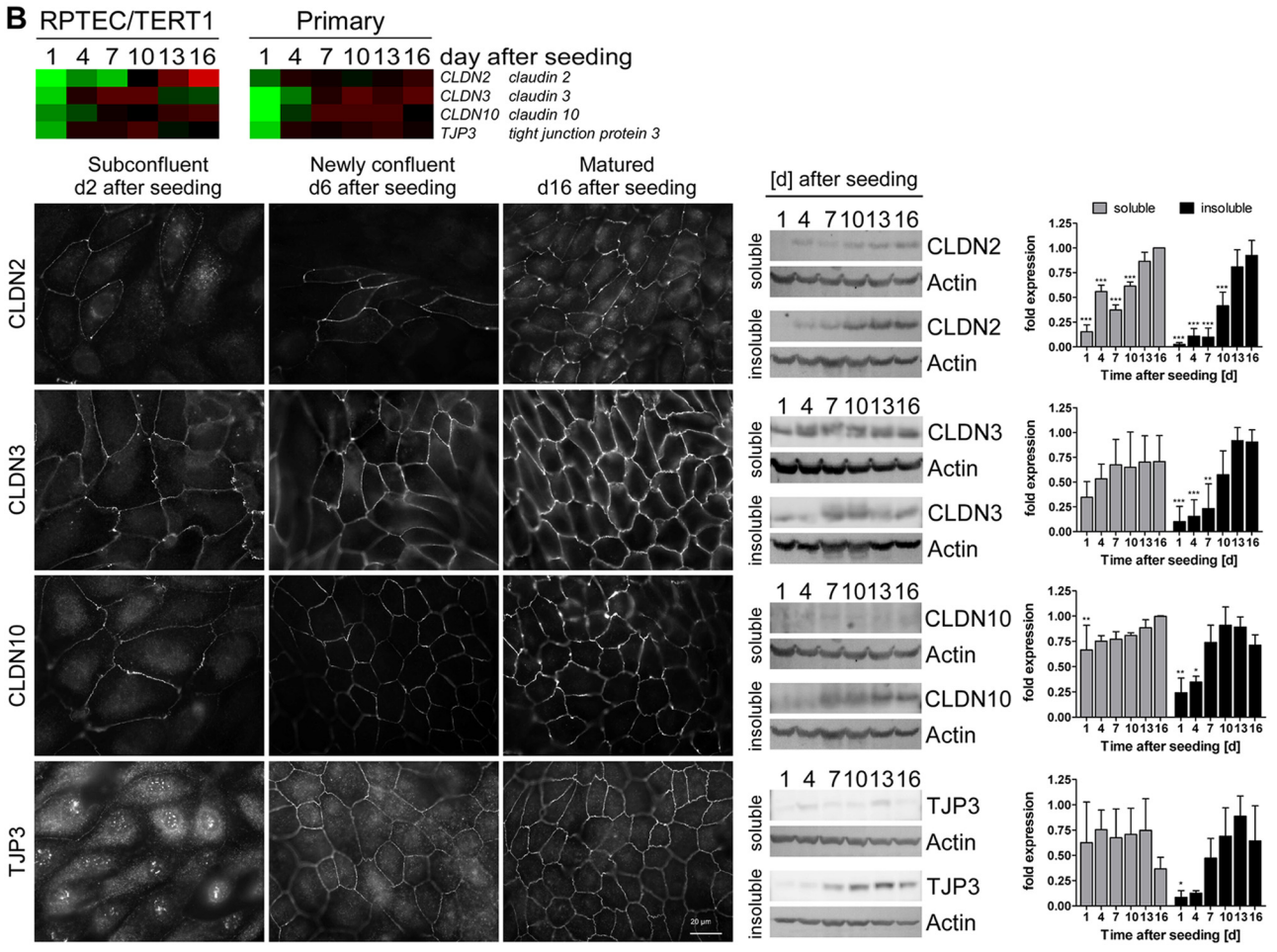
B
RPTEC/TERT1
1 4 7 10 13 16
Primary
1 4 7 10 13 16 day after seeding
CLDN2 claudin 2
CLDN3 claudin 3
CLDN10 claudin 10
TJP3 tight junction protein 3
Subconfluent d2 after seeding
Newly confluent d6 after seeding
Matured d16 after seeding
CLDN2
CLDN3
CLDN10
TJP3
[d] after seeding
1 4 7 10 13 16
soluble
insoluble
CLDN2
Actin
CLDN3
Actin
CLDN10
Actin
TJP3
Actin
fold expression
Time after seeding [d]

(3.7% ± 0.8%) were decreased. This trend continued until day 18, where 96.4% (±0.6%) of the cells were in G_0/G_1 phase, 1.8% (±0.3%) were in S phase, and 1.8% (±0.7%) were in G_2/M phase.

During the maturation process, cells switch from a highly glycolytic and oxygen-consuming metabolism to predominately oxidative metabolism and beta-oxidation of fatty acids. A number of genes involved in energy metabolism (glycolysis, tricarboxylic acid [TCA] cycle, oxidative phosphorylation, redox regulation, and fatty acid metabolism) exhibited altered expression during monolayer maturation (Fig. 5A). Two main expression patterns could be distinguished: a peak expression at early time points (day 1 to 4) and a peak expression at intermediate time points (day 7 to 10). Early highly expressed genes comprised those involved in fatty acid synthesis, including *solute carrier family 25, member 1* (*SLC25A1*) and *fatty acid synthase* (*FASN*), as well as genes implicated in redox regulation, such as *thioredoxin* (*TXN*), *thioredoxin reductase* (*TXNRD1*), *sulfiredoxin 1 homolog* (*SRXN1*), *glutathione S-transferase omega 1* (*GSTO1*), and *gamma-glutamylcyclotransferase* (*GGCT*). Two genes encoding members of the less well characterized class 3 glucose transporters, *SLC2A6* and *SCL2A12* (also known as GLUT6 and 12), exhibited the highest expression levels on day 1 and 4, respectively. Genes involved in redox regulation displayed the highest expression at intermediate time points and included *catalase* (*CAT*), *glutathione S-transferase alpha 4* (*GSTA4*), *mu 1* (*GSTM1*), *thioredoxin interacting protein* (*TXNIP*), and *NAD(P)H dehydrogenase, quinone 1* (*NQO1*). Genes involved in glycolysis and TCA cycle also demonstrated peak expression at intermediate time points and comprised *lactate dehydrogenase B* (*LDHB*), *pyruvate dehydrogenase* (*lipoamide*) *alpha 1* (*PDHA1*), and *oxoglutarate dehydrogenase-like* (*OGDHL*) as well as genes implicated in the beta-oxidation of fatty acids, such as *butyrobetaine* (*gamma*), *2-oxoglutarate dioxygenase 1* (*BBOX1*), *acyl-coenzyme A synthetase medium-chain family member 3* (*ACSM3*), *short-chain family member 1* (*ACSS1*), and *solute carrier family 25 and member 29* (*SLC25A29*). Additionally, *6-phosphofructo-2-kinase/fructose-2,6-bisphosphatase* (*PFKFB*) isoforms, responsible for the synthesis and degradation of fructose-2,6-bisphosphate, displayed an altered expression profile: *PFKFB3* was decreased in proliferating cells, whereas *PFKFB4* was increased.

NMR profiling of supernatant medium in proliferating and matured RPTEC/TERT1 cells demonstrated a decreased utilization of glutamine, tyrosine, valine, isoleucine, and glucose in the matured epithelium (Fig. 5B). The glutamine and alanine profiles are of particular interest, since the utilization of both spiked at 24 h, most likely due to catabolism of the medium supplement L-alanyl-L-glutamine (Glutamax, 2 mM). Membrane-bound aminopeptidases hydrolyze the dipeptide, releasing alanine and glutamine into the culture medium. Alanine did not seem to be further used by the cells when they were either proliferating or matured, but glutamine was consumed faster in proliferating cells. Additionally, there was a decreased rate of production of oxoisovalerate, oxo-methylisovalerate, formate, and lactate in the matured epithelium. In order to compare the kinetics of glycolysis between these two states, we measured lactate and glucose in the supernatant medium over the maturation process with biochemical assays. Glucose utilization and lactate production steadily decreased over the time course and reached a steady state at day 8 (Fig. 5C).

We originally hypothesized that this glycolytic switch would be paralleled by a switch to oxidative metabolism. However, oxygen consumption measurements revealed that proliferating cells consumed significantly more oxygen than the matured epithelium (Fig. 5D). To examine further the respiration states at different time points after seeding, we applied the uncoupler FCCP, which disrupts the proton gradient across the mitochondrial inner membrane. This causes an increase in the intracellular concentration of ADP stimulating the transfer of electrons to oxygen molecules (25). FCCP treatment can thus be used to measure the capacity of the electron transfer system. Proliferating cells and newly confluent cells showed no altered respiration with FCCP compared to their time-matched control (Fig. 5E), whereas FCCP treatment of matured monolayers resulted in a significantly higher rate of oxygen consumption than was seen in time-matched control and proliferating cells (Fig. 5E). Inhibition of complex III of the electron transfer chain by antimycin A caused a small increase in lactate production in proliferating cells, whereas nonproliferating cells reverted to a highly glycolytic metabolism (Fig. 5F). Stereological analysis of matured cells demonstrated a 2.5-fold decrease in cell volume (Fig. 5H, inset) paralleled by a slight, although not significant, increase in mitochondrial volume (Fig. 5H). In line with this trend is the observation that *peroxisome proliferator-activated receptor gamma, coactivator 1 alpha* (*PPARGC1A*), a gene involved in mitochondrial biogenesis, exhibited increased expression in matured cells (Fig. 5A). A trend pointing to a reduction in glycogen stores was also observed in matured cells by stereological analysis (Fig. 5H). Biochemical measurement of glycogen revealed the highest glycogen storage after the most intense aerobic glycolysis phase, which declined afterwards to basal levels (Fig. 5G). During this peak, the gene encoding the glycogen-degrading enzyme glycogen phosphorylase, brain (*PYGB*), was highly expressed (Fig. 5A).

Taken together, these data suggest that proliferating cells run both oxidative and glycolytic metabolism at full capacity (Fig. 5C to E), while matured cells exhibit lower energy requirements but have a higher capacity for oxidative metabolism. Furthermore, disruption of oxidative phosphorylation with antimycin A reactivates glycolysis in matured monolayers (Fig. 5F).

Genes associated with transport, proximal-tubule differentiation, and ciliogenesis were increased in the matured epithelium. The proximal tubule is the main site in the nephron for solute and nutrient reabsorption. Interestingly, the transcript levels of genes encoding three subunits of the Na^+/K^+ ATPase (*ATP1A1*, *ATP1B1*, and *FXYD2*), which is the driving force for

FIG 3 Adherens (A) and tight (B) junction protein expression during monolayer formation and maturation. (Top) Heat maps of adherens junction (AJ) and tight junction (TJ) protein genes. Average mean-centered mRNA expression values ($\log_2$) per time point and cell type were used to generate the heat maps. Cell colors reflect the value and direction of the expression value relative to the mean expression over all time points (red indicates higher expression and green indicates lower expression compared to the mean) ($n = 3$). (Bottom) Immunofluorescence staining and Western blots including band intensity quantification (RIPA buffer-soluble and -insoluble fractions; minimum $n = 4$) of AJ and TJ proteins in RPTEC/TERT1 cells at different time points after seeding. Band intensities were normalized first to actin and then to the maximum intensity per replicate. Values are means plus SD; statistical significances of changes in Western blot band intensities at day 16 were analyzed using one-way analysis of variance (ANOVA) with the Bonferroni multiple comparison test *post hoc*. *, $P < 0.05$; **, $P < 0.01$; ***, $P < 0.001$.

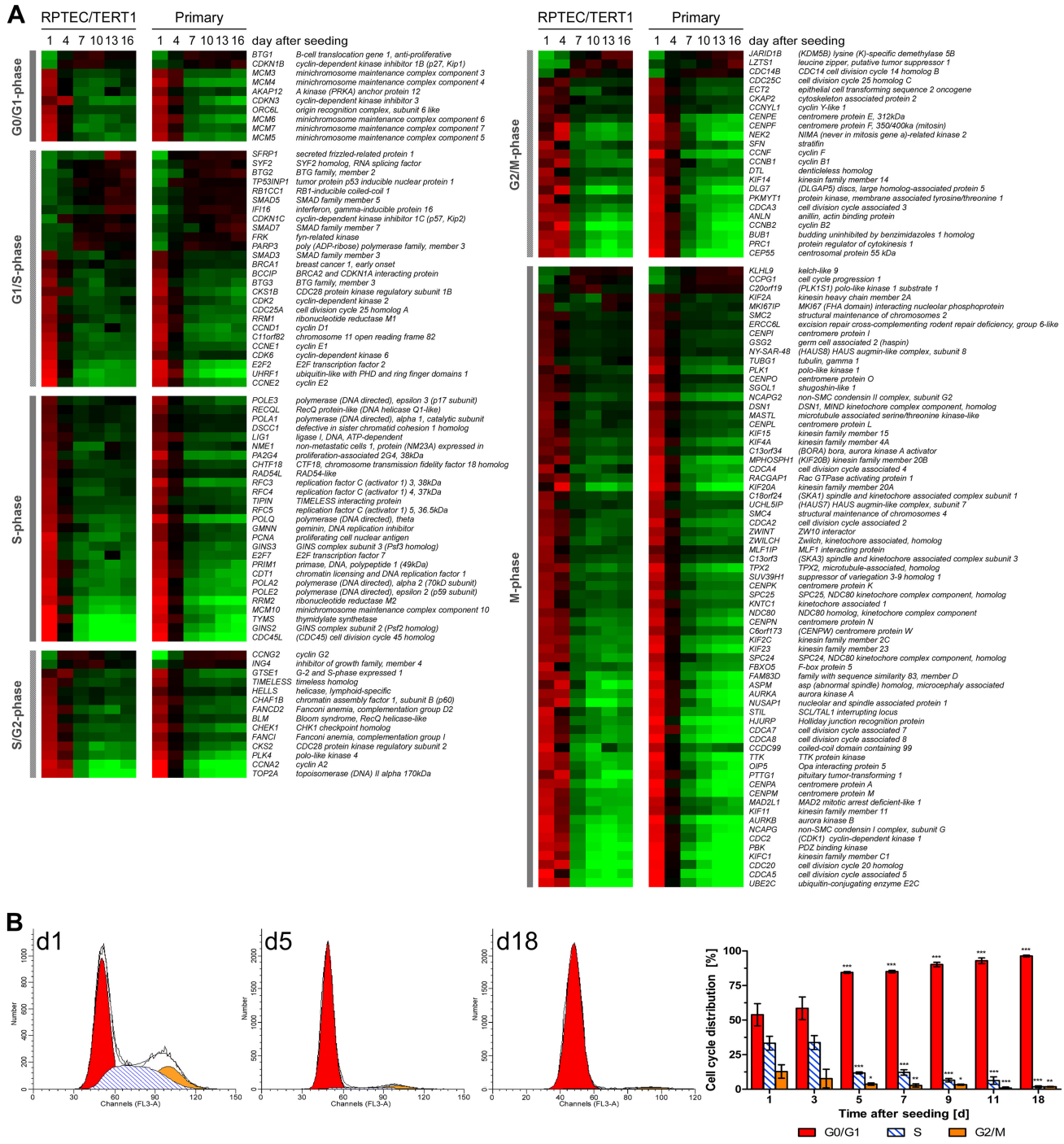

FIG 4 Cell cycle alterations over monolayer formation and maturation. (A) Heat map of cell cycle genes identified in the DEG list. Genes were assigned to G_0/G_1, G_1/S, S, S/G_2, G_2/M, or M phase of the cell cycle and then ranked within a cell cycle phase according to the difference between day 1 and 16 values in the RPTEC/TERT1 data set. Average mean-centered mRNA expression values ($\log_2$) per time point and cell type were used to generate the heat map. Cell colors reflect the expression value and direction relative to the mean expression over all time points (red indicates higher expression and green indicates lower expression compared to the mean) ($n = 3$). (B) Cell cycle distribution of RPTEC/TERT1 cells at different time points after seeding. Values are means ± SD; statistical significance of changes compared to day 1 was analyzed using two-way ANOVA with the Bonferroni multiple comparison test *post hoc*. *, $P < 0.05$; **, $P < 0.01$; ***, $P < 0.001$ ($n = 3$ to 6).

transport processes in the proximal tubule, increased over time, whereas subunit *FXYD5*, associated with decreased cell adhesiveness (26), showed the opposite expression profile (Fig. 6). Several members of the ATP-binding cassette transporter family and solute carrier family exhibited altered expression over the time course. Expression of several genes involved in important proximal-tubular functions, including *serine carboxypeptidase 1* (*SCPEP1*) (27) and *parathyroid hormone 1 receptor* (*PTHR1*) (14), were increased during the maturation process, whereas expression of a few also decreased, for example, *alanyl* (*membrane*) *amino-*

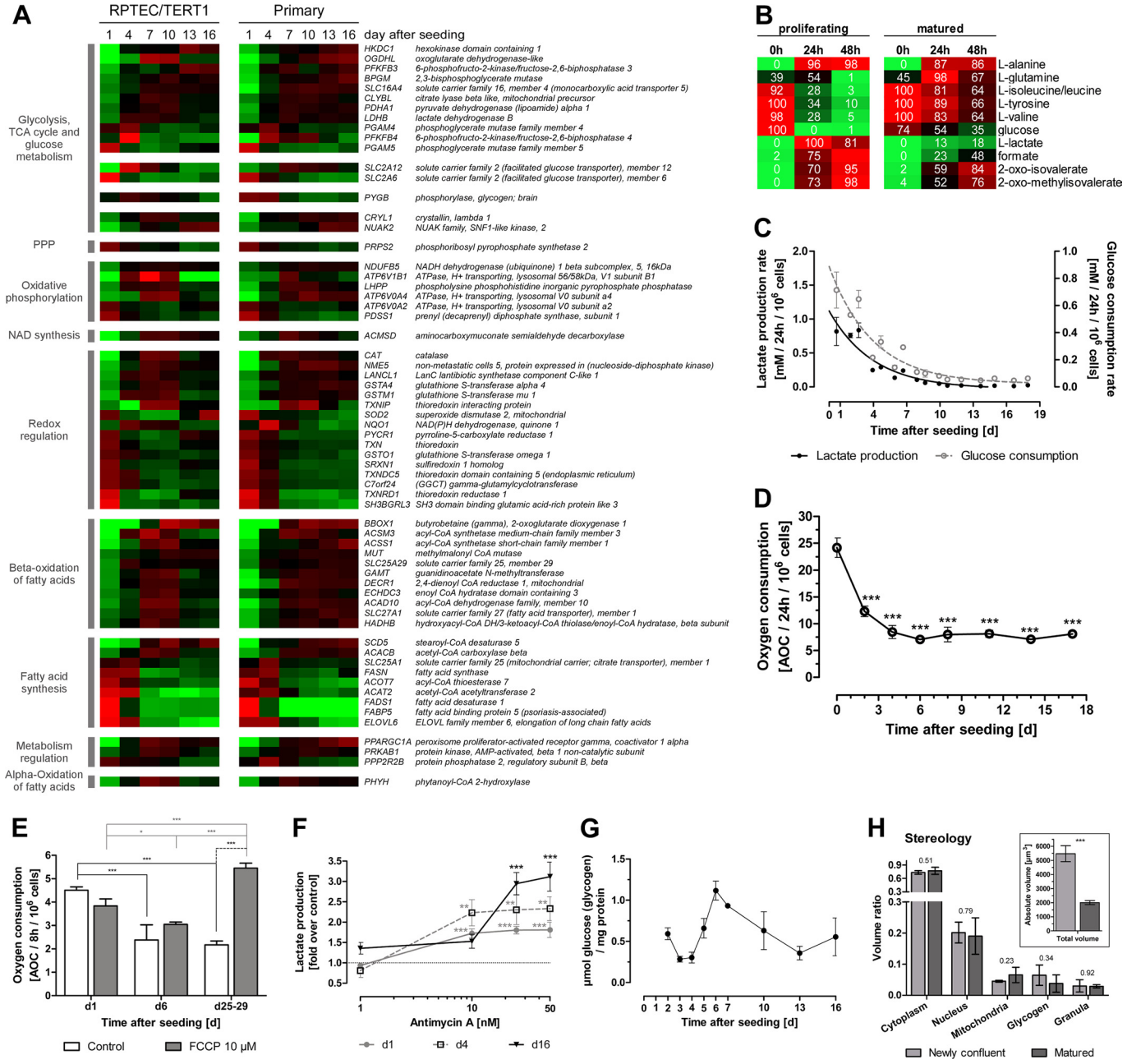

FIG 5 Alterations in energy metabolism and mitochondrial function over monolayer formation and maturation. (A) Heat map of energy metabolism-associated genes. Genes are grouped according to their function in different metabolic pathways and then ranked within the group to the difference between day 1 and 16 values in the RPTEC/TERT1 data set. Average mean-centered mRNA expression values ($\log_2$) per time point and cell type are represented in red (higher expression compared to the mean) and green (lower expression compared to the mean) ($n = 3$). (B) Metabolic alterations measured by NMR in RPTEC/TERT1 supernatant. Values are minima and maxima, in percent, normalized per metabolite. Colors represent abundances of the respective metabolites, where red indicates high abundance and green indicates low abundance ($n = 3$). (C) Lactate production and glucose consumption rates over RPTEC/TERT1 maturation time. $n = 3$. (D) Oxygen consumption rate over RPTEC/TERT1 maturation time. Statistical significance was analyzed using one-way ANOVA with the Bonferroni multiple comparison test *post hoc* ($n = 3$). (E) Oxygen consumption of RPTEC/TERT1 cells after treatment with oxidative uncoupler FCCP for 8 h. Two-way ANOVA with the Bonferroni multiple comparison test *post hoc* was used to analyze statistical significance ($n = 3$). (F) Lactate production of RPTEC/TERT1 cells after treatment with the electron transfer chain complex III inhibitor antimycin A for 8 h. Statistical significance was analyzed using one-way ANOVA with the Bonferroni multiple comparison test *post hoc* to time-matched control ($n = 3$). (G) Glycogen storage at different time points after seeding ($n = 3$). (H) Relative volume of RPTEC/TERT1 cell fractions, as determined by stereology. Insert depicts the calculated absolute volume of newly confluent and matured cells. Statistical significance was analyzed by applying a two-tailed unpaired *t* test. *P* values are indicated above the bars ($n = 3$). (B to H) Experiments were performed with RPTEC/TERT1 cells. (C to H) Values are means ± SD. *, $P < 0.05$; **, $P < 0.01$; ***, $P < 0.001$. PPP, pentose phosphate pathway.

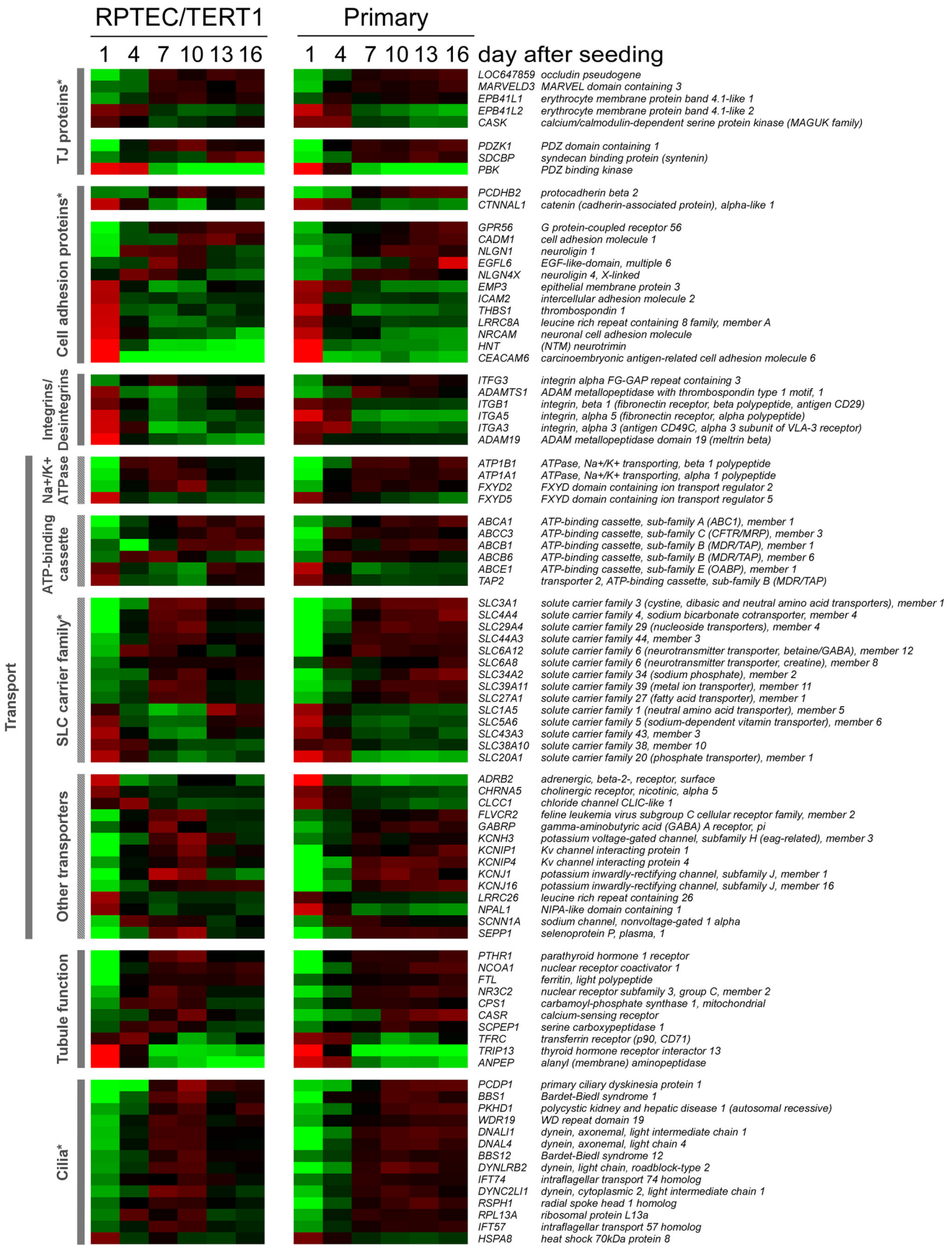
RPTEC/TERT1
Primary
1 4 7 10 13 16
1 4 7 10 13 16 day after seeding
Transport
TJ proteins*
Cell adhesion proteins*
Integrins/ Desintegrins
Na+/K+ ATPase
ATP-binding cassette
SLC carrier family*
Other transporters
Tubule function
Cilia*
LOC647859 occludin pseudogene
MARVELD3 MARVEL domain containing 3
EPB41L1 erythrocyte membrane protein band 4.1-like 1
EPB41L2 erythrocyte membrane protein band 4.1-like 2
CASK calcium/calmodulin-dependent serine protein kinase (MAGUK family)
PDZK1 PDZ domain containing 1
SDCBP syndecan binding protein (syntenin)
PBK PDZ binding kinase
PCDHB2 protocadherin beta 2
CTNNAL1 catenin (cadherin-associated protein), alpha-like 1
GPR56 G protein-coupled receptor 56
CADM1 cell adhesion molecule 1
NLGN1 neuroligin 1
EGFL6 EGF-like-domain, multiple 6
NLGN4X neuroligin 4, X-linked
EMP3 epithelial membrane protein 3
ICAM2 intercellular adhesion molecule 2
THBS1 thrombospondin 1
LRRC8A leucine rich repeat containing 8 family, member A
NRCAM neuronal cell adhesion molecule
HNT (NTM) neurotrimin
CEACAM6 carcinoembryonic antigen-related cell adhesion molecule 6
ITFG3 integrin alpha FG-GAP repeat containing 3
ADAMTS1 ADAM metallopeptidase with thrombospondin type 1 motif, 1
ITGB1 integrin, beta 1 (fibronectin receptor, beta polypeptide, antigen CD29)
ITGA5 integrin, alpha 5 (fibronectin receptor, alpha polypeptide)
ITGA3 integrin, alpha 3 (antigen CD49C, alpha 3 subunit of VLA-3 receptor)
ADAM19 ADAM metallopeptidase domain 19 (meltrin beta)
ATP1B1 ATPase, Na+/K+ transporting, beta 1 polypeptide
ATP1A1 ATPase, Na+/K+ transporting, alpha 1 polypeptide
FXYD2 FXYD domain containing ion transport regulator 2
FXYD5 FXYD domain containing ion transport regulator 5
ABCA1 ATP-binding cassette, sub-family A (ABC1), member 1
ABCC3 ATP-binding cassette, sub-family C (CFTR/MRP), member 3
ABCB1 ATP-binding cassette, sub-family B (MDR/TAP), member 1
ABCB6 ATP-binding cassette, sub-family B (MDR/TAP), member 6
ABCE1 ATP-binding cassette, sub-family E (OABP), member 1
TAP2 transporter 2, ATP-binding cassette, sub-family B (MDR/TAP)
SLC3A1 solute carrier family 3 (cystine, dibasic and neutral amino acid transporters), member 1
SLC4A4 solute carrier family 4, sodium bicarbonate cotransporter, member 4
SLC29A4 solute carrier family 29 (nucleoside transporters), member 4
SLC44A3 solute carrier family 44, member 3
SLC6A12 solute carrier family 6 (neurotransmitter transporter, betaine/GABA), member 12
SLC6A8 solute carrier family 6 (neurotransmitter transporter, creatine), member 8
SLC34A2 solute carrier family 34 (sodium phosphate), member 2
SLC39A11 solute carrier family 39 (metal ion transporter), member 11
SLC27A1 solute carrier family 27 (fatty acid transporter), member 1
SLC1A5 solute carrier family 1 (neutral amino acid transporter), member 5
SLC5A6 solute carrier family 5 (sodium-dependent vitamin transporter), member 6
SLC43A3 solute carrier family 43, member 3
SLC38A10 solute carrier family 38, member 10
SLC20A1 solute carrier family 20 (phosphate transporter), member 1
ADRB2 adrenergic, beta-2-, receptor, surface
CHRNA5 cholinergic receptor, nicotinic, alpha 5
CLCC1 chloride channel CLIC-like 1
FLVCR2 feline leukemia virus subgroup C cellular receptor family, member 2
GABRP gamma-aminobutyric acid (GABA) A receptor, pi
KCNH3 potassium voltage-gated channel, subfamily H (eag-related), member 3
KCNIP1 Kv channel interacting protein 1
KCNIP4 Kv channel interacting protein 4
KCNJ1 potassium inwardly-rectifying channel, subfamily J, member 1
KCNJ16 potassium inwardly-rectifying channel, subfamily J, member 16
LRRC26 leucine rich repeat containing 26
NPAL1 NIPA-like domain containing 1
SCNN1A sodium channel, nonvoltage-gated 1 alpha
SEPP1 selenoprotein P, plasma, 1
PTHR1 parathyroid hormone 1 receptor
NCOA1 nuclear receptor coactivator 1
FTL ferritin, light polypeptide
NR3C2 nuclear receptor subfamily 3, group C, member 2
CPS1 carbamoyl-phosphate synthase 1, mitochondrial
CASR calcium-sensing receptor
SCPEP1 serine carboxypeptidase 1
TFRC transferrin receptor (p90, CD71)
TRIP13 thyroid hormone receptor interactor 13
ANPEP alanyl (membrane) aminopeptidase
PCDP1 primary ciliary dyskinesia protein 1
BBS1 Bardet-Biedl syndrome 1
PKHD1 polycystic kidney and hepatic disease 1 (autosomal recessive)
WDR19 WD repeat domain 19
DNALI1 dynein, axonemal, light intermediate chain 1
DNAL4 dynein, axonemal, light chain 4
BBS12 Bardet-Biedl syndrome 12
DYNLRB2 dynein, light chain, roadblock-type 2
IFT74 intraflagellar transport 74 homolog
DYNC2LI1 dynein, cytoplasmic 2, light intermediate chain 1
RSPH1 radial spoke head 1 homolog
RPL13A ribosomal protein L13a
IFT57 intraflagellar transport 57 homolog
HSPA8 heat shock 70kDa protein 8

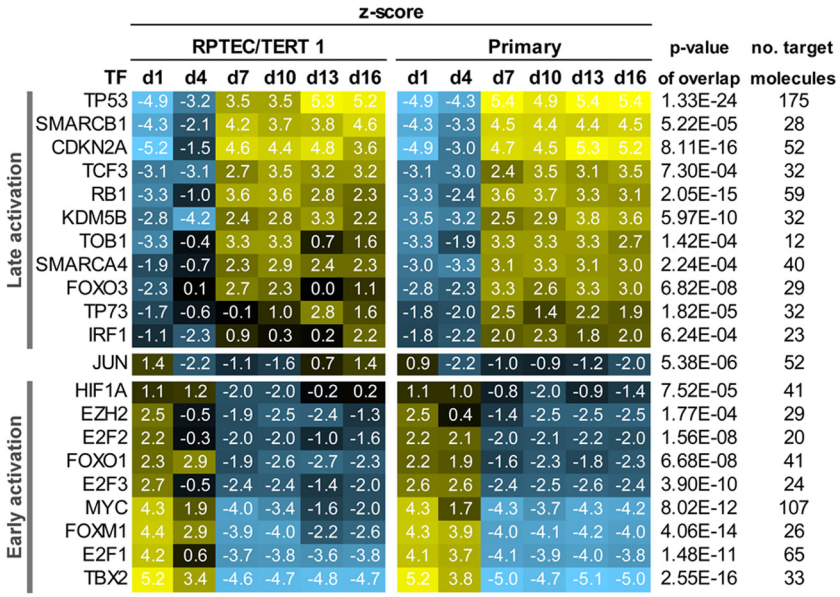

FIG 7 Predicted transcription factors (TFs) involved in the maturation process. Colors reflect the regulation *z* score and direction of regulation: yellow indicates activation and blue indicates inhibition of the given TF. All TFs in this table had a *P* value of <0.001 for the overlap and a *z* score of >2 or <-2 at at least one time point in both cell models.

peptidase (*ANPEP*) (Fig. 6). We also identified an augmentation in the expression of several genes implicated in cilium biogenesis and maintenance, including *dynein, cytoplasmic 2, light intermediate chain 1* (*DYNC2LI1*), *Bardet-Biedl syndrome 1 and 12* (*BBS1*, *BBS12*), *intraflagellar transport 57 homolog* (*IFT57*), and *primary ciliary dyskinesia protein 1* (*PCDP1*) (Fig. 6).

Identification of transcription factor master regulators of proliferation and maturation. The list of differentially expressed probes over the time course was subjected to transcription factor (TF) analysis in IPA. The refined analysis yielded 9 TFs with predicted early activation, 12 activated at later time points, and 1 (JUN) that was activated at both times (Fig. 7). Among the early active TFs were TBX2, FOXM1, MYC, HIF1A, and E2F1-3, and among the later active TFs, TP53, CDKN2A, RB1, KDM5B, and FOXO3 were identified.

From four TFs of the list of predicted TFs activity-ELISAs were performed. These assays confirmed that TP53 had the highest activity in matured cells, whereas HIF1A and c-MYC exhibited the highest activity in proliferating cells (Fig. 8A). In contrast to the prediction of its activation state, FOXO1 was highly active in matured cells.

Transcript levels of some selected genes were quantified in independent samples by qPCR (Fig. 8B). We selected a panel of genes involved in cell cycle regulation [*CDKN1A* (p53 driven) and *CDC25A* (c-MYC driven)], fatty acid metabolism (*FASN* and *BBOX1*), transport (*ATP1A1* and *ATP1B1*), and ciliogenesis (*BBS1*). The gene *cyclin-dependent kinase inhibitor 1A* (*CDKN1A*; the protein is also known as p21), which mediates the p53-dependent cell cycle G_1 phase arrest, was significantly more highly expressed only in the matured monolayer (day 16 after seeding). The gene for cell division cycle 25A (*CDC25A*), which promotes the transition from G_1 to the S phase of the cell cycle and is a target of c-MYC, exhibited an expression profile contrary to that of *CDKN1A* and was highly expressed in the subconfluent and newly confluent (day 1 and day 7 after seeding, respectively) monolayers, which corresponded to the microarray data. The gene for fatty acid synthase (*FASN*) exhibited reduced expression in the newly confluent monolayer, whereas the transcript levels of the genes for butyrobetaine (gamma), 2-oxoglutarate dioxygenase 1 (*BBOX1*), a gene involved in L-carnitine synthesis, dramatically increased in the newly confluent monolayer and further increased in the matured monolayer; the same expression trend was observed in the microarray data. Expression of genes for the alpha and beta subunits (*ATP1A1* and *ATP1B1*, respectively) of the Na^+/K^+ ATPase increased in the newly confluent monolayer, and high expression was sustained in the matured monolayer, consistent with the microarray data. The gene for the protein Bardet-Biedl syndrome 1 (*BBS1*) is implicated in cilium function, and it exhibited augmented transcript levels beginning in the newly confluent monolayer and continued to be highly expressed in the matured monolayer, as in the microarray data. The qPCR data for the selected genes corresponded well to the microarray expression data.

Figure 9 summarizes the main results.

DISCUSSION

Both primary human renal proximal-tubule cells and the telomerase-expressing human proximal-tubule cell line RPTEC/TERT1 exhibited similar growth rates and similar timelines of transition

FIG 6 Functional grouping of genes exhibiting time-dependent expression during epithelial monolayer maturation. Genes were ranked within the allocated group according to the difference between day 1 and 16 values in the RPTEC/TERT1 data set. Cell colors reflect the value and direction of the expression value relative to the mean over all time points (red indicates higher expression and green indicates lower expression compared to the mean) ($n = 3$). An asterisk indicates that the group contains members that are shown in previous heat maps.

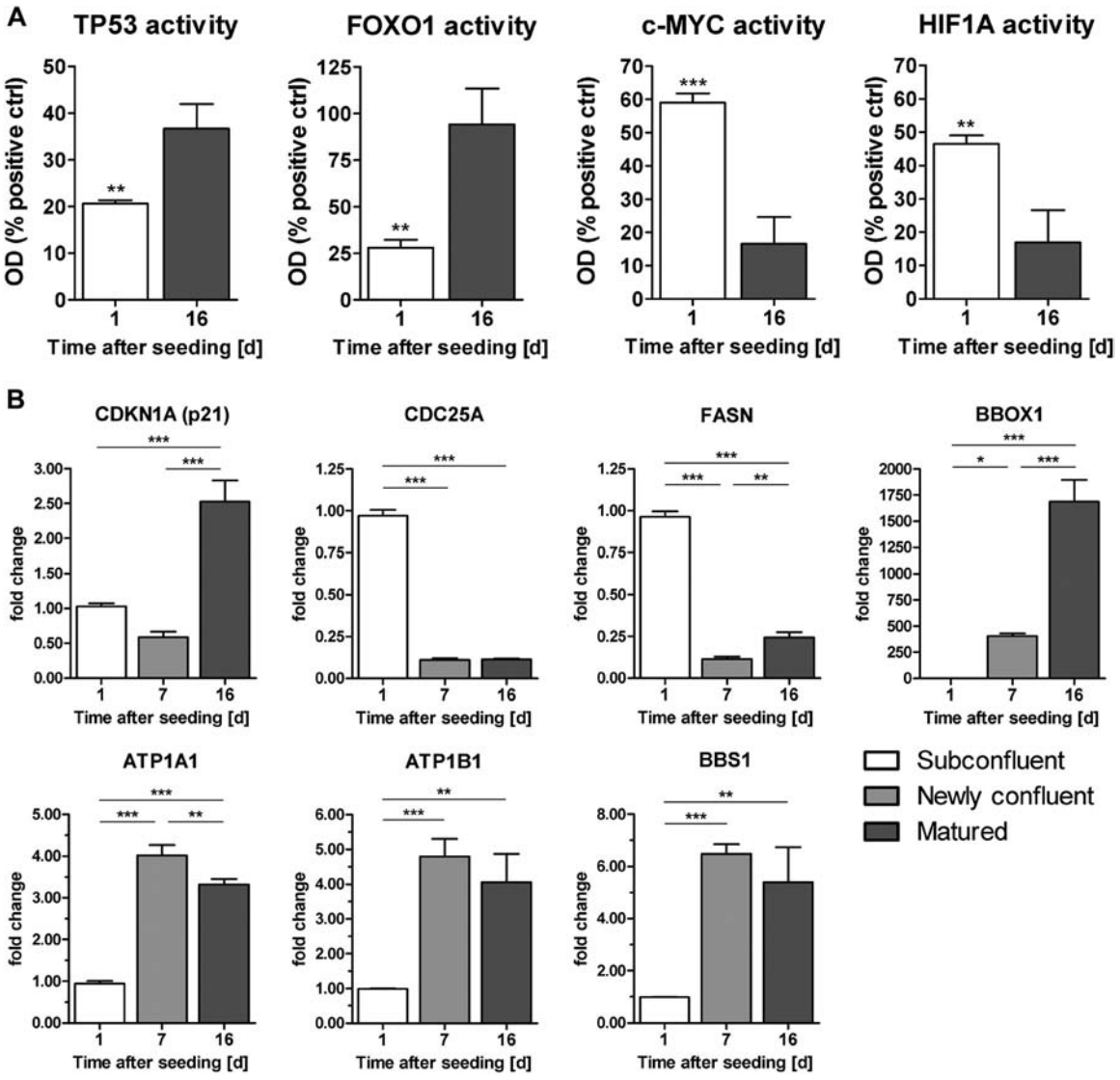

FIG 8 (A) Activation levels of TFs TP53, FOXO1, c-MYC, and HIF1A in RPTEC/TERT1 nuclear extracts at days 1 and 16 after seeding. Values are means plus SD ($n = 3$). Statistical significance was analyzed by applying a two-tailed unpaired *t* test. *, $P < 0.05$; **, $P < 0.01$; ***, $P < 0.001$. (B) qPCR of selected genes in RPTEC/TERT1 cells at subconfluent (day 1 after seeding), newly confluent (day 7 after seeding), and matured (day 16 after seeding) time points. Values are changes in copy number (fold) relative to biological replicate 1 on day 1. Values are means and SD ($n = 3$). Statistical significance was analyzed using one-way ANOVA with the Bonferroni multiple comparison test *post hoc*. *, $P < 0.05$; **, $P < 0.01$; ***, $P < 0.001$.

from mesenchymal-type morphology to confluent monolayers and ultimately dome-forming monolayers. Cadherins are integral members of the adherens junctions that function as intercellular adhesion molecules (28, 29). Here we observed an increase of *CDH1* (also known as *E-cadherin*) and *CDH16* mRNA with a decrease in *CDH4* mRNA over the maturation time. CDH1 protein was expressed in high abundance at the cell-to-cell junctions throughout the maturation process. CDH1 is pivotal for tissue formation and forms homo-*trans*-interactions with neighboring cells and homo-*cis*-interactions within its own cell plasma membrane. The combination of *trans* and *cis* interactions promotes the formation of a lattice-type adherens belt (30). CDH4 exhibited sparse junctional localization at the early time points, but junctional expression increased in the intermediate phase. Total protein expression was high at days 1 and 4 and decreased thereafter. These findings support the role of CDH4 as a facilitator of cell motility (31). CDH16 is a nonclassical cadherin lacking the histidine-alanine-valine adhesion recognition sequence and is thought to play a role in maintenance of terminally differentiated tubules rather than initiation of renal morphogenesis (32). Here, CDH16 was absent in proliferating cells, but junctional expression increased dramatically at confluence. In the matured epithelium, there was a decrease in CDH16 total protein, and expression was limited to the apices of cells in dome-forming regions. It has previously been shown that cells at the apices of domes are often mitotic (33), and thus it is plausible that CDH16 plays a role in maintenance of the epithelial barrier in dividing cells of the matured epithelium.

The expression of the claudin family of intercellular TJ proteins determines the paracellular selectivity of different epithelial

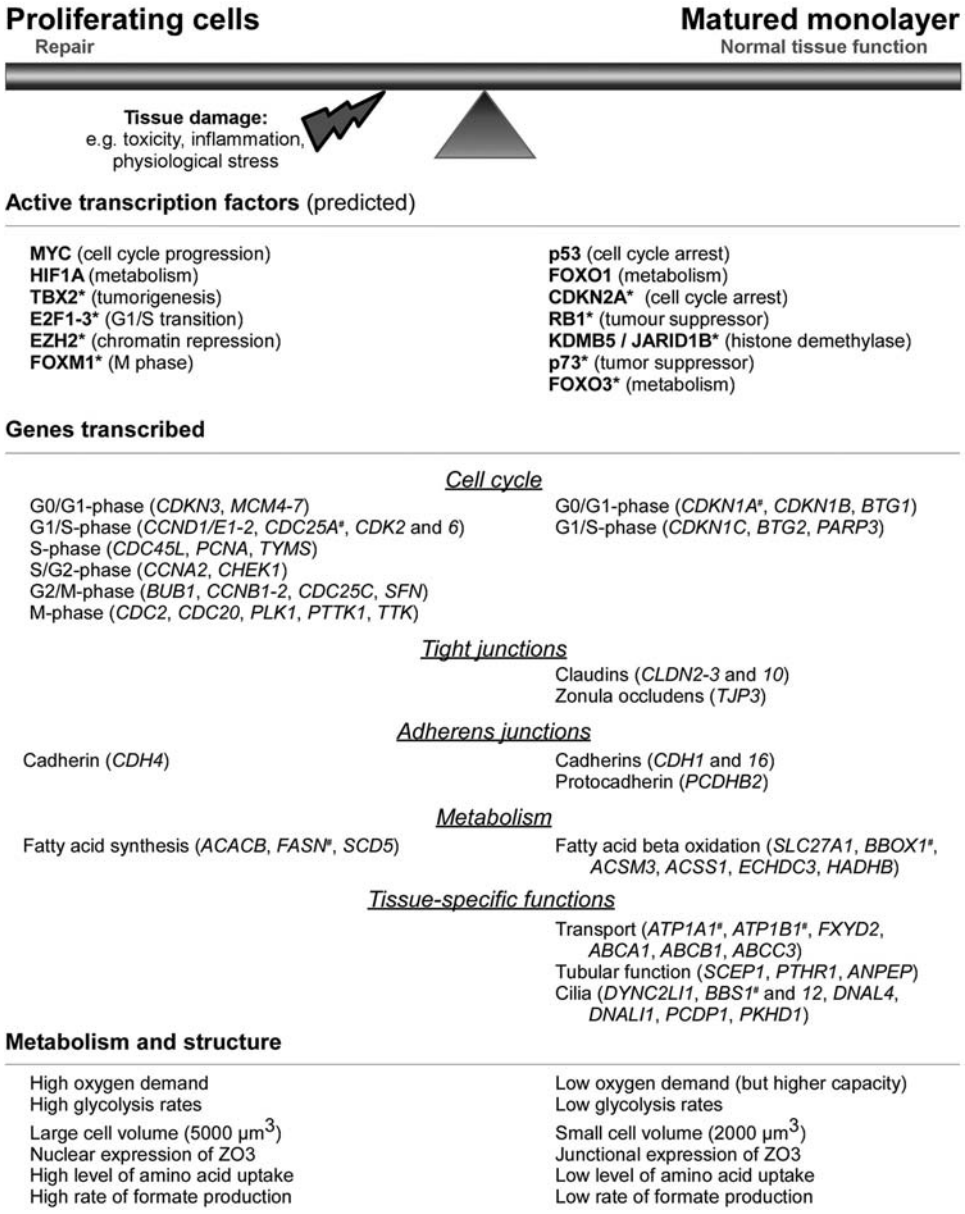

FIG 9 Summary of key mechanisms and players in epithelial monolayer maturation. *, predicted transcription factor; #, expression confirmed using qPCR.

barriers (34). Here, the expression of genes for several claudin subtypes increased during epithelial maturation, including *CLDN2* and *CLDN10*. These subtypes are highly expressed in the human proximal tubule *in vivo* (35), and their pore-forming properties are thought to be the reason for the relative leakiness of this region compared to more distal segments (2, 36–38). We recently demonstrated that oxidative stress decreases the expression of *CLDN2* and *CLDN10* (39), which would support the notion that cell injury can cause a reversal of the differentiation process (40). Other members of the tight junction (TJ) complex, the zonula occludens (ZO) protein family, act as sensors of epithelial compactness and regulate proliferation through their interaction with and sequestration of transcription modifiers (7, 12, 41–43). In our transcriptomics data, genes involved in the cell cycle were highly enriched at the early time points, and cell cycle analysis showed that the majority of cells arrest in G_0/G_1 as soon as 5 days after seeding. A small proportion of cell turnover remains thereafter. We observed an induction of TJP3 (also known as ZO3) mRNA expression over time and a strong increase in protein levels. Additionally, we could show that TJP3 is expressed in the nucleus of proliferating cells, whereas cell-to-cell junction localization was observed exclusively in the matured epithelium. Thus, it is likely that TJP3 supports proliferation in subconfluent cells but promotes cell cycle inhibition with increasing cell density, as has been previously described for TJP1 (also known as ZO1) and TJP2 (also known as ZO2) (44).

Proliferating cells require larger amounts of energy than nonproliferating cells for biomass synthesis (nucleotides, proteins, and membranes) (45). In our model, proliferating cells exhibited an increased utilization of glucose and amino acids, including

glutamine, with a concomitant increased production of lactate and formate. Matured monolayers also exhibited lower oxygen consumption and lactate production rates, further indicating a decreased energy requirement. However, we demonstrated that their oxidative capacity was higher using the uncoupling agent FCCP, and stereology analysis revealed a slightly increased mitochondrial volume. In addition, transcript levels for *peroxisome proliferator-activated receptor gamma, coactivator 1 alpha* (*PPARGC1A*), encoding a crucial factor for mitochondrial biogenesis (46) and fatty acid beta oxidation (47, 48), were increased after confluence was reached. We also observed an increase in the mRNA for the catalytic α subunit of pyruvate dehydrogenase (*PDHA1*). In mitochondria, pyruvate dehydrogenase (PDH) converts pyruvate to acetyl coenzyme A (acetyl-CoA), which is used as a precursor for fatty acid synthesis or is fed into the TCA cycle (49). In addition, genes involved in fatty acid synthesis were highly expressed in proliferating cells, whereas genes implicated in beta-oxidation were predominantly expressed in matured cells. We have previously observed that exposure of differentiated renal and hepatic cells to toxins increases lactate production (18), which is likely due to impairment of mitochondrial oxidative respiration. Thus, to establish whether low glycolysis rates in matured cells are truly dependent on mitochondrial respiration, we measured glycolysis rates after exposure to the cytochrome *c* reductase inhibitor antimycin A. Matured cells reverted back to glycolytic metabolism, thus indicating that (i) their energy requirement is primarily fulfilled by oxidative metabolism and (ii) they can switch to glycolysis when oxidative metabolism does not meet their energy requirements.

The Na^+/K^+ ATPase is the driving force of numerous secondary active transport processes generating an electrical and chemical gradient across the cell membrane (50). In the proximal tubule, approximately 77% of the energy supplied by oxidative metabolism is invested in the Na^+/K^+ ATPase (3). This pump is located on the basolateral membrane in most epithelial cells and consists of a catalytic α subunit, a β subunit, and tissue-specific FXYD proteins (51). FXYD2 is expressed in human fetal liver, pancreas, and kidney (52), as well as in rat, pig, and dog kidneys, but was not detected in several established renal cell lines (NRK-52E, LLC-PK, and MDCK) (53). Here, the mRNA levels of the α1 (*ATP1A1*) and β1 (*ATP1B1*) subunits as well as *FXYD2* were increased at confluence and maintained at high levels. In contrast, *FXYD5* was highly expressed in proliferating cells (day 1) and decreased on subsequent days. *FXYD5* overexpression has previously been shown to decrease *CDH1* and *alpha catenin* levels (26). Thus, our data suggest that the expression of tissue-specific subunits of this pump is also promoted when the cells reach confluence.

Several genes involved in the cilium biogenesis and cilium function exhibited increased expression over the maturation process, including *PCDP1*, *BBS1*, and *BBS12*. Renal epithelial cells contain a nonmotile primary cilium (14), which is thought to be involved in the maintenance of tubular integrity and luminal fluid sensing. Mounting evidence suggests a role for the deregulation of specific cilia proteins in renal cystic disease, including polycystic kidney disease and Bardet-Biedl syndrome (BBS) (54). BBS arises due to mutations in one of the several BBS-encoding genes or chaperones and has multiple nonrenal manifestations, although renal dysfunction is the major cause of morbidity and mortality (55). We recently demonstrated that carcinogen exposure can induce the loss of primary cilia and that *BBS1* is one of the genes heavily attenuated by potassium bromate and ochratoxin A exposure (56).

Utilizing the temporal alterations in the transcriptome, we performed a transcription factor activation prediction using IPA. The analysis revealed p53 (TP53) as the most active transcription factor in the matured epithelium, which was confirmed by quantifying p53 TF activity. This highlights the central role of p53 in epithelial maturation by promoting cell cycle arrest, oxidative phosphorylation, and suppression of glycolysis, as has been shown within different cellular contexts (57, 58). Other transcription factors that were predicted to be activated in the matured epithelium included CDKN2A (p16) and retinoblastoma 1 (RB1). CDKN2A disrupts cyclin D complexes (59), preventing cyclin D-mediated retinoblastoma protein (RB) phosphorylation and causing G_1 cell cycle arrest (60). In addition, hypophosphorylated RB1 binds and inhibits E2F transcription factors (61, 62). E2Fs have a central role in mediating G_1/S transition (63), and E2F1, -2, and -3 were predicted to be active during proliferation. The highest predicted activity for transcription factors during proliferation was TBX2 (T-box 2). This transcription factor is overexpressed in several cancers and promotes proliferation and metastasis by repressing $p14^{ARF}$ (an alternating reading frame product of *CDKN2A*), *CDKN1A* (also known as p21), N-*myc downregulated gene 1* (*NDRG1*) and *CDH1* (64). Additionally, c-MYC and HIF1A exhibited higher transcriptional activity rates in proliferating cells. Both transcription factors induce the transcription of *pyruvate dehydrogenase kinase 1* (*PDK1*) (65, 66), whose product phosphorylates and inactivates PDH, thereby promoting glycolysis. Here, *PDHA1* mRNA was expressed at very low levels in highly proliferating cells. FOXM1 (forkhead box M1) and FOXO1 (forkhead box O1) were also predicted to be active in proliferating cells. FOXM1 stimulates proliferation by regulating the genes involved in G_1/S, S, G_2/M, and M cell cycle phase progression. It also *trans*-activates MYC (67).

In contrast to its predicted activation state (early activation), FOXO1 exhibited higher activity in the matured epithelium. The FOXO family of TFs are tumor suppressors and have multiple roles in cell cycle inhibition, apoptosis, cellular stress response, and regulation of energy metabolism (68). The gene for insulin-like growth factor binding protein 1 (*IGFBP1*), a target of FOXO1 (69, 70), is highly expressed during proliferation in the microarray data set, consistent with the predicted activation. On the other hand, some regulated FOXO1 targets involved in cell cycle inhibition, like the *CDKN1B* protein (also known as p27) (71) and the *CDKN1C* protein (also known as p57) (72), or in the regulation of energy metabolism, like the *PPARGC1A* protein (73), are expressed at low levels in the subconfluent monolayer. Interestingly, Nowak et al. (74) reported that expression of FOXO1 and FOXO3 was induced by E2F1, another predicted early activated TF. The FOXO TFs have overlapping targets and activities, and their specificity depends on cell type, cellular context, and environmental stimuli (75). FOXO1 is ubiquitously expressed but is highest in insulin-responsive tissues, whereas FOXO3, which was predicted in this study to be in the group of late-activated TFs, is primarily expressed in kidney, brain, heart, and ovaries. Constitutively expression of FOXO1 in mouse liver resulted in the suppression of *de novo* lipogenesis, upregulation of genes involved in gluconeogenesis and protein and amino acid catabolism, whereas genes

implicated in glycolysis, pentose phosphate shunt, and fatty acid and sterol synthesis were downregulated (76).

In summary, this study provides an extensive unbiased characterization of the transcriptional, metabolic, and functional alterations during epithelial monolayer maturation of proximal tubular epithelial cells (summarized in Fig. 9). We show that proliferating cells have a higher energy demand with both increased glycolysis and oxygen consumption and exhibit an immature cell-to-cell junction complex with nuclear TJP3 expression and high activity of HIF1A and c-MYC. The matured monolayers have lower energy demands, express TJP3, claudin 2, and claudin 10 at the intercellular junctions, and exhibit high activities of p53 and FOXO1. Given the main role for these processes in physiological function and disease states such as cancer and fibrosis, these data will be of great benefit in the further delineation of these complex cellular pathways. Finally, these data will serve as a reference for the development of differentiation strategies of inducible pluripotent stem cells to a proximal-tubule phenotype.

ACKNOWLEDGMENTS

This work was primarily supported by the European Union's Seventh Framework Programme (FP7/2007-2013), project Predict-IV, grant agreement 202222. Additional funding from the Sixth Framework Project carcinoGENOMICS (PL037712) is also acknowledged.

REFERENCES

1. **Jennings P, Koppelstaetter C, Lechner J, Pfaller W.** 2008. Renal culture models: contribution to the understanding of nephrotoxic mechanisms, p. 223–250. *In* Broe ME, Porter GA (ed), Clinical nephrotoxins: renal injury from drugs and chemicals, 3rd ed. Springer, New York, NY.
2. **Muto S, Hata M, Taniguchi J, Tsuruoka S, Moriwaki K, Saitou M, Furuse K, Sasaki H, Fujimura A, Imai M, Kusano E, Tsukita S, Furuse M.** 2010. Claudin-2-deficient mice are defective in the leaky and cation-selective paracellular permeability properties of renal proximal tubules. Proc. Natl. Acad. Sci. U. S. A. **107**:8011–8016.
3. **Gstraunthaler G, Pfaller W, Kotanko P.** 1985. Interrelation between oxygen consumption and Na-K-ATPase activity in rat renal proximal tubule suspension. Ren. Physiol. **8**:38–44.
4. **Pfaller W, Gstraunthaler G.** 1998. Nephrotoxicity testing in vitro–what we know and what we need to know. Environ. Health Perspect **106**(Suppl. 2):559–569.
5. **Jennings P.** 2009. Epithelial cell cultures as tools to study human disease and the adverse effects of pharmaceuticals and chemicals. Habilitation thesis. Medizinische Universität Innsbruck, Innsbruck, Austria.
6. **Wilmes A, Crean D, Aydin S, Pfaller W, Jennings P, Leonard MO.** 2011. Identification and dissection of the Nrf2 mediated oxidative stress pathway in human renal proximal tubule toxicity. Toxicol. In Vitro **25**:613–622.
7. **Lima WR, Parreira KS, Devuyst O, Caplanusi A, N'Kuli F, Marien B, Van Der Smissen P, Alves PM, Verroust P, Christensen EI, Terzi F, Matter K, Balda MS, Pierreux CE, Courtoy PJ.** 2010. ZONAB promotes proliferation and represses differentiation of proximal tubule epithelial cells. J. Am. Soc. Nephrol. **21**:478–488.
8. **Moncada S, Higgs EA, Colombo SL.** 2012. Fulfilling the metabolic requirements for cell proliferation. Biochem. J. **446**:1–7.
9. **Ullrich SJ, Anderson CW, Mercer WE, Appella E.** 1992. The p53 tumor suppressor protein, a modulator of cell proliferation. J. Biol. Chem. **267**: 15259–15262.
10. **Syed V, Mak P, Du C, Balaji KC.** 2008. Beta-catenin mediates alteration in cell proliferation, motility and invasion of prostate cancer cells by differential expression of E-cadherin and protein kinase D1. J. Cell. Biochem. **104**:82–95.
11. **Miyoshi J, Takai Y.** 2005. Molecular perspective on tight-junction assembly and epithelial polarity. Adv. Drug Deliv. Rev. **57**:815–855.
12. **Balda MS, Garrett MD, Matter K.** 2003. The ZO-1-associated Y-box factor ZONAB regulates epithelial cell proliferation and cell density. J. Cell Biol. **160**:423–432.
13. **Jennings P, Koppelstaetter C, Aydin S, Abberger T, Wolf AM, Mayer G, Pfaller W.** 2007. Cyclosporine A induces senescence in renal tubular epithelial cells. Am. J. Physiol. Renal Physiol. **293**:F831–F838.
14. **Wieser M, Stadler G, Jennings P, Streubel B, Pfaller W, Ambros P, Riedl C, Katinger H, Grillari J, Grillari-Voglauer R.** 2008. hTERT alone immortalizes epithelial cells of renal proximal tubules without changing their functional characteristics. Am. J. Physiol. Renal Physiol. **295**:F1365–1375.
15. **Zidek N, Hellmann J, Kramer PJ, Hewitt PG.** 2007. Acute hepatotoxicity: a predictive model based on focused Illumina microarrays. Toxicol. Sci. **99**:289–302.
16. **Bolstad BM, Irizarry RA, Astrand M, Speed TP.** 2003. A comparison of normalization methods for high density oligonucleotide array data based on variance and bias. Bioinformatics **19**:185–193.
17. **Simon R, Lam A, Li MC, Ngan M, Menenzes S, Zhao Y.** 2007. Analysis of gene expression data using BRB-ArrayTools. Cancer Inform. **3**:11–17.
18. **Limonciel A, Aschauer L, Wilmes A, Prajczer S, Leonard MO, Pfaller W, Jennings P.** 2011. Lactate is an ideal non-invasive marker for evaluating temporal alterations in cell stress and toxicity in repeat dose testing regimes. Toxicol. In Vitro **25**:1855–1862.
19. **Jennings P, Aydin S, Bennett J, McBride R, Weiland C, Tuite N, Gruber LN, Perco P, Gaora PO, Ellinger-Ziegelbauer H, Ahr HJ, Kooten CV, Daha MR, Prieto P, Ryan MP, Pfaller W, McMorrow T.** 2009. Inter-laboratory comparison of human renal proximal tubule (HK-2) transcriptome alterations due to cyclosporine A exposure and medium exhaustion. Toxicol. In Vitro **23**:486–499.
20. **Ellis JK, Athersuch TJ, Cavill R, Radford R, Slattery C, Jennings P, McMorrow T, Ryan MP, Ebbels TM, Keun HC.** 2011. Metabolic response to low-level toxicant exposure in a novel renal tubule epithelial cell system. Mol. Biosyst. **7**:247–257.
21. **Pfaller W, Gstraunthaler G, Loidl P.** 1990. Morphology of the differentiation and maturation of LLC-PK1 epithelia. J. Cell. Physiol. **142**:247–254.
22. **Weibel ER.** 1979. Morphometry of the human lung: the state of the art after two decades. Bull. Eur. Physiopathol. Respir. **15**:999–1013.
23. **Giepmans BN, van Ijzendoorn SC.** 2009. Epithelial cell-cell junctions and plasma membrane domains. Biochim. Biophys. Acta **1788**:820–831.
24. **Balda MS, Matter K.** 2009. Tight junctions and the regulation of gene expression. Biochim. Biophys. Acta **1788**:761–767.
25. **Terada H.** 1990. Uncouplers of oxidative phosphorylation. Environ. Health Perspect. **87**:213–218.
26. **Ino Y, Gotoh M, Sakamoto M, Tsukagoshi K, Hirohashi S.** 2002. Dysadherin, a cancer-associated cell membrane glycoprotein, down-regulates E-cadherin and promotes metastasis. Proc. Natl. Acad. Sci. U. S. A. **99**:365–370.
27. **Lee TH, Streb JW, Georger MA, Miano JM.** 2006. Tissue expression of the novel serine carboxypeptidase Scpep1. J. Histochem. Cytochem. **54**: 701–711.
28. **Baum B, Georgiou M.** 2011. Dynamics of adherens junctions in epithelial establishment, maintenance, and remodeling. J. Cell Biol. **192**:907–917.
29. **Yonemura S.** 2011. Cadherin-actin interactions at adherens junctions. Curr. Opin. Cell Biol. **23**:515–522.
30. **Harrison OJ, Jin X, Hong S, Bahna F, Ahlsen G, Brasch J, Wu Y, Vendome J, Felsovalyi K, Hampton CM, Troyanovsky RB, Ben-Shaul A, Frank J, Troyanovsky SM, Shapiro L, Honig B.** 2011. The extracellular architecture of adherens junctions revealed by crystal structures of type I cadherins. Structure **19**:244–256.
31. **Johnson E, Theisen CS, Johnson KR, Wheelock MJ.** 2004. R-cadherin influences cell motility via Rho family GTPases. J. Biol. Chem. **279**:31041–31049.
32. **Thomson RB, Igarashi P, Biemesderfer D, Kim R, Abu-Alfa A, Soleimani M, Aronson PS.** 1995. Isolation and cDNA cloning of Ksp-cadherin, a novel kidney-specific member of the cadherin multigene family. J. Biol. Chem. **270**:17594–17601.
33. **Mullin JM, Fluk L, Tchao R.** 1985. Mitosis in domes of renal epithelial (LLC-PK[1]) cell cultures. Mol. Physiol. **8**:317–328.
34. **Li J, Ananthapanyasut W, Yu AS.** 2011. Claudins in renal physiology and disease. Pediatr. Nephrol. **26**:2133–2142.
35. **Kirk A, Campbell S, Bass P, Mason J, Collins J.** 2010. Differential expression of claudin tight junction proteins in the human cortical nephron. Nephrol. Dial. Transplant. **25**:2107–2119.
36. **Furuse M, Furuse K, Sasaki H, Tsukita S.** 2001. Conversion of zonulae occludentes from tight to leaky strand type by introducing claudin-2 into Madin-Darby canine kidney I cells. J. Cell Biol. **153**:263–272.
37. **Rosenthal R, Milatz S, Krug SM, Oelrich B, Schulzke JD, Amasheh S,**

Gunzel D, Fromm M. 2010. Claudin-2, a component of the tight junction, forms a paracellular water channel. J. Cell Sci. **123**:1913–1921.
38. **Van Itallie CM, Rogan S, Yu A, Vidal LS, Holmes J, Anderson JM.** 2006. Two splice variants of claudin-10 in the kidney create paracellular pores with different ion selectivities. Am. J. Physiol. Renal Physiol. **291**:F1288–F1299.
39. **Limonciel A, Wilmes A, Aschauer L, Radford R, Bloch KM, McMorrow T, Pfaller W, van Delft JH, Slattery C, Ryan MP, Lock EA, Jennings P.** 2012. Oxidative stress induced by potassium bromate exposure results in altered tight junction protein expression in renal proximal tubule cells. Arch. Toxicol. **86**:1741–1751.
40. **Jennings P, Limonciel A, Felice L, Leonard MO.** 2012. An overview of transcriptional regulation in response to toxicological insult. Arch. Toxicol. **87**:49–72.
41. **Capaldo CT, Koch S, Kwon M, Laur O, Parkos CA, Nusrat A.** 2011. Tight function zonula occludens-3 regulates cyclin D1-dependent cell proliferation. Mol. Biol. Cell **22**:1677–1685.
42. **Sourisseau T, Georgiadis A, Tsapara A, Ali RR, Pestell R, Matter K, Balda MS.** 2006. Regulation of PCNA and cyclin D1 expression and epithelial morphogenesis by the ZO-1-regulated transcription factor ZONAB/DbpA. Mol. Cell. Biol. **26**:2387–2398.
43. **Traweger A, Lehner C, Farkas A, Krizbai IA, Tempfer H, Klement E, Guenther B, Bauer HC, Bauer H.** 2008. Nuclear Zonula occludens-2 alters gene expression and junctional stability in epithelial and endothelial cells. Differentiation **76**:99–106.
44. **Bauer H, Zweimueller-Mayer J, Steinbacher P, Lametschwandtner A, Bauer HC.** 2010. The dual role of zonula occludens (ZO) proteins. J. Biomed. Biotechnol. **2010**:402593. doi:10.1155/2010/402593.
45. **Mulukutla BC, Khan S, Lange A, Hu WS.** 2010. Glucose metabolism in mammalian cell culture: new insights for tweaking vintage pathways. Trends Biotechnol. **28**:476–484.
46. **Lehman JJ, Barger PM, Kovacs A, Saffitz JE, Medeiros DM, Kelly DP.** 2000. Peroxisome proliferator-activated receptor gamma coactivator-1 promotes cardiac mitochondrial biogenesis. J. Clin. Invest. **106**:847–856.
47. **Burgess SC, Leone TC, Wende AR, Croce MA, Chen Z, Sherry AD, Malloy CR, Finck BN.** 2006. Diminished hepatic gluconeogenesis via defects in tricarboxylic acid cycle flux in peroxisome proliferator-activated receptor gamma coactivator-1alpha (PGC-1alpha)-deficient mice. J. Biol. Chem. **281**:19000–19008.
48. **Vega RB, Huss JM, Kelly DP.** 2000. The coactivator PGC-1 cooperates with peroxisome proliferator-activated receptor alpha in transcriptional control of nuclear genes encoding mitochondrial fatty acid oxidation enzymes. Mol. Cell. Biol. **20**:1868–1876.
49. **Sugden MC, Holness MJ.** 2003. Recent advances in mechanisms regulating glucose oxidation at the level of the pyruvate dehydrogenase complex by PDKs. Am. J. Physiol. Endocrinol. Metab. **284**:E855–862.
50. **Lingrel JB, Kuntzweiler T.** 1994. Na^+,K^+-ATPase. J. Biol. Chem. **269**:19659–19662.
51. **Geering K.** 2008. Functional roles of Na,K-ATPase subunits. Curr. Opin. Nephrol. Hypertens. **17**:526–532.
52. **Kim JW, Lee Y, Lee IA, Kang HB, Choe YK, Choe IS.** 1997. Cloning and expression of human cDNA encoding Na^+,K^+-ATPase gamma-subunit. Biochim. Biophys. Acta **1350**:133–135.
53. **Therien AG, Goldshleger R, Karlish SJ, Blostein R.** 1997. Tissue-specific distribution and modulatory role of the gamma subunit of the Na,K-ATPase. J. Biol. Chem. **272**:32628–32634.
54. **Yoder BK.** 2007. Role of primary cilia in the pathogenesis of polycystic kidney disease. J. Am. Soc. Nephrol. **18**:1381–1388.
55. **Forsythe E, Beales PL.** 2013. Bardet-Biedl syndrome. Eur. J. Hum. Genet. **21**:8–13.
56. **Radford R, Slattery C, Jennings P, Blaque O, Pfaller W, Gmuender H, Van Delft J, Ryan MP, McMorrow T.** 2012. Carcinogens induce loss of the primary cilium in human renal proximal tubular epithelial cells independently of effects on the cell cycle. Am. J. Physiol. Renal Physiol. **302**:F905–F916.
57. **Puzio-Kuter AM.** 2011. The role of p53 in metabolic regulation. Genes Cancer **2**:385–391.
58. **Wang PY, Zhuang J, Hwang PM.** 2012. p53: exercise capacity and metabolism. Curr. Opin. Oncol. **24**:76–82.
59. **Russo AA, Tong L, Lee JO, Jeffrey PD, Pavletich NP.** 1998. Structural basis for inhibition of the cyclin-dependent kinase Cdk6 by the tumour suppressor p16INK4a. Nature **395**:237–243.
60. **Shapiro GI, Edwards CD, Rollins BJ.** 2000. The physiology of p16(INK4A)-mediated G_1 proliferative arrest. Cell Biochem. Biophys. **33**:189–197.
61. **Chellappan SP, Hiebert S, Mudryj M, Horowitz JM, Nevins JR.** 1991. The E2F transcription factor is a cellular target for the RB protein. Cell **65**:1053–1061.
62. **Lees JA, Saito M, Vidal M, Valentine M, Look T, Harlow E, Dyson N, Helin K.** 1993. The retinoblastoma protein binds to a family of E2F transcription factors. Mol. Cell. Biol. **13**:7813–7825.
63. **DeGregori J, Johnson DG.** 2006. Distinct and overlapping roles for E2F family members in transcription, proliferation and apoptosis. Curr. Mol. Med. **6**:739–748.
64. **Lu J, Li XP, Dong Q, Kung HF, He ML.** 2010. TBX2 and TBX3: the special value for anticancer drug targets. Biochim. Biophys. Acta **1806**:268–274.
65. **Kim JW, Gao P, Liu YC, Semenza GL, Dang CV.** 2007. Hypoxia-inducible factor 1 and dysregulated c-Myc cooperatively induce vascular endothelial growth factor and metabolic switches hexokinase 2 and pyruvate dehydrogenase kinase 1. Mol. Cell. Biol. **27**:7381–7393.
66. **Kim JW, Tchernyshyov I, Semenza GL, Dang CV.** 2006. HIF-1-mediated expression of pyruvate dehydrogenase kinase: a metabolic switch required for cellular adaptation to hypoxia. Cell Metab. **3**:177–185.
67. **Wierstra I, Alves J.** 2007. FOXM1, a typical proliferation-associated transcription factor. Biol. Chem. **388**:1257–1274.
68. **van der Vos KE, Coffer PJ.** 2011. The extending network of FOXO transcriptional target genes. Antioxid. Redox Signal. **14**:579–592.
69. **Guo S, Rena G, Cichy S, He X, Cohen P, Unterman T.** 1999. Phosphorylation of serine 256 by protein kinase B disrupts transactivation by FKHR and mediates effects of insulin on insulin-like growth factor-binding protein-1 promoter activity through a conserved insulin response sequence. J. Biol. Chem. **274**:17184–17192.
70. **Hall RK, Yamasaki T, Kucera T, Waltner-Law M, O'Brien R, Granner DK.** 2000. Regulation of phosphoenolpyruvate carboxykinase and insulin-like growth factor-binding protein-1 gene expression by insulin. The role of winged helix/forkhead proteins. J. Biol. Chem. **275**:30169–30175.
71. **Medema RH, Kops GJ, Bos JL, Burgering BM.** 2000. AFX-like Forkhead transcription factors mediate cell-cycle regulation by Ras and PKB through p27kip1. Nature **404**:782–787.
72. **Takano M, Lu Z, Goto T, Fusi L, Higham J, Francis J, Withey A, Hardt J, Cloke B, Stavropoulou AV, Ishihara O, Lam EW, Unterman TG, Brosens JJ, Kim JJ.** 2007. Transcriptional cross talk between the forkhead transcription factor forkhead box O1A and the progesterone receptor coordinates cell cycle regulation and differentiation in human endometrial stromal cells. Mol. Endocrinol. **21**:2334–2349.
73. **Daitoku H, Yamagata K, Matsuzaki H, Hatta M, Fukamizu A.** 2003. Regulation of PGC-1 promoter activity by protein kinase B and the forkhead transcription factor FKHR. Diabetes **52**:642–649.
74. **Nowak K, Killmer K, Gessner C, Lutz W.** 2007. E2F-1 regulates expression of FOXO1 and FOXO3a. Biochim. Biophys. Acta **1769**:244–252.
75. **Calnan DR, Brunet A.** 2008. The FoxO code. Oncogene **27**:2276–2288.
76. **Zhang W, Patil S, Chauhan B, Guo S, Powell DR, Le J, Klotsas A, Matika R, Xiao X, Franks R, Heidenreich KA, Sajan MP, Farese RV, Stolz DB, Tso P, Koo SH, Montminy M, Unterman TG.** 2006. FoxO1 regulates multiple metabolic pathways in the liver: effects on gluconeogenic, glycolytic, and lipogenic gene expression. J. Biol. Chem. **281**:10105–10117.